THE UNIVERSITY OF HULL

Quantification of Bone Using a 3.0 Tesla Clinical Magnetic Resonance Scanner

being a Thesis submitted for the Degree of

Doctor of Philosophy

in The University of Hull

by

Victor Rakesh Lazar, MSc Medical Imaging (University of Aberdeen)

December, 2011

Summary of Thesis submitted for PhD degree

by

Victor Rakesh Lazar

on

Quantification of Bone Using a 3.0 Tesla Clinical Magnetic Resonance Scanner

The work in this thesis examines the potential of using magnetic resonance imaging and spectroscopy (MRI & MRS) as a quantitative tool for diagnosing bone abnormalities at multiple skeletal sites, which could be used in conjunction with routine clinical imaging.

MRI and MRS are routinely used in the clinical setting for the diagnosis of various types of diseases and abnormalities due to its advantages of providing excellent soft tissue contrast and also providing physiological and metabolic information. The use of MRI and MRS as a direct diagnostic tool for bone abnormalities is very limited at the moment due to issues of costs and standardisation. The aim in this thesis was to use the clinical 3.0 T MR scanner to acquire data from bone and bone marrow for identification of structural and chemical properties and to use those features to identify differences in bone strength and condition. The volunteers in this thesis were part of the high bone mass (HBM) study and they had additional acquisitions from dual-energy X-ray absorptiometry (DEXA) and peripheral quantitative computed tomography (pQCT).

MR acquisition protocols have been successfully optimised for each type of bone region and in-house software has also been created to process the acquired data and quantify various types of structural and chemical properties.

The MR data from distal radius and tibia demonstrated good correlation with pQCT data (e.g. Figure 8-2 & Figure 8-3) and were also able to differentiate between HBM-affected and control populations (e.g. Figure 8-26). The MR data from lumbar vertebrae also demonstrated good correlation with DEXA data and some of the measurements were also able to differentiate between the HBM-affected and control populations.

The combined results from this thesis demonstrate that both MRI and MRS are sensitive techniques for measurement of bone quantity and quality, and they are ready to be applied for clinical investigation as part of routine clinical imaging to identify bone strength in relation to abnormalities and treatments.

Acknowledgements

Most importantly, I would like to acknowledge Yorkshire Cancer Research (YCR) for its generous financial support for this research and to the Centre for Magnetic Resonance Investigations (CMRI) at The University of Hull. I would also like to acknowledge the High Bone Mass (HBM) study group from University of Bristol for their collaboration and also for identifying the volunteers and data in this thesis.

I would like to acknowledge all the volunteers who happily participated in this thesis for all the data acquisitions and experiments. I would also like to thank all the staff at CMRI for their support, advice and feedback in all the years of my research and helping me to shape my academic research.

I would like to thank Dr Gary Liney and Dr David Manton my supervisors for guiding me through each and every stage in all the years of my research with their determination, advice, support and care by being my teachers as well as friends. Dr Gary Liney for introducing me to MATLAB processing and magnetic resonance (MR) data acquisitions. Dr David Manton for introducing me to advanced MR spectroscopy (MRS) and statistical analysis. Mrs Sudha Pattan (Sri Ramachandra University, India) for her great lectures in radiology during my undergraduate years and encouraging me to proceed further with education and research. Professor Lindsay Turnbull (Scientific Director of CMRI) for giving me this great opportunity of studying at CMRI and also for her continuous support and help throughout my research. Dr Peter Gibbs for all the discussions and reviews, and Dr Martin Lowry for his help on LC-Model and MRS data processing. Dr Martin Pickles and Dr Martine Dujardin for their support and advice on this thesis.

I would like to thank Dr Celia Gregson (University of Bristol) for her continuous support and advice on HBM study and volunteer recruitment. Professor Joern Rittweger (Manchester Metropolitan University & DLR-Institute of Aerospace Medicine) for his training and support on peripheral quantitative computed tomography (pQCT) and jump mechanography. I would also like to thank the staff at the Metabolic Bone Disease Unit (Hull Royal Infirmary) for their advice and support on dual-energy X-ray absorptiometry (DEXA) used in this thesis.

I would like to thank the secretarial staff at CMRI and the graduate school (The University of Hull) for their friendly support and advice during my research years.

Dedication

To my father (Lazar), mother (Clarammal), my brothers and their family, and all my friends for their unconditional support, and also to the memory of Fr Leon de Souza and Nora Beacock.

Contents

1 Introduction to Bone and Bone-Marrow

1.1 Bones and Their Properties

Bone or osseous tissue is an active, rigid living organ, which forms an important part of the endoskeleton of vertebrates (see Figure 1-1). It is lightweight in comparison to the work it performs to support the body. It is basically composed of osseous tissue which is the hard part of the bone, marrow which is the soft tissue present as red and yellow marrow, bone cells present in both cortex and medulla, nerves which carry information to and from the brain, blood vessels for the supply of essential nutrients and cartilage for attachment with bones and joint formation [1-3]. The bones provide some or all of the following functions [3-5]:

- A shell for the protection of our internal organs.
- A structure to support and shape our body.
- A lever to create movements like walking, with the coordinated help from muscles, ligaments, tendons and joints.
- A base for the production of blood cells from its marrow content.
- A reservoir for essential elements and compounds like calcium, phosphorous and fatty acids.
- A buffer for blood pH levels.
- A filter for toxic elements and also for their removal from the system.

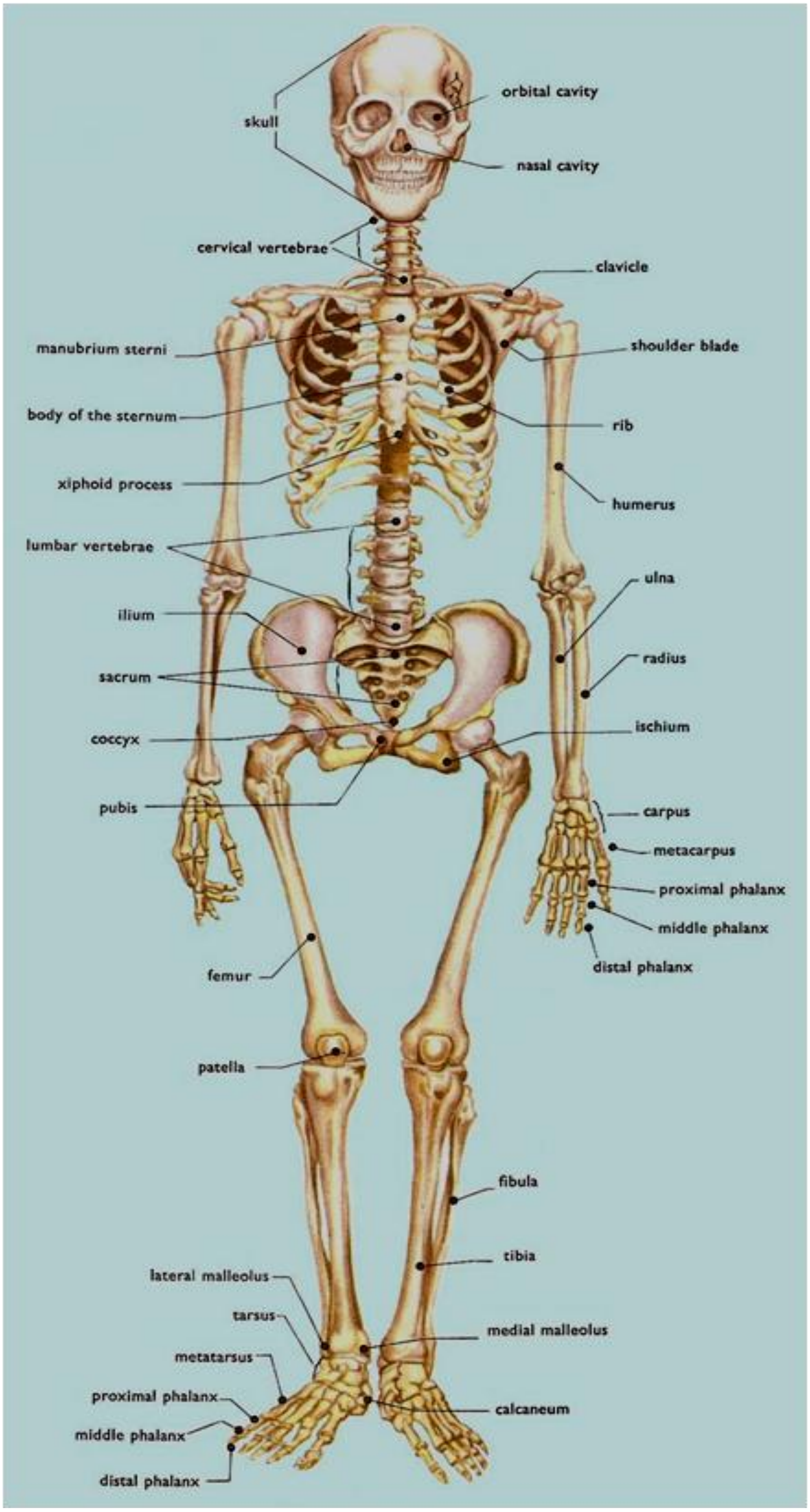

Figure 1-1 Drawing of a human skeleton with labelled anatomy.

(http://www.daviddarling.info/images/human_skeleton.jpg)

1.2 Types of Human Bone

- **Long Bones –** These are mostly composed of compact bone with some marrow in the shaft and at the proximal and distal end points. These are the bones in the limbs, e.g., humerus and femur (see Figure 1-2).
- **Short Bones –** These are club-shaped bones that have a spongy bone surrounded by a thin layer of compact bone, e.g., phalanges.
- **Flat Bones –** These are curved and thin bones with an inner layer of spongy bone sandwiched between outer layers of compact bone. Examples are the skull and sternum.
- **Irregular Bones –** These are irregular-shaped bones, e.g., vertebral bodies.
- **Sesamoid Bones –** These are bones which are strongly linked to other bones often by inclusion within a tendon. Examples are the patella and pisiform bones.

1.3 Structure of a Typical Long Bone (Osseous Tissue)

Long bones like the humerus (see Figure 1-2), radius, femur and tibia have the following structures [1, 3, 5-9].

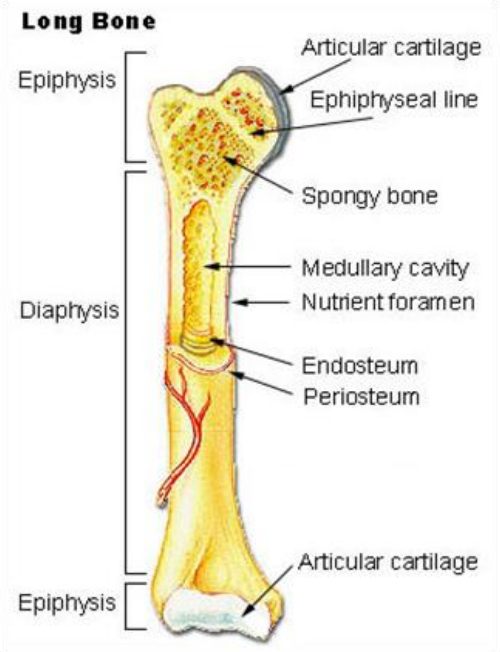

Figure 1-2 Drawing of a long bone (humerus) with illustration of important structures. (http://en.wikipedia.org/wiki/File:Illu_long_bone.jpg)

1.3.1 Diaphysis

This is the central shaft of any long bone, which is commonly cylindrical and tube-like containing the medullary cavity and is the main portion of the bone.

1.3.2 Epiphysis

This is the region in long bones forming the proximal and distal ends. This region is very important in forming joints with adjacent bones. This region commonly contains the spongy bone structure in long bones.

1.3.3 Metaphysis

This is a unique region in long bones formed at the junction between the diaphysis and the epiphysis. This region clearly differentiates the two structures and functions very importantly as the site for growth in length of long bones. In young individuals, this region contains a cartilaginous structure called the epiphyseal plate which is the structure responsible for growth in length of a bone. It forms the epiphyseal line as the bone growth terminates in late adolescence, at about 18-21 years.

1.3.4 Articular Cartilage

The articular cartilage is a layer of hyaline cartilage covering the epiphysis to form an articulating surface with other bones at the joints. This layer of cartilage is very important to protect the epiphysis region from friction and also in absorbing shocks to the bone.

1.3.5 Periosteum

The periosteum is a very thin layer of dense connective tissue which covers the outer surface of bones, except the articular cartilage. This layer is very thin (around 500 µm) and is usually invisible to the naked eye, but is very important for bone growth in thickness rather than height. This layer is important for protection, fracture repair and as attachment points for ligaments and tendons. The periosteum layer is attached to the long bone through strong collagen fibres, termed Sharpey’s fibres.

1.3.6 Medullary Cavity

The medullary cavity is the internal structure of the diaphysis forming a circular canal which commonly contains the bone marrow, blood supply and sometimes a thin network of spongy bone.

1.3.7 Endosteum

The endosteum is a thin layer of connective tissue that lines the surface of the bone tissue within the medullar cavity contained within the diaphysis. It contains a layer of bone-forming cells and connective tissue.

1.4 Individual Bone Components

Bone is not a single solid tissue, but is formed by the compactness of bone cells in matrix-forming canals separated by spaces which are essential for the supply of nutrients, removal of waste and as a storage area for red and yellow bone marrow. The size and distribution of these spaces determine two distinct categories of bone: spongy (trabecular) and compact (cortical) bone (see Figure 1-3). Nearly 80% mass of the total skeleton is cortical and 20% is trabecular bone [1, 2, 4-9].

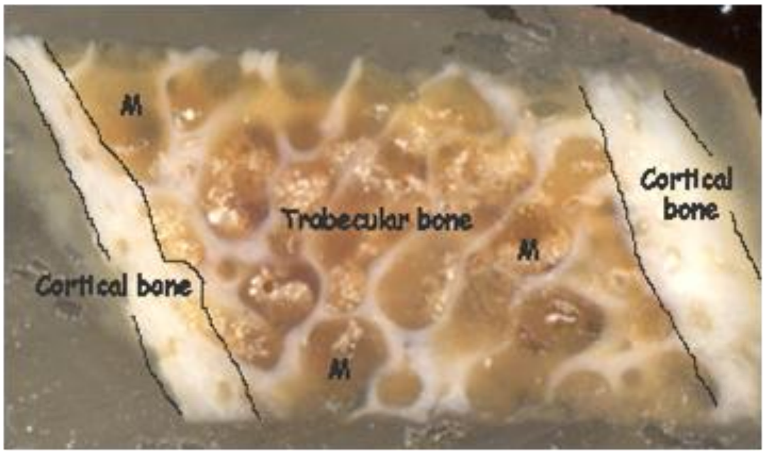

Figure 1-3 Cut section from an iliac crest bone demonstrating the bone regions in relation to cortical and trabecular bone and bone marrow (M).

(http://depts.washington.edu/bonebio/ASBMRed/structure.html)

1.4.1 Cortical (Compact) Bone

Cortical bone contributes to around 80% of the total bone mass of an adult skeleton. This component gives the smooth solid white appearance to the bone. This is also known as compact bone, and it commonly surrounds the trabecular (spongy) bone in a circular or sandwich manner depending on the configuration of the bone (see Figure 1-3 & Figure 1-4). This is the strongest form of osseous tissue, with few spaces and forms the bulk of the diaphysis in long bones. Cortical bone is important for the protection and support of the skeleton. This bone has a complex system of interconnected canals running transversely and longitudinally in relation to the long shaft of the bone. The vessels and nerves from the periosteum penetrate the compact bone through transverse canals called perforating (Volkmann’s) canals. These canals connect with the medullar cavity, periosteum and central (Haversian) canals. The Haversian canals run longitudinally to the line of the bone, surrounded by layers of calcified bone matrix called concentric lamellae, and they resemble the ring type structure found in tree trunks. The spaces between layers of concentric lamellae are called lacunae and these contain osteocytes (see 1.5.3). The lacunae have radiating structures called canaliculi which are filled with extracellular fluid and osteocytes. The canaliculi form an intricate connection with the lacunae and central canals forming interconnecting networks throughout the bone, essential for delivery of nutrients and oxygen, and for the removal of waste from the osteocytes [1-7, 9].

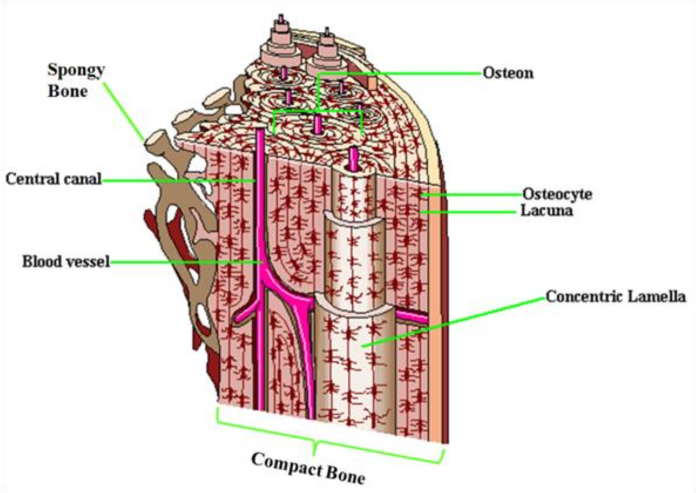

Figure 1-4 Drawing illustrates the labelled structures of compact and spongy bone. (http://www.dmacc.edu/instructors/rbwollaston/Chapter_6_Skeletal_System.htm)

The building components of compact bone, which are arranged in repeating units, are called osteons or Haversian systems. Each osteon consists of a (Haversian) central canal surrounded by lamellae, lacunae, osteocytes and canaliculi. Osteons in compact bone are orientated relative to the line of stress experienced by the bone. In the shaft of long bones, the osteons are arranged parallel to the long axis allowing the bone to withstand compressive forces. The spaces between osteons contain interstitial lamellae which are fragments of older osteons that have been partially destroyed during bone remodelling. The layer that encircles the bone just beneath the periosteum and medullary cavity is called the circumferential lamellae [1, 3-6, 9].

1.4.2 Trabecular (Spongy or Cancellous) Bone

Trabecular bone accounts for the remaining 20% of the total bone mass. This type of bone is commonly present at the epiphysis of long bones and throughout much of the structure of short, irregular and flat bones (see Figure 1-2, Figure 1-3 & Figure 1-4). It is always protected and surrounded by cortical bone. Spongy bones are not physically spongy or flexible in nature, but look spongy visually. These bones do not contain osteons, but consist of lamellae arranged in an irregular lattice of thin columns called trabeculae, giving them the alternative name of trabecular bones. The trabeculae enclose large spaces which are filled by bone marrow, most commonly red marrow but also yellow marrow. These spaces make the bone lighter, which is beneficial for movement of the skeleton. The trabeculae of spongy bone support and protect the bone marrow, which is important for the production of blood cells in haematopoiesis. Within each trabecular space there are lacunae that contain osteocytes. Canaliculi radiate outward from the lacunae. The osteocytes are located superficially and obtain nourishment directly from the blood circulating in the medullary cavity [1, 2, 4-7, 9].

The trabecular arrangement in spongy bone looks random and irregular particularly at the epiphysis and diaphysis. However these irregular patterns are carefully oriented in a direction proportional to the stress experienced by the bone, which is important for increasing the bone's strength and function. Nothing is random in bones, growth and orientation of trabeculae is precise to support the skeleton in terms of varying movements and stress throughout the life of the organism.

1.5 Bone Components and Histology

Bone is composed of an organic matrix which is primarily protein collagen, which contributes to 10% of the adult bone mass. The most abundant mineral salt in bone is calcium phosphate, $Ca_3(PO_4)_2$, which combines with calcium hydroxide, $Ca(OH)_2$, to form crystals of hydroxyapatite. These crystals combine with other mineral salts like calcium carbonate, $CaCO_3$, and ions such as magnesium, fluoride, potassium and sulphate to form hard tissue, by the process of calcification, which is initiated by osteoblasts. All these minerals contribute to about 65% of the adult bone mass. The remaining 25% of the bone mass is made up of water, which can be visualised by magnetic resonance imaging (MRI). The bones contain active living cells designed for their routine work and function (see Figure 1-5) [1, 6, 7, 9]. The cells of the bone are classified as follows:

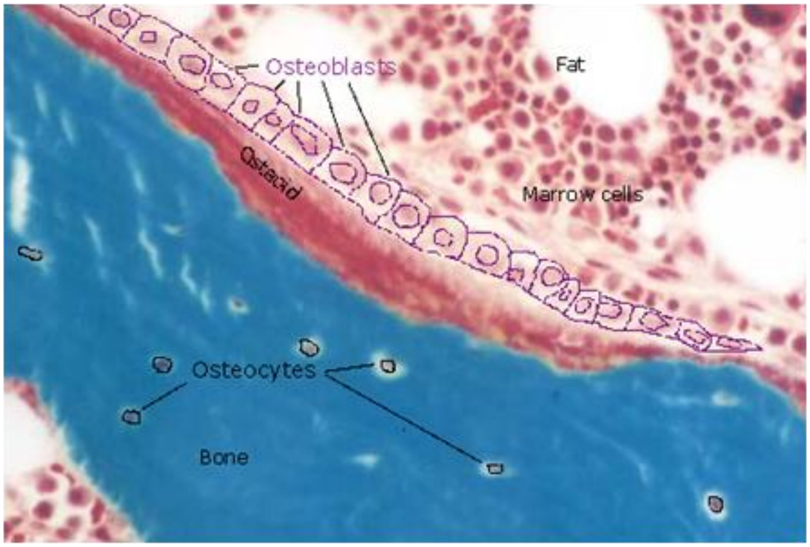

Figure 1-5 Photomicrograph of a bone demonstrating the various cellular components. Photo courtesy of Russ Turner

1.5.1 Osteogenic Cells

These are undifferentiated stem cells. These are derived from mesenchyme tissue, from which all connective tissues develop, and are the only bone cells which undergo cell division and develop into osteoblasts. These cells are commonly found in the inner portion of the periosteum, endosteum and in the canals within bone [1, 3, 5, 6, 8].

1.5.2 Osteoblasts

These are young cells involved in the creation of new bone layers and structures (see Figure 1-5). These cells produce and secrete fibers and organic components for the matrix of the bone and also initiate calcification or formation of osseous hard tissue. Osteoblasts are cells which surround themselves with their secretions to form the bone matrix and get trapped within it to become osteocytes [3, 7, 8, 10, 11].

1.5.3 Osteocytes

These are mature osteoblast cells and are the main cells in bone responsible for the daily metabolism, exchange of nutrients and waste from the blood supply (see Figure 1-5). These cells do not undergo cell division like osteoblasts. Osteocytes also act as sensory receptors for the whole bone and help in the regulation of the bone’s response to stress and load [3, 8, 12].

1.5.4 Osteoclasts

These are large multinucleated cells formed from the fusion of monocytes and are commonly found in the endosteum (see Figure 1-6). These cells are essential for bone modelling due to their work in the resorption of old bone matrix. Osteoclasts secrete powerful enzymes and acids which digest proteins and minerals in the bone, which is later filled by new bone formed by the osteoblasts. The balance between the functions of osteoclasts and osteoblasts is vital for the optimum modelling of the bone matrix. Any imbalance in their function will commonly lead to bone diseases such as osteoporosis [5-8, 13, 14].

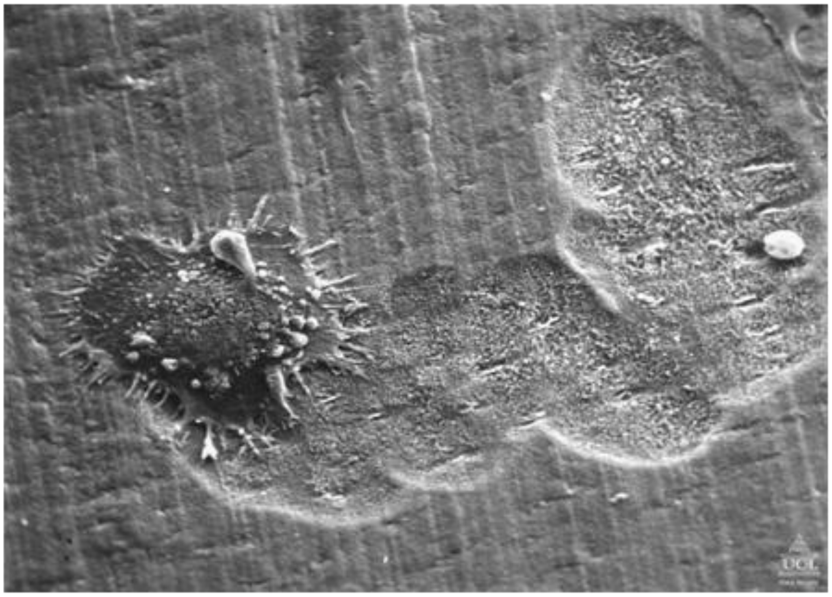

Figure 1-6 Scanning electron micrograph from a bone illustrating the osteoclast cell which is resorbing the bone.

Photo courtesy of Professor Alan Boyde, Queen Mary, University of London, UK

1.6 Bone Marrow and its Composition

Clinical magnetic resonance imaging (MRI) of cortical bone is difficult when using routine imaging sequences, due to the extremely short relaxation time of the bone. The molecules present in bone exist in a compact environment, which results in the slow tumbling of contained hydrogen protons and hence extremely short relaxation times. Routine imaging sequences do not allow the capture of signal from the relaxing spins, but newer scanners and novel sequences can image bones by using ultra short echo times (TE) to capture the signal from relaxing spins. MRI in bone marrow is possible with routine imaging sequences due to the longer relaxation times of protons in bone marrow. Red and yellow bone marrows contain multiple chemical components but predominantly water, lipids/triglycerides (TG) (see Figure 1-7) and proteins. The concentration of these chemical components varies according to the type of marrow present. Red marrow is believed to contain large amounts of water and proteins with lower concentrations of lipids. Yellow marrow is believed to contain large amounts of lipids and lower concentrations of water and proteins. These differences in composition of the marrow are related to the strength and nature of bones or what can be termed bone quality. Magnetic resonance spectroscopy (MRS) of bone marrow demonstrates a spectrum with distinct peaks, where water is resolved as a single peak at 4.7 parts per million (ppm), but triglycerides (TGs) are dispersed as multiple peaks in relation to their chemical structure and resonance frequency. Chapter 3 will explain in detail the aetiology of these peaks in the spectrum. TGs are lipids present in our body, composed of a combination of glycerol and fatty acid (FA) chains. Glycerol forms the backbone for lipids which combine with FA to form diglycerides and triglycerides, and in humans it is commonly present as TG [1, 3, 4, 8, 15-20].

1.6.1 Red (Haematopoietic) Marrow

Red marrow is essential for the production of red blood cells (RBC), white blood cells (WBC), platelets and bone cells. Up to the age of 7 nearly all bones in the human skeleton contain red marrow due to high demand during growth and development. This red marrow gradually gets replaced by yellow marrow during adulthood, old age and sometimes in disease states. Red marrow is essential due to its production of stem cells which can develop into various types of cells depending on their need and activation. In adulthood the red marrow tends to be concentrated in the axial skeleton, hip, flat bones and in the proximal ends of long bones, particularly the humerus and femur. Red marrow contains two types of stem cells: hematopoietic cells which develop into blood cells, and stromal cells which develop into fat, cartilage and bone. Red marrow contains large amounts of water, with moderate concentrations of lipid and protein. This composition is helpful in identifying the type of marrow with magnetic resonance imaging and spectroscopy [4, 7, 8, 16].

1.6.2 Yellow (Fatty) Marrow

Yellow, or fatty, bone marrow is commonly found in the peripheral bones after adulthood. As the name suggests, this marrow contains a large amount of fat when compared with red marrow, which leads to its characteristic yellow appearance. Yellow marrow is believed to be formed from red marrow as the fat content increases with age. It also acts as a storage medium for TG which can then be released during demand. Yellow marrow is sometimes responsible for the production of WBC. Yellow marrow is broadly classified into two categories: category 1, which can revert back to red marrow during extreme demand for blood cells during blood loss, injury or disease, and category 2 is the type of yellow marrow which cannot revert back to red marrow under any circumstances [4, 8, 16].

1.6.3 Water

55-60% of the human body mass is made up of water (H_2O) which is essential and is found everywhere. The concentration of water varies according to the type of tissue. The skeletal system contains a very low concentration of water (20-25%) when compared with other organs in the body (60-85%). The lower concentration of water in the skeleton is due to the presence of dense cortical bone comprising minerals of calcium and phosphorus. The spongy bone contains more water than cortical bone due to the presence of bone marrow (red and yellow). It is believed that red marrow contains more water than yellow marrow. Previous work [8, 17, 21] has illustrated, that in certain disease states, individuals have lower bone water content when compared with normal individuals.

1.6.4 Triglycerides and Fatty Acids

Lipids are a broad group of molecules which include fatty acids and their derivatives, namely phospholipids, tri-, di- and monoglycerides. Triglyceride is a form of lipid that is commonly present in bone marrow. Triglycerides contain three chains of fatty acids (FA) attached to the glycerol backbone (see Figure 1-7 (left)). The FA chains can be saturated, monounsaturated or polyunsaturated as explained in Figure 1-8 (left). The most common FAs present in bone marrow TGs are linoleic (polyunsaturated), oleic (monounsaturated), linolenic (polyunsaturated), palmitic (saturated) and stearic (saturated) acids. FAs are long or short chains of carbon with one end forming the methyl group and the other end forming the carboxyl group with the middle forming long/short chains of carbon attached to hydrogen. The methyl or ω (omega) end combined with the middle chains form the fatty component of the compound which is insoluble in water, and the carboxyl end forms the acid component which is soluble in water (see Figure 1-8 (right)). If there is a double bond after the third carbon from the methyl end, then it is normally termed ω-3. FAs can be divided into saturated and unsaturated in relation to the types of chemical bonds between carbon atoms. Saturated FAs (SFAs) are chains of carbon atoms with single bonds only. Unsaturated FAs (UFAs) are chains of carbon atom with one or more double bonds. If there is only one double bond then the compound is called an monounsaturated FA (MUFA). If there is more than one double bond then it is called polyunsaturated FA (PUFA) (see Figure 1-8 (left)). The UFAs have two configurations (cis and trans) in relation to the placement of hydrogen with respect to the carbon atom (see Figure 1-8 (right)). The most common configuration is cis where the hydrogen bonds to carbon on the same side. In the trans configuration the hydrogen bonds are attached on opposite sides. The cis configuration produces a kink/bend in the chain whilst the trans carbons align as straight lines. Trans configuration of FAs are harmful to the human body and are found in reused frying oils. Studies have shown that ω-3 and ω-6 FAs are essential to the human body due to its inability to synthesize them, hence they are called essential FAs (EFAs) [3-5, 8, 17, 18, 20, 22].

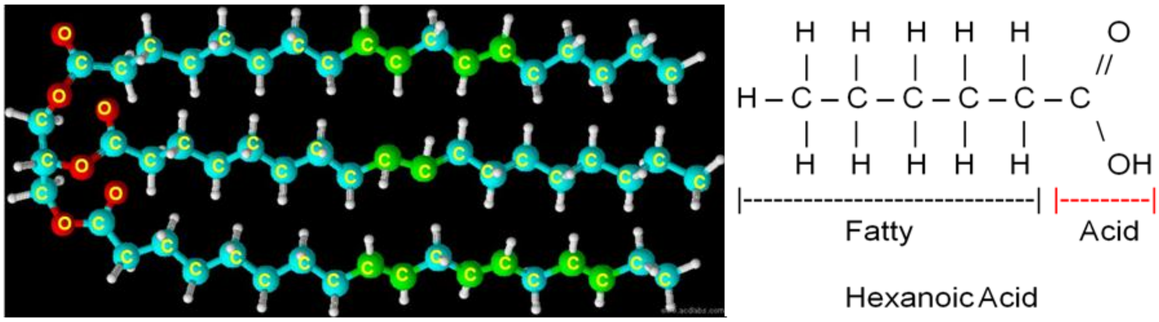

Figure 1-7 The image on the left illustrates a three dimensional chemical structure of triglyceride containing unsaturated fatty acid chains. The green carbon atom contains a double bond and the blue contains a single bond. The image on the right illustrates the chemical structure of a simple fatty acid (hexanoic acid) with description of the fat and acid components.

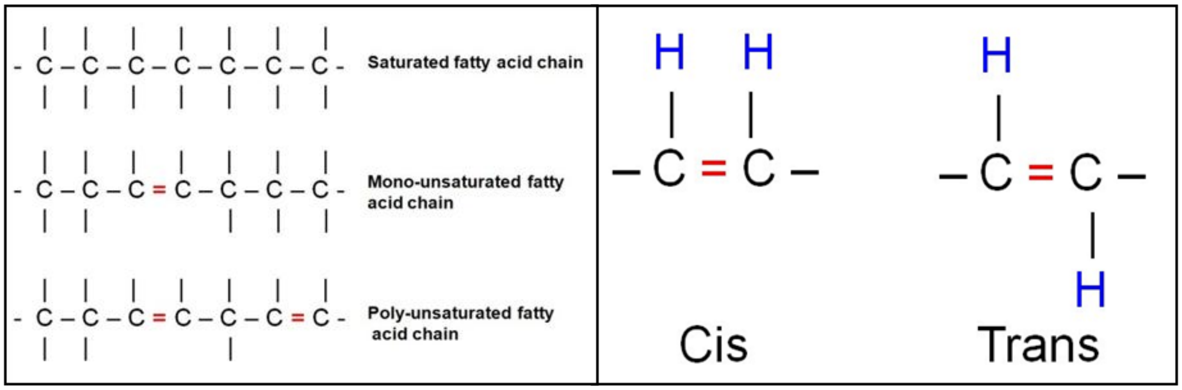

Figure 1-8 The image on the left illustrates the three common types of fatty acid chains. The image on the right illustrates the cis and trans configuration of unsaturated fatty acids.

1.6.5 Glycerol

Glycerol (see Figure 1-9) forms the backbone of triglycerides (TGs) to which the FAs are attached. Glycerol is hygroscopic and soluble in water with low toxicity. The chemical structure is $C_3H_5(OH)_3$ [3, 4, 20].

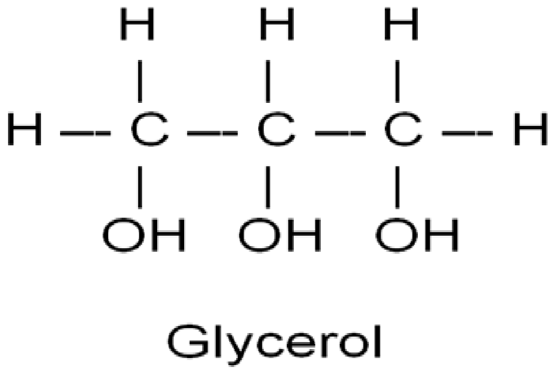

Figure 1-9 The chemical structure of glycerol.

1.7 Common Bone Conditions Which Require Quantification

1.7.1 Osteoporosis

Osteoporosis literally means “porous bones”. It is a disease that leads to an increased risk of fracture secondary to reduced bone mineral density (BMD) and protein content and disruption of the micro-architecture (see Figure 1-10). The World Health Organisation (WHO) defines osteoporosis as areal BMD T-score (see page 32) 2.5 standard deviations (SD) below the normal areal BMD of a 20 year old as measured by dual-energy X-ray absorptiometry (DEXA), a detailed explanation is given in Chapter 2. Osteoporosis is believed to occur because of the imbalance between bone formation and resorption. Medication is available to stop the disease, but they rarely help to regenerate the destroyed bone cells [21, 23-28].

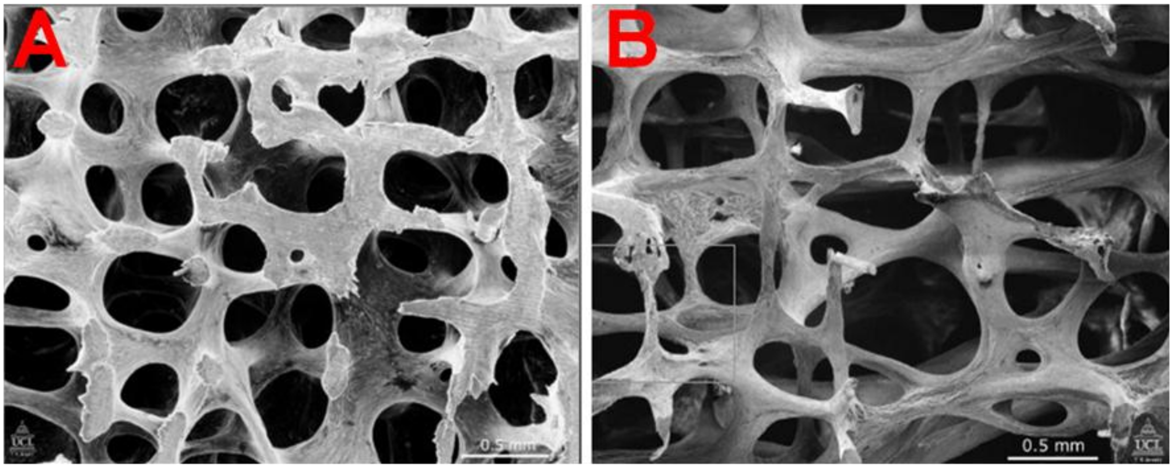

Figure 1-10 Low-power scanning electron microscope image of a normal bone (A) and osteoporotic bone (B) architecture in the 3rd lumbar vertebra of a 30 (A) and 71 (B) year old woman. Marrow has been removed to reveal thick, interconnected plates for normal bone (A) and eroded, fragile rods for osteoporotic bone (B).

Photo courtesy of Dr Tim Arnett, University College London, UK

1.7.2 Osteopaenia

Osteopaenia is a condition believed to be present when BMD is lower than normal. It is often considered as a precursor to osteoporosis, but does not always result in osteoporosis. Specifically, osteopaenia is defined as an areal BMD T-score between -1.0 and -2.5 standard deviations below the normal areal BMD of a 20 year old. A detailed explanation of T-score is given in Chapter 2. The mechanism of osteopaenia is believed to be very similar to osteoporosis [2, 24-26].

1.7.3 Osteomalacia and Ricketts

Osteomalacia and rickets are diseases of bone resulting from decreased mineralisation caused by insufficient calcium intake in the body or deficiency in vitamin-D, the vitamin required for calcium absorption. Osteomalacia and rickets have similar conditions and they are classified based on the differences in age group, osteomalacia is associated with adults and rickets with children. Osteomalacia and rickets commonly result in weakness and bone pain which is similar to osteoporosis. Treatment with vitamin-D supplements, calcium and a stable diet is an effective cure for these diseases. Vitamin-D indirectly functions as a regulator for the concentration of calcium and phosphate in the blood stream of the human body and any deficiency results in osteomalacia or rickets [29, 30].

1.7.4 Osteopetrosis

Osteopetrosis is a rare inherited bone disease which results in dense and hard bones, and literally means ‘stone bone’. It is believed that in osteopetrosis there is reduced osteoclast activity, which results in poor bone resorption and excessive production of bone due to over-active osteoblasts. This phenomenon leads to very dense bone that is inflexible and brittle, and affected people are more prone to fractures. Currently a bone marrow transplant is the only effective treatment for this disease. This might explain why areal BMD measured by DEXA is not the only important factor in bone strength, but other factors like bone quality must also be taken into consideration [10, 23, 31-34].

1.7.5 High Bone Mass

High bone mass (HBM) is a genetic condition which is believed to be influenced by a mutation in the low-density lipoprotein receptor related-protein 5 (LRP5) gene. This is believed to result in affected people having dense and strong bone. The affected people do not report clinical symptoms and lead a normal life. This condition might not be related to an imbalance between osteoclast and osteoblast activity, but may be due to increased activity of both the cell types. A detailed explanation of HBM will follow in Chapter 6 [35-39].

1.7.6 Effects of Cancer Treatments (Chemo/Radiotherapy)

One of the hidden side effects of cancer treatments from chemo or radiotherapy is the loss of bone marrow cells and the induction of an early menopause for women (see 1.7.7). Studies have shown that cancer treatments affect bone marrow cells and induce cell death which affects the turnover of bone. This leads to osteopaenia and will ultimately result in osteoporosis, affecting the normal rehabilitation of patients. Chemotherapy treatments combined with aromatase inhibitor (AI) for breast cancer patients stops the production of oestrogen, and are known to increase the incidence of osteoporosis. Androgen deprivation therapy (ADT) for prostate cancer patients are also known to increase the incidence of osteoporosis. Screening of cancer patients for bone loss might improve the quality of life [19, 40-42].

1.7.7 Menopause

Women during and following the menopause are often diagnosed with symptoms of osteopaenia and osteoporosis. The menopause arises from a loss of function of the ovary, which results in reduced synthesis of oestrogen, a hormone produced mainly by the ovary. The amount of oestrogen plays a major role in the regulation of bone turnover. Continuous screening, monitoring and treatment are an important factor for better quality of life for the affected person. Treatments are available to stop further bone loss, but often do not lead to the regeneration of the lost bone. Hormone replacement therapy (HRT) is another effective treatment for menopausal women, which regulates the level of the natural hormone and controls bone loss, but may be contra-indicated in specific clinical conditions [21, 24, 26, 43, 44].

1.7.8 Drug Related Effects

Evidence has shown that some drugs used for treatment of diseases can also affect the turnover of bone again resulting in enhanced bone loss and fractures. Glucocorticoids used to treat diseases such as allergies, asthma and auto immune conditions are known to shorten the life span of osteoblasts and osteocytes. These steroids affect bone production due to their harmful side effects on osteoblasts and osteoclasts at the genetic level [27, 45-52].

2 Imaging Modalities

2.1 Overview of the Current Diagnostic Tools for Bone Quantification

X-ray is the most common imaging method for bone evaluation. This method suffers from superimposition of tissues due to the projectional nature of the acquisition and also has the disadvantage of using ionising radiation. It is rarely used for quantification, but is commonly used for diagnosis and identification of abnormalities.

Dual-energy X-ray absorptiometry (DEXA) is also a projectional technique and is the gold standard method for quantifying bone mass in relation to disease. It can measure areal bone mineral densities (g/cm^2) throughout the whole-body and is cost effective with a radiation dose of around 0.5-35 µSv.

Quantitative computed tomography (QCT) is a method of bone quantification which uses a clinical computed tomography scanner, combined with a calibration phantom of known density and processing software. QCT acquires volumetric data (mg/cm^3) so does not suffer from superimposition of tissues, and results in accurate quantification of bone density, but suffers from increased radiation dose of around 100 µSv.

Peripheral quantitative computed tomography (pQCT) is a specific application of the CT scanner for the extremities and is commonly used in research settings due to the smaller scanner size and reduced dose. This method produces excellent separation of cortical and trabecular bone.

Quantitative ultrasound (QUS) is a method for bone parameter estimation which uses acoustic sound waves to calculate bone properties. It can be delivered by using a small portable scanner, and is usually limited to quantifying the heel (calcaneum), and is widely used in a clinical setting as a quick tool to measure bone density.

Magnetic resonance imaging (MRI) and magnetic resonance spectroscopy (MRS) have shown great potential in studying bone parameters and are currently used in research settings. Extensive research work is currently performed to optimize these techniques for clinical protocols and acquisitions.

Other research tools which are seldom used, and which will not be explained in detail include: micro computed tomography (µCT), which is a dedicated high-resolution CT scanner for two and three dimensional (2D & 3D) imaging of samples and small objects with µm resolution; micro magnetic resonance imaging (µMRI), which is a dedicated high-field MRI scanner with very small bore and coils designed for imaging small samples and objects with µm resolution similar to µCT, and single photon emission computed tomography (SPECT) and positron emission tomography (PET), which are imaging methods acquired after the injection of a radio isotope to diagnose various diseases and to observe bone metastases in advanced-stage cancer patients [53, 54]. SPECT and PET suffer from poor image resolution, but provide valuable information in relation to the dynamic and functional nature (e.g. blood flow and glucose uptake) of the organ under investigation.

2.2 X-Rays

X-ray imaging is the oldest technique that is still widely used for the diagnosis of bone abnormalities and injuries. X-rays are a form of electromagnetic waves, with very high frequency and energy, which are harmful to tissues due to their ionization properties. Therefore care should be taken while handling a radiation source, and the exposure of the patient carefully controlled and limited. X-rays are produced in an X-ray tube (see Figure 2-1) when fast moving electrons emitted from a copper cathode are focussed onto a dense anode target like tungsten-rhenium alloy or molybdenum. The bombardment of electrons results in the production of X-rays (1% of the energy) and heat (99% of energy). The X-rays are produced in the anode target by Bremsstrahlung and characteristic radiation [55-57].

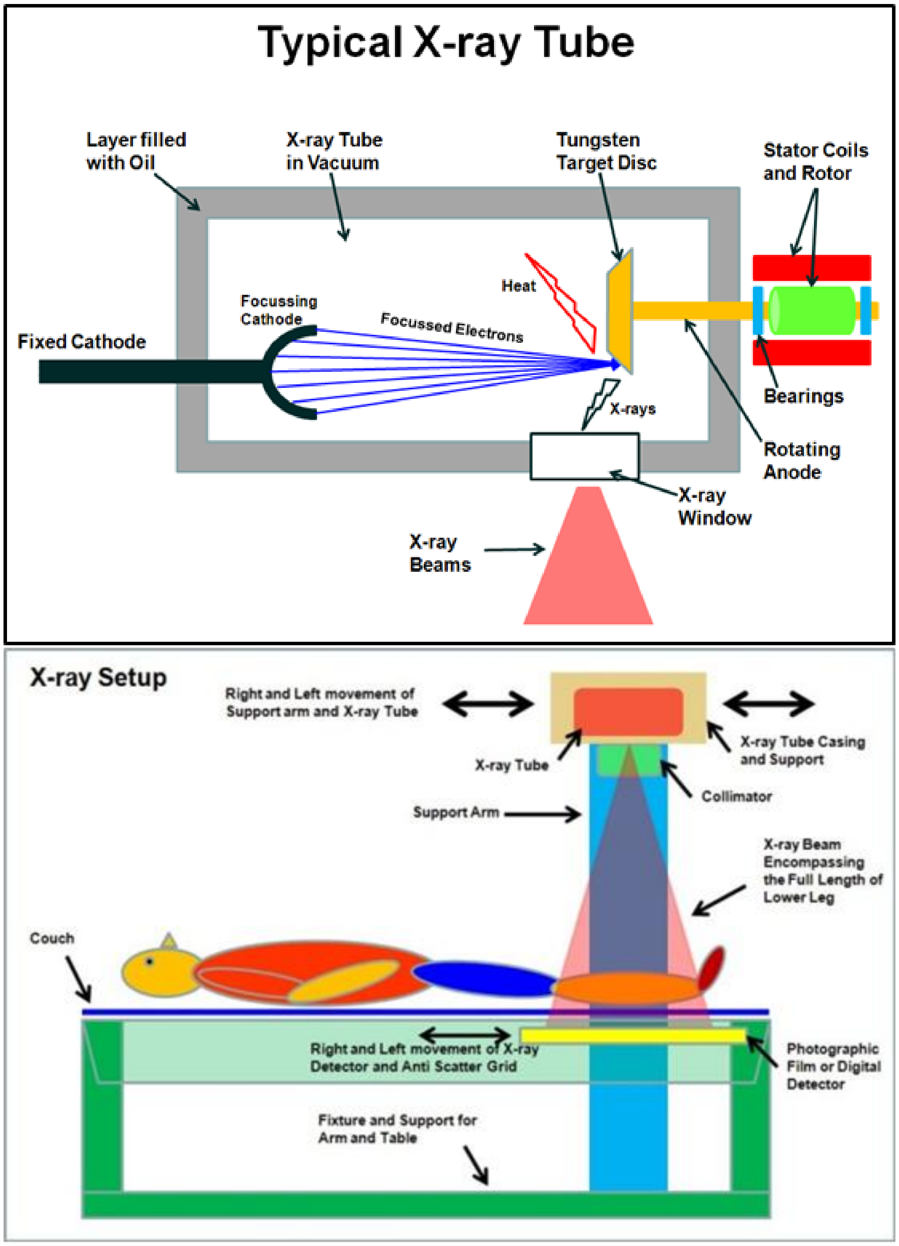

Figure 2-1 Drawing illustrates the labelled structure of an X-ray tube (top) and a full setup of X-ray equipment (bottom).

2.2.1 Bremsstrahlung Radiation

Bremsstrahlung or braking radiation is produced when negatively charged electrons interact with the positive charges of the nuclei of the anode target. The positive charge of the nucleus attracts and deflects the path of the electron which results in a loss of energy, speed and direction. The kinetic energy lost by the electron in this process is emitted as an X-ray photon. This is the most common method of X-ray production in the anode target creating a wide spectrum of X-ray energies (see Figure 2-2). The energy range depends on factors like speed of electrons, the depth of interaction in the anode target and the applied peak voltage (kVp) across the X-ray tube [55].

2.2.2 Characteristic Radiation

Characteristic radiation is produced when the bombarding electrons eject an electron from the tungsten target from any of its orbital shells, causing the atom to have an excess positive energy. To return to normal energy the atom either ejects another electron called an Auger electron or borrows an electron from one of its outer shells to release its energy. Ejection of electrons from the target is only possible when the bombarding electrons have energy similar or higher than the binding energy of the target’s atomic shells. Expulsion of Auger electrons does not produce X-rays, but transfer of electrons within the shells normally results in X-ray production. The most common shell that is affected is the K-shell, and when an electron from the K-shell is ejected it creates a vacancy which is normally filled by an electron from the outer shells like L, M or N resulting in the production of radiation with distinct energies (see Figure 2-2). Each shell in an atom has a unique energy based on its atomic number. Each target material produces a unique characteristic radiation energy based on its shells energy levels. Characteristic radiation on its own is important if we want to produce X-ray energies with a specific range and is commonly employed in mammography where a molybdenum target is utilised [55].

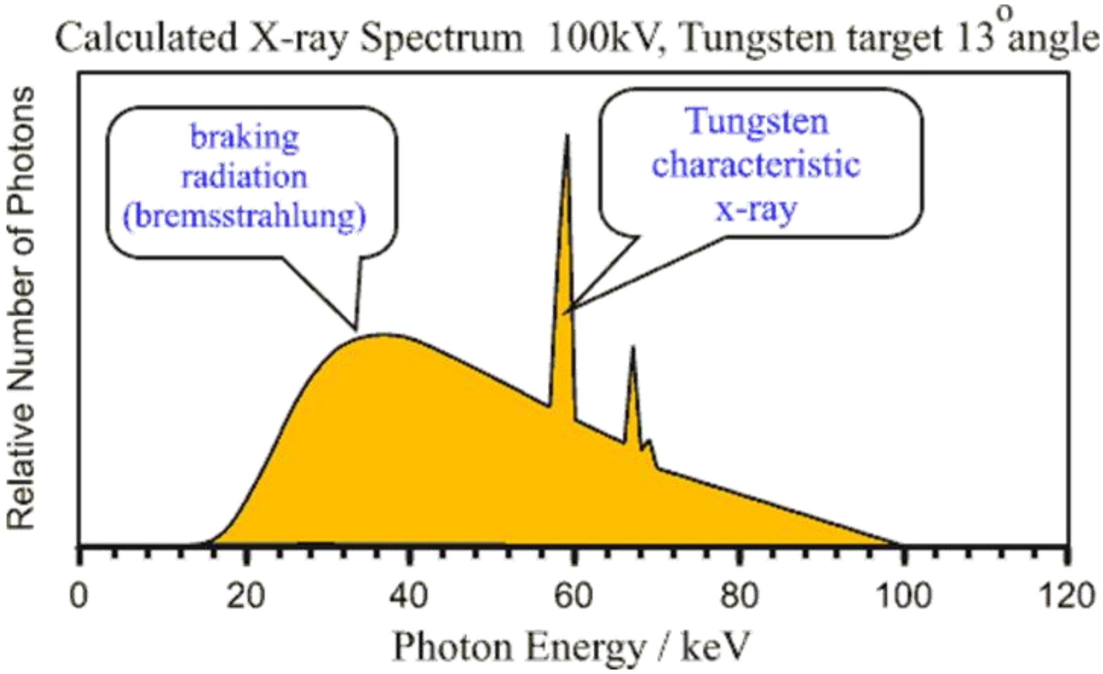

Figure 2-2 Drawing illustrates the range of X-ray energy produced in a Tungsten target and also illustrates the difference between Bremsstrahlung and characteristic radiation. (http://www.arpansa.gov.au/radiationprotection/basics/xrays.cfm)

2.3 Dual-Energy X-Ray Absorptiometry

Dual-energy X-ray absorptiometry (DEXA) is the most common bone quantification tool used for monitoring bone strength in individuals, and is used extensively in clinical settings due to its accuracy, low cost and reliability. It measures bone strength based on areal bone mineral density (BMD (g/cm^2)) and areal bone mineral content (BMC (g/cm)). The BMD and BMC are derived from two simultaneous equations describing attenuation coefficients for bone and average soft tissue at two energies. Earlier versions of dual energy photon scanners used isotopes of ^{153}Gd for the production of gamma rays with low and high energies. The isotope source was later replaced by X-rays to produce the two energies. The X-ray source is projected from under the table and is received by the detectors above the table after passing through the patient. The X-rays are projected postero-anteriorly with the patient lying supine on the table (see Figure 2-3). The high and low energy X-rays can be achieved by K-edge filtration or by voltage switching. The K-edge filtration method uses rare earth materials like cerium (Ce) or samarium (Sm) to split the X-ray beam into high and low energies which are detected by a single or dual detector. The voltage switching method is achieved by alternating the voltage generator for high and low kVp, which produces high and low energy X-rays alternatively, which are detected by a single detector [56, 58-64][55].

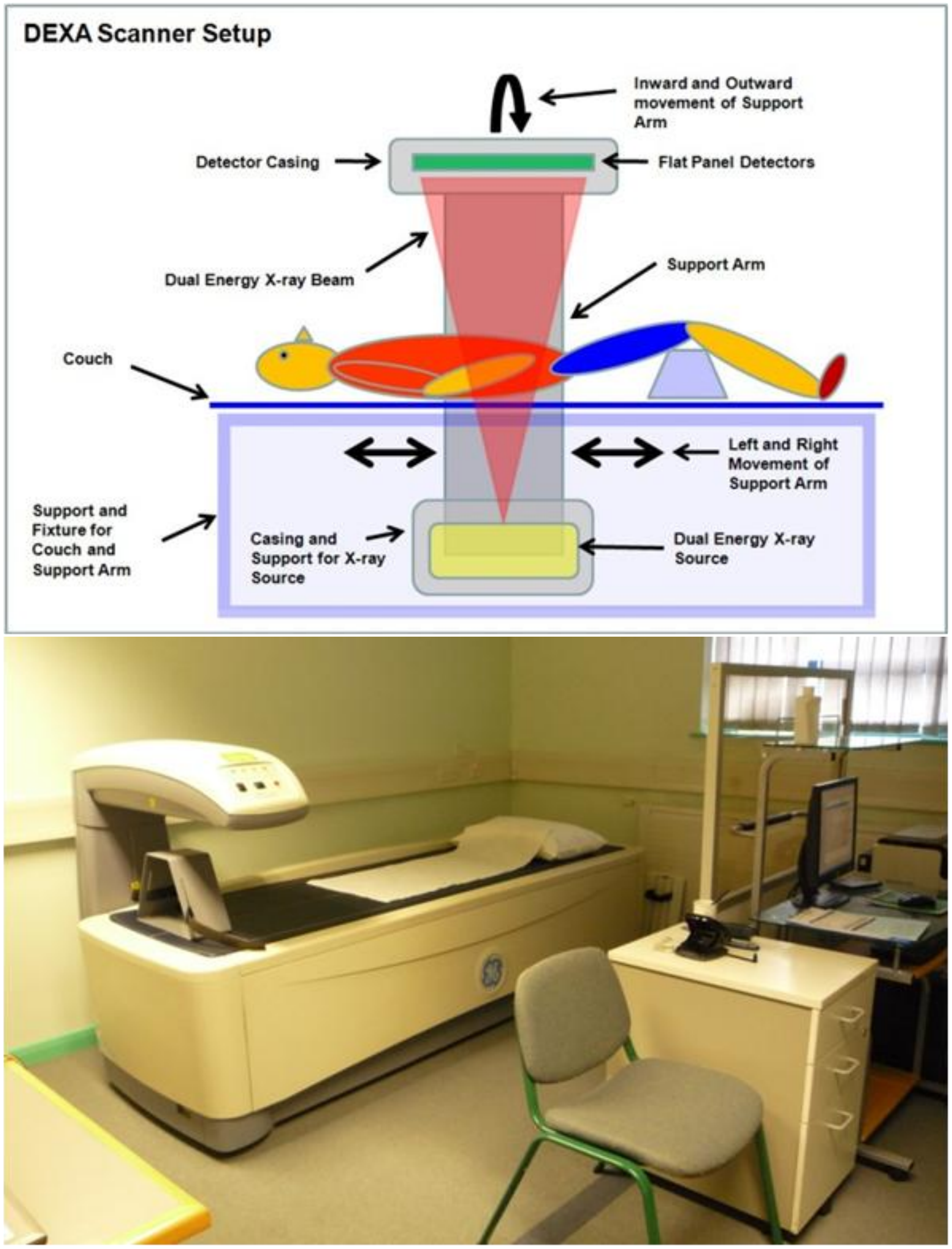

Figure 2-3 The image on the top illustrates a typical setup of a modern DEXA scanner with explanation of the various components. The image on the bottom illustrates one of the clinical scanners which were used for the project.

Earlier versions of DEXA used a pinhole to collimate the X-rays into a pencil beam which was used to scan the region of interest rectilinearly, and the beam was detected by a single or double detector. This method of acquisition was very slow and was replaced by scanners using a fan beam of X-rays coupled with a linear array of detectors. The fan beam was achieved by using slit collimators, which were able to scan the full length of the anatomy in a true linear or rectilinear sweep. This method of acquisition is extremely fast and provides high-resolution images when compared with a pencil beam scanner, but with a slight increase in radiation dose. New generation scanners use a cone beam X-ray source which is detected by a flat panel detector which has a large field of view (FOV). These are normally able to cover the full length of the anatomy under investigation eliminating the need for sweeping the full length as in the case of a fan beam. This method further reduces the scan time compared with fan beam technology [57, 58, 60, 61, 65].

2.4 Quantitative Computed Tomography

Quantitative computed tomography (QCT) is a modified version of a normal clinical computed tomography (CT) scanner combined with a calibration phantom and software to quantify absolute volumetric bone density values in the patient. Clinical CT scanners use an X-ray source combined with parallel detectors, which acquire cross-sectional data by rotating around the patient (see Figure 2-4). Modern advanced third generation CT scanners commonly acquire volumetric data with continuous table movement and gantry (combined X-ray source and detectors) rotation, which can be processed to create reformatted images in any plane. The design and properties of CT scanners have evolved over time enabling vast improvements in speed and quality. CT scanners have gone through four generations (see Figure 2-5) of technology, although the fourth generation of scanners is rarely used due to their cost and limitations. The first generation of CT scanners used a translate-rotate design with fixed table position and pencil beam X-ray source. The gantry rotated for each degree and made a translational movement to cover the anatomy, which was repeated for all degrees of rotation using a single detector and a pencil beam X-ray source. The second generation of CT scanners used a translate-rotate design with fixed table position, but with a small fan beam and an array of detectors. The gantry rotated for large angles up to 30° followed by translational movements to cover the anatomy. This method reduced the scan time to less than 2 minutes, when compared with 20 to 30 minutes with first generation CT for a single slice. Third generation CT scanners use a rotate-rotate design with a large fan beam to cover the anatomy and a linear array of detectors, thus eliminating the need for translational movement and reducing scan times for a single slice to be less than 20 seconds. The table is fixed for each slice and the gantry acquires data with a continuous 360° rotation. After one rotation the gantry has to rotate back in the other direction to acquire the next image slice due to the restriction of power cord length and power supply. The power supply limitation has been solved, by using slip ring technology which makes the gantry rotate continuously in a clockwise or anticlockwise direction, whilst at the same time the table is moved inwards or outwards during acquisition. Using this principle, CT scanners have become much faster and are able to acquire a large volume of data in milliseconds. Modern scanners have replaced the fan beam X-ray source with a cone beam, and the detectors have become arranged linearly in length and width to cover large areas in a single rotation [55, 57, 66-68].

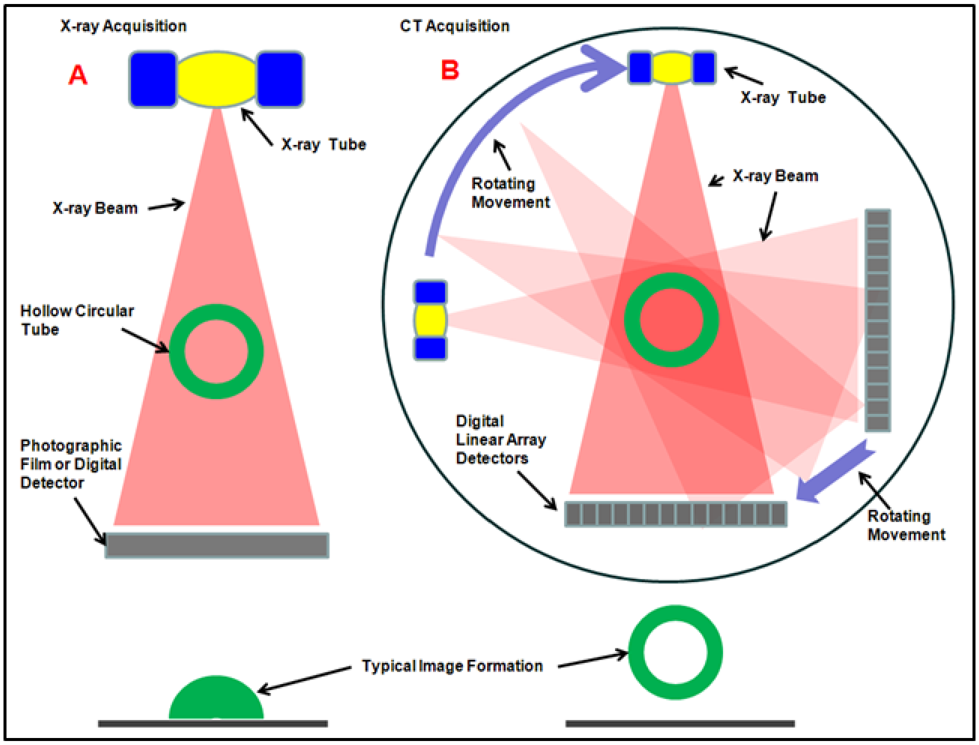

Figure 2-4 Diagram illustrates the difference in data acquisition between X-ray and CT.

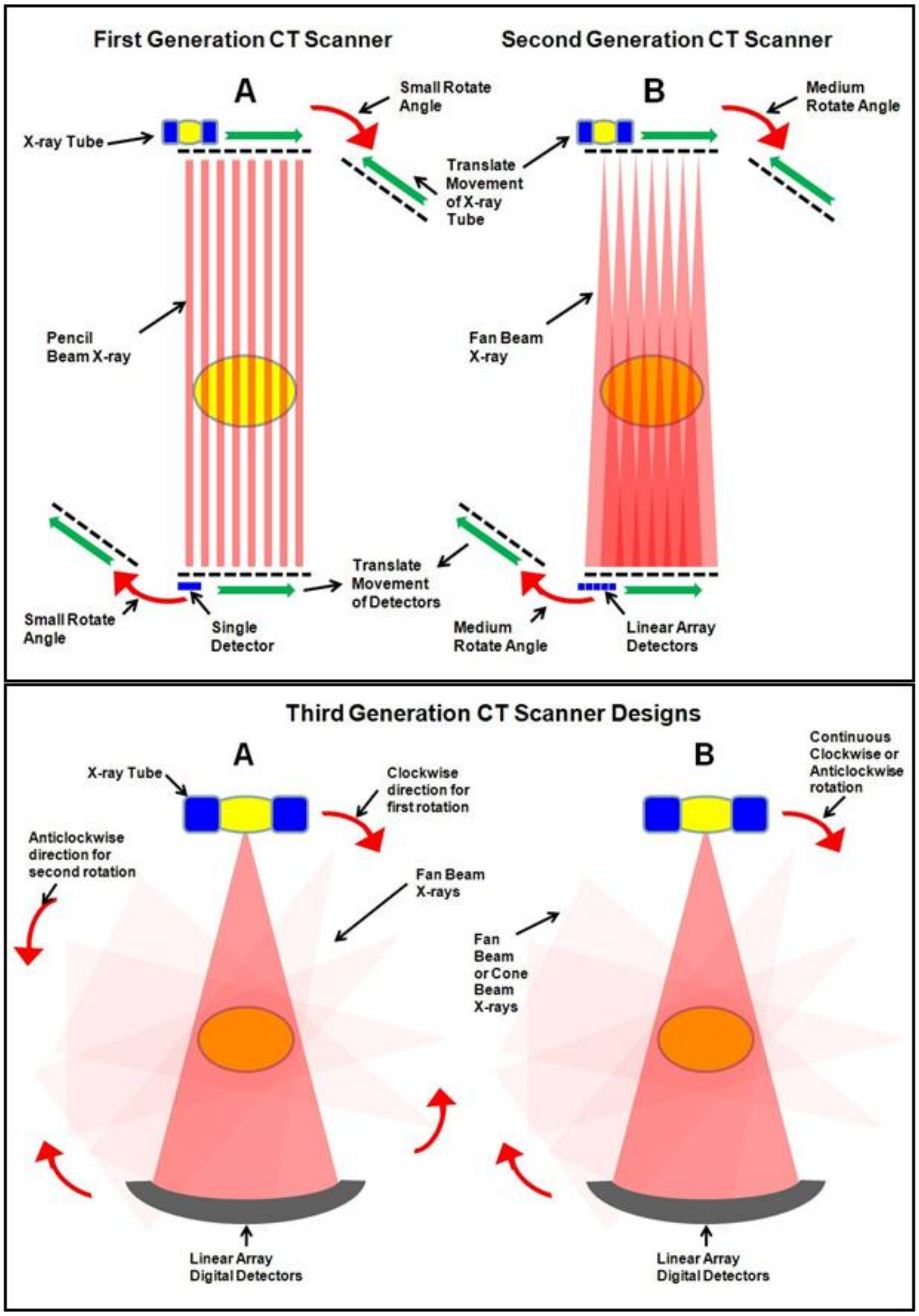

Figure 2-5 The diagrams illustrate the different generation of CT scanner design which has been used in clinical imaging with description of their structural properties. The top row illustrates the first and second generation CT scanners and the bottom row illustrates the designs of third generation CT scanners.

CT scanners display images based on the x-ray linear attenuation differences between each tissue in the body. Each tissue has a different attenuation property based on their composition; air in lungs has the least attenuation when compared with bones or soft tissues. The attenuation property of bones is very high when compared with other tissues, which results in excellent delineation of bone from other tissues. Filtered back projection algorithm is used to convert the attenuation properties into images. Initially each scanner had different attenuation values which did not necessarily match with other manufacturers. A standardised value was needed for comparison across different scanners. This was achieved by using the linear attenuation value of water as a reference value, which resulted in standardised CT values called Hounsfield units (HU) for each pixel in the CT image (named after Sir Godfrey Newbold Hounsfield). Air has a typical HU of -1000, water 0, soft tissues around 30-100 and bones around 300-3000 [55, 57, 66-71].

In QCT the volumetric BMD is evaluated by comparing the HU of the tissue with the HU of a calibration phantom with varying concentrations of $Ca_5(PO_4)_3(OH)$ (calcium hydroxyapatite). A regression equation is applied to relate HU and apparent density. The calibration phantom normally contains four to five rods with varying concentrations, and is placed under the patient or near the anatomy of interest and scanned simultaneously with the patient. After image acquisition, a region of interest (ROI) is drawn on the bone of interest and compared with the ROI on the calibration phantom. This type of quantification is very effective and repeatable, but suffers from increased radiation dose to the patient of around 100 µSv [55, 57, 68, 70-72].

2.5 Peripheral Quantitative Computed Tomography

A peripheral quantitative computed tomography (pQCT) scanner works on the same principle as QCT scanners, except for its smaller size and its rotational properties (see Figure 2-5). The unit consists of a circular ring with the bore in the middle. The circular ring contains the X-ray source at one end with the detector array placed exactly opposite to the source. The pQCT data in this thesis were acquired using a Stratec, XCT 2000 (Erlangen, Germany) scanner (see Figure 2-6) which is a second generation CT scanner with a translate-rotate configuration [56, 57, 59, 62, 67, 69, 72-82].

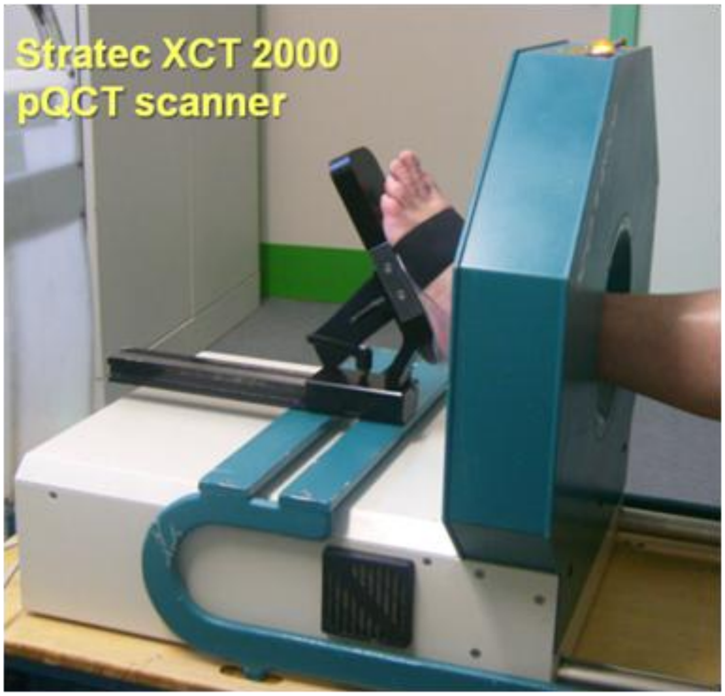

Figure 2-6 The Stratec XCT 2000 pQCT scanner which was used for the HBM project.

2.6 Quantitative Ultrasound

Ultrasound is sound waves at frequencies which are above the normal human audible range (20 to 20000 Hz). The normal range of frequency for ultrasound waves in clinical settings is from 20 kHz to nearly 100 MHz. Ultrasound waves create minute mechanical disturbances in the tissue, which can be either measured as reflected or transmitted waves. Quantitative ultrasound (QUS) (see Figure 2-7) commonly uses the principle of transmission for bone quantification using two transducers. The clinical systems normally use two transducers opposite to each other or at angles with the anatomy in-between the transducers. One transducer transmits the ultrasound waves and the other receives the transmitted waves which have passed through the anatomy. The ultrasound waves are normally produced using piezoelectric crystals commonly made of lead zirconate titanate. The different tissues in the anatomy are characterised based on the ultrasound velocity and attenuation. Three common measurements are acquired through QUS which are generally used by different manufacturers with different abbreviations and algorithms. Speed of sound (SOS) is a measure of ultrasound velocity in relation to different tissues in the anatomy, which is mostly quoted in meters per second (m/s). Broadband ultrasound attenuation (BUA) is another measurement tool for bones based on the attenuation property of ultrasound wave and is usually quoted in dB/MHz. A combined parameter of both SOS and BUA is commonly used for ease of interpretation and improved precision of the results, and this is mostly quoted as quantitative ultrasound index (QUI) or stiffness. QUS has a great advantage over DEXA due to its low cost and non-ionising property, but suffers from the restriction that it can only scan anatomy from the extremities, like the heel and the elbow [56, 57, 59, 61, 62, 81, 83-92].

Figure 2-7 Photograph of an advanced QUS scanner used commonly for the heel and elbow bone.

(http://www.mar-med.pl/goods/view/52/sonost)

2.7 Quantitative Measurements

Bone mineral density (BMD) should not be used directly to compare individuals with different ages and ethnicity. It is very important to correct the BMD measurements statistically when correlating individuals. This correction is applied statistically to the BMD data with knowledge of a reference population. A BMD result from a 40 year old male from the United Kingdom will not necessarily match with that of a 40 year old male from Africa or even a 40 year old female from the United Kingdom. There are lots of parameters which affect the BMD measurement from one type of population to another. It is very important to identify this difference and apply appropriate corrections when making comparisons [57, 58, 60].

Two standardised measurements are used for individuals with the necessary corrections applied: T-Score and Z-Score.

2.7.1 T-Score

The T-score is a comparison of a patient's areal BMD with a population peak reference value represented in standard deviations (SD) from the mean value. The T-score represents the number of SDs that a areal BMD measurement is above or below the mean peak bone mass in a young normal population matched for sex and race [57, 58, 60].

$$T - Score = \frac{(BMD_{patient} - BMD_{peak})}{SD_{peak}}$$

Equation 2-1

Where $BMD_{patient}$ is the patient areal BMD value, BMD_{peak} is the reference peak value, and SD_{peak} is the population SD. This score is commonly used for postmenopausal women and men over 50 years old.

2.7.2 Z-Score

The Z-score is a comparison of the patient's areal BMD to a population age-matched reference value (see Figure 2-8), and is commonly represented in terms of multiple of the population SD. Z-scores represent the number of SD a areal BMD measurement differs from the mean value for an age, sex and race matched reference population.

$$Z - Score = \frac{(BMD_{patient} - BMD_{age-matched})}{SD_{age-matched}}$$

Equation 2-2

Where BMD$_{patient}$ is the patient's areal BMD value, BMD$_{age-matched}$ is the reference areal BMD value at the same age as the patient and SD$_{age-matched}$ is the population SD at the patient's age [57, 58, 60]. This score is commonly used for premenopausal women and people below 50 years old, and should not be used to diagnose bone diseases like osteoporosis as described in Chapter 1.

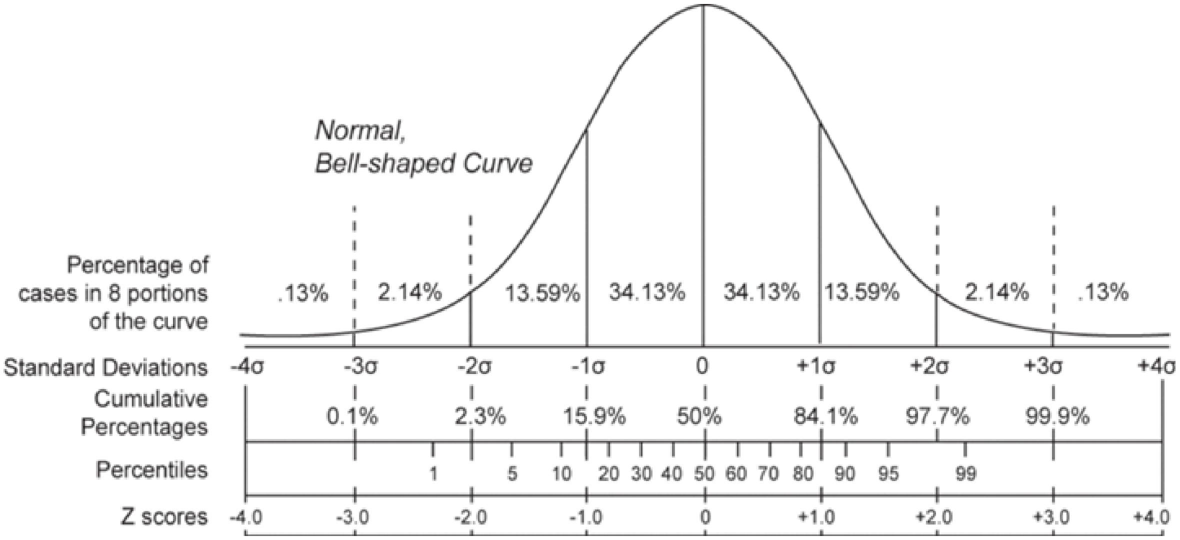

Figure 2-8 Normal distribution curve with illustration of Z-score.

(http://en.wikipedia.org/wiki/File:Normal_distribution_and_scales.gif)

2.8 Magnetic Resonance Imaging and Magnetic Resonance Spectroscopy

Magnetic resonance imaging (MRI) and magnetic resonance spectroscopy (MRS) uses a powerful magnetic field (0.5 T or above) to align the nuclear magnetisation of (usually) hydrogen atoms in the body. A rotating magnetic field at radio frequency (RF) is used to systematically alter the alignment of this magnetization, causing the hydrogen nuclei to produce a rotating magnetic field detectable by the receiver coil in the scanner. This signal can be manipulated by additional magnetic field gradients to build up enough information to construct an image of the body. Unlike QCT, pQCT, DEXA and X-rays, MRI does not use ionising radiation and produces excellent contrast for soft tissues [28, 55, 63, 68, 70-72, 77, 93-97]. A detailed protocol was developed (October 2008 to January 2009) for the HBM project in this PhD thesis, which will follow in Chapters 5&6, and a detailed description of the basics of MR will follow in Chapter 3.

Figure 2-9 The 3.0 Tesla GE MR750 which was used for this thesis.

3 Magnetic Resonance Imaging and Magnetic Resonance Spectroscopy

This chapter gives a brief description of MR physics in relation to the methods that were used in this thesis.

3.1 The Nucleus and its Interaction with the Main Magnetic Field

According to quantum mechanics, certain nuclei appear to spin about their axes known as the intrinsic spin (I), which is dependent on the atomic number and weight of the nucleus. A nucleus with an even number atomic weight and an even atomic number will result in I=0 and does not exhibit any magnetic interaction, hence cannot be studied with magnetic resonance (MR) techniques. A nucleus with an even atomic weight and an odd atomic number will have integral values for I (e.g. 1, 2, 3). A nucleus with odd atomic weight will have half-integral values for I (e.g. 1/2, 3/2). The hydrogen nucleus ^{1}H consisting of a single proton (odd atomic weight) having spin I=1/2 is commonly used for magnetic resonance imaging (MRI), due to its abundance in human tissues. Magnetic resonance spectroscopy (MRS) is commonly employed to study different types of nuclei like: hydrogen (^{1}H), carbon (^{13}C), sodium (^{23}Na) and phosphorous (^{31}P) for chemical evaluation [55, 98-103].

The intrinsic spin of a nucleus gives rise to an angular momentum vector (p), which points along the spin axis

$$p = \hbar \mathrm{I}$$

Equation 3-1

Where $\hbar = h/2\pi$ (Dirac’s constant) and h is Planck constant

The nucleus also possesses electric charge, and the effective current loop due to the rotation of this charge produces an associated magnetic dipole moment (μ).

$$\mu = \gamma p$$

Equation 3-2

Where γ is the gyromagnetic ratio, which is a constant for a given type of nucleus. For ^{1}H the value of γ is 26.75 x 10^{7} radians $s^{-1}T^{-1}$ ($\gamma/2\pi$ = 42.58 MHz T^{-1}). The magnetic dipole moment (μ) causes the nucleus to behave like a tiny bar magnet and gives rise to interactions with an external magnetic field (B_0). B_0 is measured in tesla (T) or gauss, where 1.0 T = 10,000 Gauss. In the quantum mechanical model, the nuclear magnetic dipole can only have (2I+1) orientations. A proton with I = 1/2, has two possible orientations either parallel or anti-parallel with B_0 (see Figure 3-1), which correspond to low and high energy states [55, 99-103].

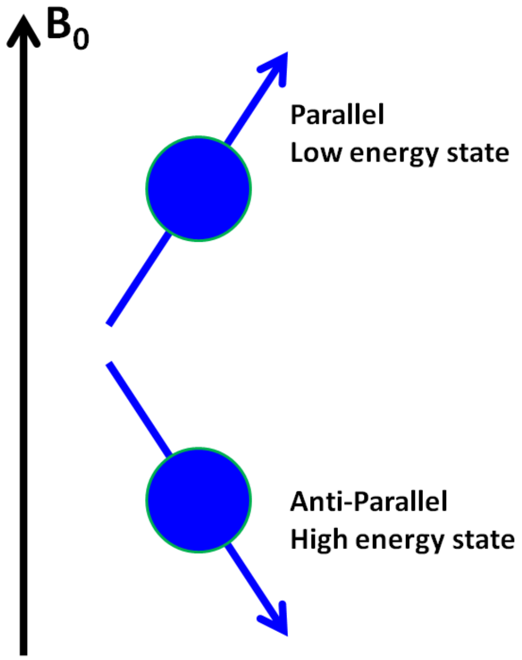

Figure 3-1 Alignment of proton spin with an external magnetic field.

The energy difference ΔE**,** between the two states (see Figure 3-2) is proportional to the strength of B_0 and is given by:

$$\Delta E = \mu B_0 / I$$

Equation 3-3

(or)

$$\Delta E = \gamma \hbar B_0$$

Equation 3-4

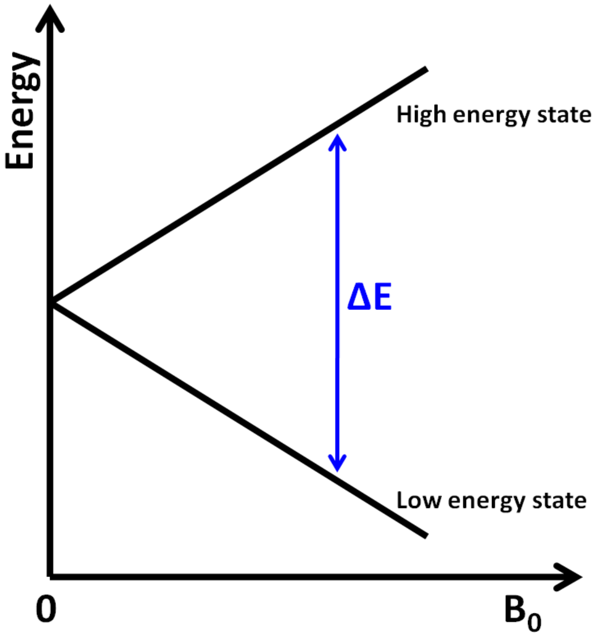

Figure 3-2 Energy level diagram for the hydrogen proton spins in a magnetic field.

Transitions between the two states can be induced by applying electromagnetic energy at a frequency called the Larmor frequency (ω_L), which results in the resonance condition and is given by [99, 101-103]:

$$\omega_L = \Delta E / \hbar = \gamma B_0$$

Equation 3-5

At absolute zero, all the spins would be parallel with B_0, but in reality, the spins are influenced by thermal motions, which results in the transition of spins between the high and low energy states. At equilibrium there is a fractional excess of spins in the low energy state, which align with B_0. The equilibrium populations are described by the Boltzmann distribution [99, 101-103]:

$$\frac{N_L}{N_U} = \exp\left(\frac{\hbar\omega_L}{kT}\right) \approx 1 + \frac{\hbar\omega_L}{kT}$$

Equation 3-6

where N_L and N_U are the number of spins in the lower and upper energy levels, k is the Boltzmann's constant and T is the absolute temperature. The fractional excess of spins, which are aligned with B_0 are described by [99, 101-103]:

$$\frac{N_L - N_U}{N_U} \approx \frac{\hbar\omega_L}{kT} = \frac{\hbar\gamma B_0}{kT}$$

Equation 3-7

The MR signal is observed only from the fractional excess spins, which is around 7×10^{-6} at 1.0 T. The small amount of fractional excess results in low MR sensitivity, and to increase the sensitivity we should either decrease the sample temperature (not practical for patients) or increase B_0.

3.2 Classical Model

In the classical model the nuclear magnetic moment experiences a torque (L) which tries to align with B_0 described by [101, 102]:

$$L = \mu \times B_0$$

Equation 3-8

The nucleus also contains angular momentum, which combined with the torque results in the nucleus precessing about B_0 in a gyroscopic nature. The rate of change of angular momentum is described by [99, 101, 102]:

$$\frac{\mathrm{dp}}{\mathrm{dt}} = L = \mu \times B_0$$

Equation 3-9

But, from Equation 3-2, $p = \mu/\gamma$, thus

$$\frac{\mathrm{d\mu}}{\mathrm{dt}} = \mu \times \gamma B_0 = \mu \times \omega_L$$

Equation 3-10

$$\omega_L = -\gamma B_0$$

Equation 3-11

The results from Equation 3-10 and Equation 3-11 illustrate that the nucleus precesses around the direction of the applied field at the rate of ω_L (resonant frequency) and the minus sign illustrates the direction of rotation, which is usually ignored [99, 101-103].

3.3 Bulk Magnetisation

It is good practice to combine the effect of all the nuclei that are influenced by B_0 rather than to explain the properties of each individual nucleus. The combined effect of all the nuclei that are in spin-up and spin-down states is known as bulk magnetisation (M). In equilibrium the bulk magnetisation (M_0) has only a longitudinal component aligning along the B_0 direction, and it does not produce an MR signal in the receiver coil. Application of additional radio frequency (RF) field at the resonant frequency disturbs M from equilibrium, resulting in the production of MR signals. In a Cartesian system which is represented by x, y and z direction, the B_0 is usually represented in the z direction.

3.4 Radio Frequency Pulses

Radio frequency (RF) pulses are electromagnetic radiation which is achieved by applying a second magnetic field B_1, perpendicular to B_0, which rotates in phase with the precessing nuclear magnetic moments at ω_L. Viewed from the laboratory frame, the B_1 field causes M_0 to tilt away from B_0, and to execute a spiral path. When B_1 is switched off, M_0 continues to precess about B_0 describing a cone of half angle α (alpha), also known as the flip angle given by:

$$\alpha = \gamma B_1 t_p$$

Equation 3-12

where t_p is the duration of the B_1 field pulse.

Visualisation of the trajectory of spins with respect to RF application is complex in a laboratory frame of reference. The motion of spins are therefore observed in a different manner in which the observer is rotating about an axis parallel with B_0, and synchronised with the precessing nuclear magnetic moments. This method of observing the spins is called the rotating frame of reference. The frame of reference is observed in the set of three mutually orthogonal axes [99, 101-103].

The duration of the B_1 field results in the application of multiple types of RF pulses (e.g. 90°, 180°), which are responsible for the alteration of M_0. A 90° RF pulse tilts the M_0 to the transverse plane (Figure 3-3(middle)) resulting in the formation of M_{xy} component and signal. A 180° RF pulse results in the formation of $-M_z$ component which lies in $-B_0$ direction (Figure 3-3 (right)) [55, 99-103].

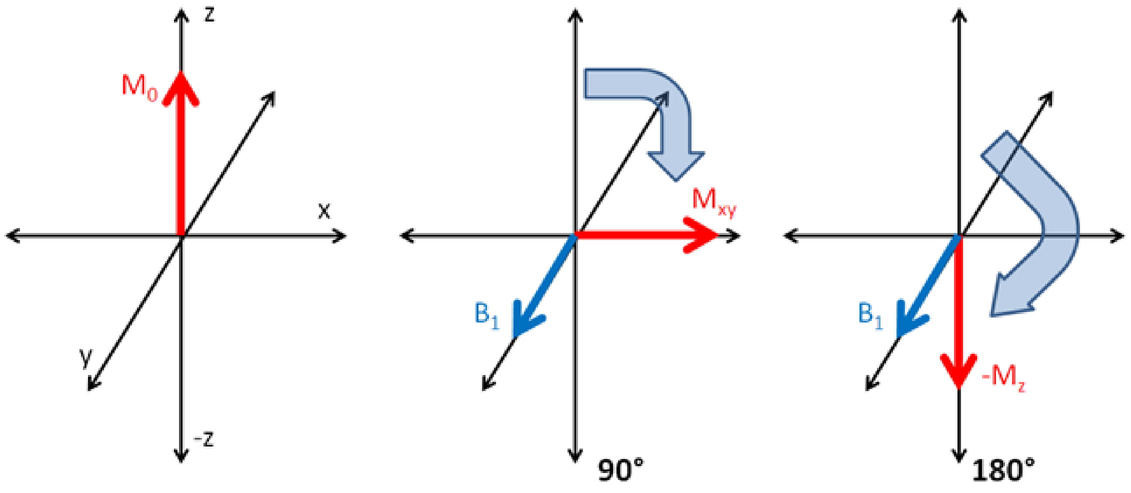

Figure 3-3 The equilibrium state of the net magnetisation (left), followed by the transverse magnetisation (middle) after the application of the 90° RF pulse, and the negative longitudinal magnetisation (right) after the application of the 180° RF pulse.

3.5 Free Induction Decay

Once the magnetization is tilted away from the B_0 direction its transverse component M_{xy} generates a rotating magnetic field. This rotating magnetic field oscillates at ω_L and induces a small voltage (dynamo effect) in the RF receiver coil. A 90^0 RF pulse maximizes the rotating transverse component. Once the RF pulse has ended however, the signal gradually decays (see Figure 3-4) as a result of relaxation processes which causes M to return to its equilibrium position M_0, parallel to B_0. This type of decaying signal is known as free induction decay (FID) [99-103].

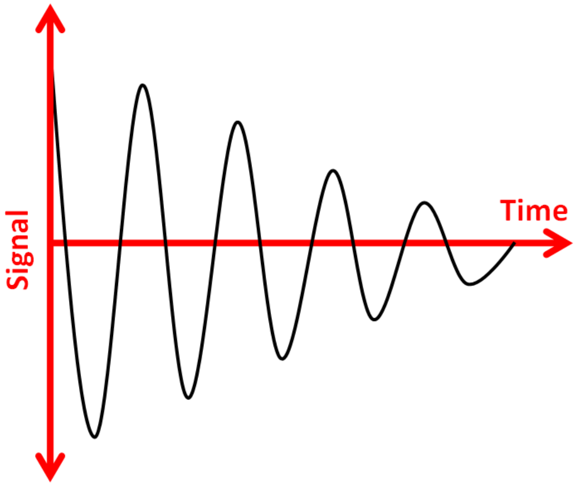

Figure 3-4 A FID signal following an RF excitation.

3.6 Relaxation

After the removal of B_1 magnetic field, the excited nucleus will try to achieve equilibrium state by dissipating its energy to adjacent nuclei (spin-spin) or to the surrounding environment (spin-lattice). The process and duration involved in the nucleus returning to equilibrium state after the application of B_1 field is known as relaxation, which results in the decay of the FID over time.

3.6.1 Spin-Lattice or T_1 Relaxation

The spin-lattice or T_1 relaxation is associated with the longitudinal component after the application of the RF pulse, and is due to the interaction of the excited nucleus with its surrounding (or) lattice environment. The spins in a sample or tissue are influenced by thermal vibration, and the excited protons transfer their energy to this environment, which results in the magnetic moments realigning with B_0 [99-103]. The M_z magnetisation component gradually recovers towards its equilibrium value of M_0 (see Figure 3-5). The longitudinal relaxation characteristic of M_z after the application of a 90° RF pulse is routinely known as T_1 (or) spin-lattice relaxation as described by:

$$M_z = M_0 \left[1 - exp\left(\frac{-t}{T_1}\right)\right]$$

Equation 3-13

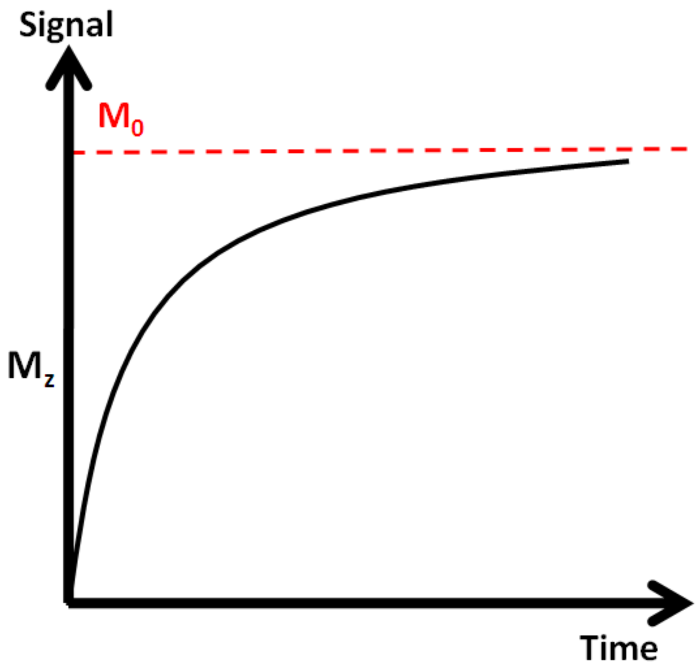

Figure 3-5 The T_1 relaxation of the magnetisation recovering back to equilibrium.

3.6.2 Spin-Spin or T_2 Relaxation

The spin-spin or T_2 relaxation occurs in the transverse (xy) plane and is caused due to the interaction of the excited nucleus with neighbouring nuclei via their magnetic moments. As described earlier (see 3.1), each nucleus creates its own magnetic field and they normally interact with adjacent nuclei, resulting in local random alterations to B_0, which results in loss of phase coherence, and exponential decay of transverse magnetisation M_{xy} (see Figure 3-6). The time constant of the decay is known as spin-spin or T_2 relaxation (see Equation 3-14).

When spin-lattice relaxation returns to equilibrium M_0, there is never any remnant transverse magnetisation component. Therefore T_2 is always less than or equal to T_1 [99-103].

$$M_{xy} = M_0 \left[exp\left(\frac{-t}{T_2} \right) \right]$$

Equation 3-14

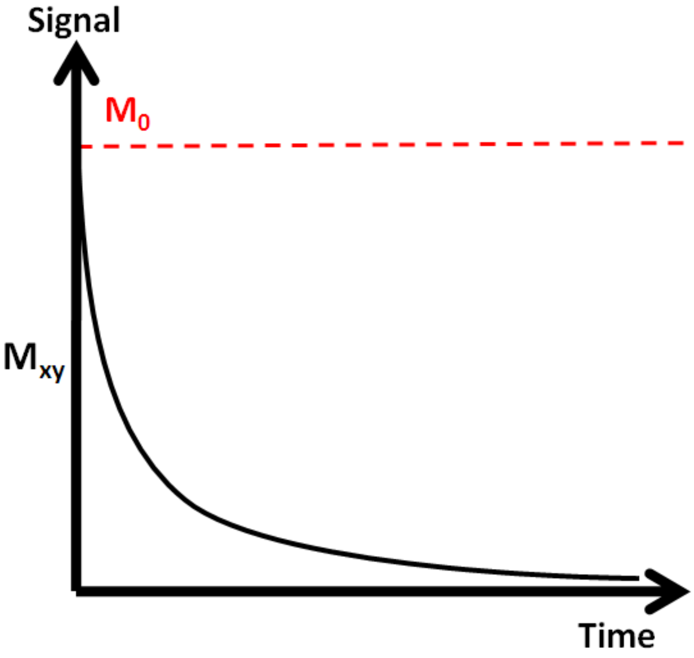

Figure 3-6 The T_2 linear exponential decay of magnetisation in the xy plane.

3.6.3 T_2* Relaxation

In a scanner, the magnetic field is not perfectly uniform. The changes in the field result in frequency variations causing additional decay described by T_2*. The T_2* is always shorter in duration when compared with normal T_2 relaxation. The T_2* relaxation is denoted by [99-103]:

$$\frac{1}{\mathrm{T}_2^*} = \frac{1}{\mathrm{T}_2} + \frac{1}{\mathrm{T}_{2\mathrm{inhom}}}$$

Equation 3-15

The T_{2inhom} illustrates the decay of signal due to B_0 inhomogeneity and is also represented as:

$$\frac{1}{T_{2inhom}} = \gamma \Delta B_0$$

Equation 3-16

The ΔB_0 is the amount of variation in the B_0 field over the scanned region.

3.6.4 Spin-Echo

The spin-echo (SE) is a simple and basic sequence employed in all MRI scanners, which uses 90° and 180° RF pulses (see Figure 3-7) to form a spin-echo signal. The sequence works based on using the 90° RF pulse to align the spins in the transverse plane M_{xy}. After the removal of the 90° RF pulse, the spins in the M_{xy} plane dephase (see Figure 3-7 (middle)) in relation to their relaxation properties. Some spins dephase slowly and some quickly based on their surrounding environment. The dephasing of the spins is normally observed as a FID in the receive coil or can be manipulated to form an echo using another RF pulse with 180°, which flips the spins in the M_{xy} plane to $-M_{xy}$ plane where the signals rephase (see Figure 3-7 (right)) to produce an echo. The signal observed from the SE contributes only to the recovery of the T_2* process which is a coherent phenomenon. The natural T_2 decay of the tissue cannot be recovered by the 180° refocusing pulse.

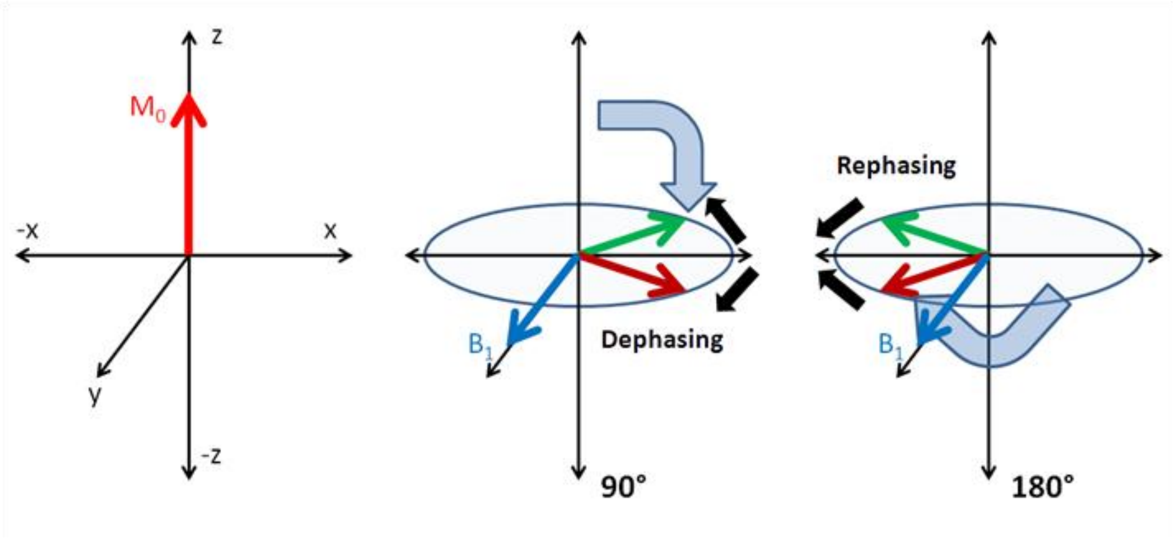

Figure 3-7 The stages of magnetisation in a spin-echo sequence followed by the application of the 90° (middle) and 180° (right) RF pulses to form a spin-echo.

3.7 Spatial Encoding

The encoding of MR signal with spatial information is essential for the isolation of finite volumes from the sample or patient and is routinely known as spatial encoding. Spatial encoding is achieved by gradient coils, that apply variations in the x, y and z directions of the main magnetic field in the z-direction. The application of gradient magnetic fields, result in a linear change in resonance frequency or phase along the gradient direction (see Figure 3-8). The gradients are usually known as slice selection, frequency and phase encoding. For a typical axial image acquisition, the slice selection gradient is usually applied along the z direction which is also the direction of B_0, and the phase and frequency encoding are applied in x or y axis [55, 99-104].

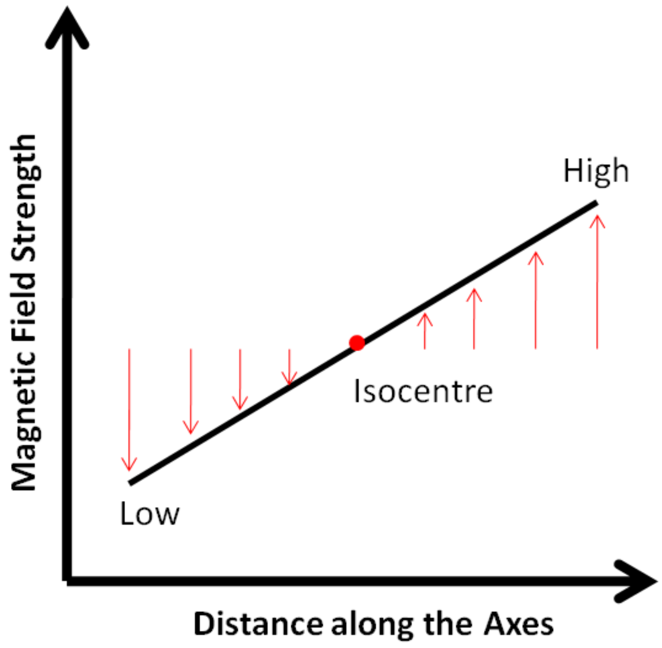

Figure 3-8 Application of a linear gradient magnetic field which results in change in frequency along the field. The isocentre is the point in the gradient in which the field strength is the same as B_0.

3.7.1 Slice Selection

A finite section or slice from the patient is acquired by using the slice selection (SS) that applies both a magnetic field gradient and an RF excitation. If we image a slice in the xy direction then the SS gradient must be applied orthogonal to this plane which is the z direction. The gradient makes the resonance frequency a function of position along the z direction and is denoted by:

$$\omega(z) = \gamma B_z(z) = \gamma(B_0 + zG_z)$$

Equation 3-17

The 90^0 selective pulse is applied as a shaped or amplitude modulated pulse so that it contains a narrow bandwidth (BW) of frequencies close to the fundamental resonance frequency of the magnet $\omega_0 = \gamma B_0$. Only those spins whose resonance frequency lies within this range will be excited. Thus a slice in the x-y plane is selected by applying a gradient in the z direction during excitation (see Figure 3-9). The width of the slice Δz is given by:

$$\Delta z = \Delta\omega/\gamma G_z$$

Equation 3-18

Where $\Delta\omega$ is the bandwidth of frequencies within the 90^0 pulse and G_z is the strength of the applied selective gradient. The bandwidth of frequencies or $\Delta\omega$ is related to the shape and duration of the pulse. If it is a Gaussian-shaped pulse, then $\Delta\omega = 2\pi/\Delta t$, where $\Delta\omega$ is the full-width at half maximum (FWHM) of the pulse's frequency spectrum and Δt is the FWHM of the pulse envelope, in seconds. The slice can be made thinner by decreasing the spectral bandwidth of the pulse (by making the pulse longer in time) or by increasing the strength of the selection gradient G_z. The slice profile is approximately the Fourier transform of the RF pulse envelope. Thus a Gaussian pulse gives roughly a Gaussian slice profile. A more rectangular slice profile can be obtained by using a sinc-shaped RF pulse [55, 99-103].

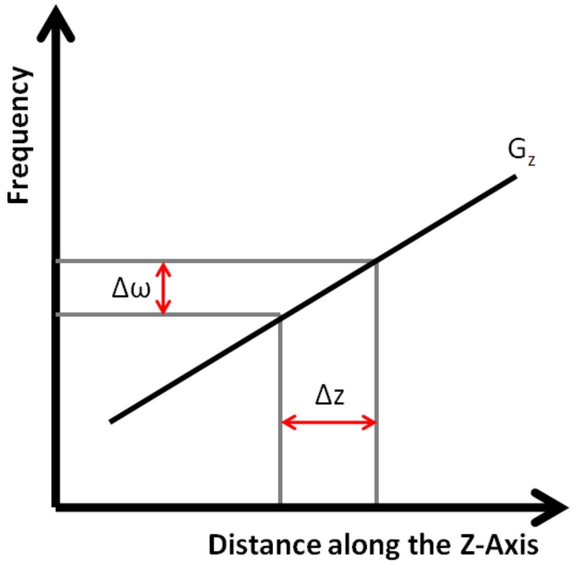

Figure 3-9 A typical SS gradient in the z-axis that is used for the selection of an image slice in relation to thickness and frequency.

3.7.2 Frequency Encoding

The signal with respect to one in-plane direction from the localised slice is acquired using the frequency encoding (FE) magnetic field gradient. The MR resonance frequency is directly proportional to the strength of the magnetic field, thus when a gradient is applied the resonant frequency is also a function of position along the gradient direction. If the gradient is applied in the x direction as G_x**,** for example, then the equation describing the variation of the resonance frequency ω with position x is:

$$\omega(x) = \gamma(B_0 + xG_x)$$

Equation 3-19

If an x gradient is applied then the resonance frequency is modified only in position along x, not y or z axis. In FE, the acquisition begins with the application of a selective RF pulse in order to excite the spins, followed by switching on of the FE gradient (for example in x direction), and observing the MR signal with the gradient turned on. The MR signal is always observed in the presence of the FE gradient, thus it is also known as readout gradient [55, 99-103].

3.7.3 Phase Encoding

The third and final method of spatial discrimination is known as phase encoding (PE) which is routinely applied prior to the FE period. PE applies a gradient magnetic field to change the frequency that results in the manipulation of the phase of spins. The PE operates in the second in-plane direction of the selected slice. The fundamental difference in PE is that the MR signal is not observed in the presence of a gradient. Nevertheless, spatial information is obtained along the direction of the PE gradient. Consider the effect of applying a 90^0 pulse followed by a PE magnetic field gradient. After the 90^0 pulse, the magnetization is in-phase everywhere, lying along the y axis, in the rotating frame. When we turn on the PE gradient, the magnetic field varies linearly with position along the y axis. If the gradient is positive, the spins at the top of the axis will experience a larger magnetic field than those in the middle and bottom and eventually will precess faster (i.e.) clockwise in the rotating frame of reference, similarly the spins at the foot of the axis will precess more slowly when the gradient is on, (i.e.) anticlockwise in the rotating frame. When the gradient is switched off, all the spins once again experience the same magnetic field B_0, and precess at the same rate, and they are all stationary in the rotating frame. However the spins remain out of phase with respect to one another, and the phase angle depending on the position along the PE direction. For MR imaging the PE gradient is applied as multiple repetitions with different amplitudes. The repetitions results in different phase information [55, 99-103].

The MR signals obtained represent the vector sum of all the spins, therefore it also depends on the size of the PE gradient applied and also on the spatial distribution of MR nuclei along the PE gradient direction. The phase is given by:

$$\phi(y) = \gamma(y) \int_0^T G_y dt$$

Equation 3-20

Where T is the time for which the PE pulse is switched on and G_y is the magnitude of the PE gradient [55, 99, 101, 102].

3.8 k-Space

k-space is a mathematical space in which the raw time domain data are stored in the computer which records the spatial frequencies of the MR signal observed from the pulse sequence with respect to applied phase and FE gradients. It can be thought as a form of raw data that contains the digital information of the MR signal from the acquisition slice which was acquired using the pulse sequence. The digital raw data of k-space are converted to the visual grayscale image using the fast Fourier transformation (FFT). The FFT is a mathematical algorithm proposed by Cooley and Tukey to implement the Fourier analysis in a computer to convert the time domain data into data represented by frequency and amplitude. The k-space region contains lines of data, where each line was filled for each application of phase and FE gradient. The PE gradient determines the position of the line of data in k-space in the vertical-axis. The FE gradient is responsible for the filling of the line of data with the digital signal in the horizontal-axis (see Figure 3-10). Each point in k-space has information for the whole-image, hence sections of k-space cannot be assigned to sections in the image. The k-space images in this thesis were processed using ImageJ (open source programme). The outer region of k-space contains higher spatial frequencies, which contain information in relation to edge/detail (see Figure 3-11 (top)). The centre region of k-space usually contains information with respect to signal and contrast (see Figure 3-11 (bottom)). It is important to acquire full k-space data to produce the image. Partially filled k-space can be used to reconstruct a reasonable image more quickly, provided more than half of the k-space is filled. The remaining k-space lines of data can be either filled with zeroes or extrapolated based on the acquired lines [99-103, 105].

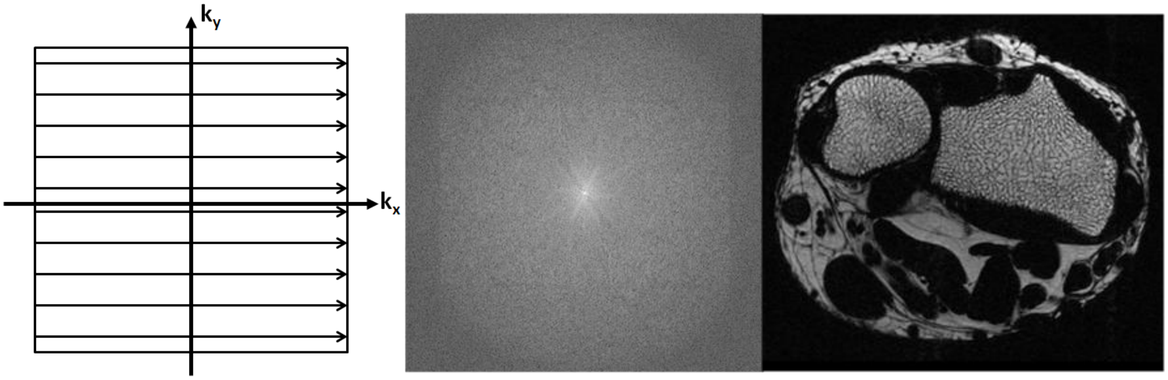

Figure 3-10 The image on the left illustrates the trajectory of k-space based on the phase (k_y) and frequency (k_x) encoding gradients. The image in the middle is the actual raw k-space for an image. The image on the right is an FT processed grayscale image from the whole region of the raw k-space.

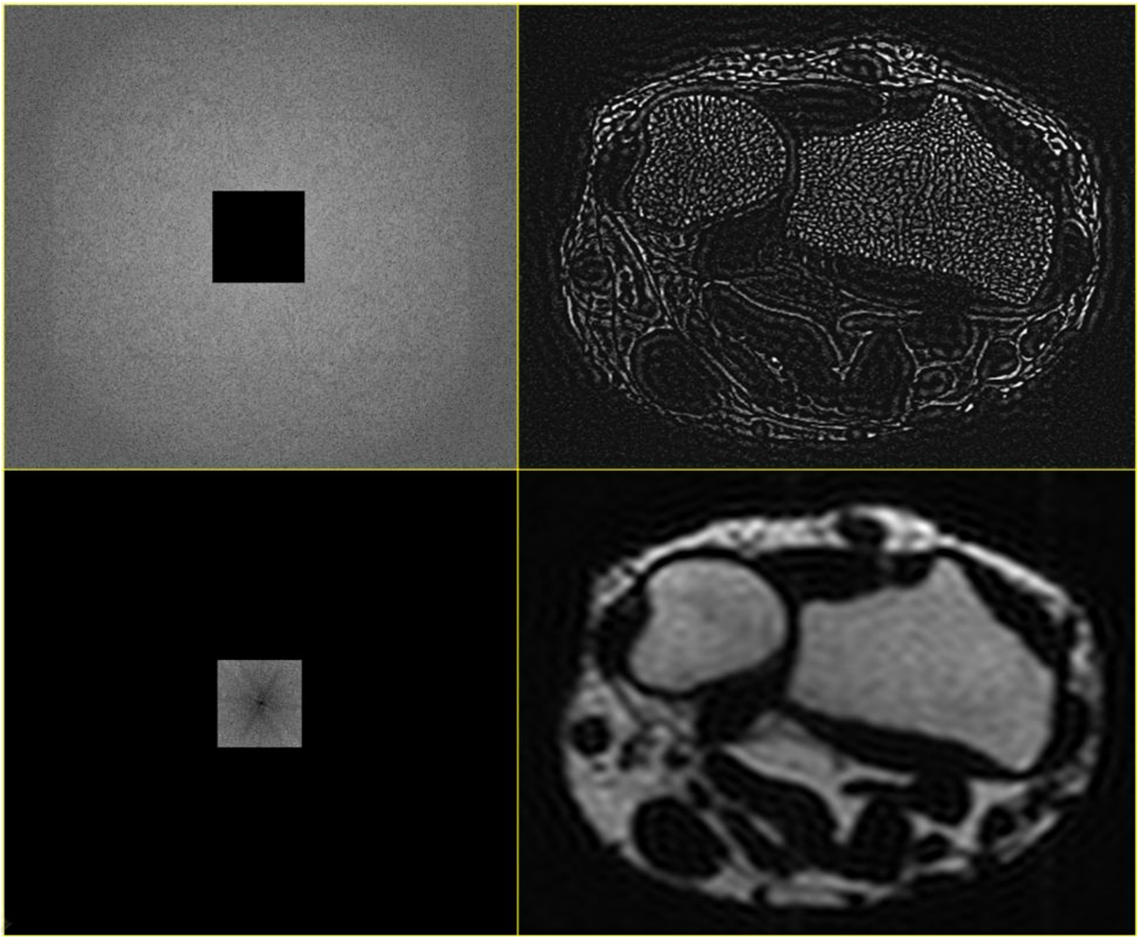

Figure 3-11 The top row illustrates the outer region of k-space which was processed resulting in an image with only information in relation to detail or edge. The bottom row illustrates the central region of k-space which was processed resulting in an image with information in relation to signal and contrast. Note that it is important to have both the regions of k-space to produce a reasonable image.

Modern imaging sequences like echo planar imaging (EPI) use zigzag or continuous (see Figure 3-12 (left)) or spiral k-space filling, and ultra-short TE (UTE) sequences use radial k-space filling (see Figure 3-12 (right)). Both the techniques result in faster data acquisitions, but with reduced image quality, since some regions of k-space are left out [99, 101-103, 106].

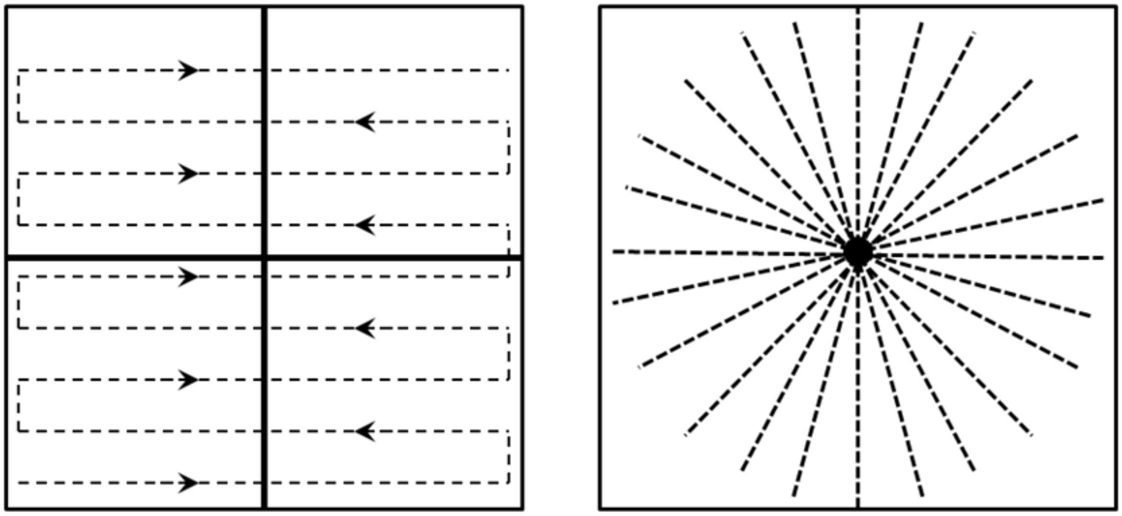

Figure 3-12 The image on the left is a k-space with continuous trajectory commonly used for fast imaging sequences like EPI. The image on the right is a k-space with radial trajectory commonly used for UTE imaging type of sequences.

3.9 Signal-to-Noise Ratio

The signal-to-noise ratio (SNR) is one measurement of image quality and is dependent on the main magnetic field, RF coils, relaxation properties of tissues and the sequence parameters. The signal displayed as pixels in the image is the representation of the MR signal from the tissue based on the described parameters. The MR signal in the pixel is primarily dependent on the number of protons within it. The noise is the random differences in the pixel value, which gives the image its grainy appearance. The noise primarily originates from the tissue under investigation. The MR data comprises a mixture of both signal and noise, and the ratio of the two is known as SNR. It is always essential to have high SNR in images for diagnostic importance [99-103].

SNR are improved by using dedicated anatomical coils, since they are designed to encompass the whole region by limiting the space between the coil and anatomy. SNR are also improved by increasing the number of signal averages (NSA), but it also increases the acquisition time. The signal in the image increases proportionately with NSA since it is coherent, but noise is random and thus the increase in NSA results in the square root of noise. Thus the ratio of signal and noise depends on the square root of NSA. The other common methods of increasing the SNR are by increasing the slice thickness and voxel volume to increase the number of protons, but trade-off with reduced spatial resolution. Reduction in receiver bandwidth also improves SNR, but also results in other effects like chemical-shift artefact. SNR is essential in MR, but increasing it is based on a balance of other factors [99, 101, 102].

3.10 Imaging

3.10.1 Spin-Echo Imaging

The SE imaging is similar to the SE sequence (see 3.6.4), but is modified to be acquired with spatial encoding gradients to form an image (see Figure 3-13). The sequence uses 90° and 180° RF pulses in the presence of slice selection (SS) gradient for selective excitation of the slice. In-between the two RF pulses, the phase encoding (PE) gradient is applied with desired amplitude for filling of each line of k-space. After the application of the 180° RF pulse, the SE is collected in the presence of the frequency encoding (FE) gradient. The cycle repeats again, but with different PE amplitude to fill another line of k-space. If the matrix is 256 × 256 then there will be 256 PE steps with different amplitude. The duration between the first RF pulse from each repetitive cycle is known as the repetition time (TR). The time duration between the 90° RF pulse and the occurrence of the SE is known as the echo time (TE). The midpoint (TE/2) between the 90° and SE is exactly the point of application of the 180° RF pulse. Therefore the application time of the 180° pulse always determines the occurrence time of the SE so that we can accurately detect it [99-103].

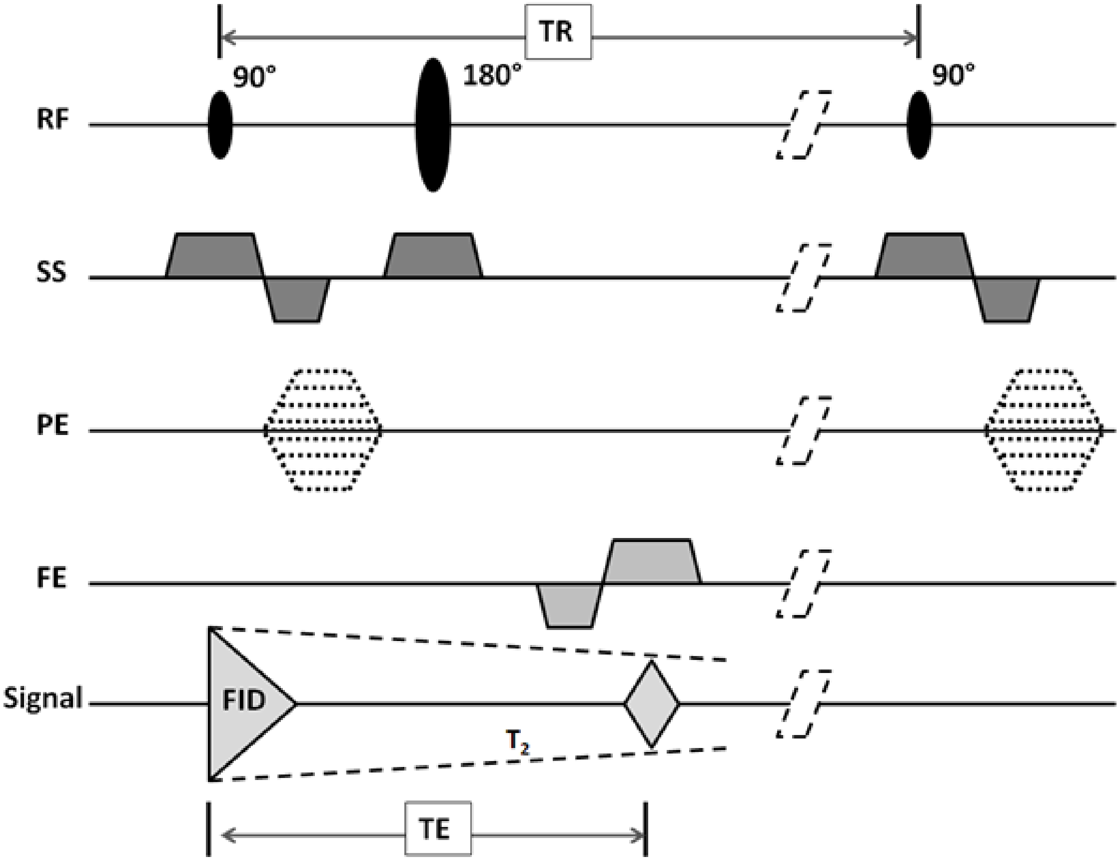

Figure 3-13 The pulse sequence diagram for a spin-echo sequence.

3.10.2 Fast Spin-Echo Imaging

The fast spin-echo (FSE) sequence is a modified version of spin-echo sequence designed to reduce the acquisition time. The FSE sequence uses a 90° RF pulse followed by multiple 180° RF pulses within each TR (see Figure 3-14). The number of 180° pulses applied is usually known as the echo train length (ETL). Each of the 180° pulses permits different PE gradient amplitude to reduce scan time by a factor equal to ETL, which fills multiple lines of k-space for each image in a single TR. The cycle is repeated until all the lines of k-space are filled. The use of multiple RF refocusing pulses results in the degradation of signal, where the first refocusing RF pulse will contain a higher signal when compared with the last pulse. The use of multiple 180's results in multiple TEs for a single image and the TE is averaged from all the echoes to be denoted as effective TE for image contrast [99-103].

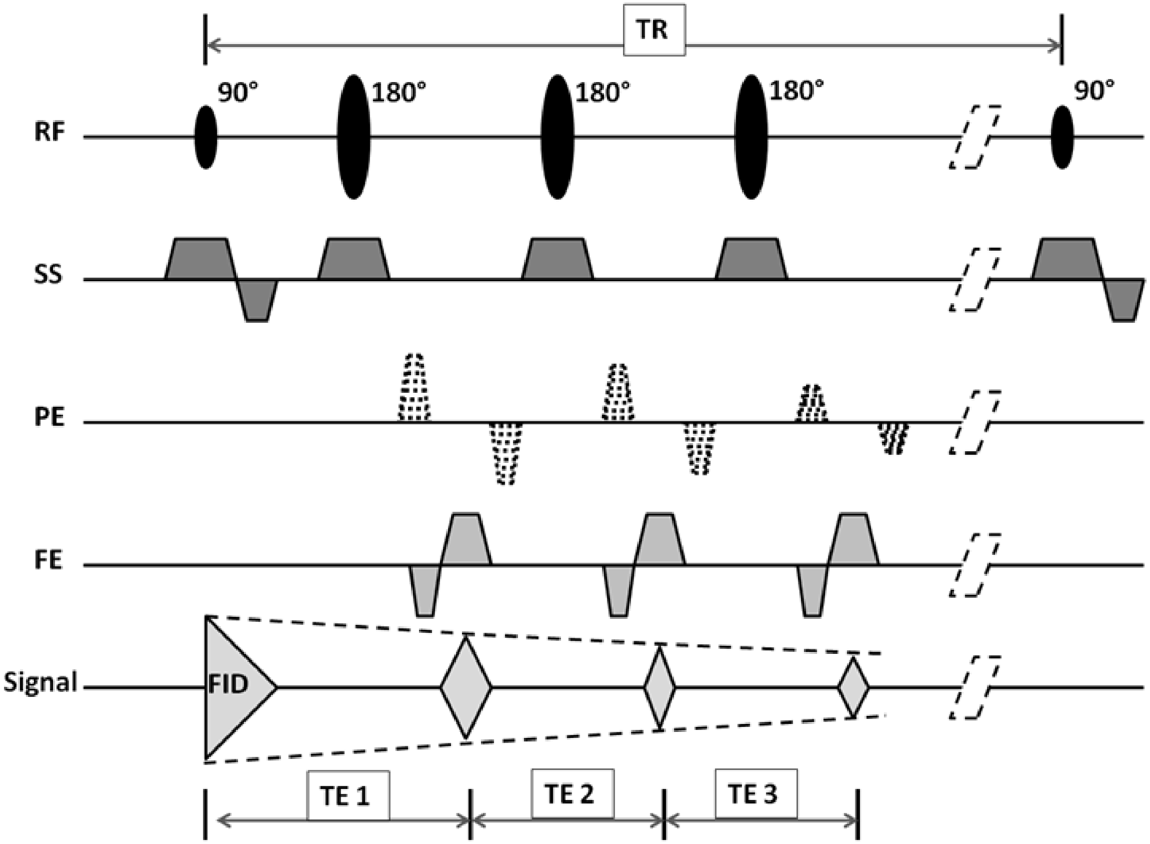

Figure 3-14 The pulse sequence diagram for fast spin-echo sequence.

3.10.3 Gradient Echo Imaging

Gradient echo (GRE) imaging is a type of MR technique, which produces an MR signal by applying a variable flip angle in the presence of the slice selection gradient and then applies the PE gradient followed by FE gradient to produce an echo by gradient dephasing and rephasing (see Figure 3-15). GRE imaging are fast imaging sequences since they do not use 180° RF pulses and are by default T_2* weighted since the decay due to B_0 inhomogeneities are not recovered. GRE imaging is prone to susceptibility artefacts due to the elimination of the 180° RF pulses.

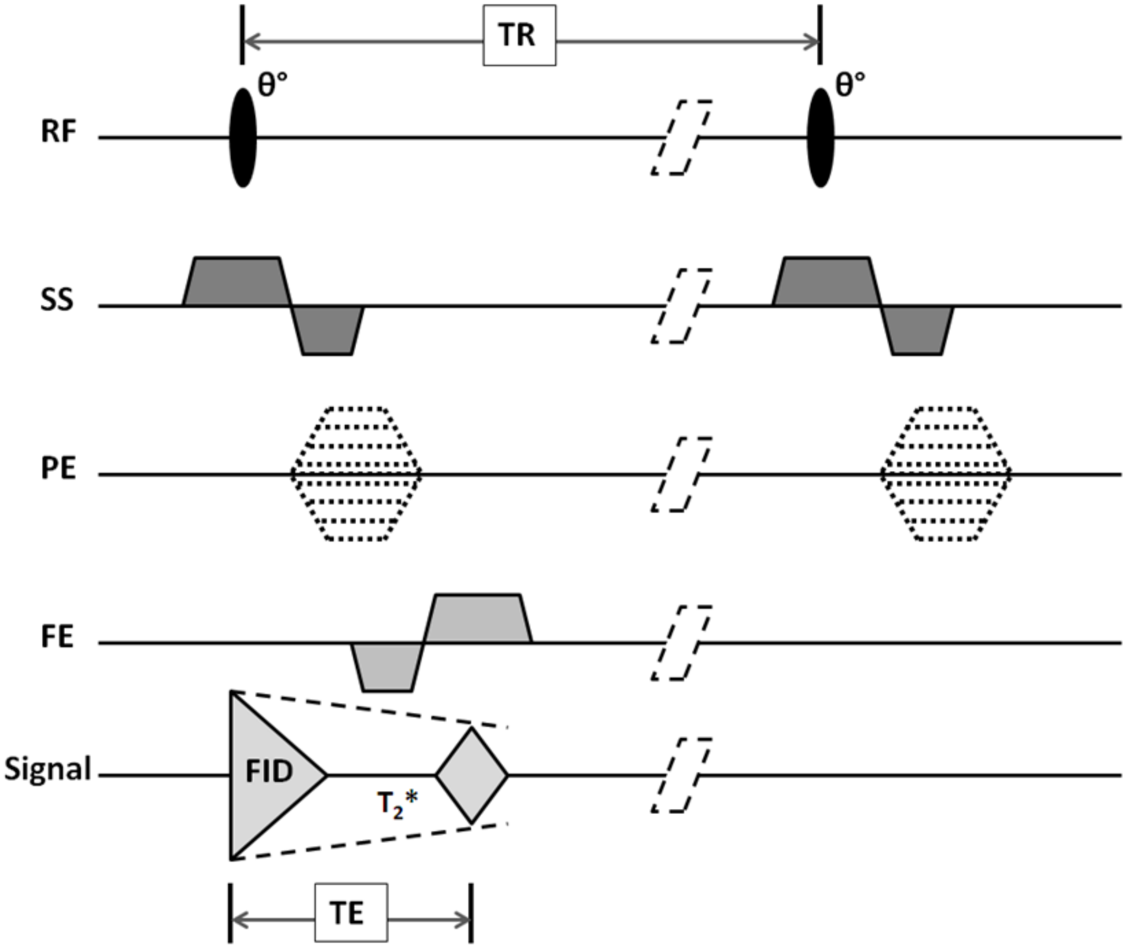

Figure 3-15 The pulse sequence diagram for gradient echo sequence.

3.10.4 Chemical-Shift Imaging

Imaging of fat and water is an active topic of research and there have been various methods proposed for imaging either or both of these. MRS is advantageous compared to imaging, in differentiating the various components of fat based on their chemical nature, but suffers from poor spatial resolution. Imaging of fat and water is preferred since it has better spatial resolution. Fat or water suppression techniques are used to image fat and water separately as two different acquisitions. The Dixon technique is another useful technique, which acquires data based on the phase difference between fat and water. The original technique acquires two image data one with both fat and water in-phase and the other data with water and fat 180° out-of-phase (see Figure 3-16). The phase difference between fat and water occur at distinct times and it is important to apply the TE at that particular duration to collect the data. The summation of in-phase and out-of-phase data results in the image having only the water component. The subtraction of in-phase and out-of-phase data results in the image with only fat components. This technique was known as the two-point Dixon technique [107]. The technique was good in separating fat and water, but suffered from B_0 inhomogeneity resulting in phase errors that led to contamination of fat and water components.

A modified version of Dixon technique was proposed to correct for these phase errors known as three-point Dixon technique. The three-point Dixon technique uses three echoes to measure three phase position of the spins (e.g. 0°, 180°, 360°). Using the additional phase information the sequence was able to mathematically correct for phase errors from the image due to B_0 inhomogeneity. Currently three-point Dixon technique is the commonly used fat and water imaging method and GE uses the modified version of this technique known as iterative decomposition of water and fat with echo asymmetry and least squares estimation (IDEAL) sequence [108-111]. The three-point Dixon technique is occasionally prone to phase wrapping artefact resulting in improper calculation of fat and water images. This technique also assumes that fat and water are two components, but in reality the fat is composed of nearly ten peaks with distinct chemical-shift and it is impossible for this technique to accurately quantify all the fat, resulting in contamination of water with fat [108, 110, 112-116]. Newer versions of Dixon techniques are used that acquire six echoes that take into consideration the presence of multiple fat peaks as well the correction of phase errors. GE scanners call the modified IDEAL technique IDEAL-IQ.

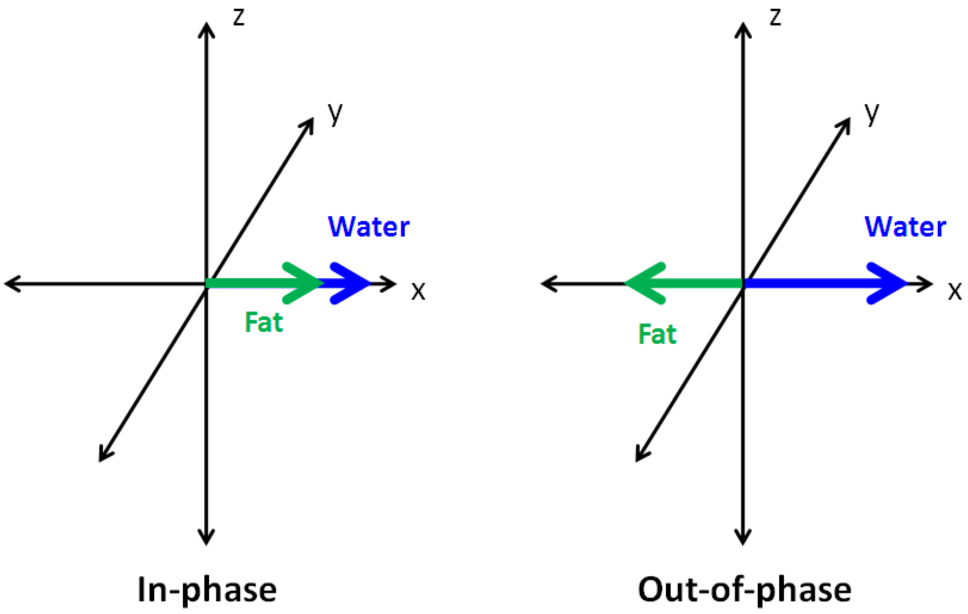

Figure 3-16 A typical Dixon technique with illustration of the in-phase and out-of-phase signals of fat and water.

3.10.5 Image Contrast

The manipulation of the TE and TR normally results in controlling the weighting of the acquired image. There are three common types of MR image weighting which results in differences in contrast between different tissues in the anatomy. The three image weightings are T_1, T_2 and proton density (PD). The T_1-weighted image predominantly contains signal information with respect to T_1 relaxation properties of the tissues. The T_1-weighted image is usually acquired when short TR (<500ms) and short TE (<50ms) are used, and is visualised by dark signal in fluids due to their long T_1 relaxation, which do not reach full equilibrium. The T_2-weighted image predominantly contains signal information with respect to differences in the T_2 relaxation properties of the tissues. The T_2-weighted image is usually acquired when long TR (>2000ms) and long TE (>100ms) are used, and is usually visualised by bright signal from fluids due to their long T_2 relaxation. The PD-weighted images predominantly contain signal information with respect to spin density from the tissues. The PD-weighted image is usually acquired when long TR and short TE are used [99-103].

3.11 Artefacts

An artefact is any undesired signal in the acquired image which is not present in the anatomy. Following is a brief description of some of the common artefacts observed in MR.

3.11.1 Motion (Ghosting)

The most common artefact in MR is not due to hardware, but due to the patients movements, which may be caused due to voluntary or involuntary actions. The voluntary movements are often decreased by making the patient as comfortable and immobilised as possible, or provide alternative methods (e.g. sedation, decreasing scan time) to decrease movements. The movements result in images being affected by ghosting or blurring (see Figure 3-17) which often result in repeating the scan.

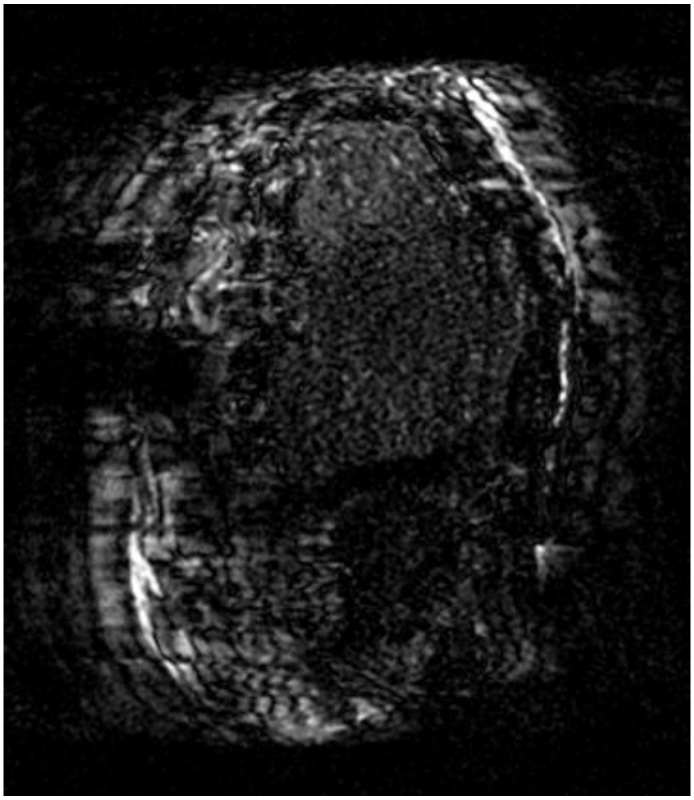

Figure 3-17 A typical axial image acquired at distal radius using the wrist coil illustrates, severe motion artefact due to the voluntary movement of the patient. Note the severe ghosting and blurring in the image due to the motion.

Motion of anatomical organs is another common artefact and also results in blurring and ghosting artefacts. The anatomical motions are often contributed by e.g. respiratory, cardiac, peristalsis and blood vessel flows. The artefacts are mostly observed in the PE direction due to its multiple repetition and time gap between acquisitions. Cardiac and respiratory gating are useful methods of decreasing these artefacts, but result in increased acquisition time. The respiratory movements are decreased by breath-holding and advanced fast imaging sequences. Peristalsis is the natural movement of intestines, and these movements are sometimes reduced by specific drugs or fast imaging sequences. Artefacts due to blood flow are also a common occurrence and result in signal void or ghosting. Flow artefacts (see Figure 3-18) are commonly reduced by using saturation bands outside the field-of-view (FOV) or slice direction. Other techniques like flow compensation gradients also reduce the artefacts but at the expense of increasing the TE to accommodate the gradient application [99-103, 117].

Figure 3-18 A typical water-only axial image from Dixon imaging acquired at distal radius illustrates flow artefacts due to the flow of blood in the blood vessels.

3.11.2 Chemical-Shift Artefact

MR signal predominantly arises from hydrogen protons present in fat and water. Water is a small molecule containing hydrogen and oxygen, but fat is a large molecule made up of chains of triglycerides attached to glycerol, containing carbon, hydrogen and oxygen atoms. The different chemical composition results in differences in their resonance frequency and is commonly known as chemical-shift (see 3.14.1). Chemical-shift differences between fat and water are desired for spectroscopy, but create an artefact in imaging. Imaging sequences use FE for spatial information. The chemical-shift artefact is caused due to the mismapping of fat and water, which results in the shifting of fat signal by a number of pixels in the FE direction of the image. The shifting of pixels appear as dark and light bands (see Figure 3-19) on the anatomy. The shift of the pixels is mainly dependent on the receiver bandwidth used. Lower bandwidth results in worse chemical-shift artefacts. The artefact is usually avoided by using large bandwidths at the expense of reduced SNR in the image [99-103, 117, 118].

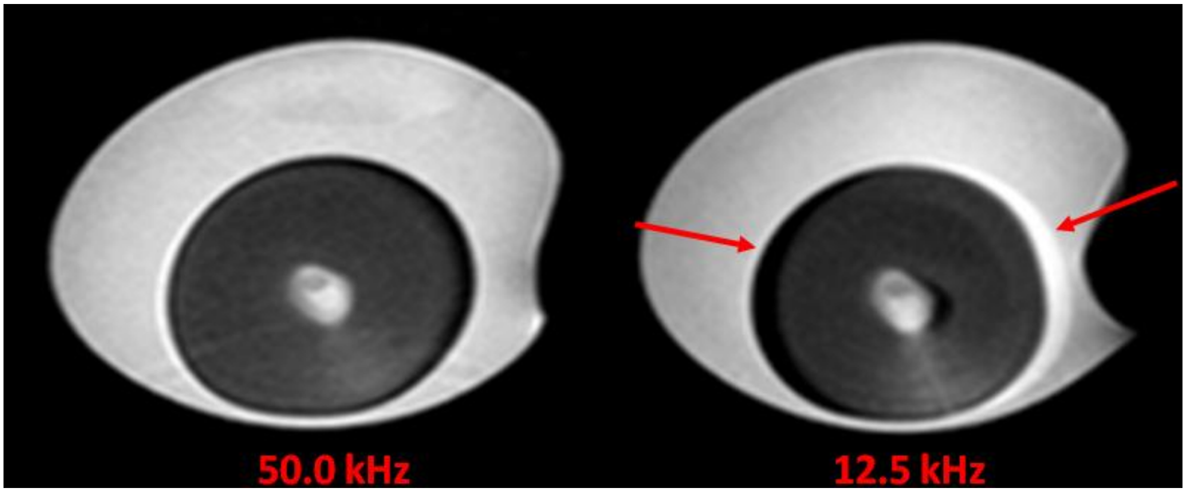

Figure 3-19 A typical chemical-shift artefact observed in egg. The image on the left was acquired with high receive bandwidth, which resulted in reduced chemical-shift artefact. The image on the right was acquired with low receive bandwidth, which resulted in severe chemical-shift artefact. Note the high and low bands of signal in the artefactual region.

3.11.3 Wrap Around Artefact

The wrap around artefact is a common artefact observed in the PE direction, when the anatomy is larger than the applied FOV. This results in the image of the tissue just outside of the FOV to be wrapped into the opposite side of the image in the PE direction (see Figure 3-20). The common method of reducing this artefact is to use saturation bands just outside the FOV or to apply phase oversampling. The phase oversampling acquires a larger FOV image around the prescribed FOV in the PE direction with additional number of PE steps. After acquisition, the unwanted FOV region is discarded and only the prescribed FOV is displayed [99-103, 117].

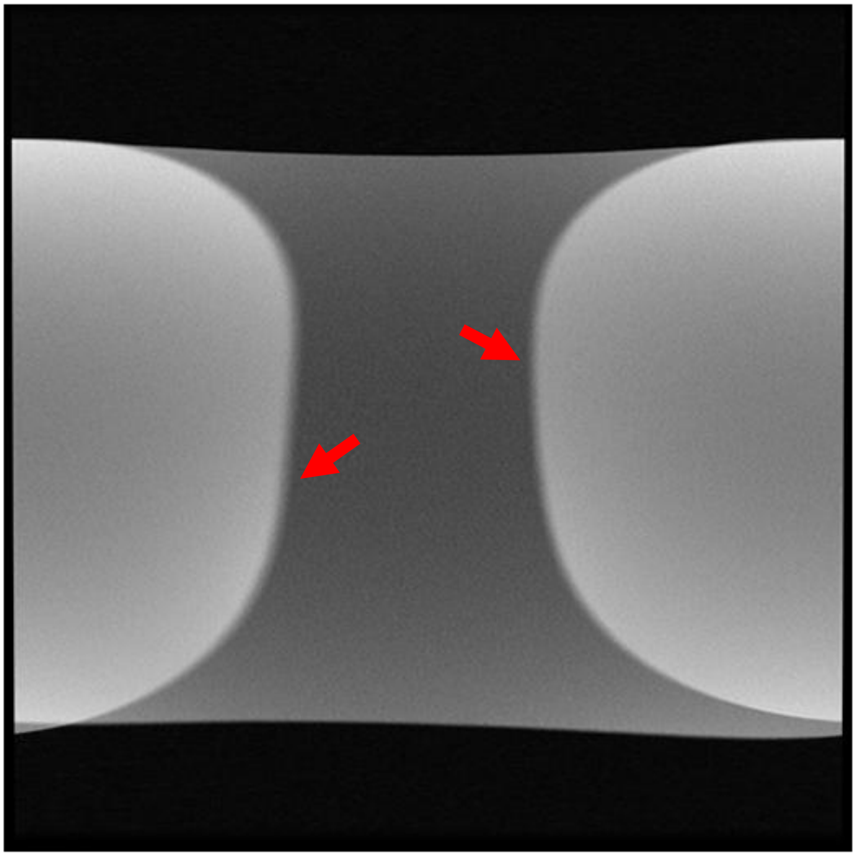

Figure 3-20 An image acquired on a phantom with reduced field of view using the wrist coil. The image is affected by wrap around artefact where the image is contaminated by signal from the outer edges of the phantom.

3.11.4 Susceptibility Artefact

Susceptibility is the ability of the material to be temporarily magnetised when subjected to an external magnetic field. Different types of tissues have different susceptibility properties and they create microscopic fields, which increases the dephasing of protons around boundaries of tissues, which thereby changes the linearity of the applied gradients. Metals have higher susceptibility, whereas bone and air have lower susceptibility and tissues lie in-between. The interface between these types of materials results in gross signal voids and distortion and is often known as susceptibility artefacts. The artefacts are common in organs at boundaries of air and tissue (e.g. lungs, skull) and also in interfaces between trabecular bone and marrow. Metallic implants create gross artefacts due to their higher susceptibility. Susceptibility artefacts are worse with gradient echo images and spin-echo imaging with short TEs are usually preferred to reduce the artefacts. The susceptibility artefacts become severe with higher magnetic field strengths [99-103, 106, 117].

3.11.5 RF Inhomogeneity Artefact

RF inhomogeneity artefact is a common artefact observed in MR scanners, which results in non-uniform variation in signal intensity across an image (see Figure 3-21). The artefact is caused due to non-uniform B_1 field transmission and/or a non-uniform detection in the RF coils. The artefacts are common in phased array and surface coils. The surface and phased array coils are receive only where the B_1 transmission is applied by the large integrated body coil in the scanner, and the coils are sensitive to signal detection in relation to distance, thus the signal intensity reduces as the distance between the coil and the tissue increases. Birdcage coils have much better uniformity due to their better B_1 transmission and better detection of the signal, which results in reduced RF inhomogeneity artefact. There are a variety of techniques (e.g. post processing, calibration, multi-transmit) available to correct this artefact. Post processing tools are common techniques that use dedicated algorithms and filters to correct for non-uniformity in the image. Calibration techniques acquire additional calibration data with B_1 maps before the normal image acquisition, and use the information from the B_1 map to correct for non-uniformity in the acquired image. A more advanced method is to correct for B_1 imperfections in the coil itself by using multi-transmit technology that adjusts the transmission of B_1 in relation to different regions of the anatomy to create a more uniform B_1 transmission which results in more uniform signal intensity in the acquired image [99-103, 117].

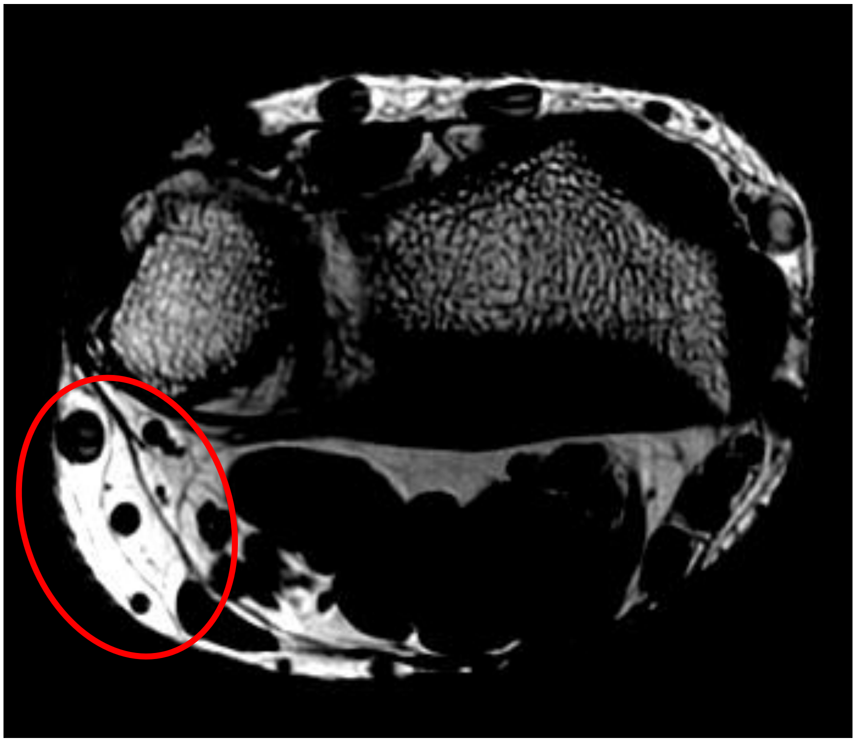

Figure 3-21 A typical axial image from distal radius acquired using the phased array wrist coil. Note the non-uniform signal intensity in the image, where there is high signal intensity inside the drawn region of interest and normal signal intensity in the rest of the image.

3.12 Hardware

An MR scanner typically contains multiple components. Following is the brief description of the five important components: main magnet, RF coils, gradient coils, shim coils and computer system.

3.12.1 Main Magnet

The main magnet is an important component of the MR scanner responsible for the production of the B_0 field. The magnets used for research or clinical purposes typically fall in one of the three categories of resistive, superconducting and permanent magnets. The superconducting magnet is the only magnet design which is capable of reaching very high magnetic fields when compared with all the other types, and this is commonly used in clinical settings. The direction of the magnetic field is usually dependent on the type of magnet design. Superconducting magnets used in clinical setting usually have a horizontal bore for horizontal field direction. The superconducting magnets achieve their field strength by using super cooled superconducting coils, surrounded by liquid helium or nitrogen, which contain a large flow of electric current. Resistive magnets use the flow of electric current through the coil to create a magnetic field and require systems for cooling of the coil during operation. The heat produced in the magnetic coil elements limits the amount of power supply and limits the field strength. Permanent magnets use large magnets constructed from rare-earth or ferrite-based materials to create low to medium (0.2 – 0.4 T) magnetic fields. The designs of these types of magnets are usually bulky/heavy and limit the strength of the magnetic field [99-103, 117].

3.12.2 Radio Frequency Coils

The RF coils are responsible for the production of the B_1 magnetic field for the generation and detection of MR signals. There are many types of RF coil designs including birdcage and circular loop (surface coil). The birdcage RF coils (see Figure 3-22) are designed to both transmit and receive (transceivers) and produce high uniformity of transmission, whereas the surface coils are usually designed for receiving only. A large permanent birdcage coil is integrated in the clinical scanner for transmission and receiving, and is known as the body coil. It is important to collect the signal from the anatomy by placing the coil as close as possible to increase the SNR. Coils with birdcage design are commonly used as head coil. Surface coils are routinely used as phased-array (PA) designs, which are a combination of multiple surface coils, that in-turn could be used as a volume (surrounding the anatomy) or surface coil (placing near the anatomy). PA coils are designed for receive only, which require the body coil for the transmission of the RF pulse. PA coils are used for improved anatomical coverage and also in improving SNR. Quadrature coil design are also used which contain two receivers present 90° to one other for distinguishing real and imaginary components of the received signal. Quadrature coil designs improve SNR by a factor of square root of two [99-103, 119].

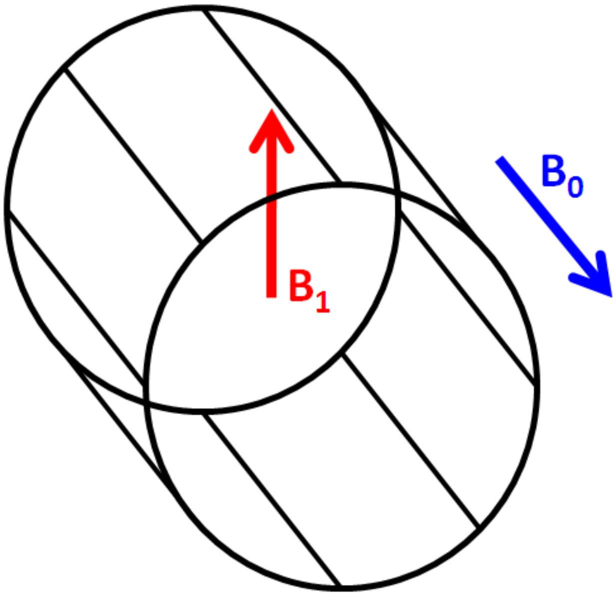

Figure 3-22 A typical birdcage RF coil design with illustration of the direction of the B_1 and the B_0 magnetic field.

3.12.3 Gradient Coils

Gradient coils are responsible for producing linear magnetic fields in multiple planes in the scanner. The three field directions are produced by two main gradient coil designs: Maxwell pair and Golay set (see Figure 3-23). The Maxwell pair is mainly responsible for creating gradient magnetic fields in the axial plane (z) or in the direction of the main magnetic field B_0. The Golay set are coils designed to produce gradient magnetic fields in the transverse plane of x or y direction. The x and y directions are achieved by using two Golay sets present 90° to one another [99-103, 119].

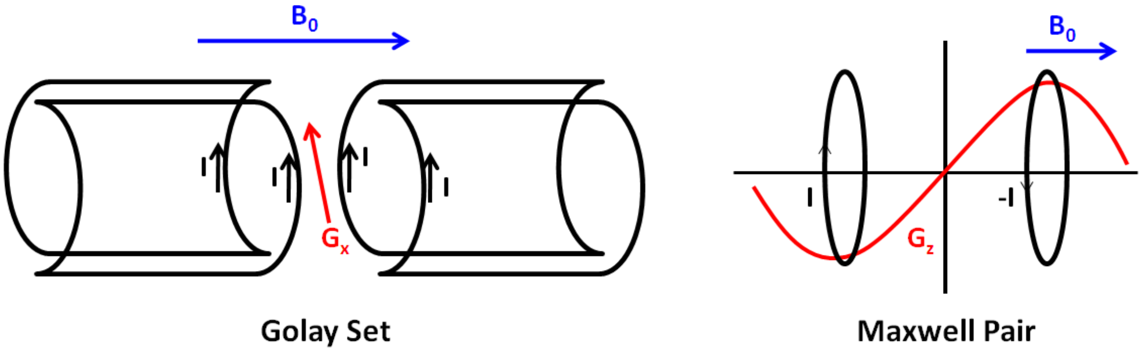

Figure 3-23 The image on the left is the Golay set gradient coil design, used for the production of the gradient magnetic field in the x or y axis. The image on the right is the Maxwell pair gradient coil design, used for the production of the gradient field in the z axis.

3.12.4 Shim Coils

The B_0 field produced by main windings in the magnet is not perfectly homogeneous. During manufacture of magnets there are a lot of inevitable manufacturing and procedural errors and there are additional factors like gravity and the magnetic forces between conductors causing deformation in the magnet's geometry. The errors lead to variation in the magnetic field with respect to spatial position. Major field inhomogeneities across the gradient direction are undesirable since the spins present in these inhomogeneities will have complex nature and result in loss of phase coherence in the region with inhomogeneity [99, 101-103, 120, 121].

Excellent magnetic field homogeneity is an absolute must for acquisition with MRS. Spectroscopy acquires signal from individual metabolites based on their differences in resonant frequency or chemical-shift. An MRS spectrum is illustrated as multiple peaks present at different frequency. If the magnetic field is inhomogeneous, the individual spectral peaks broaden and result in overlapping of adjacent peaks.

It is important to maintain a homogenous magnetic field for imaging and spectroscopy and it is commonly achieved by introducing extra fields that correct the unwanted inhomogeneities. There are two common types of shimming known as active and passive shimming. Passive shimming is achieved by manual placement of metal to add or cancel fields and is routinely used during the initial stages of the installation of a new scanner. Active shimming was proposed by Golay when he developed the shim coils to cancel B_0 inhomogeneities. The shim coils are similar in design to the Golay set that was used for the production of the gradient magnetic fields. The shim coils produce linear magnetic fields in all directions to cancel the main magnetic field inhomogeneities [98, 99, 101-103, 120-123].

Earlier versions of magnets required manual active shimming, but in recent years the active shimming is done automatically by the scanner during prescan based on acquiring B_0 field maps and using a mathematical algorithm to correct the inhomogeneities in the B_0 map by adjusting the current flow in the shim coils. The shimming is commonly applied at the beginning of each sequence. Manual high order shimming with much more complicated shim profiles is also preferred in MRS with large voxel volume to improve the magnetic field.

3.12.5 Computer System

The computer system is an essential component of the MR hardware, which comprises of three major components of host computer, pulse programmer (PP) and array processors. The host computers are under the control of the operator for prescribing the scans, display and processing of acquired images, archiving and networking. The PP is used for the control of the hardware for the different type of pulse sequences. The array processors are used for the image reconstruction from the raw signals.

3.13 Prescan Adjustments

Before the acquisition of images or spectra, the MR system initiates an automatic prescan routine. The automatic prescan results in optimisation of scanner properties including the centre frequency (Ax) in relation to water peak, automatic shimming to correct for B_0 inhomogeneities, the transmitter gain (TG) and flip angle for an effective RF pulse transmission, the analogue (R1) and digital (R2) receiver gains for effective detection of the signal and the chemical-shift selective (CHESS) pulse for water or fat suppression. The prescan for imaging can be applied manually if the automatic prescan fails. The prescan for spectroscopy can also be applied manually which additionally includes higher order shimming [98, 99, 101, 120, 122, 124-127].

3.14 Spectroscopy

Spectroscopy can be considered as a non-invasive biopsy technique used for the analysis of the chemical structure of the tissue or anatomy. Spectroscopy in MR can be acquired by using different types of nucleus (e.g. ^{1}H, ^{31}P, ^{13}C), and in this thesis the spectroscopy was primarily acquired by using ^{1}H. The basis of spectroscopy is the chemical-shift effect, which identifies the individual chemical components based on their differences in their resonant frequency. Thus it is essential to have a highly uniform B_0 to differentiate the chemical components [98-103, 122-124, 126, 128-130].

3.14.1 Chemical-Shift

When a nucleus is placed in a magnetic field B_0, its electron cloud circulates around it and causes an induced magnetic field B_i, which commonly aligns opposite to the magnetic field (see Equation 3-21), resulting in the effect known as shielding. Due to shielding, the nucleus experiences a reduced effective field $B_{eff} = B_0(1-\sigma)$, where σ (sigma) is called the shielding or screening constant, which results in a slightly different Larmor frequency given by:

$$\omega = \gamma B_0(1 - \sigma)$$

Equation 3-21

This effect is dependent on the type of chemical bond the nucleus forms with other nuclei. If the nucleus bonds with a highly electronegative compound like oxygen, then its electrons around it will be stolen by the electronegative pair resulting in less shielding. The effect of shielding is pronounced with H-C bonds (see Figure 3-24). The effects of shielding allows nuclei to be identified by frequency in spectroscopy and are expressed in terms of the chemical-shift (δ), which is a difference in parts per million (ppm), between the Larmor frequency of a nucleus in a particular chemical bond, ω, and the frequency of the same nucleus in a standard reference compound ω_{Ref}.

$$\delta = \frac{(\omega - \omega_{Ref})}{\omega_{Ref}} \times 10^6$$

Equation 3-22

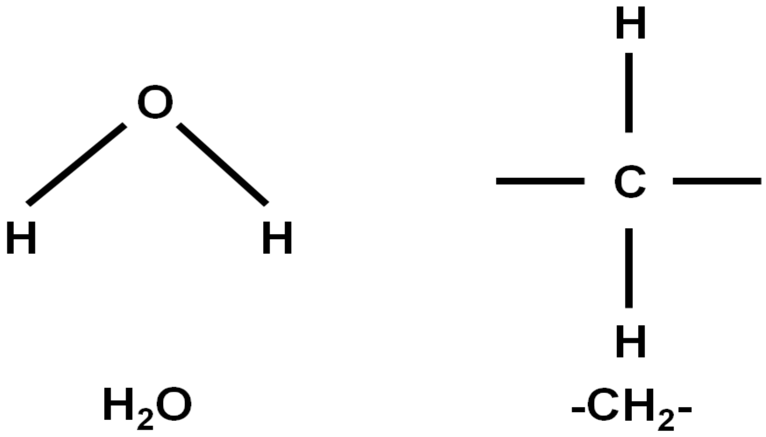

Figure 3-24 Chemical structure diagram.

For ^{1}H spectroscopy the reference compound is tetramethylsilane (TMS), chosen because it contains almost totally shielded protons. Chemical-shifts are independent of field strength (e.g. 1.3 ppm fat, 4.7 ppm water). The absolute separation of spectral lines increases with B_0 due to larger differences in precessional frequency [98-103, 118, 122, 123].

3.14.2 Features of Magnetic Resonance Spectroscopy

Spatial localisation techniques for proton spectroscopy fall into two general categories: either single-voxel techniques, where a spectrum is recorded from a single region, or multi-voxel technique, where multiple regions are acquired simultaneously, which is also known as MR spectroscopic imaging (MRSI) or chemical-shift imaging (CSI). The two most commonly used single voxel methods are stimulated echo acquisition mode (STEAM) and point resolved spectroscopy (PRESS). For MRSI, a variety of different approaches are used but most commonly two or three dimensional MRSI is performed, often using PRESS or STEAM excitation [98, 99, 101-103, 131].

The basic principle underlying nearly all single voxel localisation techniques is to use three mutually orthogonal slice selective RF pulses and design the pulse sequence only to collect the echo signal from the volume in space (voxel) where all three slices intersect (see Figure 3-25). Signals from regions outside the desired voxel are commonly eliminated by saturation slabs and crusher gradients. The saturation slabs apply a 90° RF pulse before the normal imaging sequence, which tips the spins in the slab to the transverse plane. Thus the spins in the slab will have no longitudinal magnetisation and will not be excited when the normal imaging sequence begins, which results in no signal from the slab region. It is common to use default saturation slabs which surround the voxel of interest (VOI) in all voxel dimensions.

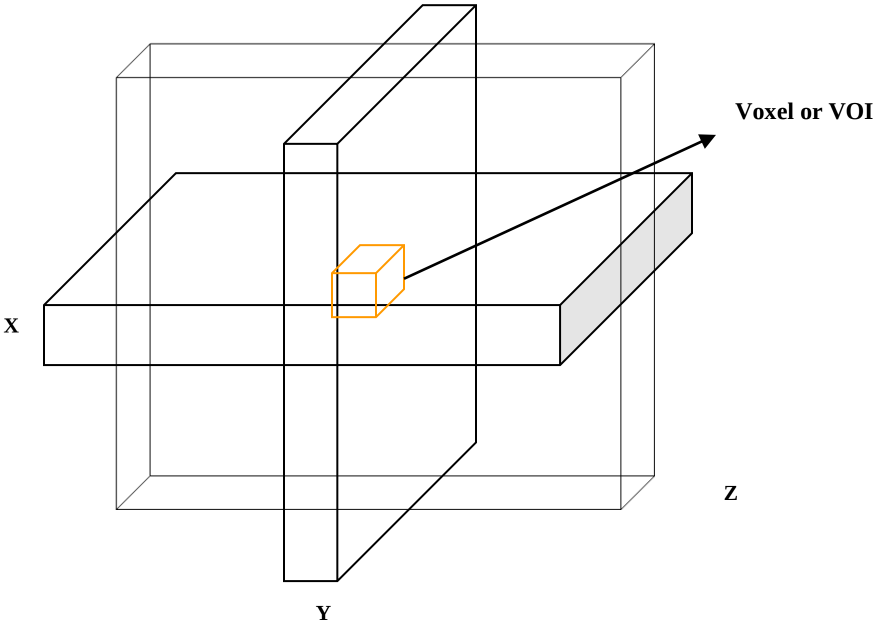

Figure 3-25 A typical voxel in spectroscopy sequences, which is formed at the intersection of all three slices.

In MRS, the large signal from water is normally suppressed in-order to facilitate the observation of the minuscule signal from metabolites (e.g. N-acetyl aspartate (NAA), creatine and choline). Effective water suppression is achieved by preparation pulses before the beginning of the normal acquisition. The preparation pulse is known as CHESS, which applies a narrow bandwidth pulse centred exactly at the water Larmor frequency, followed by the application of crusher gradients to spoil any remaining transverse magnetization. The crusher gradients are usually applied in all three gradient directions. Accuracy of CHESS is important for effective suppression of water [98, 99, 101, 102, 126, 132].

3.14.2.1 Stimulated Echo Acquisition Mode

The stimulated echo acquisition mode (STEAM) sequence uses three 90° pulses, where the third RF pulse transforms the longitudinal magnetization stored by the second RF pulse back into the transverse plane to form the stimulated echo (STE). The format of the sequence is of 90°-(TE/2)-90°-(TM)- 90°-(TE/2)-STE (see Figure 3-26). The sequence is usually combined with three CHESS pulses in the beginning to suppress water if required. For the STEAM sequence the duration between the second and third 90° RF pulse is known as the mixing time (TM). An important feature of STEAM is that only half of the transverse magnetization prepared by the first 90° pulse is transferred into longitudinal magnetization by the second 90° pulse, decreasing signal-to-noise ratio (SNR) by a factor of 2. During the TM period, longitudinal magnetization decays with T_1. The three slice selective gradients for the 90° pulse forms the voxel of interest (VOI) in the scan. In-between the 90° pulses and CHESS pulses there are lots of other gradients known as crusher gradients which effectively dephase unwanted signals from other echoes and FID’s. STEAM sequences were often preferred for spectral acquisition with short echo times (TEs), since they do not employ the use of 180° RF pulse as in the case of PRESS, but recent improvements in hardware has resulted in PRESS sequences that can be acquired with shorter TEs [98, 99, 101-103, 122, 123, 128].

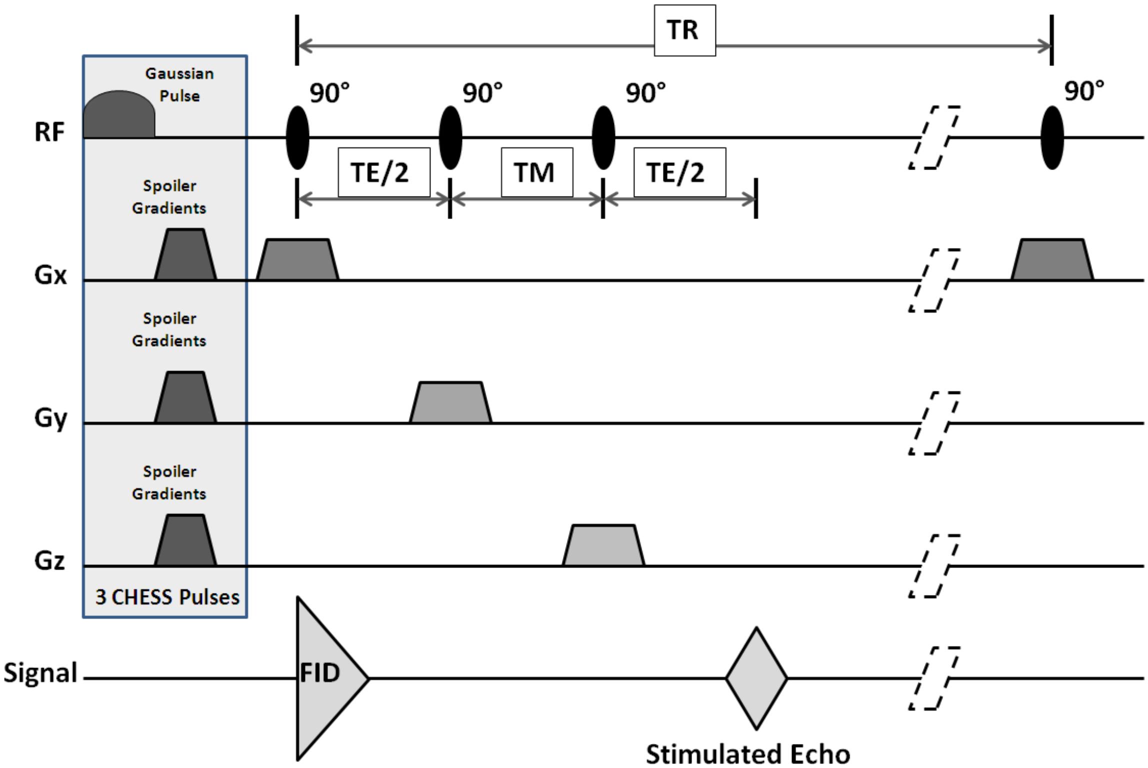

Figure 3-26 Pulse sequence diagram for a STEAM sequence.

3.14.2.2 Point Resolved Spectroscopy

The point resolved spectroscopy (PRESS) sequence is very much similar to that of a STEAM sequence, but instead of using three 90° pulses, it uses one 90° pulse followed by two 180° pulses. This method produces a spin-echo (SE) rather than a STE, resulting in better SNR than STEAM. The pulse sequence begins routinely with the CHESS pulse if water suppression is required and has 90°-180°-(SE1)- 180°-SE2 (see Figure 3-27). With a PRESS sequence the final signal is collected from the second spin-echo (SE2), which is the representative signal from the whole voxel. The PRESS sequence also uses lots of crusher gradients to dephase the unwanted signals and uses three selection gradients for the VOI. All spectra in this thesis were acquired using PRESS, due to its advantage of increased SNR compared to STEAM. The CHESS pulse was routinely switched off manually, to acquire signal without any water suppression, since we require both water and fat for quantification of bone marrow [98, 99, 101-103, 122, 126, 128, 132].

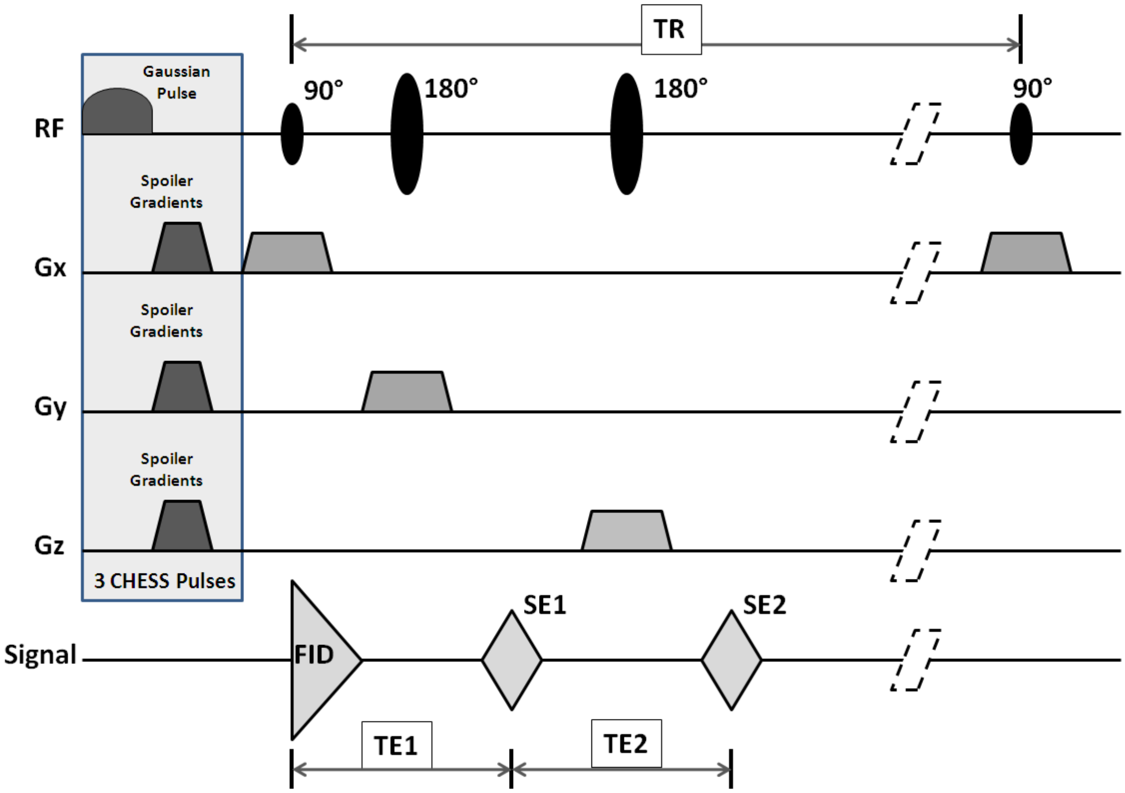

Figure 3-27 Pulse sequence diagram for a typical PRESS sequence.

3.15 Eddy Currents

Eddy currents are induced due to the rapid application of gradient pulses. These eddy currents create additional magnetic fields, which are normally classified into two categories of: zero and first order. The Zero order eddy currents do not affect the SNR but just gives a frequency dependent phase shift from the region of. First order eddy currents produce dephasing effects within the region of interest thus resulting in the decrease in SNR. Both the type of eddy currents and field inhomogeneity will affect spectroscopy peak shapes resulting in difficult spectral quantification and fitting with modelled line shapes. Eddy current artefacts are commonly corrected by dividing the ^{1}H spectra time domain signal from the unsuppressed water time domain signal [98, 99, 101, 102, 122, 127, 133].

3.16 Spectroscopy Analysis

The raw data from spectroscopy sequences have to be processed for quantification of the individual peaks or metabolites. Multiple types of software are available for processing the raw data. At our centre there are two: spectroscopy-analysis in GE (SAGE) and linear-combination model (LCM) [134-136]. SAGE was the default analysis software provided by GE to process the spectroscopy data from the scanner, which is normally advantageous for a quick assessment of spectral data, but requires manual inputs and coding to quantify spectra on a routine basis. LCM is a third-party software for automated analysis of *in vivo* spectra.

3.16.1 Spectroscopy Analysis Using SAGE

The SAGE package offers step-by-step tools for processing and analysis of the raw data. The raw data can be processed by manual tools or by automatic pre-processed macros with a list of processing functions. Following are some of the common methods that were applied for processing and analysis of the spectroscopy data in this thesis.

3.16.1.1 Spectral Processing

The spine coil used for the HBM project acquired signal from the lower three elements for lumbar spine acquisition, resulting in signal from a total of six channels. The signal received from the voxel depends on the number of active elements in the coil and the distance from the elements to the voxel of interest (VOI). For spectral processing it is very important to effectively combine the signals from all the active elements rather than using the signal from only one element which may or may not be in close proximity with the voxel. To get the optimum data, the signals from multiple elements were combined using the default coil combine algorithm, which combines the signal in the frequency domain. The default method was not effective, which resulted in poor SNR, distortion of individual peaks, gross phase artefacts and long processing time. To overcome the artefacts and processing time, the raw signals were processed by an in-house algorithm developed by the department staff to effectively combine the individual signals using the weighted average principle. The algorithm extracts the magnitude channel of the first frame of free induction decay (FID) and uses the mean of the first 5 points from the FID as the SNR weighting factor for all the signals from the remaining elements. This method of processing resulted in reduced artefacts, processing time and improved SNR when compared with the default coil combine algorithm [98, 137-139].

Spectroscopy data are usually acquired in frames based on the number of excitations (NEX) and the number of signal averages (NSA) used in the protocol. The default sequence acquires the first two frames of data without water suppression (water reference frames) and the rest of the frames with water suppression. Zero filling was applied to the resultant data to improve the spectral resolution. Zero filling is commonly applied to the time domain data after coil combine, and in SAGE it can be applied in any dimension of the data. Applying zero fill once converts a 1024 point raw FID to a 2048 point processed FID (see Figure 3-28). All spectra in this thesis were processed with one application of zero fill [98, 122, 123, 126, 140].

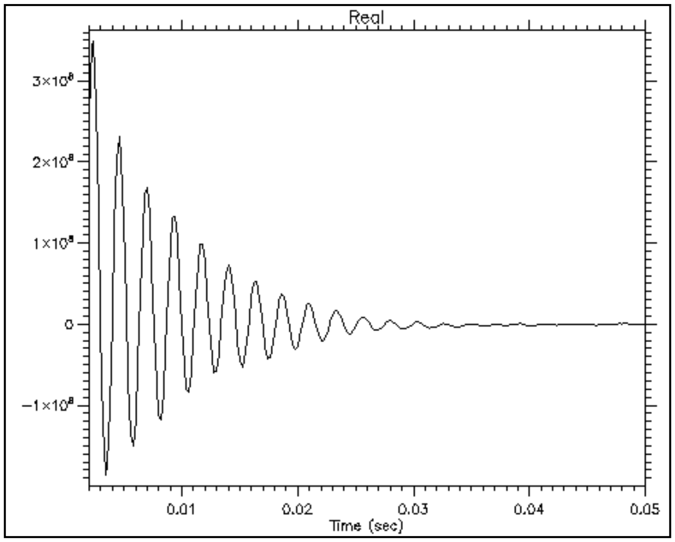

Figure 3-28 A typical raw FID data which has been coil combined and zero filled.

The water reference frames are useful in sequences that apply water suppression and can be used for optimisation, quantitation and eddy current corrections. The spectroscopy data in this thesis requires the presence of both water and fat, and hence the water suppression was turned off, resulting in all of the frames containing both fat and water. The spectroscopy data acquired in this thesis consisted of 8 NEX and 16 NSA, resulting in four frames of data (see Figure 3-29 (left)) two water reference frames and the two acquired frames. For this type of data, all the frames are combined together using the ‘average lines tool’ in SAGE to provide a single optimal frame (see Figure 3-29 (right)). Average line tool finds the average of all or selected frames in all dimension of the dataset by calculating the sum of all frames and dividing it with the total number of frames, resulting in a single averaged frame. The resultant time domain data or FID (see Figure 3-30 (left)) was converted to spectral data (see Figure 3-30 (right)) using fast Fourier transform (FFT) based on the Cooley and Tukey algorithm [98, 99, 101, 102, 122].

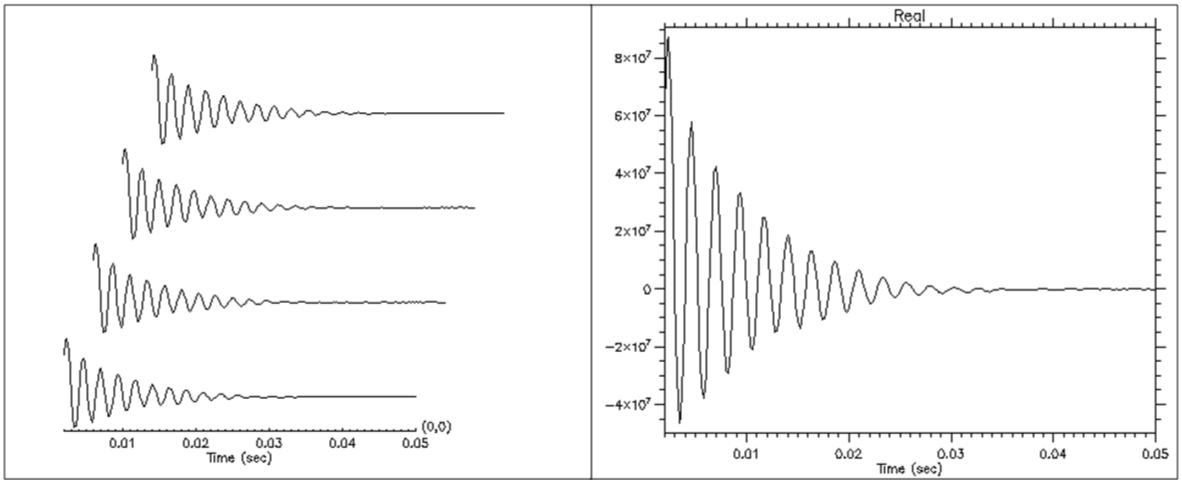

Figure 3-29 The process of averaging which combines the four frames of acquired data (left) into a single frame data (right).

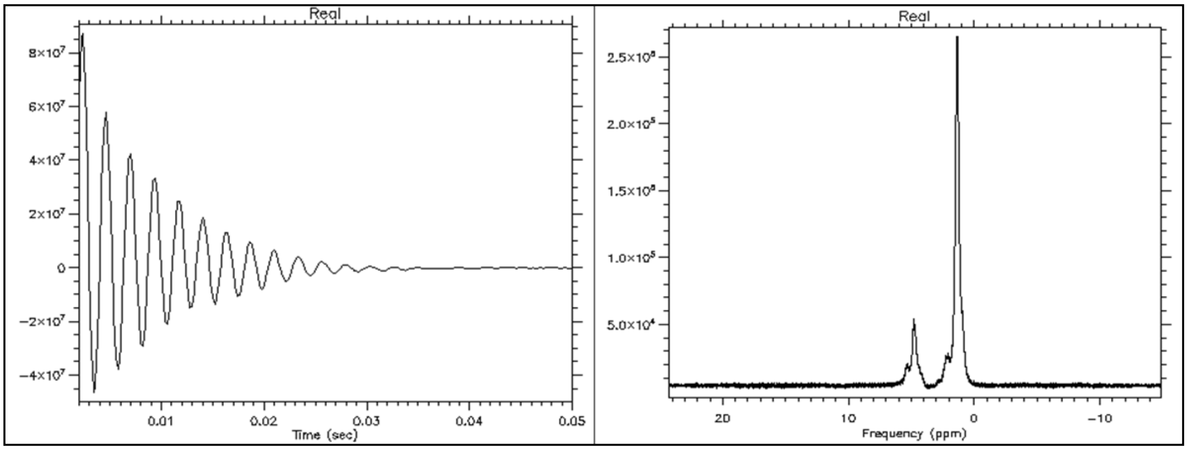

Figure 3-30 The process of converting a time domain data (left) into a frequency domain data (right) by the process of Fourier transformation.

Metabolite peaks are commonly quantified based on peak area or amplitude. In both cases we should ideally have a flat baseline. Distortions of baseline around the peaks can either over or underestimate the concentration of the metabolites, which may lead to poor diagnostic accuracy. Most spectra have baseline distortions after FFT and processing (see Figure 3-31 (left)) which is easily corrected using various processing tools like direct current (DC) offset, linear tilts and cubic/higher order splines. SAGE applies a cubic spline to correct baseline distortions (see Figure 3-31 (right)), and was used for all spectra in the research project. The data points for the spline were applied automatically by the tool for all the spectra in this thesis, by using the start and end point of the spectrum. Multiple manual points can also be applied to the spectrum with very poor baseline, but it was not necessary for the spectra in this thesis and thus it was not applied [98].

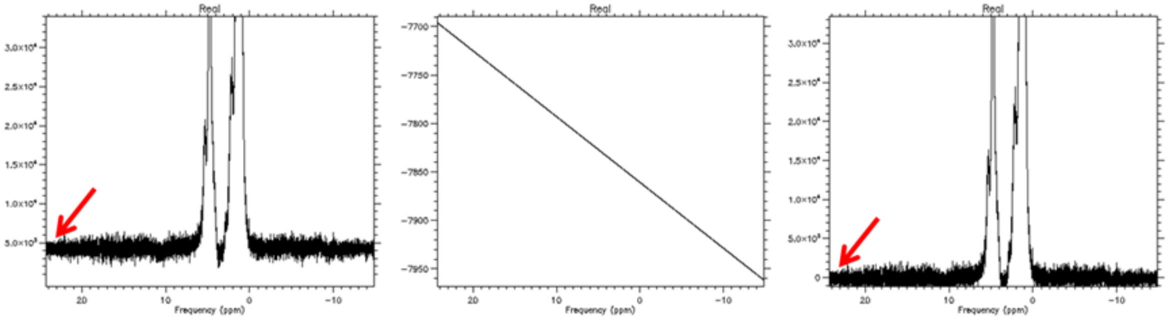

Figure 3-31 The application of baseline correction to the spectrum (left) using the cubic spline function (middle), which results in the baseline to align with 0 in the y axis (right).

Phase correction is an important post-processing tool to align spectral peaks when the beginning of the FID is not zero. Automatic phase correction was applied using SAGE, which corrected the spectra on voxel-by-voxel spatial locations using first point algorithm (see Figure 3-32) [98].

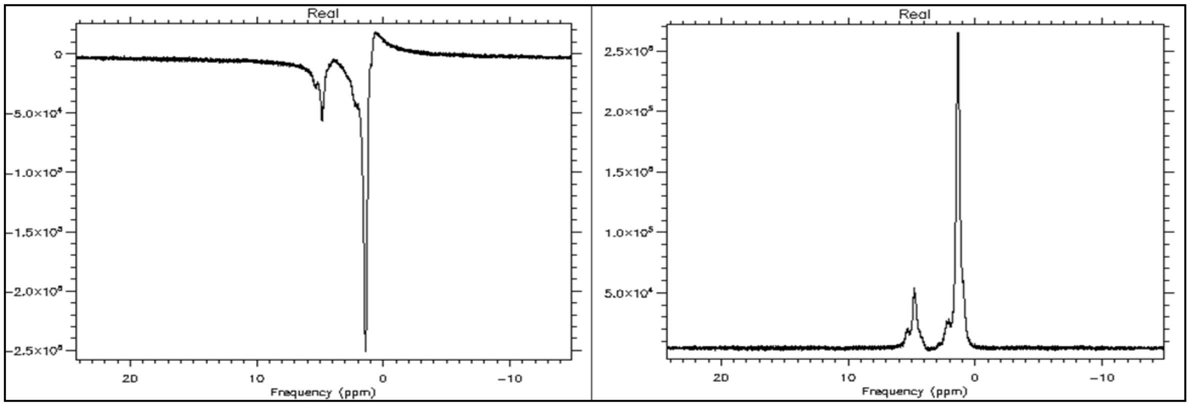

Figure 3-32 The method of correcting phase artefacts.

Sometimes during the acquisition of MR spectra, the scanner misinterprets the exact frequency of water reference peak by a few Hertz (Hz), which leads to the misalignment of metabolite peaks. This was corrected manually by using the peak registration tool in SAGE. The reference peaks that were used for registration was usually the lipid peak at 1.3 ppm or 0.9 ppm which are more stable to temperature changes when compared with water peak at 4.7 ppm.

Spectral zooming is usually applied to display spectra over a specific range to improve the visualisation in a particular part of spectrum. For bone spectra a fixed zoom region was selected from 6.3 ppm to -0.5 ppm, which normally includes all the lipid and water peaks from the spectra (see Figure 3-33).

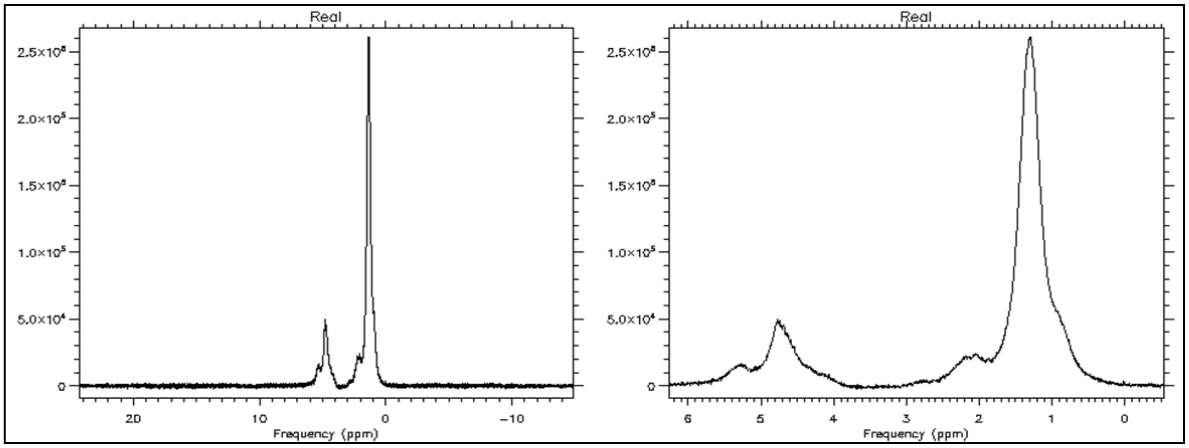

Figure 3-33 The method of zooming the spectra to display the range of desired peaks from the original spectrum.

3.16.1.2 Spectral Analysis

After the processing of spectra, the next important process is to quantify the spectral peaks in term of concentrations or ratios with respect to other metabolites. The SAGE package offers a wide variety of analysis tools, which could be used in manual or automatic mode to quantify the individual metabolites from the spectra. A manual analysis tool that uses manual data points to measure peak amplitude or integrate between a range of points was commonly used for quick and easy quantification of peaks which is user dependent and was very subjective. Due to these limitations, the tool was only used for measurement of full-width at half maximum (FWHM) of peaks from the clinical spectra. Most of the spectra from phantoms were processed with SAGE.

Frequency domain fitting (FDF) is an automated quantification tool which was manually pre-coded to fit and quantify individual peaks from the spectrum. FDF is a robust tool which relies on prior knowledge of peaks and can apply complicated fitting models of: Gaussian (see Figure 3-34), Lorentzian (see Figure 3-35) and Voigt (see Figure 3-36), to fit the spectra. The Voight model is a linear sum of both Gaussian and Lorentzian line shapes. The FDF method has to be pre-coded for individual peaks in the spectrum with information of frequency, phase, amplitude, line shapes and width, to function optimally. The individual information can be applied as fixed or free models for effective fitting of the peaks. An FDF coded for bone spectra in 1.5 T scanner will not be able to process optimally a bone spectra from 3.0 T or even a brain spectra from 1.5 T.

Quantification of spectra in SAGE is very versatile due to its varied types of analysis tools from manual analysis to automatic pre-coded FDF. SAGE offers the advantages of quantifying peaks using amplitude, rough integral of peaks or a more accurate quantification of each peak in the spectra. During the initial stages of the project, the FDF was experimented to fit clinical bone marrow spectra using different types of models. The FDF method of quantification using Gaussian (see Figure 3-34) and Lorentzian (see Figure 3-35) models was not reliable and resulted in large residuals. The in-house Voigt model (see Figure 3-36) resulted in good fitting of the individual peaks but resulted in unexpected outputs from the peaks, thus SAGE was used only for the measurement of full width at half maximum (FWHM) from water (4.7 ppm) and lipid (1.3 ppm) peaks from *in vivo* spectra and the rest of the quantification was done by LCM. Experimental spectra acquired using phantoms were processed primarily with SAGE.

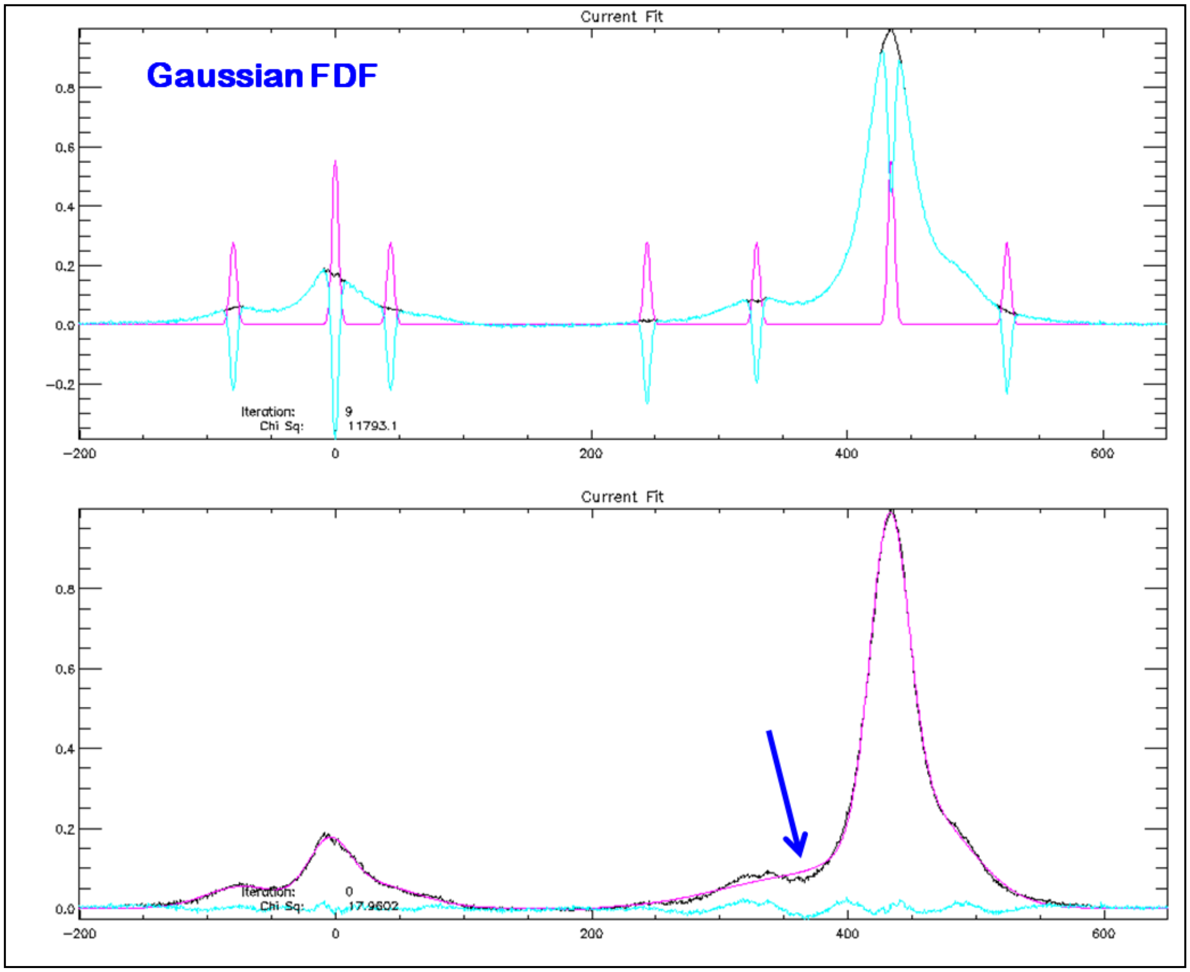

Figure 3-34 The method of frequency domain fitting using Gaussian line shape. The black line illustrates the original spectrum, the pink line illustrates the fitting model and the blue line illustrates the residual. The image in the bottom is the processed spectrum with the arrow pointing at some improper fitting of the original data.

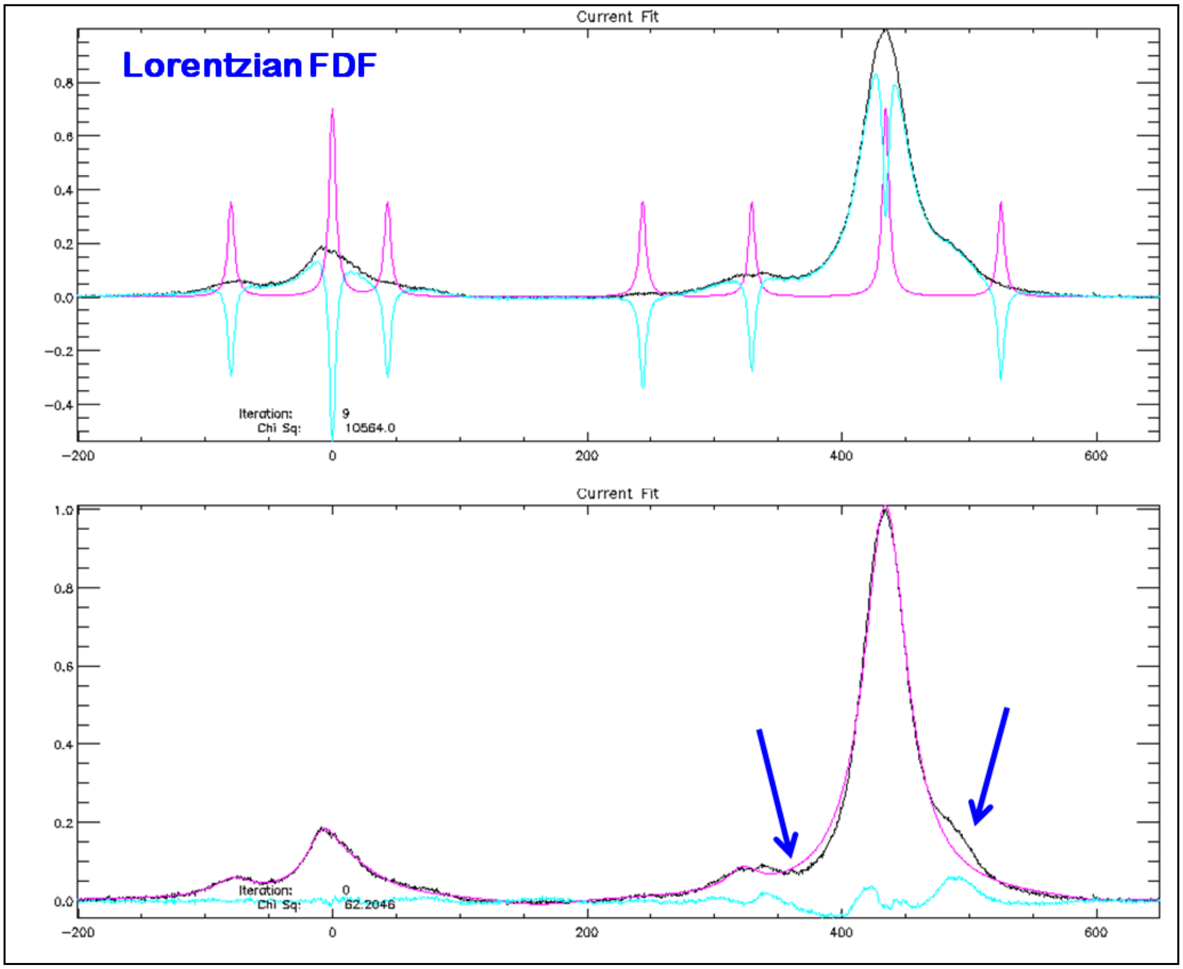

Figure 3-35 The method of frequency domain fitting using Lorentzian line shape. The image in the bottom is the processed spectrum with the arrows pointing at some improper fitting of the original spectrum.

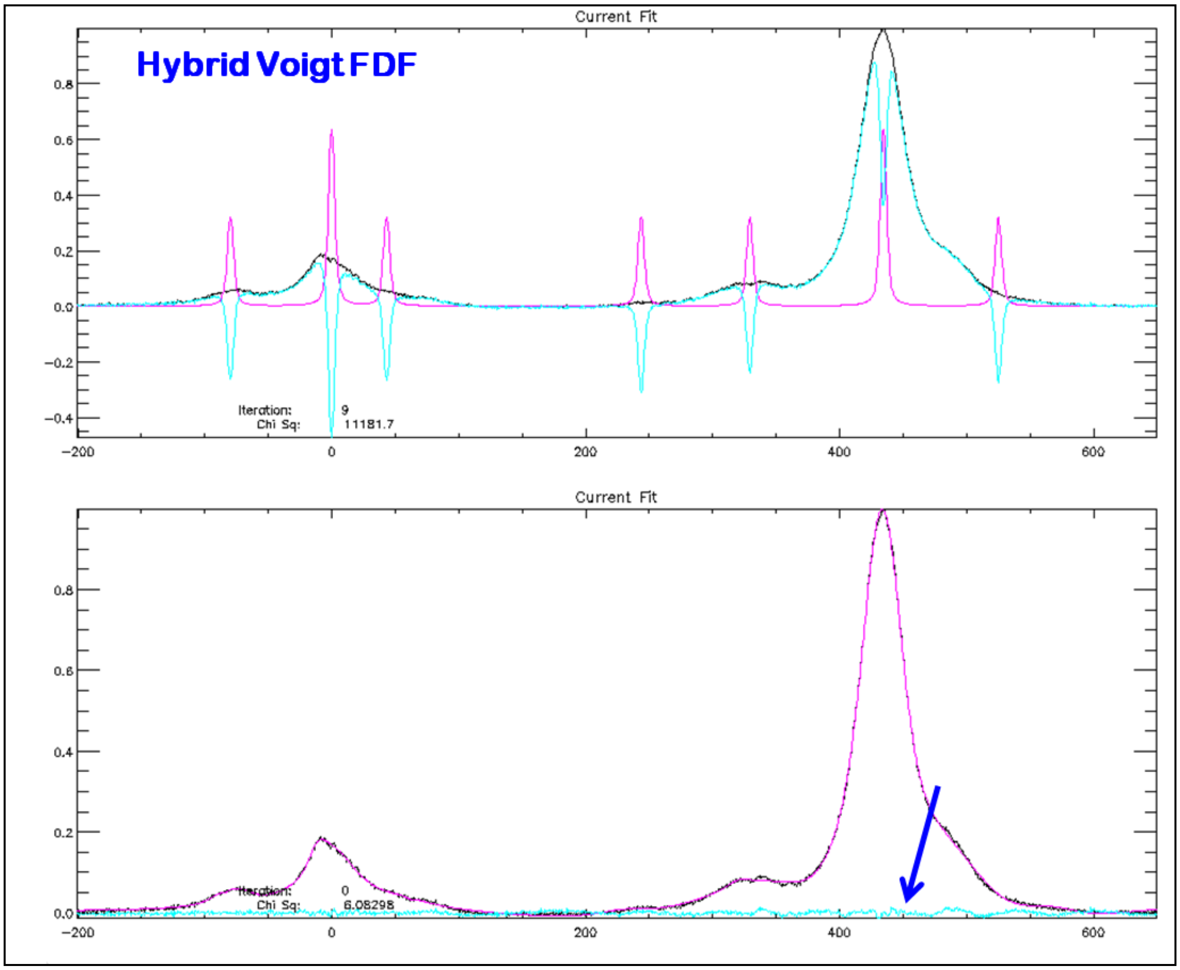

Figure 3-36 The method of frequency domain fitting using hybrid Voigt line shape. The image in the bottom is the processed spectrum with the arrow pointing at the residual after processing. The residual is minimal when compared with other line shapes.

3.16.2 Linear Combination Model

The linear combination model (LCM) [134, 135] is a well-established third party program for processing of clinical MR spectra to quantify concentrations of known individual metabolites. All *in vivo* spectra were exclusively processed using LCM to provide individual concentration of the lipid metabolites and water, due to its standardised approach of processing, accuracy, repeatability, removal of user bias and global recognition. The LCM uses extensive prior knowledge of spectra based on basis sets of full spectra for metabolites acquired from solutions in the appropriate magnetic fields to produce the best fit and estimation. Simulated basis sets are used for fitting of lipids. The basis sets are the most important factor in LCM for accurate fitting. During the application of LCM to *in vivo* spectra it is very important to select the right basis set with acquisition parameters that closely match the *in vivo* data.

The processing for an individual type of spectrum is completely automatic and works well for repeated measurements from the same or different centres. LCM is known to work well for *in vivo* acquisition from a range of scanners with different field strengths and setup, as long as their basis sets are loaded into the program before the processing.

LCM recommends a ppm range for processing of different types of spectra. For bone marrow spectroscopy, the recommended range is around 8 to -2.0 ppm which includes the whole range of metabolites present in the spectra including water. It is very important to apply the optimum range since LCM operates only on that range and discards the signal present outside the range.

Water scaling is an important processing tool in LCM which is routinely applied for most type of spectra, especially from single voxel data. The tool uses the water reference frames acquired during spectroscopy to estimate absolute concentrations of metabolite peaks. With water scaling, LCM scales the water peak of the reference data with basis set data. LCM applies zero and first order phase correction to the spectral data based on the type of spectra and the method in which it was acquired (see Figure 3-37). Phase correction is very important to the data as explained previously for effective processing, LCM spends a lot of time in extensive preliminary analysis to get the optimum starting values for the phases and reference shift in the final analysis. LCM works faster and better if prior information of approximate phase correction is known. The prior information is described by an expectation value and its standard deviation. There are individual recommendations (e.g. phase correction value for brain spectra may be different when compared with bone marrow) for the type of prior information which needs to be applied based on the type of manufacturer in LCM.

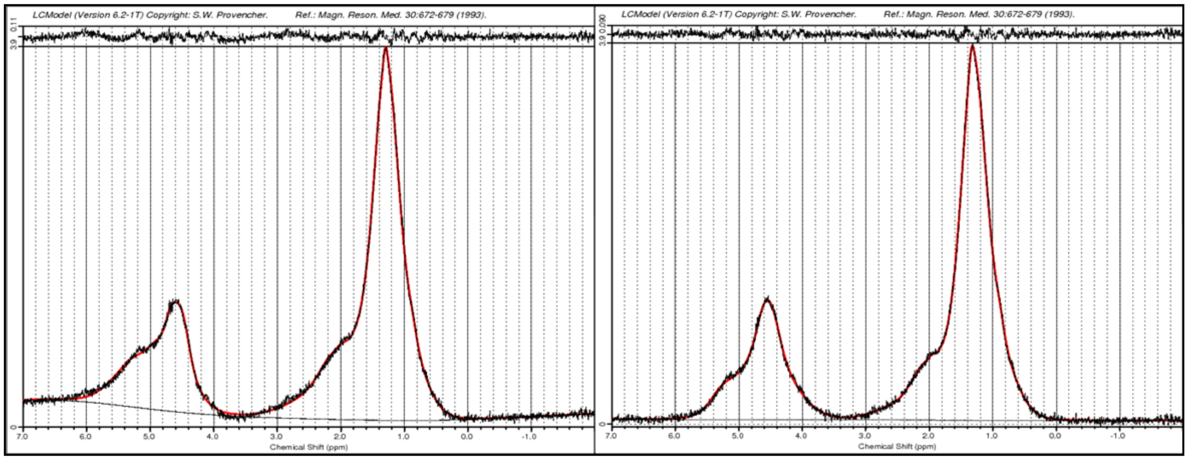

Figure 3-37 The left image illustrates the spectra with wrong phase correction parameters. The right image illustrates the spectra with proper phase correction parameters.

LCM processes the spectra and displays the concentrations from individual metabolites. The outputs are different according to the spectral type that was selected for the processing of the spectra. The spectral type ‘lipid-3’ is designed for this work as magnitudes for five metabolites (see Figure 3-38) and their method of output is described as follows:

- Lip13 – Estimates the magnitude of signal present under the peak of 1.3 ppm from methylene protons of saturated fatty acids ($–(Ch_2)_n$-). It is not clearly known if LCM fits the 1.6 ppm peak which is normally under the 1.3 ppm peak or just combines both the signal as Lip13.
- Lip09 – Estimates the magnitude of signal present under the peak of 0.9 ppm from terminal methyl protons of saturated, oleic and linoleic acids ($-CH_3$).
- Lip20 – Estimates the magnitude of signals present under the peaks of 2.02, 2.23 and 2.76 ppm from allyl methylene, α-methylene and divinyl methylene protons.
- Lip53 – Estimates the magnitude of signal present under the peak of 5.3 ppm from olefinic protons.
- Water – Estimates the magnitude of signal from peak present at around 4.65 ppm, from the hydrogen protons of H_2O.

Sometimes adjacent peaks are difficult to resolve and in which case it is safe to estimate the magnitude from the sum of adjacent peaks, which are described as follows:

- L20 + L13 + L09
- Lip09 + Lip13
- Lip53 + Water

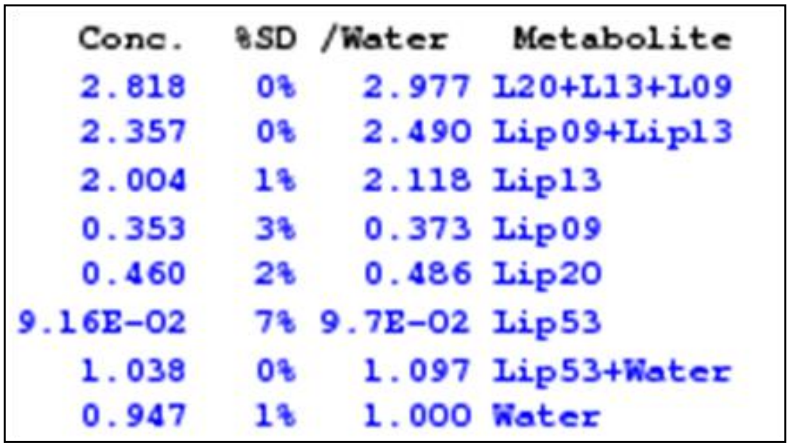

```
   Conc.  %SD /Water   Metabolite
   2.818   0%   2.977 L20+L13+L09
   2.357   0%   2.490 Lip09+Lip13
   2.004   1%   2.118 Lip13
   0.353   3%   0.373 Lip09
   0.460   2%   0.486 Lip20
9.16E-02   7% 9.7E-02 Lip53
   1.038   0%   1.097 Lip53+Water
   0.947   1%   1.000 Water
```

Figure 3-38 A typical result output from LCM with respect to concentrations of individual peaks and a combination of peaks.

4 Magnetic Resonance Investigation of Bones

4.1 Advantages of Using MR for Evaluation of Bones

Imaging of bones is an important topic of research in identifying abnormalities based on its structure and composition. Various imaging techniques are available for measurement of bone properties, but very few modalities are capable of quantifying both structure and composition. Quantification of bone has always focussed on identifying the two important features of bone quantity and quality. The bone quantity is the feature based on structural properties like trabecular bone structure, cortical bone structure, bone density, bone mineral content and physical features (e.g. area, thickness, and volume). Bone quality is the feature based on marrow (red and yellow), porosity, diffusion, perfusion and metabolic markers.

Dual-energy X-ray absorptiometry (DEXA) is the current gold standard clinical technique used for the evaluation of bone strength and it is primarily based on bone parameters related to bone quantity. DEXA measures properties of areal bone mineral density (BMD) by using dual-energy X-rays to differentiate between soft and hard tissue. Disadvantages of this technique include: (i) projectional data acquisition resulting in superimposition of anatomical information into a two-dimensional image and (ii) use of ionising radiation. Quantitative computed tomography (QCT) and peripheral quantitative computed tomography (pQCT) are other imaging techniques that are commonly employed to evaluate bone properties based on volumetric BMD as well as structural details of trabecular network and cortical bone. They eliminate superimposition but suffer from anatomical limitation and radiation exposure.

Magnetic resonance (MR) is a technique that is capable of providing bone information related to both bone quantity and quality from the whole-body. MR evaluation of bones is an active topic of research for investigation and quantification by using various techniques such as anatomical imaging, spectroscopy, perfusion, diffusion and mathematic modelling (clustering and finite element analysis). Direct MR imaging of bones, results in a signal void due to the extremely short relaxation properties of tightly-bound hydrogen protons in the solid bone components of cortex and trabeculae. Routine clinical sequences are not capable of collecting signals from the fast decaying spins, thus specialised sequences like ultra-short TE (UTE) are used for collecting information from solid bone components directly, but at limited resolution and signal-to-noise ratio (SNR). In future, with the advancement in hardware and sequences, it may be possible to image bones directly at high-resolution. In normal sequences the structure of the bones is usually evaluated from images based on the signal void. The processing of bone structure is evaluated using the inverse image of the original acquisition. Previous work has demonstrated that structural data from MR correlate well with DEXA data and other techniques that commonly evaluate bone quantity.

The marrow component of bone exists in a soft tissue nature surrounded by bony trabeculae and cortex. The marrow components are visualised in detail using routine sequences and using specialised sequences like the Dixon technique, which acquires individual fat and water images from the same slice location, based on the phase differences between fat and water signal components. The fat content from marrow has been evaluated to identify diseases and weakness of bones. Extensive research is ongoing in the use of MR for the differentiation of the bone marrow components. Diffusion weighted imaging (DWI) is also used for the evaluation of water molecule diffusion within cells, and may be used as a marker of bone abnormalities. The supply of blood inside bone and marrow are evaluated using perfusion and dynamic contrast enhancement. MR spectroscopy (MRS) is also employed to identify the composition of bone marrow, mainly the differences in fat and water components. Multi-nuclear spectroscopy, like ^{31}P, is used for evaluation of metabolic processes.

The MR evaluation of bone is becoming a useful clinical tool due to its capabilities of measuring various parameters from bones some of which cannot be observed from other modalities. Other major advantages of using MR include the use of non-ionising radiation, it being a non-invasive examination and its ability to acquire images in any anatomical plane.

4.2 Quantification of Bones Using MR

The use of MR for quantification of bone structure and composition has been suggested for a long time. This section reviews some of the published literature concerning the use of MRI and MRS for the quantification of bone and marrow at multiple skeletal sites. The structural properties of bones assessed by MR are mostly categorised as the quantity of bone, and the evaluation of bone physiology and bone marrow are mostly categorised as the quality of the bone. MRI has been widely preferred for evaluation of bones due to the advantage of acquiring both bone quantity and quality, a phenomenon which is rarely achieved by routine quantitative methods.

4.2.1 Bone Quantity

The concept of using the structural property of the bone for quantification and diagnosis of bone abnormalities has been proposed by many groups [70, 71, 141-161] [81, 162-169]. In 1997 Majumdar *et al.* [156] described a standard technique of analysing the trabecular bone network from high-resolution *in vivo* MR images of the distal radius in normal and osteoporotic subjects. The study included three groups of women: ten premenopausal, nine postmenopausal and eleven osteoporotic postmenopausal. A 1.5 T GE scanner was used to acquire images which were processed to measure apparent trabecular bone volume fraction (app BV/TV), trabecular thickness (Tb.Th), trabecular spacing (Tb.Sp) and trabecular number (Tb.N). The study demonstrated that the premenopausal subjects had a dense trabecular network when compared with postmenopausal osteoporotic subjects which indicated that high-resolution MR images of bone may be useful for quantifying differences in trabecular bone structure as part of bone quantity.

In 2002 Newitt *et al.* [167] published an article on characterisation of trabecular structure from high-resolution MR images at distal radius by using in-house processing and analysis tool. The in-house tool was developed using the IDL (Research Systems, Boulder CO) and C program language for automated coil inhomogeneity correction, trabecular bone region segmentation, serial image registration, bone/marrow binarisation, structural evaluation and micro-finite element analysis for measurement of mechanical properties. Structural analysis was performed to measure apparent trabecular properties of bone fraction (app. BV/TV), separation (app. Tb.Sp), thickness (app. Tb.Th) and number (app.

Tb.N). Reproducibility of the processing and measurements were also done. The results described a good method of processing MR images and the image alignment was found to cause small but significant changes in some structural parameters. The automated processing provided a 3-fold decrease in trained operator time over manual methods. Reproducibility was found to be dependent on image quality for most of the parameters.

In 2002 Wehrli *et al.* [165] presented a study of 68 postmenopausal subjects using quantitative MRI (QMRI) for the evaluation of bone marrow and structure by measuring R_2* and bone volume fraction (BVF). The aim of the study was to identify if MR at multiple skeletal sites can distinguish women with/without vertebral fractures. R_2* was calculated from the line-width of the methylene proton signal in the bone marrow spectrum, BVF was measured from the bone image region. In addition areal BMD was acquired using DEXA. The results demonstrated that both BVF and R_2* in the calcaneum correlated with R_2* at the femoral sites and also with the areal BMD at the femoral and vertebral sites. The calcaneal R_2* was able to differentiate patients with vertebral fracture from those without fractures. The data described that R_2* measures a property of the trabecular network that is only partially captured by the areal BMD.

In 2005 Gomberg *et al.* [147] presented an article on the method for cortical bone structure analysis on 1.5 T MR images acquired from volunteers and specimens at multiple skeletal sites. MR images from tibia and femur were processed to measure bone properties like cortical area and bone area. Reproducibility experiments were also performed to assess the processing method. The cortical boundary detection was achieved by radial tracing of intensity profile that intersected the periosteal and endosteal boundaries of bone. DEXA data were also acquired from some volunteers for comparison with MR measurements. The results described a reproducibility of about 2%. Cortical cross sectional area from femoral neck correlated strongly with height, and cortical diameter versus age approached significance. Measurements in specimens for cortical parameters indicated a dependence on resolution. In conclusion the article successfully created processing tool for analysis of cortical bone properties, which was applied on standard clinical MR data at arbitrary anatomical locations to yield quantitative results.

In 2006 Wehrli *et al.* [164] presented a review article on the use of quantitative MRI for the assessment of bone structure and function. The study described the recent advances in MRI for the assessment of bone structure which could be useful in diagnosing bone diseases like OP and also the advantage of MR data in relation to standard bone densitometry techniques. There are various methods available for quantification of bone structure: indirect methods that do not require high-resolution use the induced magnetic field in the intertrabecular space for the measurement of R_2*, which is the recoverable component of the total transverse relaxation rate. High-resolution MRI has been used to quantify trabecular network. High-resolution bone structural analysis is technically demanding in terms of image acquisition and algorithm needed to extract the structural information. Motion correction and image registration are important for effective reproducibility. The review demonstrated that quantitative MR assessment has useful applications in targeting fracture risk prediction and evaluation of the effect of therapeutic intervention.

In 2008 Majumdar *et al.* [154] presented a review article on the potential of using MRI for evaluation of OP. The article suggested that DEXA does not capture all factors contributing to bone strength and also suggested the potential for using MRI for evaluation of the micro-architecture of the bone using high-resolution imaging. The article also suggested the importance of using the common structural measurements like app BV/TV, Tb.N and Tb.Sp. Previous studies had shown that MR-measured structural properties correlated with age, menopausal status, OP and fracture status. In conclusion the review showed the increased potential and advantages of using MR for evaluation of fracture risk in parallel with DEXA techniques.

In the same year Ladinsky *et al.* [169] presented a study on the use of MRI for quantification of trabecular bone structures. Trabecular bone architecture has been suggested to contribute to overall bone strength independent of vertebral areal BMD measurement from DEXA, but there are only few *in vivo* studies to support the hypothesis. To observe the effect 98 postmenopausal women were recruited to the study and data were acquired from MRI, DEXA, broadband ultrasound and pQCT. MRI data were acquired from radius and tibia to measure bone structural properties. A spinal deformity index (SDI) was measured from midline sagittal MR images of thoracic and lumbar vertebrae to measure structural and deformity burden. The structural measurements from radius were correlated with SDI, which demonstrated significant negative correlation for topological surface density and trabecular bone volume fraction. pQCT trabecular volumetric BMD was also weakly associated, but ultrasound absorption was not. No significant association between SDI and structural properties were found at tibia. In conclusion the structural properties at distal radius obtained by MRI explained a significant portion of the variation in total spinal deformity burden in postmenopausal women independent of areal BMD.

In the same year Kazakia *et al.* [168] presented a study for *in vivo* determination of bone structure in 52 postmenopausal women comparing high-field MR images with high-resolution pQCT. The study acquired MR and pQCT data from radius and tibia to measure structural properties of cortical thickness (Ct.Th), BV/TV, Tb.N, Tb.Th and Tb.Sp. DEXA data were also acquired to measure areal BMD from radius, proximal femur and lumbar spine. The results demonstrated good correlation between MR and pQCT for all the structural measurements. Minimal correlations were observed between MR or pQCT parameters and DEXA areal BMD measurements. In conclusion the study demonstrated the advantages of using MR and pQCT for evaluation of structural properties in bone quantification.

In the same year Krug *et al.* [150] described a feasibility study for *in vivo* ultra high-field 7.0 T MR imaging of trabecular bone structure, which was compared with measurements from 3.0 T and pQCT. The study was performed on ten healthy volunteers and the images from MR and pQCT were processed to measure BV/TV, Tb.Sp, Tb.N and Tb.Th. The results demonstrated significant differences between field strengths and modalities for all the structural parameters except Tb.N. In conclusion the study showed the increased potential of using ultra high-field MRI for quantitative analysis of bone structure. There was a mild overestimation of measurements at 7.0 T when compared with 3.0 T due to increased magnetic susceptibility effects, but the gain in SNR at 7.0 T was thought to lead to increased spatial resolution.

In 2003 Gibbs *et al.* [170] presented a method of textural analysis for analysis of contrast-enhanced MR images of the breast. The aim of this study was to evaluate a method of lesion discrimination between benign and malignant in 79 female individuals. Each lesion was segmented and converted to a co-occurrence matrix for the measurement of textural properties as defined by Haralick *et al*. [171, 172] The results showed significant differences in textural features between benign and malignant lesions, which demonstrated the potential of using textural analysis for breast lesion discrimination which could, in turn, reduce benign lesion biopsies. One of the aims of this thesis is to use the principal of textural analysis in bone structure, to identify changes in relation to bone strength and properties.

The results from the literature on bone structure measured using MR provided evidence for a good correlation with standard quantitative techniques like pQCT and DEXA, and they also demonstrate the potential to differentiate between bone conditions and strength for individuals affected with bone abnormalities. The papers reviewed in this section informed the primary aim of this thesis: to use MR measured bone structural properties for identification of bone properties in the high bone mass (HBM) affected and normal population, and also to identify the associations with standard quantitative techniques. The aim is to observe a dense trabecular network in HBM-affected individuals when compared with controls, since the HBM condition results in increased bone density and is believed to have an increased bone structure when compared with the opposite condition of OP. An additional aim in this thesis was to use the post processing technique of textural analysis on the trabecular bone structure to possibly identify differences in bone strength and condition, since textural analysis has been previously used for differentiation of tumours based on the structural changes in image intensity.

4.2.2 Bone Marrow Composition

The analysis of bone physiology and bone marrow composition for quantification and diagnosis of bone abnormalities has been proposed by many groups [17, 95, 173-193] [109, 194-217] [218-220]. The aim of the following paragraphs is to review some of the literature which has used bone marrow composition for diagnosis of abnormalities.

In 2003 Bouxsein *et al.* [176] presented a review article on bone quality and its use in diagnosing abnormalities. The article described the technologies and physiology related to bone strength in terms of diagnosing bone abnormalities. In conclusion the study recommended additional research in order to understand the relative contribution of the various aspects of skeletal fragility, to develop new diagnostic methods and to offer interventions designed to treat the causes of skeletal fragility.

In 2000 Schellinger *et al.* [203] presented a preliminary study of 57 subjects (27 male & 30 female) investigating proton MR spectroscopy at lumbar vertebrae in relation to location, age and sex differences. Some subjects had both multi-voxel and single voxel spectroscopy examinations. All of the spectroscopy data were acquired using the STEAM sequence and with water suppression turned off. The spectroscopy data were processed to measure fat-fraction (FF) and water line-width (LW). The results demonstrated a variation in FF between the voxels in the multi-voxel data. The FF progressed with age in a linear fashion for both the sexes with higher FF in the male group. The LW was significantly larger in the male group when compared with females. In conclusion the study demonstrated the possibility of using MRS as an add-on to routine spinal imaging which could be advantageous in diagnosing abnormalities like OP. Comparison with gold standard techniques was not carried out for validation, and the usefulness of LW in determining bone density was also uncertain.

The next year Schellinger *et al.* [204] presented a new study on the potential value of vertebral proton MRS in determining bone weakness by using FF and LW. The MRS data were acquired from second lumbar vertebra of 72 control subjects and 22 subjects with bone weakness. The results demonstrated a linear increase in FF with age and the male subjects had higher FF than females; results which were similar to those of their previous study. The FF was relatively higher in subjects with weakened bone when compared with controls in all age categories. The LW from the entire group had a slightly higher value for weakened bone when compared with controls. In conclusion the study demonstrated the use of FF to serve as a measure of bone quality and also as a marker of bone weakness. A larger population and the examination of all lumbar vertebrae were recommended.

In 2001 Kugel *et al.* [192] presented a study to show the differences in vertebral bone marrow ^{1}H spectrum in relation to age and sex in 154 volunteers. Unsuppressed single voxel spectroscopy was acquired from the third lumbar vertebra using the PRESS sequence and the spectrum was processed to measure fat content. The results demonstrated an increase in fat content with age till 60 years and then it remained constant. The fat content for females was lower when compared with males in all age groups. There was no correlation between fat content and body mass index (BMI). In conclusion the study confirmed the age and sex dependent changes in the fat content of the vertebral bone marrow.

In 2004 Schellinger *et al.* [205] presented a pilot study that showed that bone weakening can be affected by agents other than BMD. The study suggested that bone marrow fat (BMF) may have a direct link to bone loss. The study was performed on 26 subjects with normal and structurally weakened bones by using DEXA and ^{1}H-MRS of lumbar vertebral bodies. DEXA was used for the measurement of areal BMD and MRS was used for the measurement of BMF. The results showed a weak negative correlation between BMF and areal BMD, but neither of the parameters was suitable to be used as an independent indicator. The BMF/BMD ratio showed significant diagnostic power to detect bone weakening. In conclusion the study demonstrated that BMF can be used to diagnose reduced bone strength nearly as well as areal BMD, but individually neither BMF nor areal BMD was validated as a reliable indicator. The BMF/BMD ratio could be used as a reliable diagnostic indicator. A study with larger population was recommended.

In 2004 Shih *et al.* [210] presented a study of 52 pre and post menopausal female subjects assessing the relationship between MRS measured lipid water ratio (LWR) and LW from vertebral bone marrow with areal BMD from DEXA. The results demonstrated that areal BMD and LWR were significantly different between the two groups, that a borderline difference was observed for lipid LW and that no significant difference was observed for water LW. The LWR was positively correlated with age and negatively correlated with areal BMD. Lipid LW was negatively correlated with age and positively correlated with areal BMD. Water LW showed no significant correlation with age or areal BMD. In conclusion the positive correlation of LWR with age suggested an increase in lipid fraction with the aging process. The findings suggest that lipid metabolism might affect the pathogenesis of OP.

In 2005 Yeung *et al.* [217] presented a study of 53 postmenopausal women and 12 control premenopausal women to establish if OP is associated with increased marrow fat content and decreased marrow unsaturation by using MRS. DEXA data were acquired from the lumbar region and MRS data were acquired from the third lumbar vertebrae. The MRS data were processed to measure fat content and unsaturation index (UI) followed by measurement of water and lipid line-widths. The results demonstrated that premenopausal subjects had lower fat content and higher UI when compared with postmenopausal subjects. OP and osteopaenic subjects had a higher fat content than subjects with normal bone density and an opposite trend was observed for UI. Water and lipid LW showed no clear trend between subjects with different bone densities. A weak negative correlation was observed between bone density and fat content and a moderate positive correlation was observed between bone density and UI. In conclusion the study suggested that as marrow fat increases, saturated lipids appear to increase preferentially compared to unsaturated lipids. These results could potentially be applied to the non-invasive assessment of marrow lipids for diagnosis of abnormalities.

In 2005 Reeder *et al.* [109] presented a fast spin-echo (FSE) imaging technique known as iterative decomposition of water and fat with echo asymmetry and least squares estimation (IDEAL) for separation of fat and water signal components. The IDEAL technique was compared with standard techniques to observe the effectiveness of separation of fat and water in phantom and tissue. The results demonstrated an increased image quality with IDEAL when compared with other techniques. The clinical IDEAL images showed improved uniformity of fat suppression across the image when compared with normal fat suppression sequences. In conclusion the study established that the noise performance of IDEAL matched the theoretical maximum, thus demonstrating its efficiency. The study concluded that IDEAL in clinical imaging with different weighting has great applications.

In 2007 Liney *et al.* [194] presented a preliminary MRS study of 16 subjects by using 3.0 T for the assessment of normal bone marrow composition and the assessment of the variations in terms of age, gender and skeletal site. Data were acquired using MRS, DEXA, in-phase out-of-phase imaging (IOP), and IDEAL at lumbar spine and in some cases the heel. The data from MR were processed to measure FF from the vertebra. The results showed that the FF from heel was considerably higher than spine but did not correlate significantly with age. The results also described a significant correlation of FF with age and gender in spine. Female subjects exhibited lower FF compared to male subjects of similar age. FF measured from imaging sequences was correlated with MRS FF, which also showed that IDEAL correlated better with MRS than IOP. A negative correlation was observed between areal BMD and FF from MRS. In conclusion the study demonstrated a significant variation in normal bone marrow in relation to age, gender and skeletal sites. FF may be added to conventional MRI examinations and so play an important role in OP in studying the late effects of cancer treatments.

In 2007 Shen *et al.* [209] presented a study demonstrating the potential of using whole-body bone marrow adipose tissue (BMAT) measurements for diagnosis of bone abnormalities. The study was performed on 56 subjects using whole-body MRI and DEXA. DEXA was used for the measurement of areal BMD, total body fat and percentage fat. BMAT was measured from the whole-body MRI images by using a fixed pixel threshold. The results demonstrated a strong negative correlation between pelvic BMAT and areal BMD from total body, pelvis and spine. Good negative correlation was also observed between total body BMAT and areal BMD from total body, pelvis and spine. BMAT correlated significantly with visceral adipose tissue at total body and pelvis. In conclusion the study showed that MRI-measured BMAT strongly correlated with DEXA data which suggests a biological relationship between osteoblasts and BMAT adipocytes in the pathogenesis of OP.

In 2008 Bernard *et al.* [173] presented a phantom study at 3.0 T comparing various quantification methods using MRI and MRS. The study was performed on 11 water-fat emulsion phantoms with varying concentrations of fat and water, which were imaged using chemical-shift saturation MRI, opposed-phase MRI, IDEAL and compared with single-voxel MRS. The data were processed to measure FF from a specified region of interest in each phantom. The results demonstrated good correlation between the known FF (by composition volume) from each phantom against the FF from MRS. Good correlation was also observed for FF measured from imaging methods against MRS values. IDEAL correlated most strongly out of all the imaging methods against MRS values. Bland-Altman limits of agreement plots revealed a general underestimation of FF for all imaging sequences at high FF when compared with MRS. FF obtained using IDEAL and MRS were similar in those breast and lumbar vertebrae cases presented. In conclusion the study provided evidence that high-resolution imaging techniques offer an alternative to MRS for fat quantification, which would be crucial in a wide range of clinical applications.

In 2009 Reeder *et al.* [110] presented a study of newly-developed chemical-shift based IDEAL imaging method for fat quantification that accounts for the complex spectrum of fat comparing it to an MRS method. The study measured liver FF in 33 patients using three types of models in IDEAL image reconstruction and MRS. The three models were single peak, multi-peak pre-calibrated and multi-peak self-calibrated. The single peak model was the default technique which assumed that fat has only one large peak. The multi-peak models assume that the fat is made up of multiple peaks and tries to create true fat images based on the signals from multiple fat peaks. The results demonstrated that the FF measured by all three IDEAL models correlated highly with FF from MRS, but that the pre-calibrated multi-peak reconstruction demonstrated the closest agreement. It was noted that validation will be required using biopsies. In conclusion the study demonstrated the potential of using advanced IDEAL models for better *in vivo* diagnosis of abnormalities.

The results from most of the above literature in relation to bone marrow composition measured using MR demonstrated a good correlation with standard quantitative technique like DEXA and they also describe the potential to differentiate between bone conditions and strength with individuals affected with bone abnormalities. These papers all informed the primary aim of this thesis: to use MR measured bone marrow composition for identification of bone properties in the high bone mass (HBM) affected and normal population, and also to identify the associations with standard quantitative techniques. The aim was to observe a lower FF, increased LW and increased UI in HBM-affected individuals when compared with controls, since the HBM condition results in increased bone density when compared with the opposite condition of OP which contains lower bone density and affected by high FF, lower LW and UI. An additional aim in this thesis was also to compare the measurement of FF in relation to MRI and MRS methods of acquisition.

4.3 High Bone Mass Condition

The aim in the following paragraphs is to describe some of the literature which has explained the condition of HBM and the possible reasons for its occurrence [35-39, 221-226], which is useful for the description of the population investigated in this thesis.

In 2002 Little *et al.* [224] presented a genetic study on the cause of HBM in a large population, with the help of DEXA measurements. The study showed that the HBM trait was originally localized to chromosome 11q12-13, which was then refined further to identify other types of markers. After further genetic analysis, the HBM phenotype was traced to a mutation of the low-density lipoprotein receptor-related protein 5 (LRP5). From analysis of more than 1000 individuals, the mutation was observed only in affected individuals from the HBM kindred. The DEXA measurements were evaluated for the affected and non-affected individuals and the results described clear differences between the two populations, with affected individuals having a combined Z-score for hip and spine greater than 4, and all individuals below that score coming from the non-affected population. In conclusion the study suggested that the HBM mutation confers a unique osteogenic activity in bone remodelling and this understanding may facilitate the development of novel therapies for the treatment of OP.

In 2007 Qiu *et al.* [226] presented a genetic *in vivo* and in-vitro study demonstrating that a genetic mutation in the LRP5 gene affects Wnt (wingless integration) signalling and so leads to changes in bone mass in humans. The study was performed on bone samples from nine individuals affected by HBM and five normal controls, which were observed with microscopy to measure adipose tissue volume (ATV) and trabecular bone tissue volume (TBV). The results demonstrated increased TBV and decreased ATV in HBM-affected individuals when compared with controls. The results from the study showed that an activated mutation of LRP5 enhances osteogenesis and inhibits adipogenesis, and an inactivated mutation of LRP5 exerts the opposite effects. In conclusion the study suggested that LRP5 mutations, and the level of Wnt signalling, determine the differentiation fate of human mesenchymal stem cells (hMSCs) into either osteoblasts or adipocytes. Activation of Wnt signalling can provide a novel approach to increase bone mass.

In 2007 Gregson *et al.* [35] presented a study to determine the causes and interpretation of high areal BMD using conventional DEXA scans. The study suggested that the most common causes for increased areal BMD are artefacts, focal increases in areal BMD and generalised increases in areal BMD. The primary aim of this study was to identify the cause of increased areal BMD based on genetic mutations especially with respect to the role of LRP5. The study aimed to investigate patients found to have a lumbar spine or hip Z-score greater than 3. The investigation was based on a review of archived DEXA scans, collection of patient's history, blood tests and radiological examination. In conclusion the study showed that an elevated T- or Z-score is not necessarily normal, metabolic bone diseases can cause elevated DEXA scores and that an elevated T-score (> 4) may indicate a HBM phenotype.

In 2011 Gregson *et al.* [36] presented a large study following on from the previous paper to determine the clinical characteristics of individuals affected with HBM. The aim of the study was to determine if HBM-affected individuals harbour an underlying genetic disorder, and to characterise unexplained HBM and determine the potential for an underlying skeletal dysplasia. The study also presented a Z-score based set of criteria that were used to classify individuals as HBM-affected and controls. The results from the study showed that in individuals with unexplained HBM there was an excess of sinking when swimming, mandible enlargement, extra bone at tendon/ligament insertions and a broad frame. HBM cases also had a larger shoe size and increased BMI. In conclusion the individuals with unexplained HBM had an excess of clinical characteristics associated with skeletal dysplasia and their relatives were also commonly affected, suggesting that many may harbour an underlying genetic disorder affecting bone mass.

The results from most of the above literature in relation to increased bone mass suggest a genetic cause which may be related to LRP5. The studies also show that the affected individuals have distinct skeletal characteristics and that they can be screened by using non-invasive DEXA measurements and genetic tests from blood samples. These papers were the motivation behind the aim of this thesis to evaluate the potential of using MR quantitative techniques to differentiate between HBM and non-HBM-affected individuals, which could be used as a diagnostic tool in future for bone abnormalities.

5 Optimisation of Magnetic Resonance Sequence Parameters

This chapter describes the problems and solutions in developing the MR protocols for data acquisition at radius, tibia and lumbar vertebrae. The final optimised protocol will be detailed in Chapter 6.

5.1 Introduction

The magnetic resonance imaging and spectroscopy (MRI & MRS) acquisition protocols for the high bone mass (HBM) study were evaluated and optimised prior to commencing studies of subjects and controls. This optimisation work was initially done with the pre-existing 3.0 T GE HDx system during October-November 2008. In December 2008, the system was upgraded to a new 3.0 T GE MR750 scanner with a dedicated wrist coil, which resulted in the carrying over of the optimisation studies from the old to the new scanner.

5.2 Aim of Optimisation

The first aim was to use iterative decomposition of fat and water with echo asymmetry and least squares estimation (IDEAL) [109-111], and/or T_1-weighted imaging techniques at distal radius and tibia to acquire quantitative information of fat-fraction (FF) and trabecular bone structure. The image acquisition from distal radius and tibia were to be similar in location to the peripheral quantitative computed tomography (pQCT) data acquisition for effective comparison and analysis. The second aim was to acquire quantitative information from lumbar vertebrae by using IDEAL and an MRS technique. The processed data from the vertebrae could be used for comparison with dual-energy x-ray absorptiometry (DEXA) data that were acquired at same site. The third aim was to use IDEAL fat and water images at distal radius and tibia for segmentation of the cortical bone.

5.3 GE HDx 3.0 T Scanner

The HDx 3.0 T scanner was used for preliminary IDEAL and spectroscopic (see later) data acquisition from the distal radius. The scanner was not equipped with a dedicated hand coil, hence the quadrature knee coil was used. Sequences with reasonable imaging time were used for data acquisition with routine imaging protocols being selected and modified to acquire optimised images from volunteers. An IDEAL sequence employing fast spin-echo (FSE) was selected for axial image acquisition at 4% length of the distal radius, and the acquisition protocol is detailed in Table 5:1.

Repetition time (TR) / Echo time (TE)	1500.0 / 27.5 ms
Bandwidth (BW)	62.5 kHz
Field-of-view (FOV)	120 × 72 mm
Slice thickness / slice separation	4.0 / 0.3 mm
Scan time	1 minute, 12 seconds
Imaging matrix (frequency encoding (FE) × phase encoding (PE))	320 × 256
Number of excitations (NEX)	3
Echo train-length (ETL)	12
Frequency direction	anterior – posterior
In-plane resolution	375 µm × 281 µm

Table 5:1 The parameters which were used for the IDEAL image acquisition from distal radius using the knee coil in the HDx 3.0 T scanner.

This sequence provided reasonable images (see Figure 5-1) with no significant artefacts and they were good for differentiating tissues and for measuring FF from the trabecular bone region. The images were limited in resolution and hence were not capable of identifying the internal trabecular bone structure. Overall the sequence provided a baseline for IDEAL image acquisition in bones of the extremities. In-house software (MATLAB) was used for analysis of these images and was primarily designed to process the IDEAL dataset with two images (fat and water) to measure parameters of FF, cortical thickness and dimensions of the cortical and trabecular bone. The software used for MR image processing will be explained in Chapter 7 in detail.

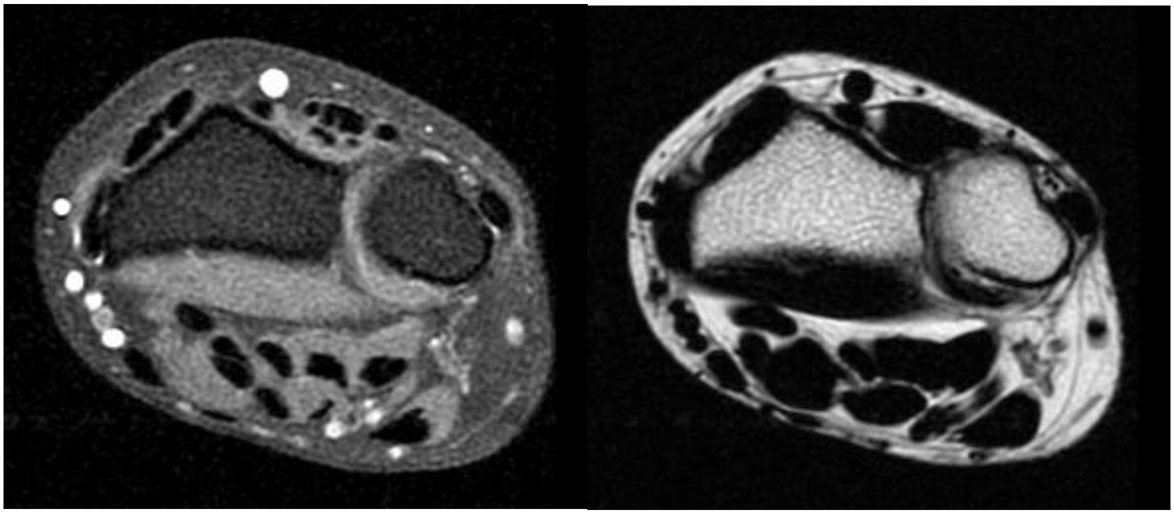

Figure 5-1 The water (left) and fat (right) images acquired using the IDEAL sequence in the HDx scanner at 4% region of the distal radius. Note the good image quality with the knee coil.

In the early work, two additional acquisitions were evaluated at distal radius: (i) MRS acquisition at 4% region of the distal radius, and (ii) IDEAL image acquisition at 60% region of the distal radius. The spectroscopy data acquisition was possible but the voxel required careful positioning and smaller dimensions due to the small size of the radial bone. The IDEAL imaging at 60% region of the distal radius required repositioning of the patient in the coil, since the coil was not able to cover the full length of the radius bone. Both of these data acquisitions were later abandoned in order to reduce the acquisition time and to increase the patient comfort. In the future, it is hoped to use better IDEAL sequences that can acquire images at higher resolution for delineation of trabecular and cortical bone structures in addition to providing FF information (discussed in Chapter 9).

5.4 GE MR750 3.0 T Scanner

The new MR750 system was fully operational by the end of December 2008 and had better gradient specifications than the previous scanner (50 mT/m amplitude and 200 T/m/s slew rate). Data from distal radius were acquired using the new dedicated eight-channel phased array wrist coil (Invivo, Gainesville, FL, USA), which was specifically purchased as part of the HBM project. Data from distal tibia were acquired using a birdcage head coil since the new scanner was not equipped with a dedicated foot/ankle coil. Data from the lumbar vertebrae were acquired using the phased-array spine coil.

5.4.1 Distal Radius

The dedicated wrist coil provided the advantages of improved signal-to-noise ratio (SNR) and better spatial resolution. The wrist coil was also advantageous in permitting different coil positions, where the coil could be placed either at the centre or at the sides of the patient table. The coil positioned at the centre of the table is the routine position for most of the MR coils, since the centre of the table is very near to the magnet's isocentre resulting in better B_0 homogeneity. The wrist coil positioned at the centre of the table is difficult for patient positioning, since the patient has to lie in the prone position and extend their arm above their head ("Superman" position). This type of positioning causes discomfort for the patient, and thereby reduces the time that they can stay stationary during acquisition. The coil positioned at the side of the table is around 10-15 cm away from the isocentre and is affected by inhomogeneity of the magnet (B_0) and the radio frequency field (B_1) from the integrated body coil. However it is an ideal position for the patient, since the patient can lie comfortably in supine position and simply insert their hand inside the coil with their arm at the side of their body.

From late December 2008, preliminary experiments were conducted on volunteers by using the wrist coil to identify the ideal coil position for patient comfort and good image acquisition. The aim was to acquire IDEAL or T_1-weighted images with high spatial resolution. Various factors were considered to improve the images during optimisation, and to set a final protocol for image acquisition in the HBM study. The parameters in the imaging protocol were modified to acquire images in a reasonable scan time of less than five minutes, which was usually achieved by reducing the repetition time (TR), number of excitations (NEX) and increasing the echo train length (ETL). The shorter scan time was preferred to help the patient to stay stationary during the acquisition period, which reduces patient movement and results in reduced image blurring. Importance was given to acquire images with high spatial resolution to detect the trabecular bone structures inside the radial bone. The increased spatial resolution was achieved by reducing the field of view (FOV) and slice thickness, and by increasing the number of frequency and phase encoding steps.

Preliminary images were acquired in both superman and supine positions to identify the best image with good quality and reduced artefacts. During the preliminary stages of image acquisition, it was also observed that the wrist coil vibrated with certain sequences resulting in additional blurring of images. The vibrations were severe with IDEAL sequences when compared with spin-echo (SE) sequences, and they were also severe when the coil was placed at the side of the table. To reduce the vibrations, the coil was manually strapped to the table using Velcro straps.

5.4.1.1 Comparison of Coil Positions for Image Quality

Experimental images were acquired at 4% region of the distal radius from volunteers to compare image quality and sequences with respect to the two positions. Axial images from both IDEAL (see Figure 5-2) and T_1-weighted (see Figure 5-3) sequences were compared at each position. The sequences were commonly optimised by changing parameters such as number of phase and frequency encoding steps as well their applied directions, ETL, scan time, bandwidth (BW), TR and echo time (TE).

The IDEAL images (see Figure 5-2) were affected by blurring, which was caused by the coil vibration and sometimes due to volunteer movement. The acquisition from the side of the table was affected by B_0 and B_1 inhomogeneity, resulting in poor signal uniformity across the image (see Figure 5-2 (right)). The IDEAL images acquired from the centre of the table required an uncomfortable volunteer position, but provided better image quality than images by the side.

The T_1-weighted images (see Figure 5-3) were better in quality with reduced artefacts (e.g. motion, blurring, flow) when compared to IDEAL images. There were minimal vibrations with this sequence which resulted in reduced blurring. The images acquired from the side of the table were mildly affected by B_0 inhomogeneity resulting in poor signal uniformity across the image (see Figure 5-3 (right)).

The coil position at the centre of the table was selected as the default position even though it was uncomfortable for the volunteer, since it provided better image quality with reduced artefacts, when compared with the coil position at the side of the table.

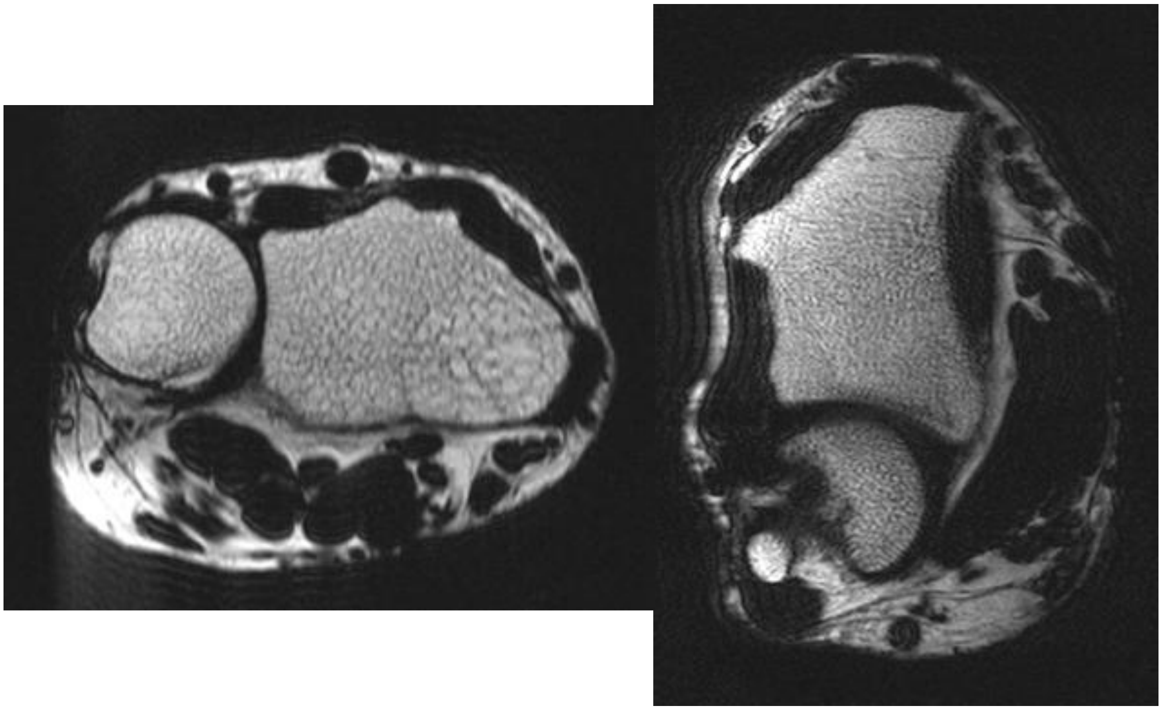

Figure 5-2 The axial fat-only images from the IDEAL sequence acquired using two coil positions at around 4% region of the distal radius for different subjects. The left image was acquired with the coil placed at the centre of the table, and the right image was acquired with the coil placed at the side of the table. Note the image on right being affected by blurring and poor signal uniformity.

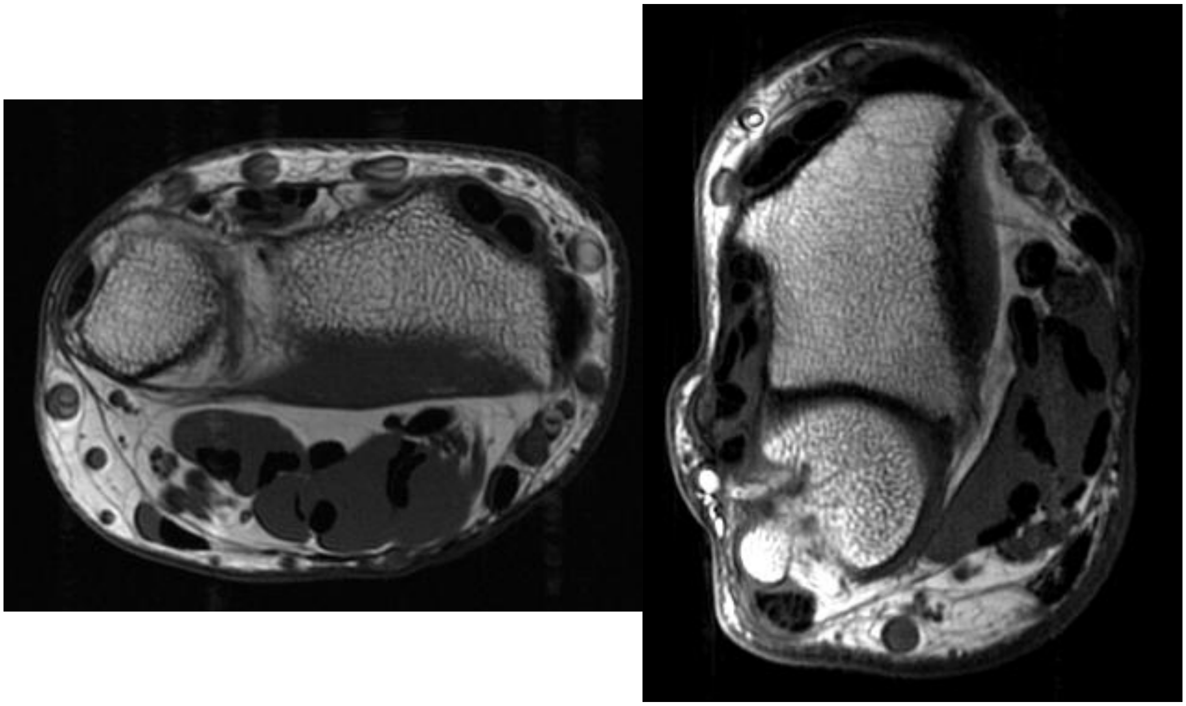

Figure 5-3 The axial T_1-weighted images acquired using two coil positions at around 4% region of the distal radius for different subjects. The left image was acquired with the coil placed at the centre of the table, and the right image was acquired with the coil placed at the side of the table. Note the better image quality with reduced artefacts when compared with the IDEAL images.

5.4.1.2 Comparison between IDEAL and T_1-weighted Imaging

The IDEAL and T_1-weighted imaging techniques were compared with each other using the coil at the bed centre. A high-resolution IDEAL imaging was investigated, since it could potentially provide structural bone details with the addition of fat and water information. Various types of IDEAL images with different types of optimisation parameters were acquired to identify the best protocol. The IDEAL images were inconsistent and were affected by coil vibrations in both fat and water images and were also affected by flow artefacts in water-only images. The artefacts were severe with sequences that used a higher ETL (see Figure 5-4).

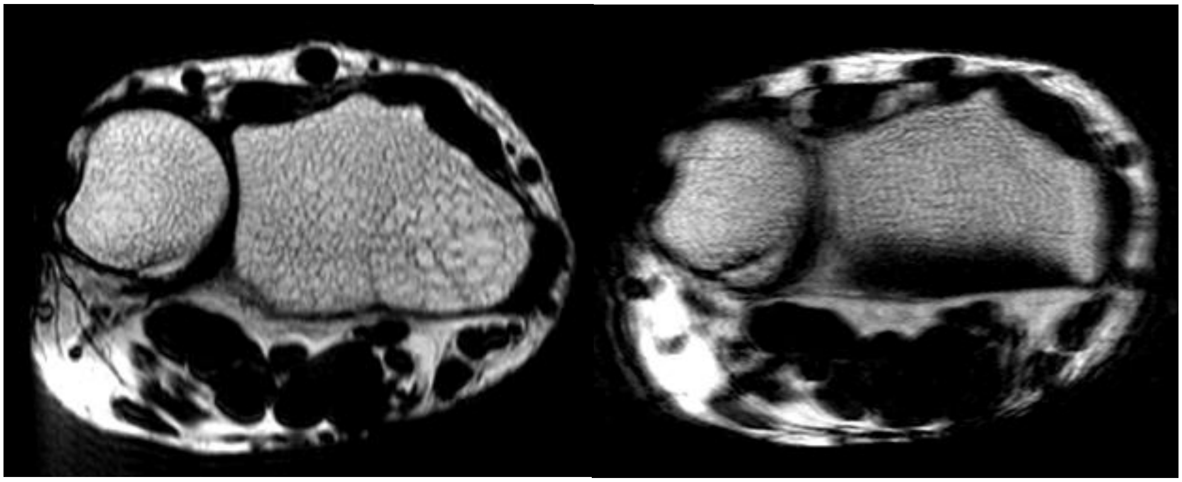

Figure 5-4 The fat-only axial IDEAL images in relation to differences between ETL. The left image was acquired with ETL=2 and the right image was acquired with ETL=3.

The T_1-weighted images were acquired using the SE technique and they consistently provided the best image quality with reduced motion or flow artefacts when compared with IDEAL images.

The best IDEAL (see Figure 5-5 (left)) and T_1-weighted (see Figure 5-5 (right)) images were compared with each other to identify the imaging technique that could be used for the HBM study. The IDEAL images were inconsistent which led to them being excluded from patient imaging in the HBM study. The T_1-weighted images had better spatial resolution and were able to differentiate the trabecular bone in detail, but were not able to acquire fat and water information unlike IDEAL. An IDEAL protocol at sufficient resolution to demonstrate trabecular detail could not be achieved. In conclusion the T_1-weighted imaging was selected as the default imaging technique at distal radius due to its consistency and trabecular bone detail, whilst accepting the loss of fat and water information which could have been useful for FF quantification.

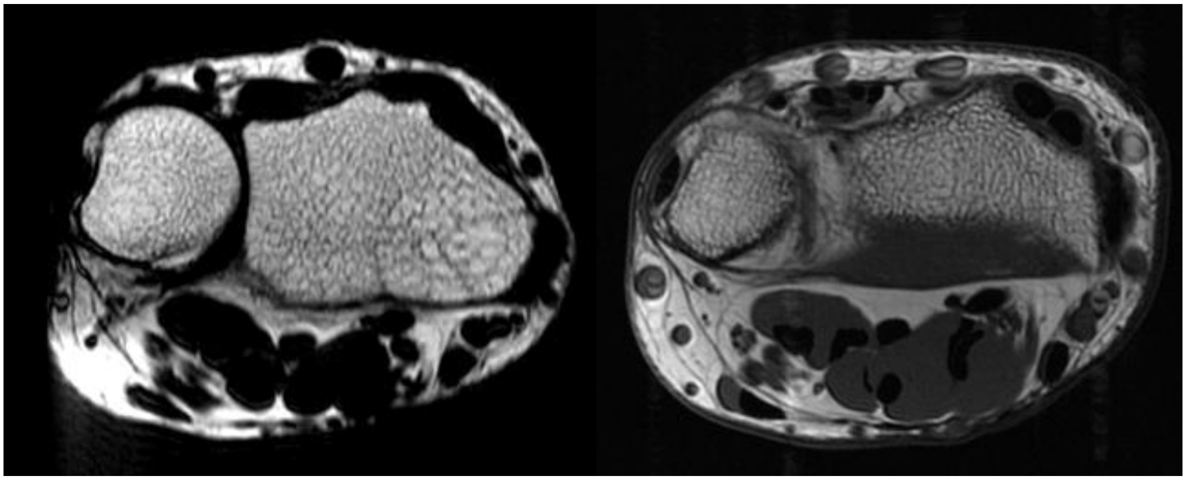

Figure 5-5 Optimum images acquired from IDEAL and T_1-weighted sequences. The image on the left is the fat-only image from IDEAL and the image from the right is the T_1-weighted image. Note the excellent image quality in T_1-weighted image when compared with the IDEAL image, which is affected by motion and blurring.

5.4.1.3 Optimisation of T_1-weighted Images

The T_1-weighted sequence was optimised further to improve image resolution and to reduce the scan time. The shorter scan time would be advantageous for the patient to stay stationary in the difficult superman position, and the higher spatial resolution would be advantageous for effective identification of trabecular bone structures.

Preliminary experimental images (see Figure 5-6 (top)) were acquired with long scan times and lower spatial resolution. The scan times were around 5 minutes and 28 seconds, and the in-plane spatial resolution was around 281 µm. The parameters were modified further on the basis of NEX, frequency and phase encoding to improve the image acquisition. The best T_1-weighted image based on qualitative visual inspection (see Figure 5-6 (bottom)) was acquired in a scan time of around 3 minutes and 8 seconds, with a resolution of less than 200 µm. The image was consistent in different volunteers and had minimal artefacts with respect to other protocols. This protocol was subsequently used in the HBM study for imaging 4% radius length and is shown in Chapter 6.

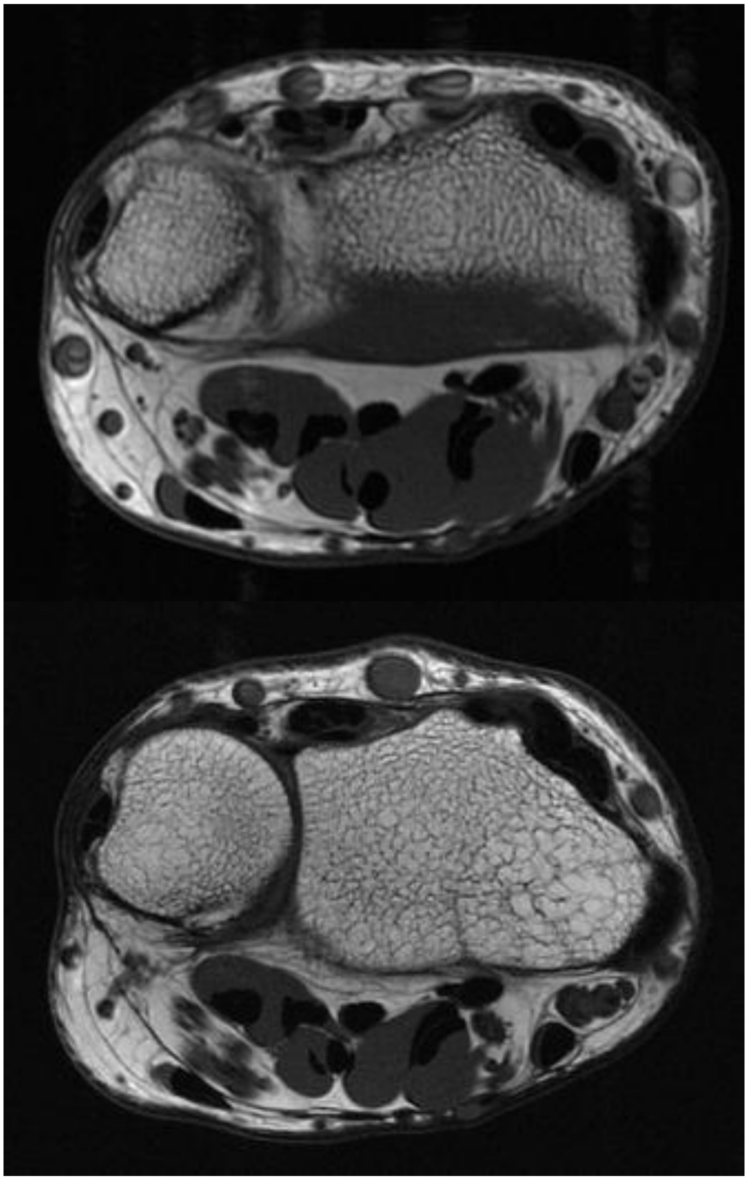

Figure 5-6 The T_1-weighted images compared with respect to scan time and spatial resolution. The image on the top is the experimental image acquired in a scan time of around 5 minutes. The image on the bottom has better resolution and was acquired in 3 minutes.

5.4.2 Distal Tibia (Head Coil)

Imaging with the IDEAL and/or T_1-weighted sequences was also the preferred method of data acquisition from the distal tibia in order to acquire information in relation to FF and/or trabecular structure. The scanner was not equipped with a dedicated foot and ankle coil, and hence a birdcage head coil was used for data acquisition from 4% region of the distal tibia. The birdcage head coil provided good signal uniformity, but poorer SNR, compared what would be expected with a dedicated foot and ankle coil. Experimental data were acquired from volunteers to optimise the protocol to be used in the HBM study population. Sequences with longer scan times of around 5 minutes were not a concern since the positioning of the volunteers for distal tibia was more comfortable than the positioning for radius imaging. For this scan the volunteers were in a comfortable supine position with the legs in a natural position with feet first direction to the scanner bore with the head coil at the centre of the magnet. Preliminary IDEAL and T_1-weighted data were acquired with different parameters and the sequences were optimised in relation to changes in number of phase and frequency encoding steps as well their applied directions, number of ETLs, scan time, BW, TR, TE, FOV and slice thickness.

5.4.2.1 Comparison between IDEAL and T_1-weighted Imaging

The best IDEAL acquisition was acquired by using the FSE technique, with a scan time of around 3 minutes and 5 seconds, and with an in-plane resolution of 223 µm × 182 µm. The acquired images (see Figure 5-7) were affected with poor SNR for the water-only image, but were not affected with motion or flow artefacts. The water-only image was consistently affected with loss of SNR (probably due to lower water content) when compared with the fat-only image, which resulted in difficulty in extracting FF measurements from the data.

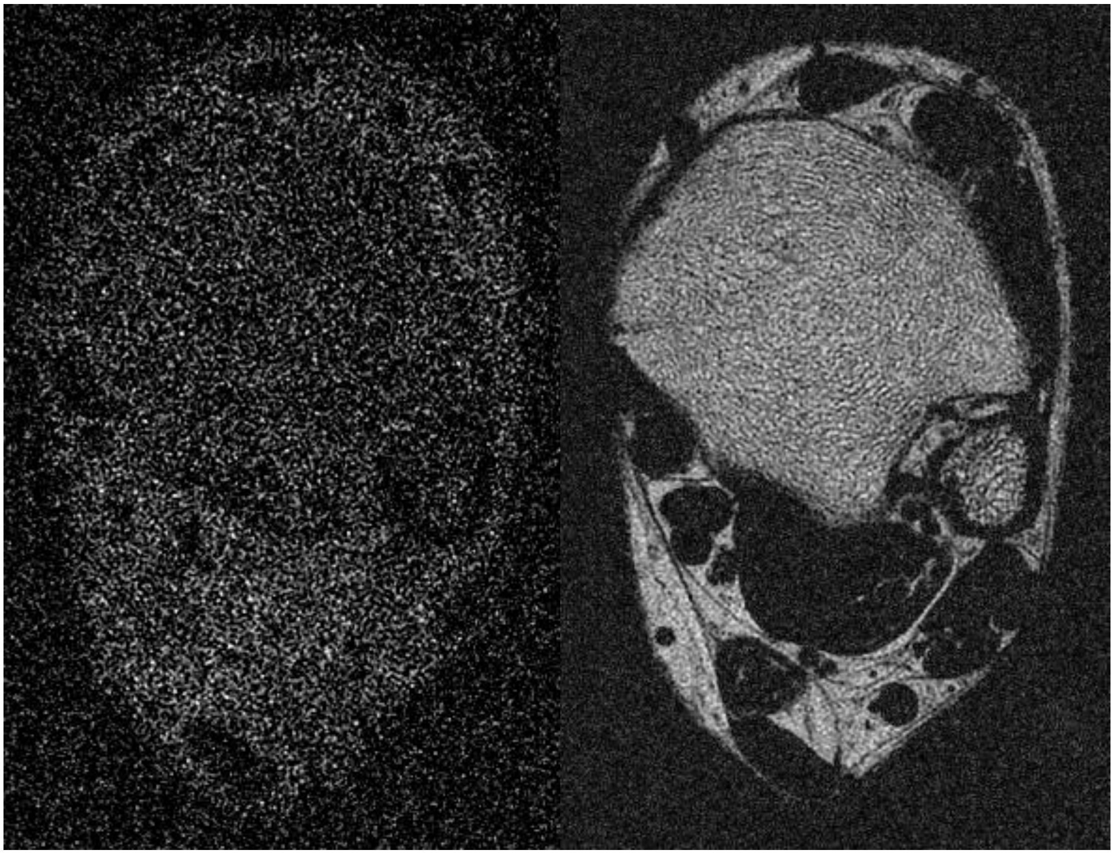

Figure 5-7 The axial IDEAL images acquired at the 4% region of the distal tibia. The images were acquired by using the birdcage head coil. The image in left is water-only and the image in right is fat-only. Note the poor SNR in the water-only image even with the optimum parameters.

The T_1-weighted images were acquired with different parameters to identify the best image with good delineation of the trabecular bone structures and SNR. Initial T_1-weighted images were acquired in a scan time of 2 minutes and 14 seconds, and with a spatial resolution of 223 µm × 195 µm (see Figure 5-8 (left)). To further improve the SNR, additional NEX was applied from one to two, which resulted in improved SNR in the image (see Figure 5-8 (right)) at the expense of increased scan time of 4 minutes and 52 seconds, which was still thought to be reasonable.

Figure 5-8 The axial T_1-weighted images acquired at 4% region of the distal tibia. The image on the left was acquired with NEX=1 and the image on the right was acquired with NEX=2. Note the improved SNR in the right-hand image at the expense of twice the acquisition time.

Imaging with IDEAL was abandoned in the head coil, due to the poor signal in the images, and only the T_1-weighted protocol was used for the HBM study and is shown in Chapter 6.

5.4.3 Proximal and Distal Tibia (Body Coil)

The aim of this thesis was to acquire MRI data in locations, which match closely with locations of pQCT and DEXA acquisitions. The pQCT of the leg routinely involved imaging at 4%, 14% and 66% region of the distal tibia, but high-resolution MRI imaging from all these locations would take a long time because it would require repositioning of the leg in the head coil, since the coil cannot cover the whole length of the lower leg. To improve the coverage the integrated body coil was used for data acquisition from the whole length of the distal tibia at the expense of lower SNR due to large coil volume. Both proximal and distal tibia were imaged since the coil was able to cover the whole region of both legs.

Low resolution IDEAL images were preferred to acquire data from 4% and 66% positions. The IDEAL data would provide the FF information from the trabecular bone which could be used for comparison with the pQCT data. The image at 66% region of the distal tibia was designed to measure the muscle properties and the cortical thickness of the tibial bone.

IDEAL images (see Figure 5-9) were initially acquired with contiguous imaging slice regions (slabs) that covered the whole length of the distal tibia (see Figure 5-10 (left)). To cover the full length, the protocols used large slice gaps of around 10 mm and thick slices of around 5 mm. A large FOV was used to cover the regions of both legs in the axial plane, which resulted in lower spatial resolution. The use of the single slab of acquisition resulted in discrepancies in position of one leg with respect to the other, even after applying oblique prescription. This resulted in images where the acquisition slice went through 4% region for one leg and went through by 14% region for the other leg (see Figure 5-9 (top row)), or completely missed the 4% region for either or one leg.

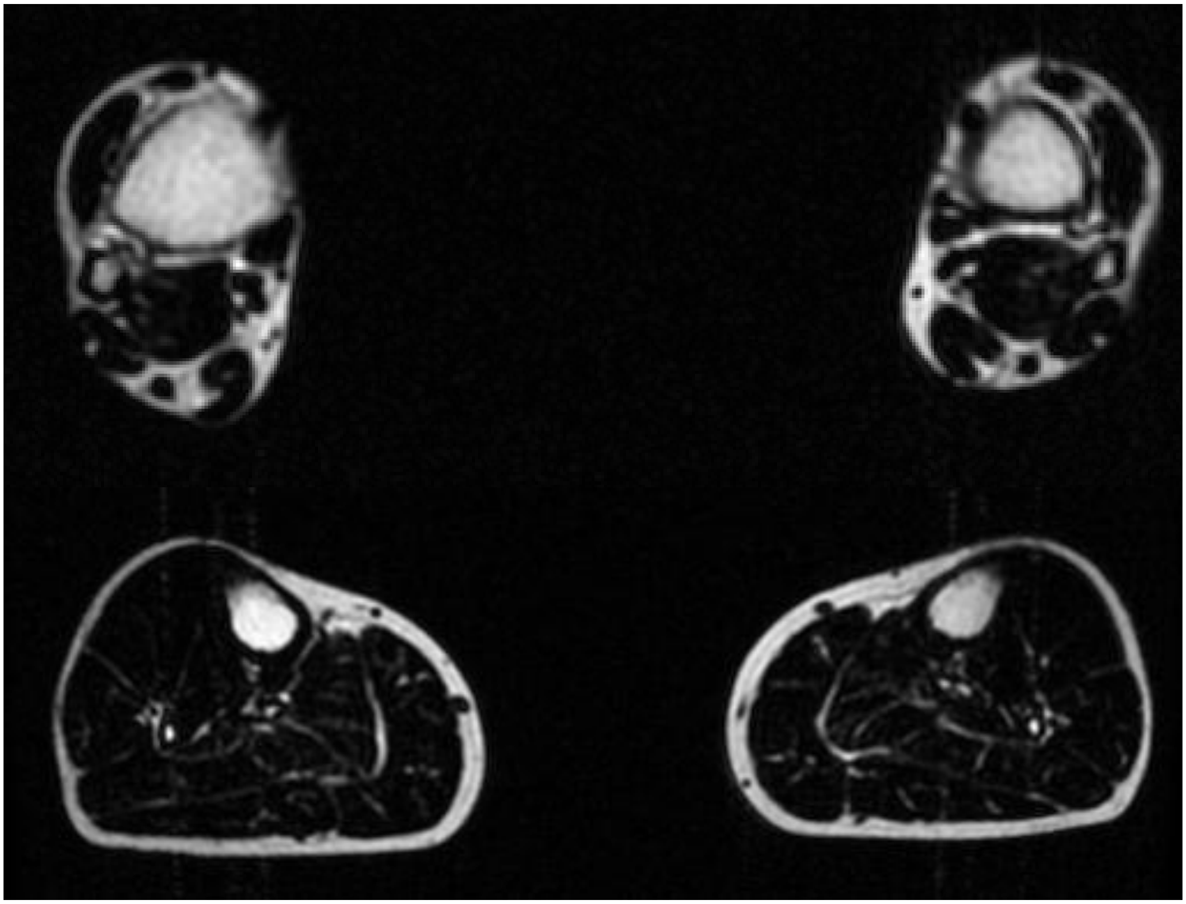

Figure 5-9 The fat-only images from IDEAL sequence at two locations of proximal and distal tibia. The images were acquired as part of a single slab extending the whole length of the lower leg. The image on the top is from the 4% position and the image on the bottom is from the 66% position of the distal tibia. Note the difference in bone area at the 4% position image.

To improve the localisation, the images were acquired as two slabs, with one slab positioned in the 4% region and the other slab positioned at the 66% region of the distal tibia (see Figure 5-10 (right)). The use of two slabs resulted in decreased slice gaps and was also useful in applying oblique slabs with different angles that accounted for differences due to patient position. The acquired images (see Figure 5-11 & Figure 5-12) were better than with the previous acquisition and provided nearly symmetrical slice localisation in both legs. This protocol was subsequently used in the HBM study for imaging both proximal and distal tibia and is shown in Chapter 6.

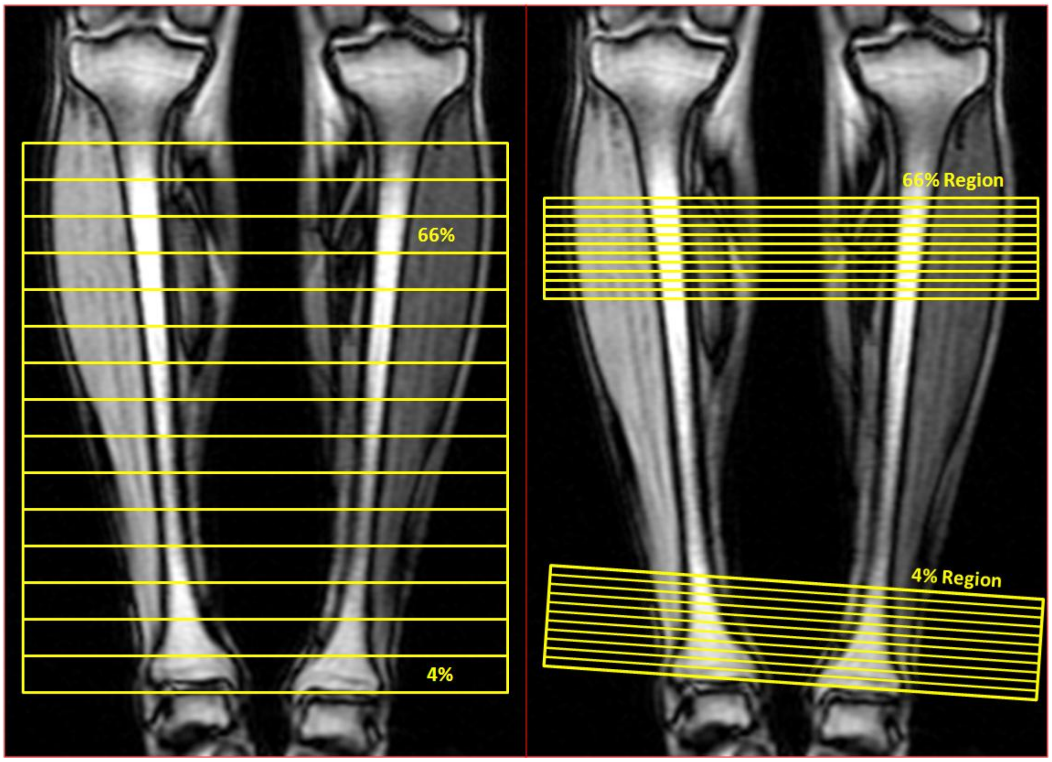

Figure 5-10 Axial image localisation for both legs. The image on the left illustrates the localisation method with the use of a single imaging slab. The image on the right illustrates the localisation method with the use of two imaging slabs for each region in the leg. Note the right image where the slabs can be individually angulated according to the anatomical region.

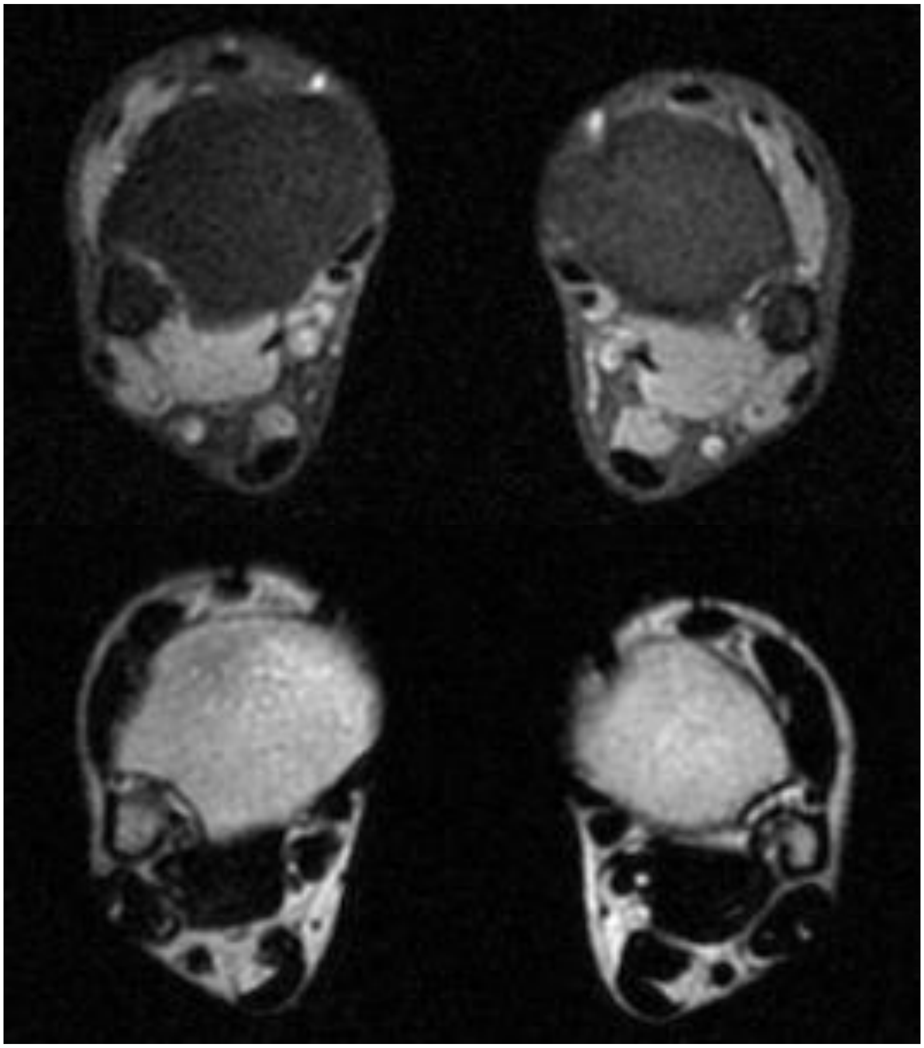

Figure 5-11 IDEAL axial images acquired at the 4% region of both proximal and distal tibia. The images were acquired as two imaging slabs. Note the improved uniformity of the anatomical location where the image has been acquired in nearly similar location for both the legs. The top image is water-only and the bottom image is fat-only.

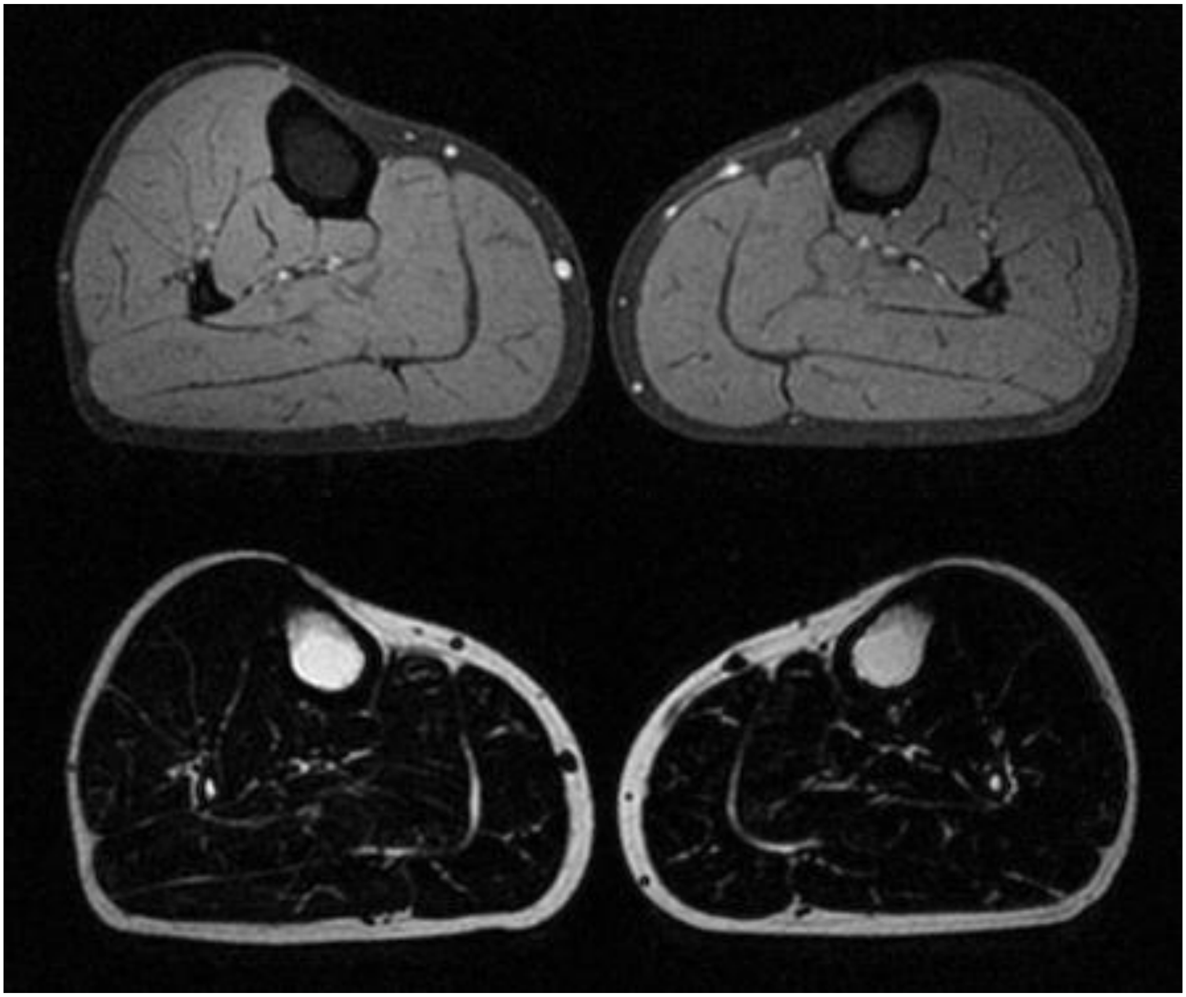

Figure 5-12 IDEAL axial images acquired at the 66% region of both proximal and distal tibia. The top image is water-only and the bottom image is fat-only.

5.4.4 Lumbar Vertebrae

In lumbar vertebrae the aim was to acquire MRS data in relation to fat and water and also to quantify their concentrations by using FF maps from each vertebra. The IDEAL sequence was the preferred imaging technique to quantify the FF from individual vertebra due to its good spatial resolution. Spectroscopy was acquired in individual vertebrae since it provided information on additional fat peaks and could also be used as a gold-standard for comparison with IDEAL. A single voxel point resolved spectroscopy (PRESS) sequence with no water-suppression was used for spectral data acquisition by using the lower three elements of the dedicated spine coil. All volunteers were in the supine position with head first direction to the scanner bore.

5.4.4.1 Imaging

A standardised IDEAL protocol, which was previously used in the department for FF quantification from individual lumbar vertebrae, was used for data acquisition in the volunteers. The acquired images (see Figure 5-13) were of good quality with minimal artefacts, and were able to differentiate each vertebra. This protocol was subsequently used in the HBM study and is shown in Chapter 6.

Figure 5-13 The sagittal IDEAL images acquired from the lumbar vertebrae region. The images were acquired by using the dedicated spine coil. The image on left is water-only and the image on right is fat-only. Note the good quality of the images with good delineation of the individual vertebra.

5.4.4.2 Spectroscopy

Three individual PRESS spectra were acquired in the first, third and fifth lumbar vertebra (L1, L3 & L5) for comparison with IDEAL and DEXA data acquired in similar vertebra. In vertebral bone-marrow spectroscopy, signal from both water and fat has to be acquired in order to estimate the FF. Hence the water suppression or CHESS (chemical-shift selective) pulses, which are routinely used for water or fat suppression, were switched off to acquire full water signal. Accurate localisation of the PRESS voxel in the lumbar vertebra is essential to avoid contamination of signal from surrounding tissues. To achieve good localisation or voxel placement, it is important to acquire reference images in two or more planes.

To begin with, reference images in sagittal and coronal plane were acquired for positioning of the PRESS voxel. T_2-weighted images using FSE technique were acquired in the sagittal plane and T_1-weighted fluid attenuated inversion recovery (FLAIR) images were acquired in the coronal plane. Using these images, a PRESS voxel box was positioned inside the third lumbar vertebral body (see Figure 5-14). Positioning of the voxel in L3 and L5 vertebrae were difficult, since they were more angulated when compared with L1 vertebra.

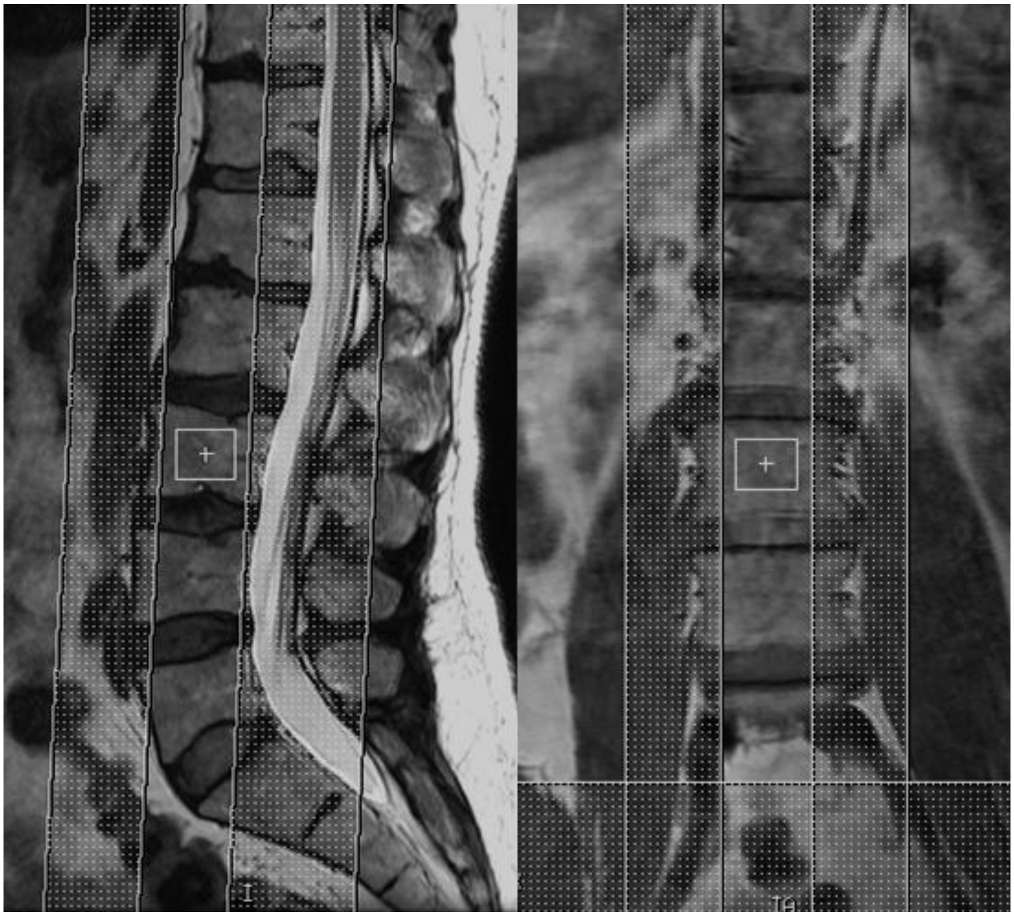

Figure 5-14 The sagittal (left) and coronal (right) images, which were used for effective positioning of the PRESS voxel in the third lumbar vertebrae. Note the additional manual saturation pulses, which were used to eliminate signals from surrounding tissues that may contaminate the voxel signal.

To improve the voxel positioning, the sagittal and coronal acquisition were abandoned in favour of using oblique T_2-weighted axial images from L1, L3 and L5, and by using the sagittal IDEAL image as the reference. The axial images were acquired obliquely according to the axis of the vertebra (see Figure 5-15 & Figure 5-16 (left)). The PRESS voxel localisation could then be angulated by using the axial images. The sagittal image from IDEAL acquisition was used for positioning of the voxel in the other plane.

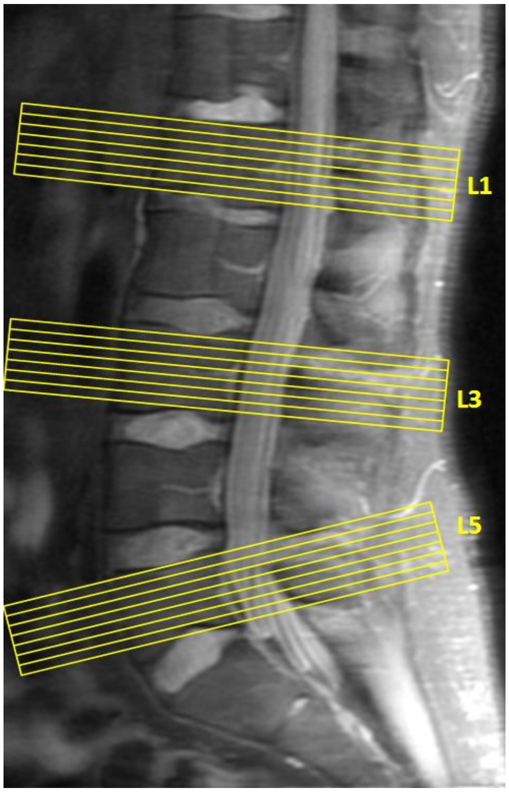

Figure 5-15 A typical water-only sagittal IDEAL image with illustration of slices used in axial image acquisition from L1, L3 and L5. Note the angulation of the axial acquisition with respect to each vertebral body.

Thus the axial T_2-weighted and the sagittal IDEAL images (see Figure 5-16) from the lumbar vertebrae were used to position the spectroscopy voxels in all the volunteers from the HBM study and is shown in Chapter 6.

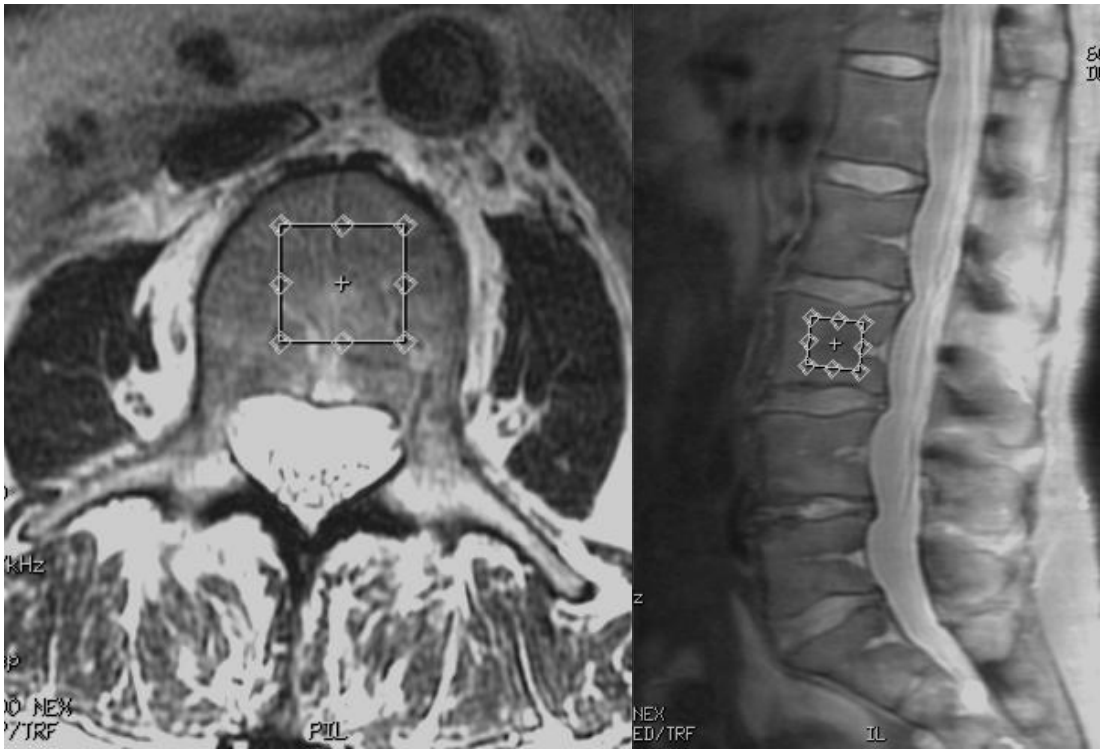

Figure 5-16 The T_2-weighted axial (left) and IDEAL sagittal (right) images, which were used for effective positioning of the PRESS voxel in the third lumbar vertebra. Note the voxel which is angulated according to the individual vertebra in the sagittal image. Also note the absence of the additional manual saturation pulses, which were creating artefacts.

The methods of acquiring PRESS spectra were optimised to acquire a spectrum in the lumbar spine within a reasonable clinical scan time. In spectroscopy, it is essential to protect the voxel signal from contamination arising from surrounding tissues and environment. The contamination is usually avoided by applying saturation bands around the voxel for sharp voxel profile as described in Chapter 3. In GE scanners the voxel is usually surrounded by saturation bands with the provision to add in some extra manually prescribed saturation bands at different locations. The number of additional saturation bands depends on the limitations of the pulse sequence. During the initial stages of the project, experimental spectra were acquired with the default saturation pulses and with some additional manual saturation pulses. The manual saturation pulses were added in different planes (see Figure 5-14) to remove signals from anatomical regions (e.g. aorta and spinal cord) which may cause artefactual signal within the voxel. The results from these spectra provided non uniform measurements. After further investigation, it was discovered that the default saturation pulses were being replaced by manual saturation pulses when the pulse sequence did not have enough time to apply additional pulses. All the spectra from the HBM study were not acquired with additional manual saturation pulses (see Figure 5-16). This was done to maintain experimental uniformity and to avoid the loss of the default saturation pulses.

Before the spectroscopy acquisition, the changes to the pulse sequence with respect to water suppression and offset were applied manually by altering their specific control variables (CVs). Following the change of parameters the new variables were downloaded to the pulse programmer. Automatic prescan was applied to the sequence for voxel shimming and optimisation of centre frequency, and transmitter and receiver gains. The protocol that was used in the HBM study for single voxel spectroscopy acquisition is shown in Chapter 6.

An example spectrum is shown in Figure 5-17, which demonstrates high SNR and reasonable spectral resolution given the short acquisition time (1 minute). The spectral resolution was limited to resolve closely spaced metabolites, but was able to visualise the main fat and water signals. The acquired spectra were processed by default scanner software (SAGE) and also by using a third-party software called linear-combination model (LCM), as detailed in Chapter 3.

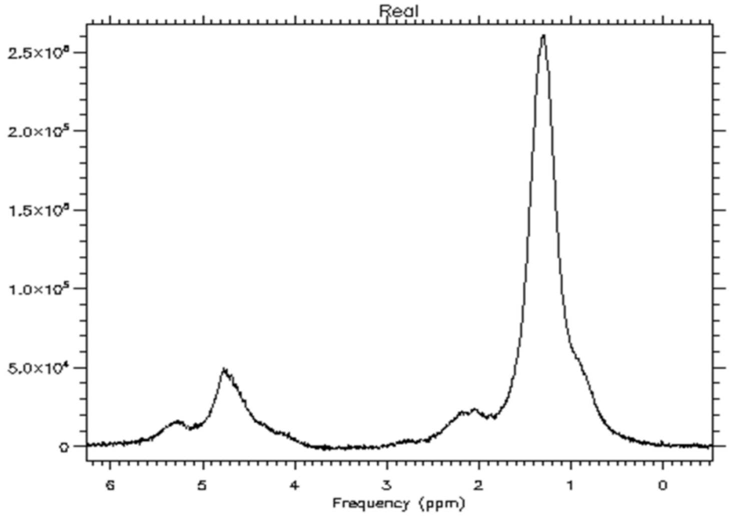

Figure 5-17 A typical single-voxel spectrum from lumbar vertebrae in a volunteer demonstrating peaks from fat (mainly 1.3 ppm and 5.3 ppm) and water (4.7 ppm). Note the excellent SNR achieved in only 1 minute, due to the relatively high concentrations of fat and water.

6 High Bone Mass Study

6.1 Introduction

The high bone mass (HBM) project is an on-going molecular genetics study being run by Prof. Jon Tobias (Principal Investigator) from the Musculoskeletal Research Unit, University of Bristol, aimed at identifying individuals affected by genetic mutations that cause increased bone mass. HBM has been evaluated and is associated with decreased bone resorption, increased bone formation, or a combination of both. HBM either can be advantageous to an individual, i.e. stronger bone which is resistant to fracture, or be disadvantageous, i.e. weaker bone with predisposition to fracture. The occurrence of stronger or weaker bone in HBM individuals may be due to a lot of factors. HBM with weaker bone may be caused by the presence of osteopetrosis disease and HBM with stronger bone may be caused by any specific genetic mutation [35, 36].

A previous study of a family with HBM showed that they were reported with a genetic abnormality localised to 11q12-13 gene. Studies of osteoporosis pseudoglioma syndrome (OPS), which is a recessive disorder with premature osteoporosis and bone weakness, identified the cause as an inactivation mutation in the low-density lipoprotein-receptor-related protein 5 (LRP5) gene. HBM condition results from an activation mutation of LRP5 gene, leading to stimulation of osteoblastic bone formation [36, 222, 223, 225].

Several families with the HBM condition due to LRP5 mutation or other mutations in this gene have been identified by earlier studies. The HBM condition is occasionally known to be associated with minor skeletal abnormalities, such as torus palatines, widening of mandible, and thickened cortices. Some affected individuals have demonstrated severe phenotypes of neurological complications. The occurrences of HBM with and without abnormalities are unclear and are being investigated [38, 227].

Identification of molecular pathways such as LRP5 resulting in the HBM phenotype may provide a platform for developing new anabolic therapies for the treatment of osteoporosis. Teriparatide is the first of a new type of skeletal anabolic agents which stimulate bone formation rather than suppressing bone resorption and further bone loss commonly effected in conventional therapy. Teriparatide appears to be effective at increasing bone mass and reducing fracture risks, but it mainly contains recombinant protein which requires parenteral administration and it is also expensive. The identification of novel pathways such as LRP5 may provide alternative methods based on orally administered enzyme inhibitors. Newer agents with means of enhancing bone formation through stimulation of LRP5 are being researched and developed [35, 36].

Certain individuals with HBM features were identified at Bristol Royal Infirmary using dual-energy X-ray absorptiometry (DEXA). The family members of the individuals were also screened, which resulted in the demonstration of a dominant inheritance of HBM in the family. Based on these results the DEXA database was screened further in Bristol to identify individuals who had a T-score greater than four in spine or hip, after excluding subjects with artificially elevated areal BMD (e.g. subjects with calcified aorta). Investigation of the underlying gene defect in the HBM cases may lead to the identification of a mutation in LRP5 or may lead to identification of novel genes resulting in conditions related to HBM [35, 36].

6.2 Objectives of the Study

The main study aims are to identify new genetic and biochemical pathways that may cause HBM in individuals with the following sub-aims [35, 36]:

- Determining whether HBM cases identified in the study from all individuals are influenced by known LRP5 or novel gene mutation
- Identifying similar results from HBM cases across UK by searching the DEXA databases
- Screening family members of HBM individuals who are not affected by LRP5 and to identify novel genes which may be responsible for their condition.

The results in this thesis are from a sub-study with the secondary aim of characterising the HBM condition with quantitative *in vivo* magnetic resonance (MR) imaging and spectroscopy.

6.3 Study Design and Patient Recruitment

The index (primary) population for the HBM study was identified by screening the DEXA database in Bristol and other large centres in the UK. The identification of an index population is based on the individual having a T-score greater than four at spine or hip. After identification, the individuals were informed of the study and its protocol using a letter and an information sheet, followed by telephone calls. Spouses and blood relatives were also recruited through the index individuals. All individuals were recruited into the study only after acquiring informed consent. The volunteers who were recruited for MR data acquisition underwent additional safety screening for identification of metallic implants and devices. A total of 555 people were recruited from all the participating centres in UK, of whom 258 people were index cases, 236 people were relatives and 61 people were spouses. From the 236 relatives, 94 people were classified as HBM-affected and the remaining 142 people were classified as unaffected. From the 61 spouses, 3 people were classified as HBM-affected and the remaining 58 people were classified as unaffected [35, 36].

The project was approved by the Bath Research Ethics Committee (COREC Ref 05/Q2001/78) and site specific approval (SAA) was obtained from the Central and South Bristol Research Ethic Committee (SAA Ref 05/2006/60). Funding for the study was provided by the Wellcome Trust (Euston, London, UK) [35, 36].

6.4 Procedures

The study procedure for all individuals involved a DEXA scan of the lumbar spine, hip and total body, plain radiographs and venous blood sampling. Some centres acquired peripheral quantitative computed-tomography (pQCT) data from the distal radius and tibia, and carried out a jump test to measure muscle strength as an indirect marker for bone strength. The centre in Hull was involved in acquiring additional data using magnetic resonance imaging and spectroscopy (MRI & MRS) at the lumbar spine, distal radius and tibia [36].

DEXA data were acquired in all centres using the local scanners and staff. Different types of scanner were used for DEXA acquisition in centres across UK but following a standardised measurement protocol. The DEXA data were processed to measure areal bone mineral density (BMD), bone mineral content (BMC), and T- and Z- scores from all anatomical sites. Plain radiographs were acquired of the lumbar spine (anteroposterior and lateral), pelvis, knees and hand/wrist (AP view). The radiographs were acquired at the local radiology centres by registered radiographers. Individuals under the age of 40 were omitted for radiographs of lumbar spine and pelvis to avoid radiation exposure. Venepuncture was performed on participating individuals by a registered nurse or doctor, with approximately 25-50 ml of blood being collected. The blood was used for the evaluation of basic bone biochemistry (full blood count, calcium, phosphate and alkaline phosphatase levels), bone turnover markers and for DNA analysis [36].

At Hull, the pQCT data were acquired using the Stratec Medizintechnik XCT-2000 scanner (Pforzheim, Germany). The scanner was used for axial data acquisition from distal tibia and radius to measure volumetric BMD from the trabecular or the whole bone. A total of 169 Caucasian individuals underwent pQCT examination from 2008 to 2009, of whom 118 (70%) people were female and 49 (29%) people were male and two (1%) people's information was not available [36].

Jumping mechanography is a test to measure leg muscle strength. The examination is very simple and requires the volunteer to jump on a jump plate using each individual leg and then both legs together. The jump plate has integrated sensors that measure the power and force that was applied by the volunteer's jumps. The device is simple and safe and is an easy method of measuring velocity, from which power is calculated. The results from the jump test describe the strength of the muscle surrounding the bone, which may indirectly influence the strength of the bone [36].

MR data were acquired only at Hull, using a 3.0 Tesla GE MR750 whole-body scanner (Milwaukee, WI, USA). Imaging and spectroscopy data were acquired from lumbar spine and imaging-only data were acquired from distal radius and tibia. A total of 52 Caucasian female individuals underwent MR examination from 2009-2010, of whom 32 people were from the index and 20 people were from the family members population, more detail will be provided in section 6.6.

6.5 Peripheral Quantitative Computed Tomography

Axial pQCT images were acquired from the forearm (radius) and lower leg (tibia) for individuals from the HBM project. The left forearm and lower leg were selected for all individuals to maintain a standardised methodology. Patient history was collected to identify factors which could affect the pQCT measurement values. If the individual had previous bone fractures in the left forearm or lower leg, then the right side was used for acquisition. This was done to avoid bias of volumetric BMD values due to fracture and associated metabolic processes at that location. Postmenopausal women and others who underwent hormone replacement therapy (HRT) treatments were identified for relationships with bone densities.

6.5.1 pQCT Proximal and Distal Radius

Three locations were selected for acquisition in the forearm. The approximate length of the radius bone in the forearm was measured manually using a ruler from wrist to elbow. From this measurement, three longitudinal locations at 4%, 60% and 66% region (see Figure 6-1) were calculated to be imaged by the pQCT scanner. The image at 4% region was used for the measurement of volumetric BMD, and the images at 60% and 66% regions were used for measurement of cortical thickness and muscle diameter. If the total length of the radius bone was 30.0 cm for example, then the 4% location was calculated as 1.2 cm from the wrist and 60% was calculated as 18.0 cm from the wrist and 66% was calculated as 19.8 cm from the wrist. These measurements were input to the pQCT scanner for acquisition points.

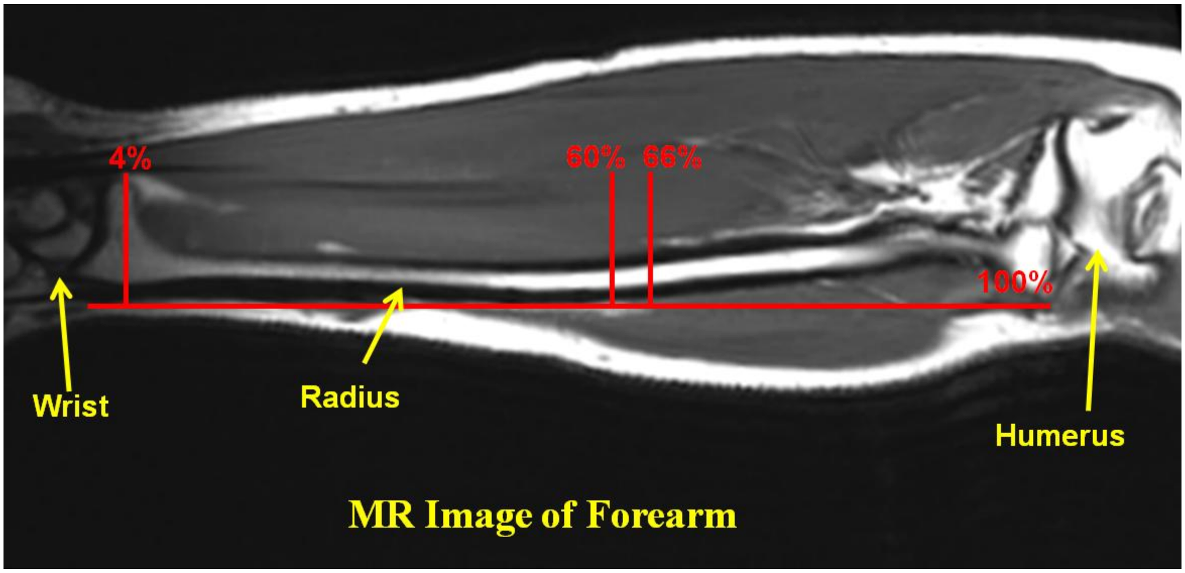

Figure 6-1 MR Image from a subject's forearm, illustrating the longitudinal locations for pQCT data acquisition in radius.

6.5.2 pQCT Proximal and Distal Tibia

Three locations were selected for acquisition in the lower leg. The approximate length of the tibial bone in the lower leg was measured manually using a ruler from ankle to knee. From the total measurement of the tibia three longitudinal locations at 4%, 14% and 66% regions (see Figure 6-2) were calculated to be imaged by the pQCT scanner. The image at 4% region was used for measurement of volumetric BMD, the image at 14% region was used for measurement of cortical thickness, and the image at 66% region was used for measurement of cortical thickness and muscle diameter.

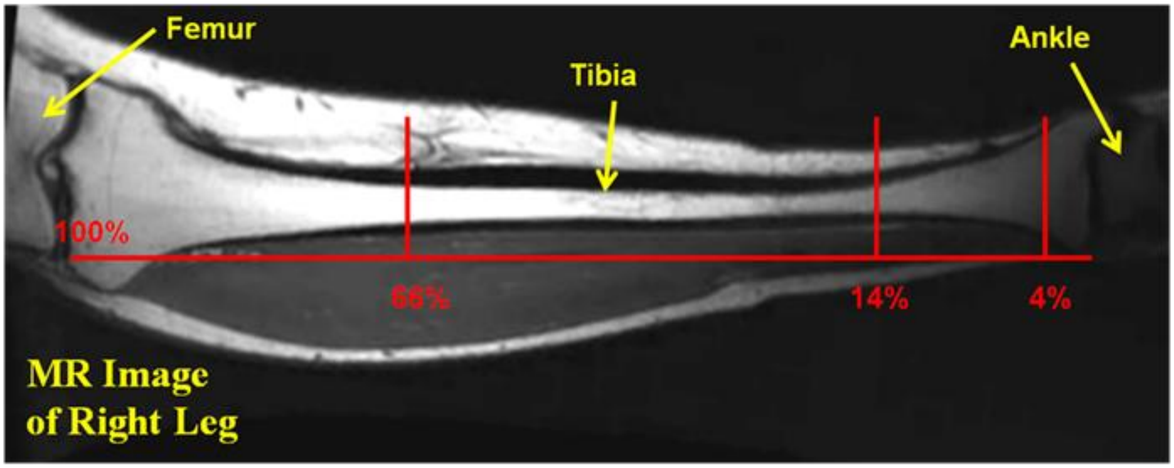

Figure 6-2 MR Image from a subject's lower leg, illustrating the longitudinal locations for pQCT data acquisition in tibia.

6.6 Magnetic Resonance Imaging and Spectroscopy

The MR protocol was developed and optimised in detail for different anatomical locations from October 2008 to January 2009 using the old (GE HDx) and new (GE MR750) 3.0 T scanner (see Chapter 5), but all the MR data in this thesis were acquired using the newer GE MR750 scanner.

6.6.1 Study Population

Only female individuals from the pQCT population (i.e. index and family members) in Hull were invited for MR data acquisition, due to the majority of research studies, having been performed in women. A total of 52 female individuals (Mean Age (years) 58 ± 13 SD) comprising of index and family members from the pQCT population were scanned. From the total 52 individuals, 38 people (Mean Age (years) 59 ± 13 SD) were classified as HBM-affected, 12 people (Mean Age (years) 53 ± 13 SD) were classified as non-affected and two people (Mean Age (years) 62 ± 1 SD) were classified as borderline HBM-affected. All the individuals in this thesis were classified based on the recommended criteria set by the primary investigators of the HBM study. The classification was based on their DEXA measurements with index, spouses and relatives having different criteria for classification as HBM-affected, non-affected and borderline HBM. The HBM categorisation criteria for index and spouses were either: (i) having a L1 Z-score greater than or equal 3.2 in addition to a hip Z-score greater than or equal to 1.2, or (ii) a hip Z-score greater than or equal to 3.2 in addition to L1 Z-score greater than or equal to 1.2. For relatives the criteria for HBM categorisation was based on them having a sum of L1 and hip Z-scores to be greater than or equal to 3.2. The criteria for the borderline HBM categorisation for only the index population was very narrow and was based on them having their L1 or hip Z-score to be between 3.0 and 3.2. The categorisation of controls was applied to all the relatives and spouses who did not fulfil the criteria for HBM and borderline HBM [36].

6.6.2 MR Protocol

The total MR exam time for all the volunteers in the HBM study inclusive of screening, positioning and scanning was around 45 minutes. The MR protocol consisted of:

- T_1-weighted, high spatial resolution axial images from distal tibia and distal radius to demonstrate the trabecular detail. The T_1-weighted images were used because they demonstrated good differentiation of bone structures (i.e. trabeculae, marrow and cortex), and they were acquired only at the 4% region in the distal tibia and radius. The T_1-weighted images were post-processed to measure bone volume fraction (BVF), Entropy and trabecular bone texture.
- A three-point Dixon-type technique known as iterative decomposition of water and fat with echo asymmetry and least squares estimation (IDEAL) was used for the acquisition of separated fat and water images at lumbar vertebrae and proximal and distal tibia. These data were later processed by in-house software to produce fat-fraction (FF) maps. At proximal and distal tibia for both legs the IDEAL data were acquired at 4% and 66% regions. The data at 4% region was acquired to measure FF maps from the bone marrow and the data from 66% region was acquired to measure the cortical thickness and muscle diameter. The IDEAL images from proximal and distal tibia were later excluded, since they suffered from poor image quality.
- A PRESS-based double spin-echo spectroscopy sequence (PROBE-P) was used for spectral data acquisition at L1, L3 and L5. The spectral data were later used for measurement of FF, unsaturation index (UI) (a marker of the amount of unsaturated fatty acids present in the bone marrow) and full-width at half-maximum (FWHM) of water and lipid peaks which is believed to be a surrogate measurement for trabecular bone density.

6.6.2.1 MR Proximal and Distal Tibia

An IDEAL sequence using fast spin-echo (FSE) was used for axial image acquisition at 4% and 66% regions of the distal tibia from both lower legs (see Figure 6-3). The protocol that was used for IDEAL acquisition is described in Table 6:1.

Repetition time (TR) / Echo time (TE)	1500 / 32 ms
Bandwidth (BW)	50 kHz
Field-of-view (FOV)	300 × 204 mm
Slice thickness / Slice separation	5.0 / 1.5 mm
Scan time	3 minutes, 9 seconds
Imaging matrix (frequency encoding (FE) × phase encoding (PE))	256 × 256
Number of excitations (NEX)	3
Echo train-length (ETL)	4
Frequency direction	right - left
In-plane resolution	1.17 mm × 0.80 mm

Table 6:1 The parameters, which were used for the IDEAL image acquisition from both proximal and distal tibia.

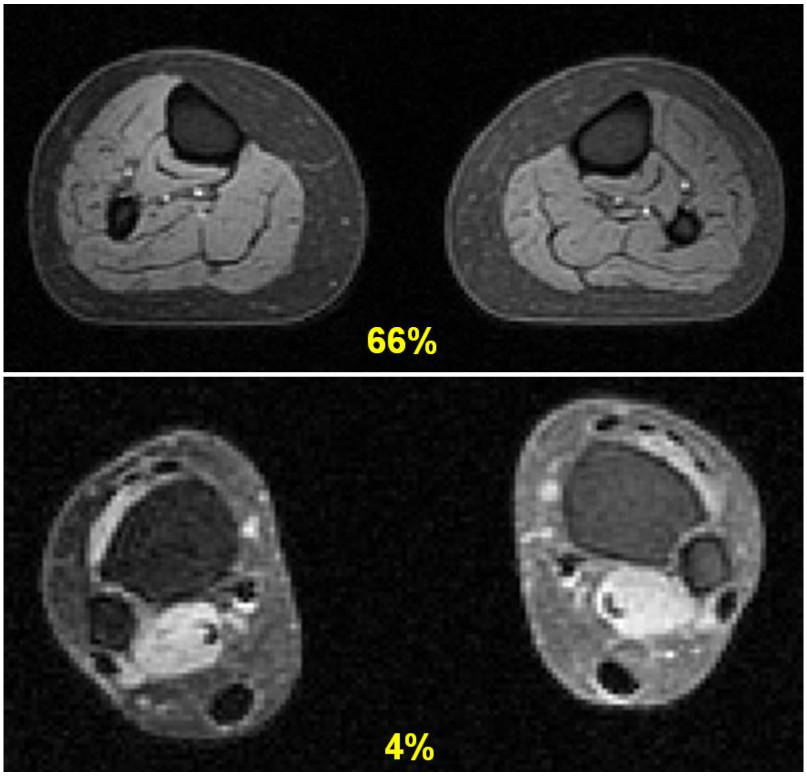

Figure 6-3 The axial water-only IDEAL image acquired in a volunteer at 66% region of the distal tibia from both legs (top), and the corresponding water-only image acquired at 4% region of the distal tibia from both legs (bottom). Note the relatively poor spatial resolution in both of the images.

High-resolution axial T_1-weighted imaging using a spin-echo (SE) sequence was acquired at 4% region of the distal tibia (see Figure 6-4). The protocol that was used for the image acquisition is described in Table 6:2.

TR / TE	500 / 13 ms
BW	27.8 kHz
FOV	100 × 75 mm
Slice thickness / slice separation	2.5 / 0.2 mm
Scan time	4 minutes, 52 seconds
Imaging matrix (FE × PE)	448 × 384
NEX	2
ETL	SE
Frequency direction	anterior - posterior
In-plane resolution	223 μm × 195 μm

Table 6:2 The parameters, which were used for the SE T_1-weighted image acquisition at 4% region of the distal tibia.

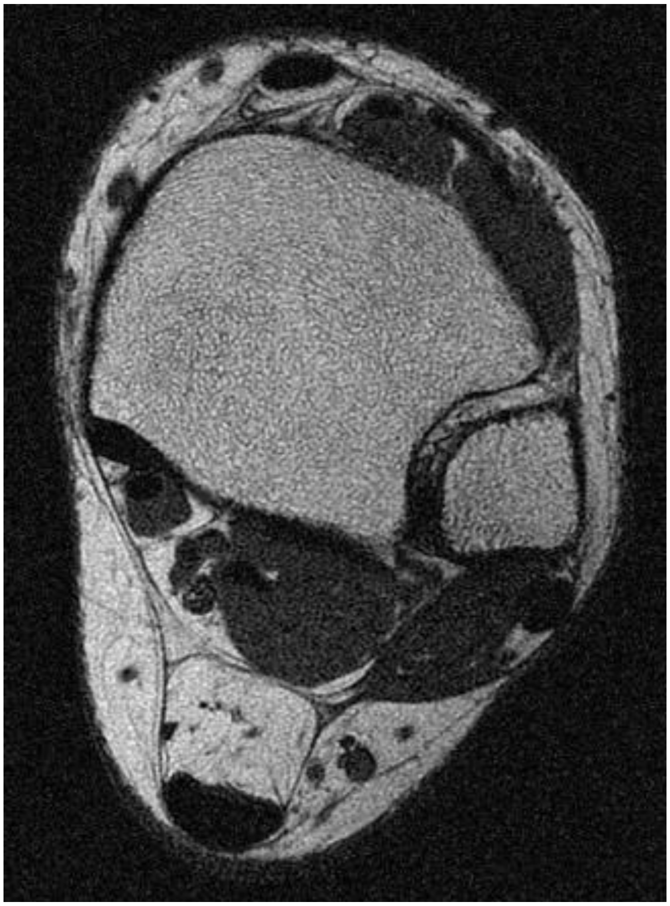

Figure 6-4 High spatial resolution axial spin-echo image acquired at 4% region of the distal tibia in a volunteer. Note the high spatial resolution and well-defined trabecular bone detail.

6.6.2.2 MR Distal Radius

High-resolution T_1-weighted SE axial images were acquired at 4% region of the distal radius (see Figure 6-5). The protocol that was used for image acquisition is described in Table 6:3.

TR / TE	500 / 14 ms
BW	27.8 kHz
FOV	90.0 × 67.5 mm
Slice thickness / slice separation	2.0 / 0.2 mm
Scan time	3 minutes, 8 seconds
Imaging matrix (FE × PE)	512 × 480
NEX	1
Frequency direction	right - left
In-plane resolution	176 µm × 141 µm

Table 6:3 The parameters, which were used for the SE T_1-weighted image acquisition at 4% region of the distal radius.

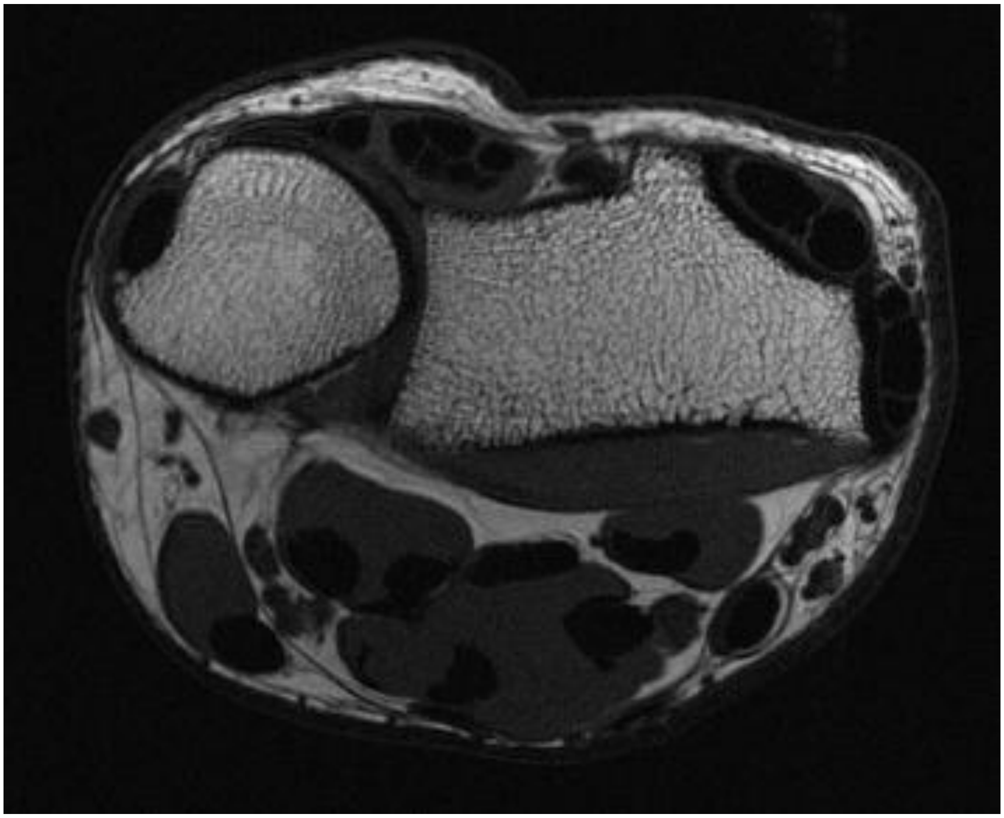

Figure 6-5 A high-resolution spin-echo axial image acquired at 4% region of the distal radius in a volunteer. Note the high spatial resolution, SNR and well-defined trabecular bone detail.

6.6.2.3 MR Lumbar Vertebrae

An IDEAL sequence using FSE was used for sagittal image acquisition from the lumbar vertebrae (see Figure 6-6). The protocol that was used for the image acquisition is described in Table 6:4.

TR / TE	1500.0 / 10.9 ms
BW	62.5 kHz
FOV	360 × 360 mm
Slice thickness / slice separation	4.0 / 1.3 mm
Scan time	2 minutes, 33 seconds
Imaging matrix (FE × PE)	416 × 256
NEX	6
ETL	16
Frequency direction	superior - inferior
In-plane resolution	0.86 mm × 1.41 mm

Table 6:4 The parameters, which were used for the IDEAL image acquisition of the lumbar spine.

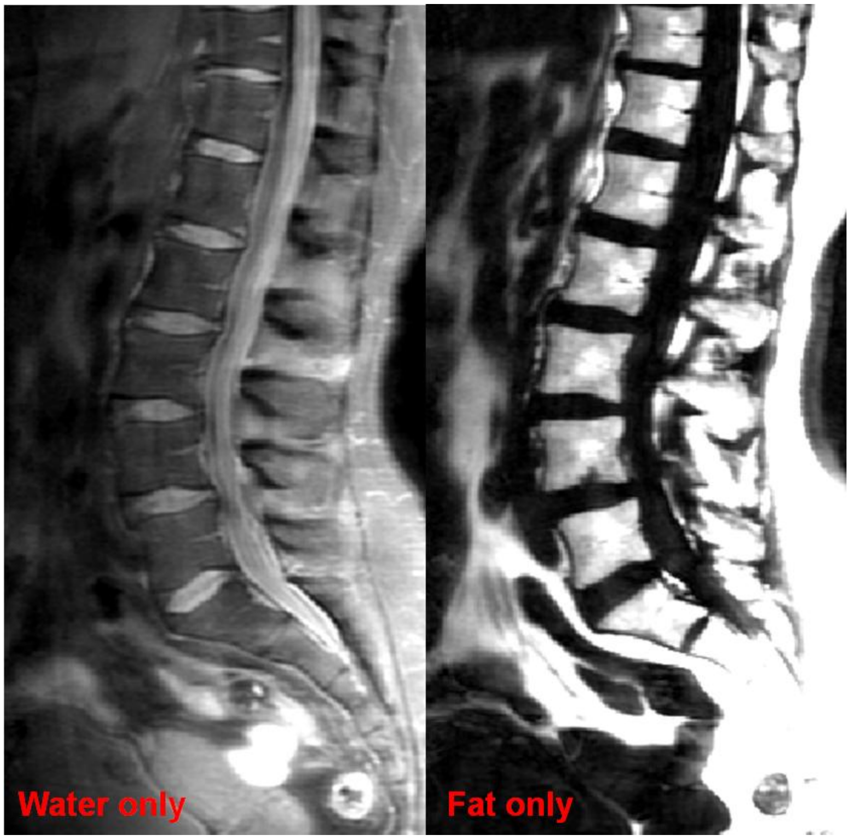

Figure 6-6 Sagittal IDEAL images from lumbar vertebrae with separate images for water (left) and fat (right) signal.

A PRESS (PROBE-P) single-voxel technique was used for spectroscopy data acquisition from L1, L3 and L5. The protocol that was used for the spectral acquisition is described in Table 6:5.

TR / TE	1500 / 28 ms
Voxel volume	typically 1.8 – 5.4 cm^3
Scan time	1 minute
NEX	8
Number of signal averages (NSA)	16
Number of saturation bands around the voxel	6 (default)
Voxel slice selection offset (off_rf1, 2 and 3)	- 460 Hz
Chemical-shift selective saturation (CHESS)	off
RF pulse angles	90° 137° 137°
RF pulse bandwidths	2366.67 Hz 1384.62 Hz 1384.62 Hz

Table 6:5 The parameters, which were used for the IDEAL image acquisition of the lumbar spine.

6.6.3 Summary

Table 6:6 lists the different anatomical sites, which were investigated using MR, followed by the type of imaging sequence used and the types of measurements obtained.

Anatomy	Sequence	Data to be Quantified
Distal Radius	T_1-weighted SE	Bone volume fraction (BVF), entropy and textural analysis (contrast, correlation, energy and homogeneity)
Proximal and Distal Tibia	T_1-weighted SE	BVF, entropy and textural analysis (contrast, correlation, energy and homogeneity)
	IDEAL	Fat-fraction (FF) (Excluded due to poor image quality)
Lumbar Vertebrae	IDEAL	FF
	PRESS spectroscopy from L1, L3 and L5	FF, full width at half maximum (FWHM) and unsaturation index (UI)

Table 6:6 The list of anatomical sites with their corresponding imaging sequences and the type of quantification.

7 Software

7.1 MATLAB

MATLAB (Matrix Laboratory, The MathWorks, Inc. Natick, USA) is a matrix based high-performance mathematical language widely used for a range of applications such as signal/image processing, communication, designing, measurement testing, etc. MATLAB employs a list of individual pre-programmed codes (functions) that can be added into existing code to perform tasks, and is also advantageous for integration with other programming languages like C, C++ and FORTRAN. In this thesis, MATLAB (version R2006a) was used as the default programming platform to develop in-house software for processing and quantifying data from magnetic resonance imaging (MRI) and peripheral quantitative computed tomography (pQCT) [147, 164, 167, 228, 229]. Two major programs were created to process the image data from the high bone mass (HBM) project.

1. ‘BVF Extremities’ was created for the semi-automated segmentation and processing of T_1 weighted axial images from distal radius and tibia, resulting in the quantification of trabecular bone volume fraction (BVF), trabecular bone area, entropy and four textural properties for comparison with data from pQCT.
2. ‘Spine FF’ was created for the semi-automated segmentation and processing of individual lumbar vertebrae from IDEAL data, resulting in the quantification of an average fat-fraction (FF). This program was used to measure the average FF from the three lumbar vertebrae of L1, L3 and L5.

Following is the detailed description of the individual program:

7.1.1 BVF Extremities

The program ‘BVF Extremities’ was created to process T_1 weighted axial images of the distal radius and tibia. The program is capable of segmenting trabecular bone semi automatically. The program processes the segmented bone to quantify BVF, trabecular bone area, entropy and four basic textural properties of contrast, correlation, energy and homogeneity.

7.1.1.1 Accessing the Images

MATLAB has functions to read a DICOM (digital imaging and communication in medicine) file, which contains a number of attributes including text and pixel value data. The pixel values from the DICOM file were interpreted as an m-by-n array and displayed as a grayscale image. MATLAB can also recreate a header from text attributes which was accessed to identify information like matrix size, pixel resolution and patient identification that were used for the analysis. After reading the image file, the data is displayed as an image (see Figure 7-1) for subsequent processing.

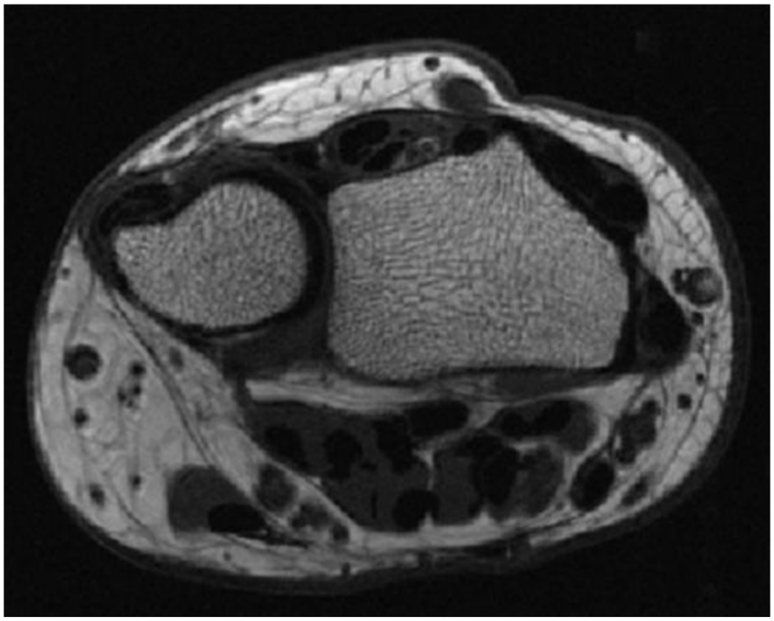

Figure 7-1 T_1-weighted axial image from distal radius.

7.1.1.2 Image Processing

MR images acquired using multi-channel coils often suffer from coil inhomogeneity artefacts, which results in regions of image having poor uniformity when compared with adjacent regions due to variations in the B_1 field. These signal variations often result in poor image processing during histogram thresholding and require correction algorithms to make the image more uniform. Various correction techniques are provided by the scanner manufacturers which can be applied during or after acquisition. Both phased array uniformity enhancement (PURE) and surface coil intensity correction (SCIC) were provided on the scanner to correct for image inhomogeneities. PURE uses a separately acquired calibration scan to correct the image for inhomogeneities, and SCIC is purely a post processing technique that applies image filters. However these methods were not available during the initial stage of the project, hence were not included in the protocol. The resultant inhomogeneities had to be corrected off-line using the software. This was essential in radius, which was acquired using an 8 channel phased array wrist coil. A contrast-limited adaptive histogram equalisation (CLAHE) algorithm was used to enhance the contrast of the grayscale image by operating on small regions in the image called tiles. The contrast within each tile was manipulated individually to produce a more uniform signal distribution in the image histogram. The neighbouring tiles were combined using bilinear interpolation to eliminate artificial boundaries. Images from HBM project were processed with a tile size based on an optimal value determined by evaluating various sizes. Figure 7-2 describes the measurement of BVF processed with and without CLAHE. Figure 7-2 (1) is the original image and Figure 7-2 (2) is the BVF estimation based on using the original image. Figure 7-2 (3) is the CLAHE processed image and Figure 7-2 (4) is the BVF estimation based on using the CLAHE processed image. Note the improved measurement of BVF in Figure 7-2 (4) when compared with Figure 7-2 (2).

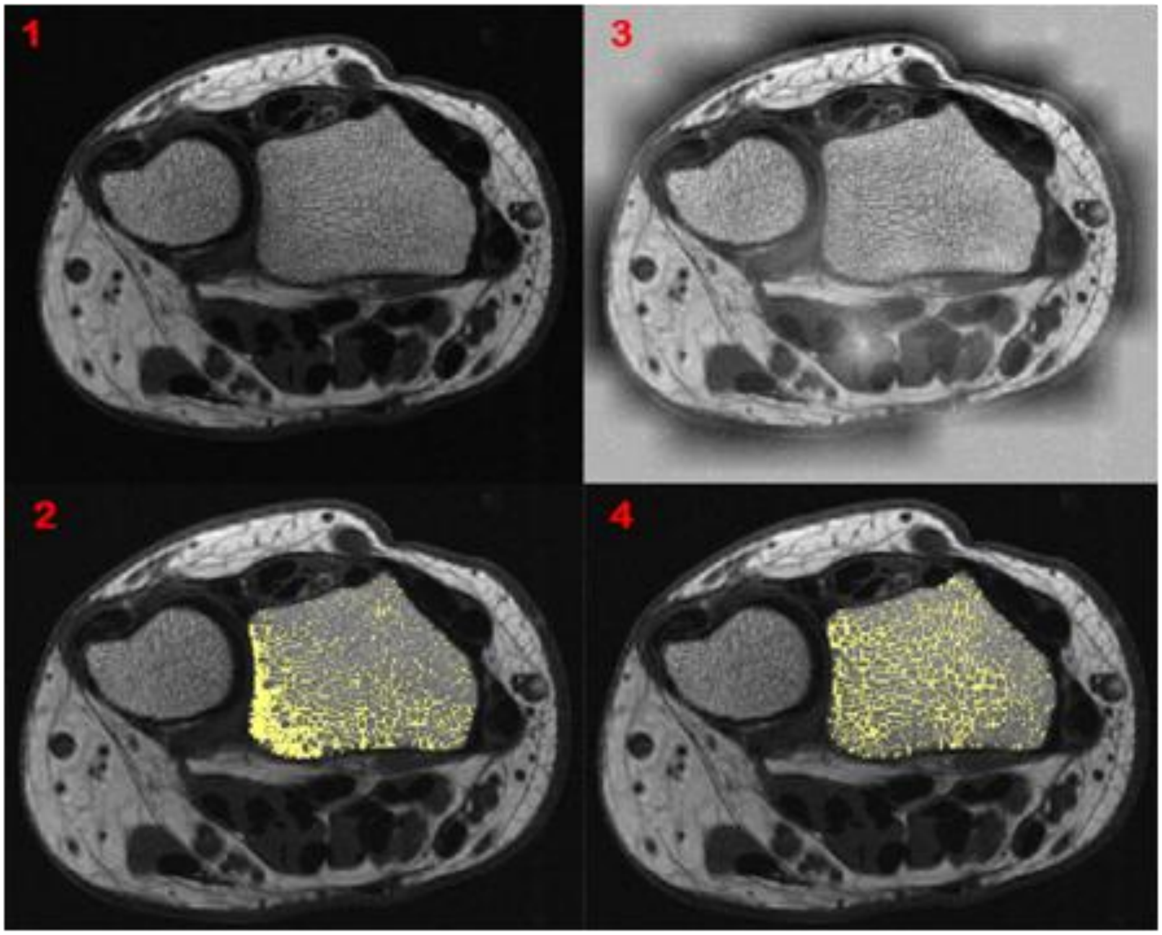

Figure 7-2 The images illustrate the difference in BVF estimation based on them being processed with (right side) and without (left side) CLAHE.

The original grayscale image was converted to a binary image (see Figure 7-3) using Otsu’s method [230]. The Otsu algorithm assumes that the whole image contains two classes of pixels, and then calculates an optimum signal threshold value to minimise the intraclass variance of the two classes. The trabecular component of the radius bone was segmented (see Figure 7-4 (left)) from the binary image by selecting connected pixels around a pixel seed point provided manually by the user. The selection works by assessing a specified range of connected pixels (n) (see Figure 7-5), and in this thesis a default of the eight surrounding pixels was used (see Figure 7-5 (right)). Image processing was subsequently applied on the binary image to fill image regions and holes which were missed during binary conversion (see Figure 7-4 (right)).

Figure 7-3 The binary image from distal radius processed using Otsu's method.

Figure 7-4 The segmented binary image (left) of radius followed by filling of holes (right).

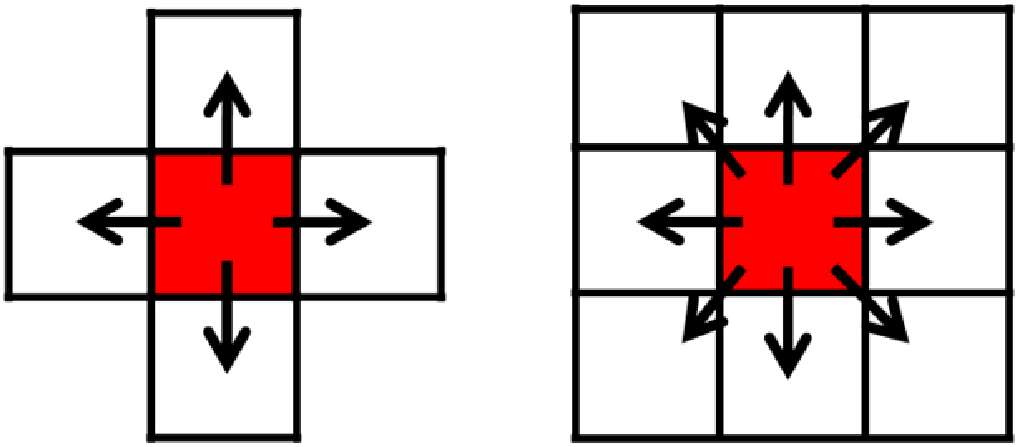

Figure 7-5 The images illustrate the method of identifying the number of connected pixels in relation to the pixel seed point (red). The left image is the representation of 4 connected pixels and the right image is the representation of 8 connected pixels.

The next stage was to convert the binary image to the gray scale image by matrix multiplication of the segmented binary and the whole histogram equalised image (see Figure 7-6). If the segmented bone contains soft tissues around it, then manual editing of the tissues was applied to remove them at this stage. Images from distal radius often required manual editing (40-50% cases) when compared with images from distal tibia (10-20% cases).

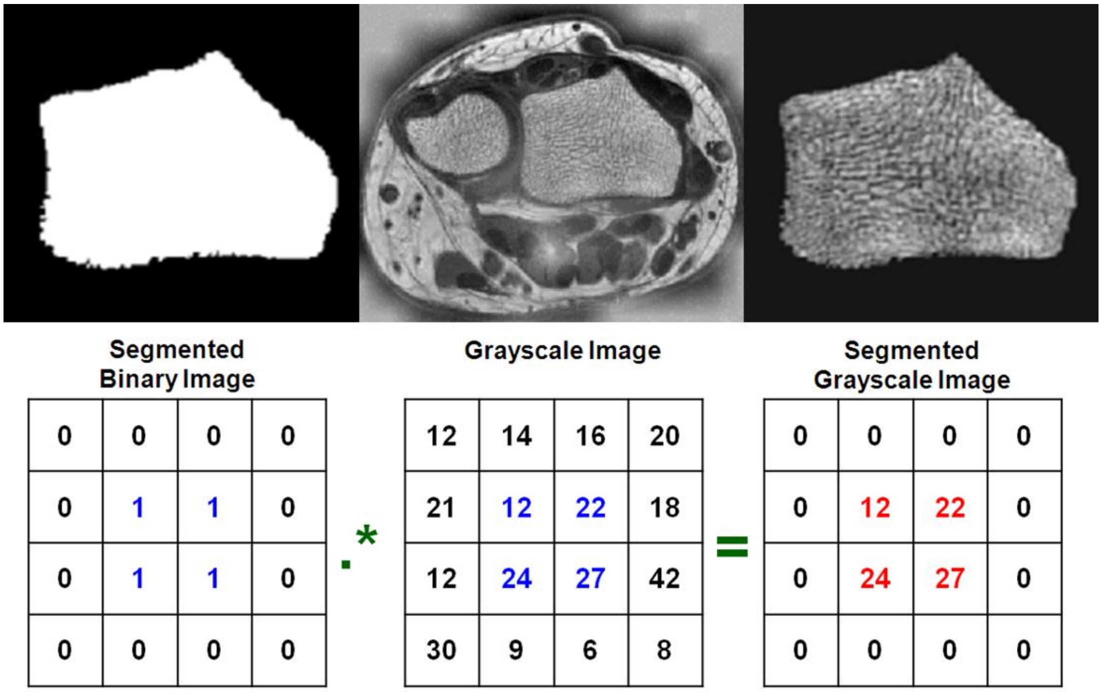

0	0	0	0
0	1	1	0
0	1	1	0
0	0	0	0

12	14	16	20
21	12	22	18
12	24	27	42
30	9	6	8

0	0	0	0
0	12	22	0
0	24	27	0
0	0	0	0

Figure 7-6 The process involved in converting the segmented binary image of radius to a grayscale image. The method is illustrated as an image (top row) as well as a matrix with numbers (bottom row).

The Otsu algorithm was applied to the pixels from the segmented trabecular bone to identify optimum global threshold values which resulted in a binary image of the segmented bone with good differentiation of trabeculae and marrow (see Figure 7-7). The inverted binary image containing the trabeculae was processed further using morphological skeletonisation, which removes pixels from the boundaries of the objects but does not allow the objects to break apart. The final trabeculae map can be overlaid on the original grayscale image (see Figure 7-8).

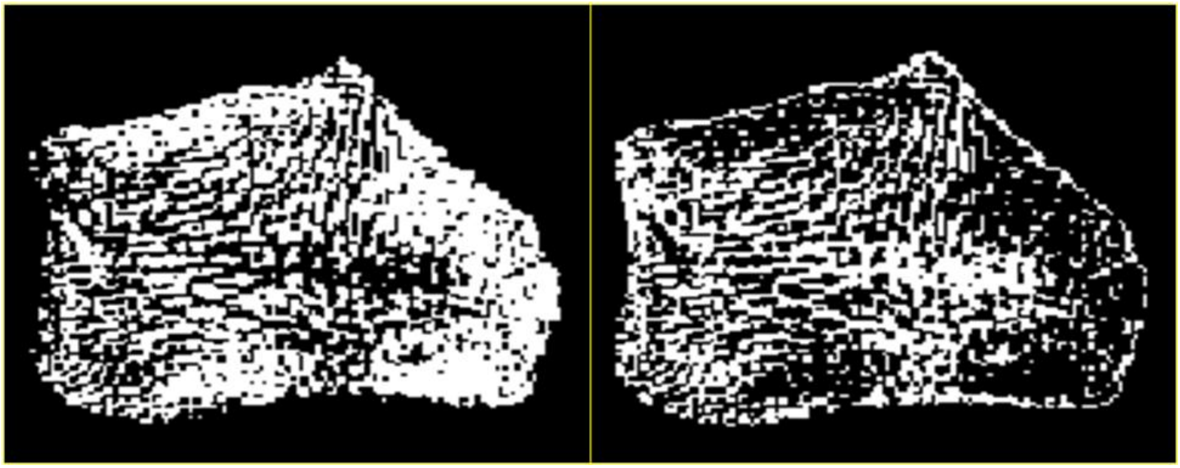

Figure 7-7 Binary image of trabecular spaces (left) can be inverted to show to trabecular bone (right).

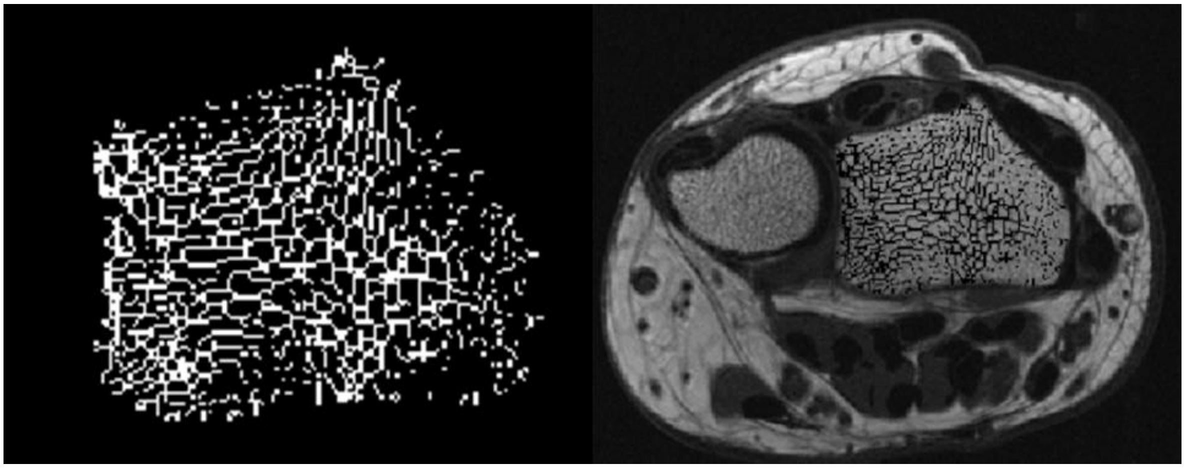

Figure 7-8 The skeletonised trabeculae from the binary image of radius (left) which was overlaid onto the original grayscale image of distal radius (right).

7.1.1.3 Quantification

The segmented trabecular bone was quantified to produce measurements of BVF, entropy and four textural properties [170-172, 231-233] of contrast, correlation, energy and homogeneity for the evaluation of bone strength. pQCT images were not used for measurements of entropy and textural properties, since they were acquired in low image resolution and were not able to resolve the individual trabeculae within the bone.

The BVF was measured as a percentage of trabeculae bone present inside the total segmented area. Two binary images were processed individually, one containing the trabeculae pixels alone and the other containing the pixels for the whole segmented region.

The size and total number of pixels present in each image was measured which was used for the measurement of BVF as a percentage (%) value.

$$BVF\,\% = 100\ \times \frac{trabeculae\ bone}{segmented\ area}$$

Equation 7-1

Entropy is a statistical measure of randomness of pixels within the segmented bone region and is given as:

$$-sum(p.* \log(p))$$

Equation 7-2

where (p) contains the histogram counts of the segmented bone region. The four textural parameters were measured by converting the segmented grayscale image of m-by-n into a gray-level co-occurrence matrix (GLCM) of m-by-n-by-p array. Before converting the segmented grayscale image into a GLCM, it is essential to remove unwanted 0 pixels surrounding the segmented bone in the image. If all the pixels in the segmented image including 0 are used, it would lead to poor processing of the GLCM function. For effective processing, the 0 pixels outside the segmented bone were converted to not-a-number (NaN), which was not read by the GLCM function. A grayscale image containing NaN values outside the bone region was generated by dividing the segmented grayscale image by the segmented binary image (see Figure 7-9). A GLCM was created from this image by calculating how often a pixel with intensity value (i) occurs horizontally to an adjacent pixel with value (j). The spatial dimensions can be user dependent and is based on the applied offsets. Figure 7-10 is an example for the calculation of a GLCM from a 4-by-5 input image with an angle of 0°. In the example input image the 1 and 7 value are adjacent to each other two times, thus the GLCM matrix has a value of 2 representing the number of times 1 and 7 were adjacent to each other. The offset is an important parameter in GLCM which works as a p-by-2 array of integers, specifying the distance, between the pixel of interest and its neighbour, and is often expressed as an angle. Figure 7-11 is a typical example on how an offset will work on the GLCM.

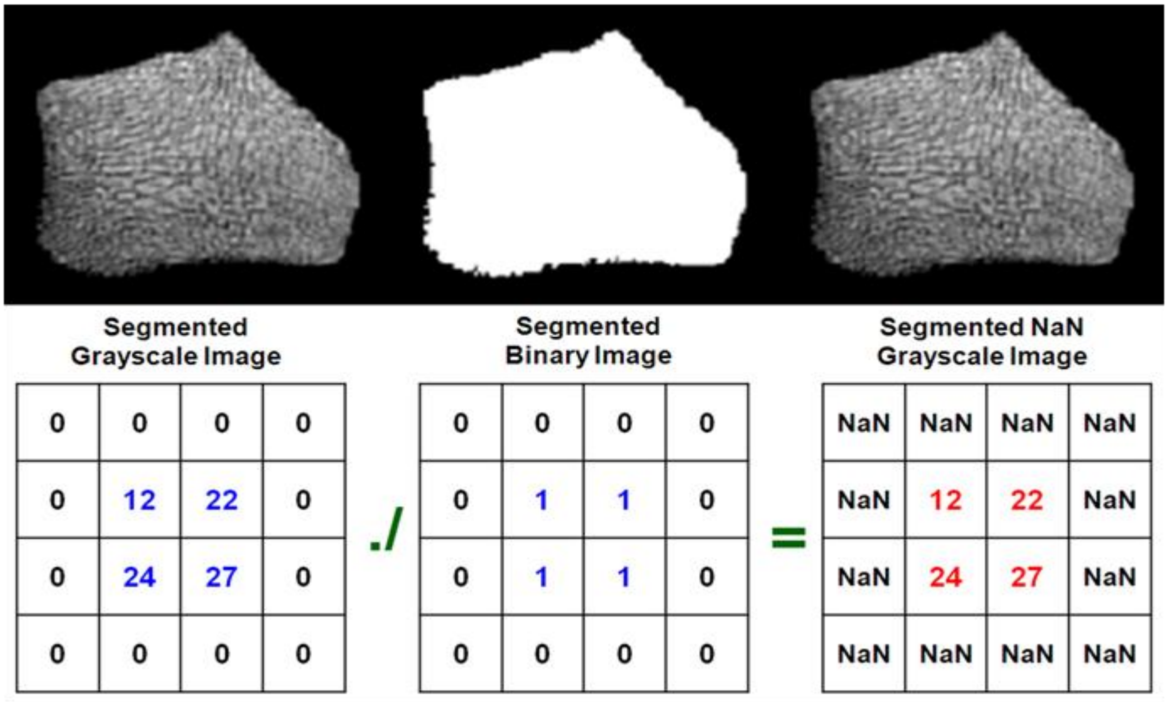

$$\begin{bmatrix} 0 & 0 & 0 & 0 \\ 0 & 12 & 22 & 0 \\ 0 & 24 & 27 & 0 \\ 0 & 0 & 0 & 0 \end{bmatrix} ./ \begin{bmatrix} 0 & 0 & 0 & 0 \\ 0 & 1 & 1 & 0 \\ 0 & 1 & 1 & 0 \\ 0 & 0 & 0 & 0 \end{bmatrix} = \begin{bmatrix} NaN & NaN & NaN & NaN \\ NaN & 12 & 22 & NaN \\ NaN & 24 & 27 & NaN \\ NaN & NaN & NaN & NaN \end{bmatrix}$$

Figure 7-9 The method of converting a normal grayscale image into a segmented grayscale image with NaN values. The method is illustrated as an image (top row) and as well as a matrix (bottom row).

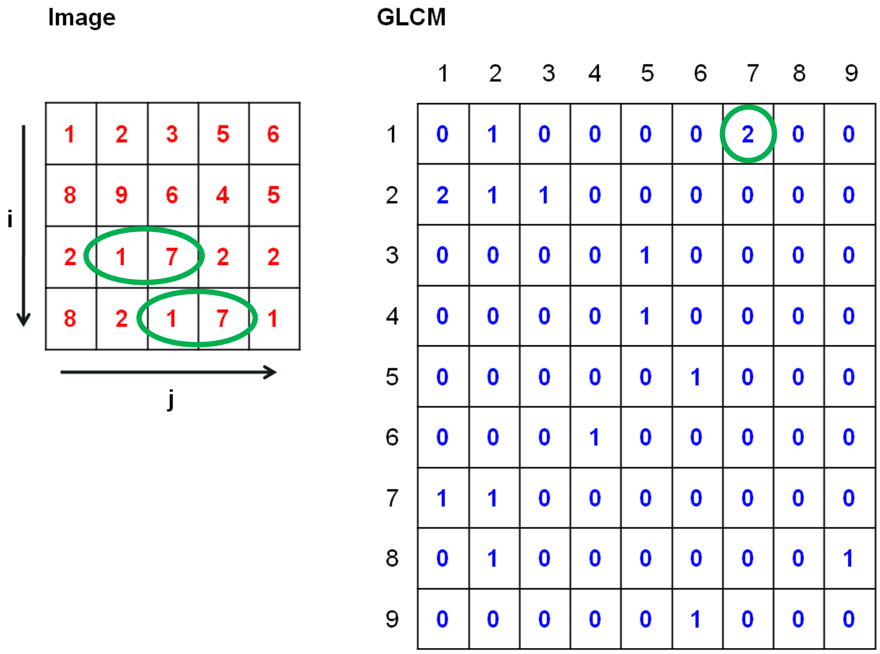

$$\begin{bmatrix} 1 & 2 & 3 & 5 & 6 \\ 8 & 9 & 6 & 4 & 5 \\ 2 & 1 & 7 & 2 & 2 \\ 8 & 2 & 1 & 7 & 1 \end{bmatrix}$$

$$\begin{array}{c|ccccccccc} & 1 & 2 & 3 & 4 & 5 & 6 & 7 & 8 & 9 \\ \hline 1 & 0 & 1 & 0 & 0 & 0 & 0 & 2 & 0 & 0 \\ 2 & 2 & 1 & 1 & 0 & 0 & 0 & 0 & 0 & 0 \\ 3 & 0 & 0 & 0 & 0 & 1 & 0 & 0 & 0 & 0 \\ 4 & 0 & 0 & 0 & 0 & 1 & 0 & 0 & 0 & 0 \\ 5 & 0 & 0 & 0 & 0 & 0 & 1 & 0 & 0 & 0 \\ 6 & 0 & 0 & 0 & 1 & 0 & 0 & 0 & 0 & 0 \\ 7 & 1 & 1 & 0 & 0 & 0 & 0 & 0 & 0 & 0 \\ 8 & 0 & 1 & 0 & 0 & 0 & 0 & 0 & 0 & 1 \\ 9 & 0 & 0 & 0 & 0 & 0 & 1 & 0 & 0 & 0 \end{array}$$

Figure 7-10 The method of converting a normal image matrix to a GLCM matrix by using 0° angle, which looks for repetition of pixel pairs.

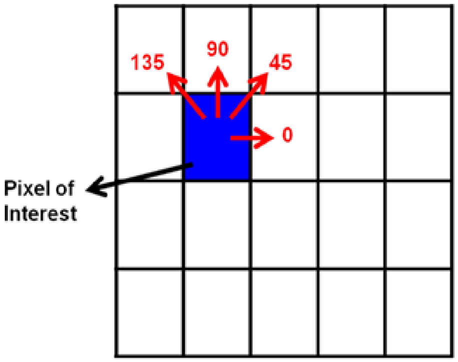

Angle (degrees)	Offset	Values
0	[0 D]	[0 1]
45	[-D D]	[-1 1]
90	[-D 0]	[-1 0]
135	[-D -D]	[-1 -1]

Figure 7-11 The different offset parameters that can be applied, as well as their influence on the angle of processing.

The textural property of contrast is a measure of the intensity contrast between adjacent pixels. Contrast is also known as variance and inertia.

$$Contrast = \sum_{i,j} |i-j|^2 \, p(i,j)$$

Equation 7-3

The textural property of correlation is a measure of the correlation of a pixel in relation to its neighbour.

$$Correlation = \sum_{i,j} \frac{(i-\mu_i)\left(j-\mu_j\right) p(i,j)}{\sigma_i \sigma_j}$$

Equation 7-4

The μ and σ are the mean and standard deviation of p with respect to i and j.

The textural property of energy is a value determined from the sum of squared elements in the GLCM. Energy measures the overall probability of having distinctive grayscale patterns in the image. Energy is also known as uniformity, uniformity of energy and angular second moment.

$$Energy = \sum_{i,j} p(i,j)^2$$

Equation 7-5

The textural property of homogeneity measures the closeness of the distribution of elements in the GLCM to the diagonal GLCM.

$$Homogeneity = \sum_{i,j} \frac{p(i,j)}{1 + |i - j|}$$

Equation 7-6

7.1.2 Validation of Software Measurement

The primary aim of this section was to design a computed-tomography (CT) and MR compatible phantom that could be used to develop protocols for bone imaging on a clinical scanner. The secondary aim was to use the phantom to validate software and measurements made with the clinical protocol. The phantom was imaged using an X-Tek HMX 160 micro CT (µCT) and our clinical 3.0 T MR (MR750) scanner. The images from µCT were used to provide a gold standard dataset that could be compared with the MR data.

A phantom with four compartments of varying structure (see Figure 7-12) was created at Queensland University of Technology (QUT), Brisbane (Prof Christian Langton), using a high definition 3D polymer printing technique (3D systems Inc, CA). The dimensions of the phantom were about 4 cm in height, 2 cm in diameter and contained four compartments of varying pore size (800-100 µm) and thickness of around 1 cm. The µCT data were acquired with an isotropic resolution of 42 µm. The MR data were acquired by immersing the phantom in a water filled sample tube. The data were collected by using the 8-channel wrist coil with slice thickness of 1 mm and in-plane resolution of up to 98 µm × 59 µm. The initial MR images were acquired with the T_1-weighted spin-echo (SE) technique, but the images were affected with chemical-shift artefacts. The IDEAL acquisition technique was subsequently used to produce high-resolution water and fat-only images. The fat-only image contained the chemical-shift artefact and was eliminated from processing, thus the water-only image was subsequently used for processing of the images. Two type of IDEAL images (IDEAL Protocol 1 & 2) were acquired and they were compared with µCT images. The images from IDEAL Protocol 1 were acquired with 1.0 mm slice thickness and with a moderate spatial resolution (156µm × 117µm). The images from IDEAL protocol 2 were acquired with 1.5 mm slice thickness and with a good spatial resolution (98µm × 59µm).

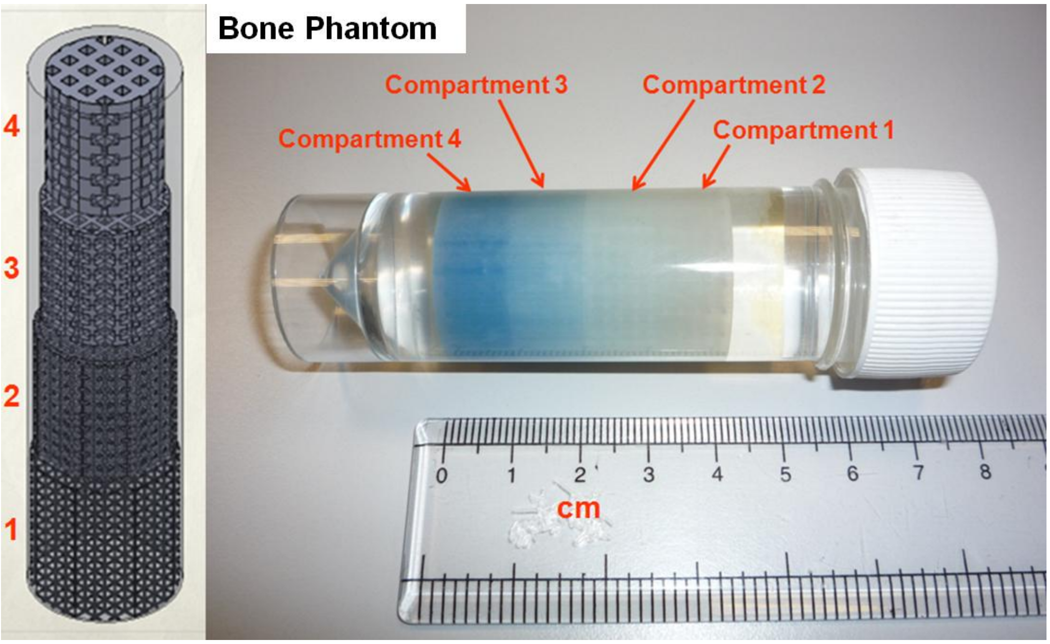

Figure 7-12 The image on the left is the CAD diagram of the phantom, and the image on the right is the phantom immersed in water in a sample tube, with illustration of the different compartments and the dimensions.

The images from both the imaging modalities were processed using the in-house software (MATLAB) to measure the solid volume fraction (SVF), which is the ratio of the amount of solid material present inside the volume of interest and it is very similar to the measurement of BVF. The images from µCT (see Figure 7-13) provided gold standard SVF values in all the compartments. Corresponding MR images for each compartment are shown in Figure 7-14.

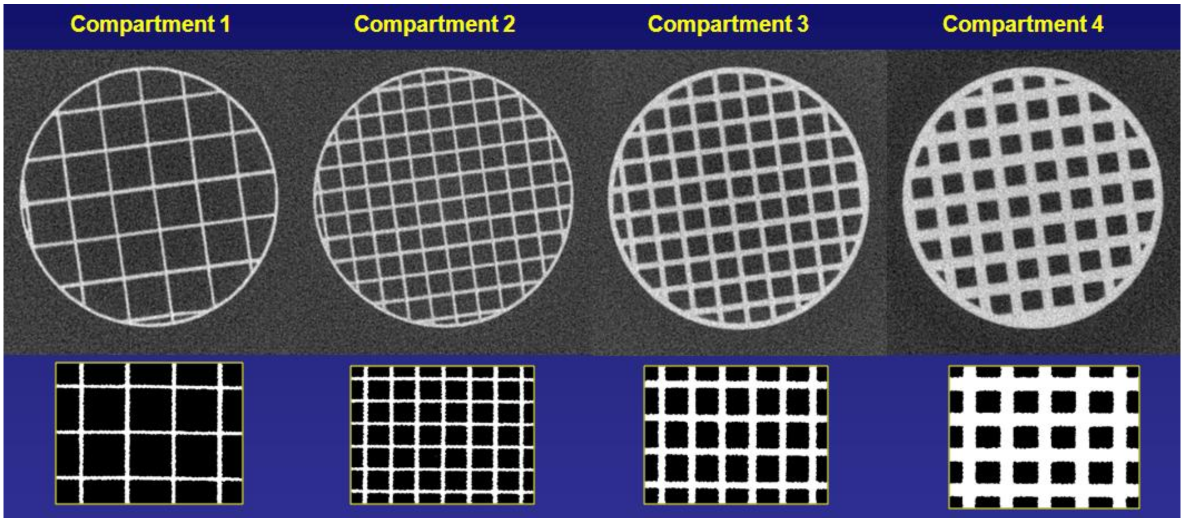

Figure 7-13 The top row illustrates the µCT images from the four compartments in the bone phantom. The bottom row illustrates the processed image from a region of interest in the individual compartments, which were used for the measurement of SVF. Note the good image quality from all the compartments.

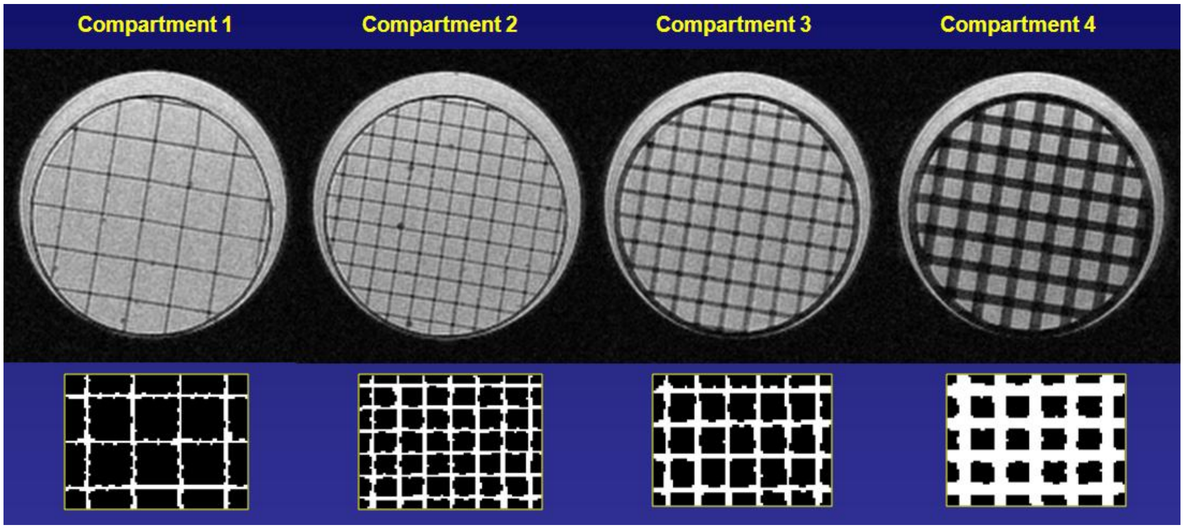

Figure 7-14 The top row illustrates the water-only IDEAL Protocol 1 MR images from the four compartments in the bone phantom. The bottom row illustrates the processed image from a region of interest from the individual compartments, which were used for the measurement of SVF. Note the good image quality from all the compartments.

The phantom was successfully used in both the imaging modalities. The SVF values were compared with both the imaging techniques in all the compartments, by using Bland-Altman plots (see Figure 7-15). The results described close similarities between the two techniques, with < 5 % agreement. The MR imaging technique of IDEAL worked well with high-resolution imaging and with good differentiation of the phantom structures. The aim in future is to fill the phantom with fat-water emulsions that would also provide bone marrow information in addition to SVF. Other quantitative parameters like trabecular width and cortical thickness could also be evaluated in future using this phantom.

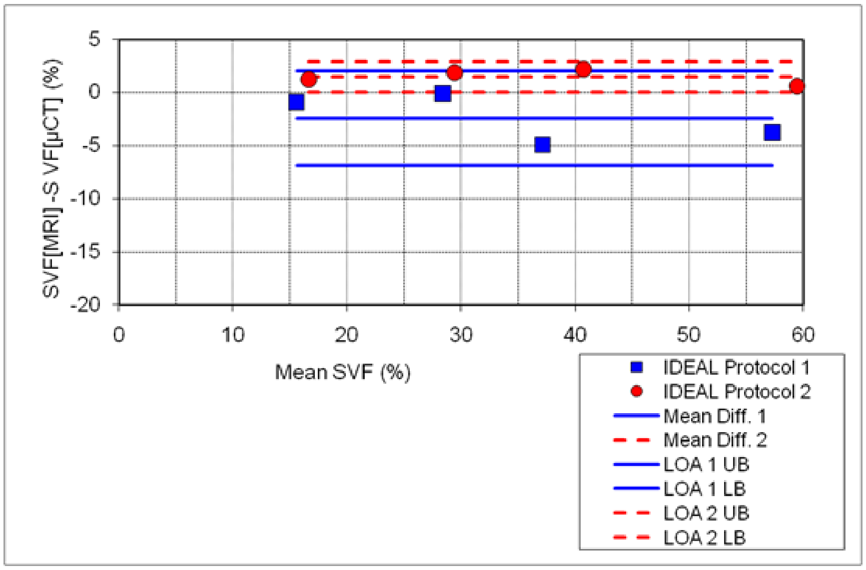

Figure 7-15 The Bland-Altman plot for comparison of SVF measurements from two IDEAL techniques with the SVF measurement from µCT. Note the close similarities between both the techniques.

7.1.3 Limitations of the Software

The BVF software was successfully used in the HBM study for the processing of images from the distal radius and tibia. The CLAHE method was applied for all the images to correct for signal non uniformity. The tool worked well for all the images from the distal tibia, since it was acquired using a birdcage head coil that resulted in good signal uniformity. The tool was limited in processing the data from the distal radius, since it was acquired using the phased array coil that resulted in signal non uniformity. The limitation of CLAHE resulted in successful or unsuccessful processing of images from distal radius (see Figure 7-16). The successful processing was essential for accurate BVF measurement from the bones, thus some of the BVF measurements from radius were excluded (based on visual inspection) when the software was unsuccessful in processing the images (see Figure 7-16 (bottom)). The CLAHE tool was only essential for the processing of BVF, thus the physical dimensions and the textural analysis of the bone were not affected during unsuccessful processing of the software. The physical dimensions and texture were measured from all the volunteers at distal radius except for two cases due to very poor image quality.

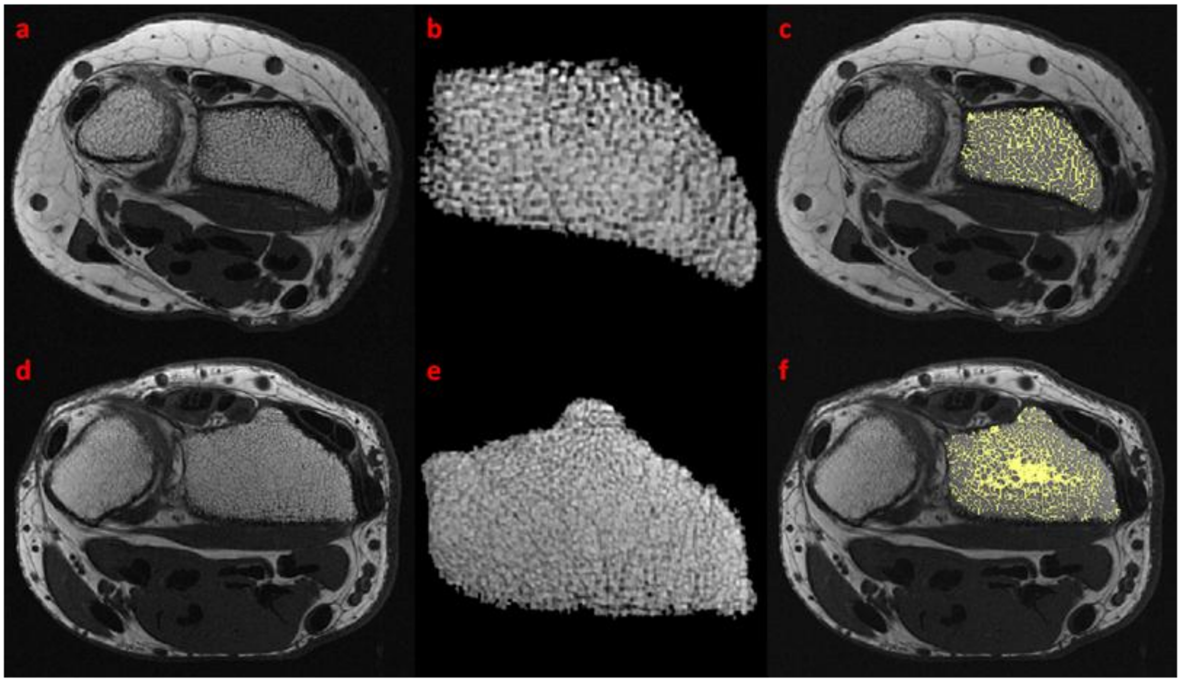

Figure 7-16 Images from distal radius with illustration of the segmentation and the processing of BVF. The images on the left column are the original images, the images on the middle column are the segmented images of radius and the images on the right are the processed images for the measurement of BVF. The images on the top row are example data illustrating successful processing of software for the measurement of BVF (c), dimensions and textural analysis (b). The images on the bottom are example data for unsuccessful processing of the software for the measurement of BVF (f), but the segmented bone region (e) was used for the measurement of dimensions and textural analysis.

7.1.4 Spine FF

The program ‘Spine FF’ was created to process sagittal IDEAL images of vertebrae which contain separate images of fat and water. The program was designed to work on both these images and calculate an average fat fraction (FF) map from individual vertebrae of interest. The program applies semi-automated segmentation of individual vertebrae with an option for manual editing to remove unwanted tissues around the vertebrae of interest. The DICOM attributes from the raw image were accessed to extract important information like: matrix size, pixel resolution and patient identification.

7.1.4.1 Fat Fraction Mapping

Fat fraction (FF) mapping (see Figure 7-17) was calculated for the whole image matrix on a pixel-by-pixel basis. An appropriate threshold was applied to remove noise from the image data. The FF was calculated as a percentage (%) using the formula of:

$$FF(\%) = 100 \times \frac{F}{(\mathrm{F} + \mathrm{W})}$$

Equation 7-7

Where F is fat-only image and W is water-only image from IDEAL dataset. The resultant FF image was used later for processing and analysis of segmented vertebrae.

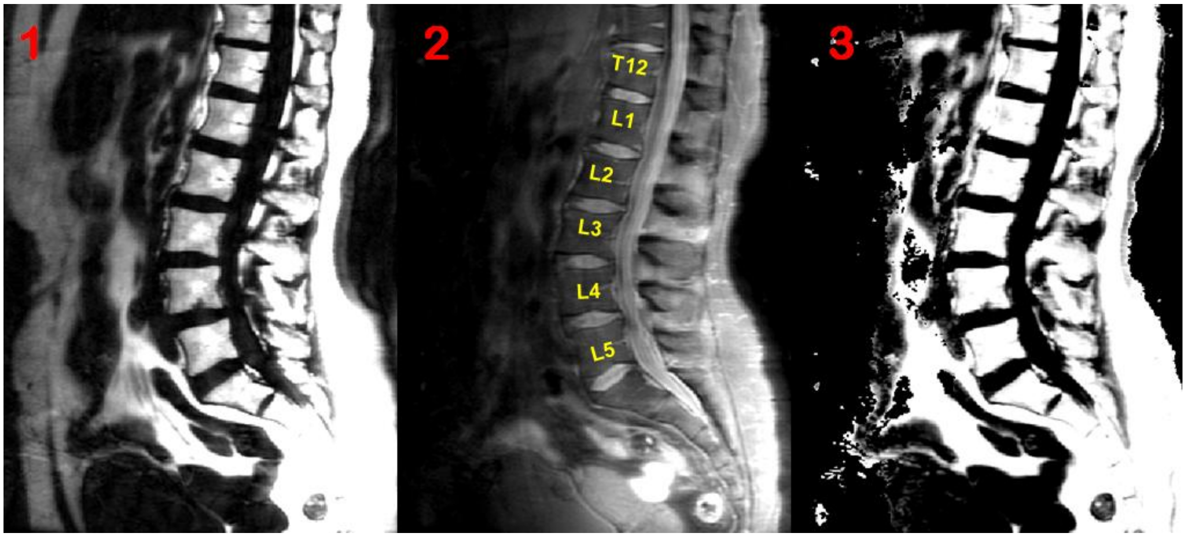

Figure 7-17 The method of estimating a FF image (3) using the images of fat (1) and water (2) from the IDEAL dataset. The middle image illustrates the location of individual lumbar vertebrae.

7.1.4.2 Vertebral Segmentation

The vertebral segmentation was achieved using the information from only the fat image (F) due to its better signal intensity differences between bone and adjacent tissues. The segmentation was achieved by manual cropping of a region of interest (ROI) around the desired vertebrae (see Figure 7-18). The cropped image (see Figure 7-19 (1)) was processed with CLAHE resulting in an intensity corrected image (see Figure 7-19 (2)). This image was processed with the Otsu algorithm for conversion to a binary image (see Figure 7-19 (3)), followed by vertebral selection. As described previously, additional processing was applied to the selected binary vertebral image to fill image regions and holes which were missed during binary conversion (see Figure 7-19 (4)). The resultant output image was a binary image of the selected vertebrae with or without additional tissues around it (see Figure 7-19 (4)) depending on the applied threshold.

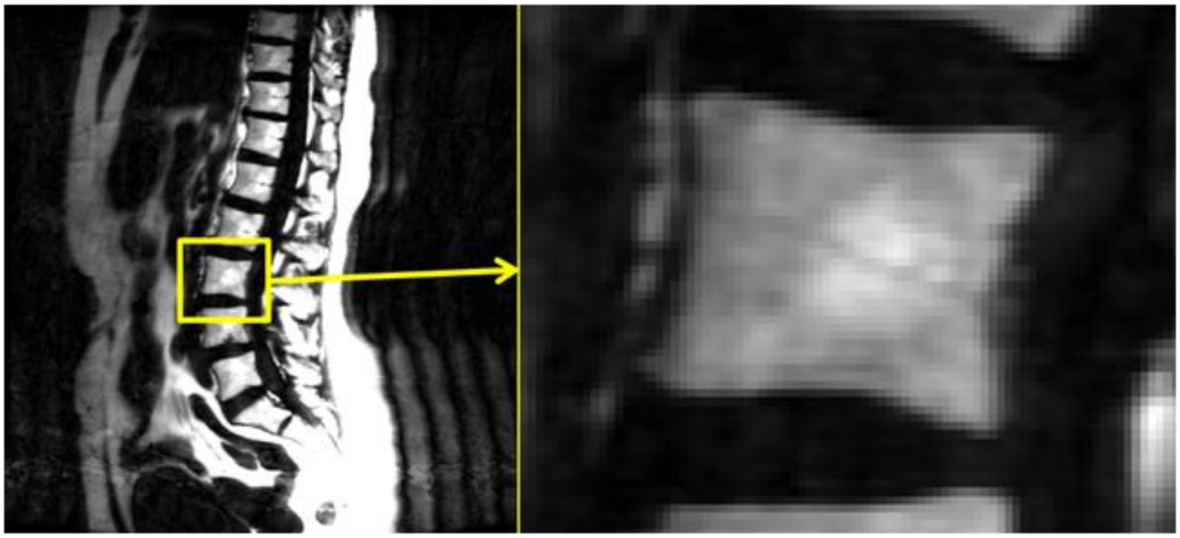

Figure 7-18 The method of segmenting an individual vertebra. The example illustrates the cropped region (left) drawn for the segmentation of L3 vertebra and the display (right) of the cropped region.

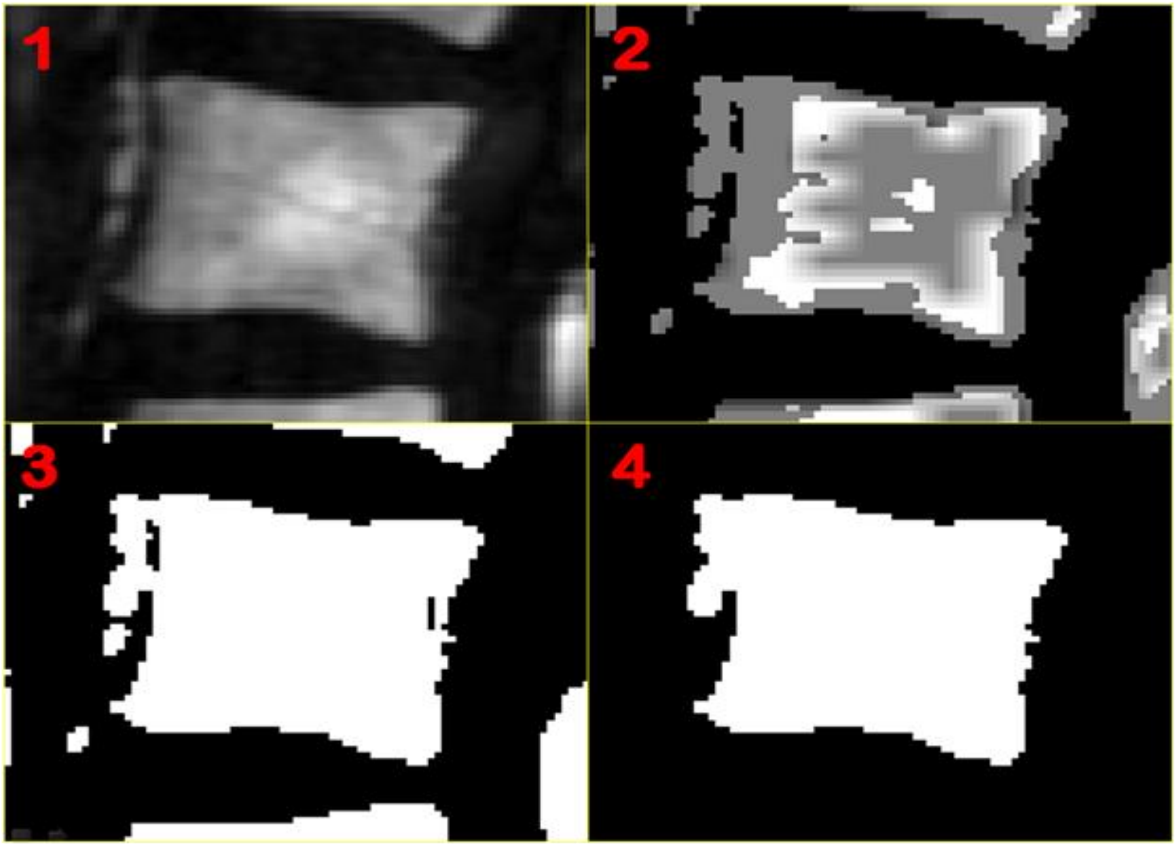

Figure 7-19 The method of processing the cropped image (1) from applying histogram equalisation (2) to converting the histogram equalised image to a binary image using Otsu method (3) and filling holes in the binary image (4).

The dimension of the cropped matrix was converted back to the original image matrix by padding elements to match exactly with the original image matrix size and exact coordinates in relation to x and y. The padded image was multiplied with FF image to convert the binary pixels of the vertebrae to its original FF gray value pixels (see Figure 7-20 (2)). The conversion is similar to method described in previous section (see 7.1.1). The resultant image may contain unwanted tissues around the desired vertebrae, which was manually edited and colour mapped. The resultant colour mapped FF image (see Figure 7-20 (3)) was free from unwanted tissues and contained only the vertebra of interest. The pixel value from the resultant image was used for the measurement of an average FF from the individual vertebra.

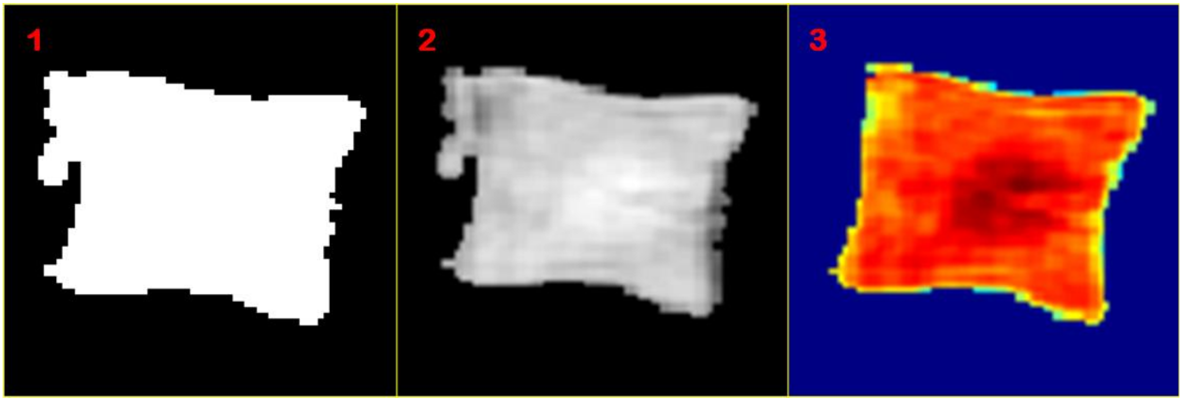

Figure 7-20 The method of converting the matrix of the cropped binary image (1) to the matrix of the original image. The padded segmented image was overlaid onto a FF image (2) and was edited further to remove unwanted tissues to be displayed as a colour map image (3).

8 Results

8.1 Introduction

The results in this thesis are from the volunteers who were involved in the high bone mass (HBM) study. Magnetic resonance imaging and spectroscopy (MRI & MRS) data were acquired from 52 female individuals who were previously scanned using peripheral quantitative computed-tomography (pQCT) and dual-energy X-ray absorptiometry (DEXA). The primary aim of this thesis was to identify whether MR measurements from bones can provide quantitative information that is similar to other gold standard quantitative techniques and also to identify if it can provide additional information that is not achieved by other techniques. The secondary aim was to identify whether MR measurements are able to differentiate population groups based on their bone physiology. The results from DEXA, pQCT and MR were analysed to identify associations and differences, by using statistical tools from SPSS 15.0 (IBM Corporation, New York, USA) and Microsoft Office Excel 2007 (Microsoft Corporation, Washington, USA) for performing Pearson linear correlations, t-test and confidence interval of slopes [234-236]. The list of measurements that were acquired from each imaging modalities with respect to anatomical location are illustrated in Table 8:1.

The results in this chapter are described as two sections: (1) the MR data were compared with other X-ray quantitative techniques at multiple skeletal sites to identify associations and differences between the modalities, (2) the MR data from the individual populations were compared with potential covariates like age and body mass index (BMI) to identify associations and differences between the populations.

Modality	Anatomical Site	Measurement
DEXA	From First to Fourth Lumbar Vertebrae	➢ Mean areal bone mineral content (BMC) from L1-L4 ➢ Mean T-score from L1-L4 ➢ Mean Z-score from L1-L4
pQCT	4% Along the Length of the Distal Radius	➢ Volumetric BMD ➢ Bone Area
	4% Along the Length of the Distal Tibia	➢ Volumetric BMD ➢ Bone Area
MRI	4% Along the Length of the Distal Radius	➢ Bone volume fraction (BVF) ➢ Trabecular Area ➢ Entropy ➢ Textural Analysis (TA) Contrast ➢ TA Correlation ➢ TA Energy ➢ TA Homogeneity
	4% Along the Length of the Distal Tibia	➢ BVF ➢ Trabecular Area ➢ Entropy ➢ TA Contrast ➢ TA Correlation ➢ TA Energy ➢ TA Homogeneity
	From Lumbar Vertebrae using IDEAL	➢ Mean fat-fraction (FF) from L1, L3 & L5
MRS	From First, Third and Fifth Lumbar Vertebrae	➢ Mean FF from L1, L3 & L5 ➢ Mean unsaturation index (UI) from L1, L3 & L5 ➢ Mean full width at half maximum (FWHM) of water peak (4.7 ppm) from L1, L3 & L5 ➢ Mean FWHM of lipid peak (1.3 ppm) from L1, L3 & L5
General	Whole-body	➢ Age ➢ Body mass index (BMI)

Table 8:1 The list of imaging modalities and their corresponding measurements in relation to each anatomical site.

At distal radius and tibia the MR and pQCT data were acquired at 4% region of the distal bone. The MR data were processed for the measurement of bone volume fraction (BVF), trabecular bone area, entropy and four textural analysis (TA) properties of contrast, correlation, energy and homogeneity. The pQCT data were processed for the measurement of volumetric bone mineral density (BMD) and bone area.

The data from lumbar vertebrae were acquired using DEXA and MR techniques. The data from MR were compared with DEXA data and also with the physical parameters of age and BMI. The DEXA data from the lumbar vertebrae were acquired from the first to fourth lumbar vertebrae (L1-L4), which provided areal results of Z-score, T-score and bone mineral content (BMC) from each vertebra. The DEXA measurements from all four vertebrae were averaged (mean) to produce an effective single measurement representative of the whole lumbar vertebrae.

The MR data were acquired from first, third and fifth lumbar vertebra (L1, L3 and L5) using both IDEAL imaging and MRS. The IDEAL imaging resulted in measurement of FF from each vertebra. MRS resulted in measurement of FF, unsaturation index (UI), and water/lipid full width at half maximum (FWHM) from each vertebra. The data from MRS for the measurement of FF and UI were processed using the linear combination model (LCM) and the FWHM were measured using the SAGE tool described previously in Chapter 3. A mean increase of 1% FF was observed from L1, L3 and L5 in general, which suggested an increased FF in lower lumbar vertebrae when compared with upper lumbar vertebrae. The measurements from each vertebra using IDEAL and MRS were averaged (mean) to produce an effective single measurement representative of the whole lumbar vertebrae.

All the volunteers in this thesis were selected from the HBM study, and were either the index, spouse or relative populations. The individual populations were further classified into HBM, borderline HBM and controls by using their DEXA Z-scores from the first lumbar vertebra (L1) and the hip region. The criteria for the classification were set by the primary investigators of the HBM study, which has been followed in this thesis. The classification criteria are different for each type of population. The HBM categorisation criteria for index and spouses were either: (i) a L1 Z-score greater than or equal 3.2 in addition to a hip Z-score greater than or equal to 1.2, or (ii) a hip Z-score greater than or equal to 3.2 in addition to L1 Z-score greater than or equal to 1.2. For relatives the criteria for HBM categorisation was based on them having a sum of L1 and hip Z-scores to be greater than or equal to 3.2. The criteria for the borderline HBM categorisation for only the index population was based on them having their L1 or hip Z-score to be between 3.0 and 3.2. The categorisation of controls was applied to all the relatives who did not fulfil the criteria for HBM and borderline HBM [36]. The combined criteria for the classification of all the volunteers are illustrated in Figure 8-1.

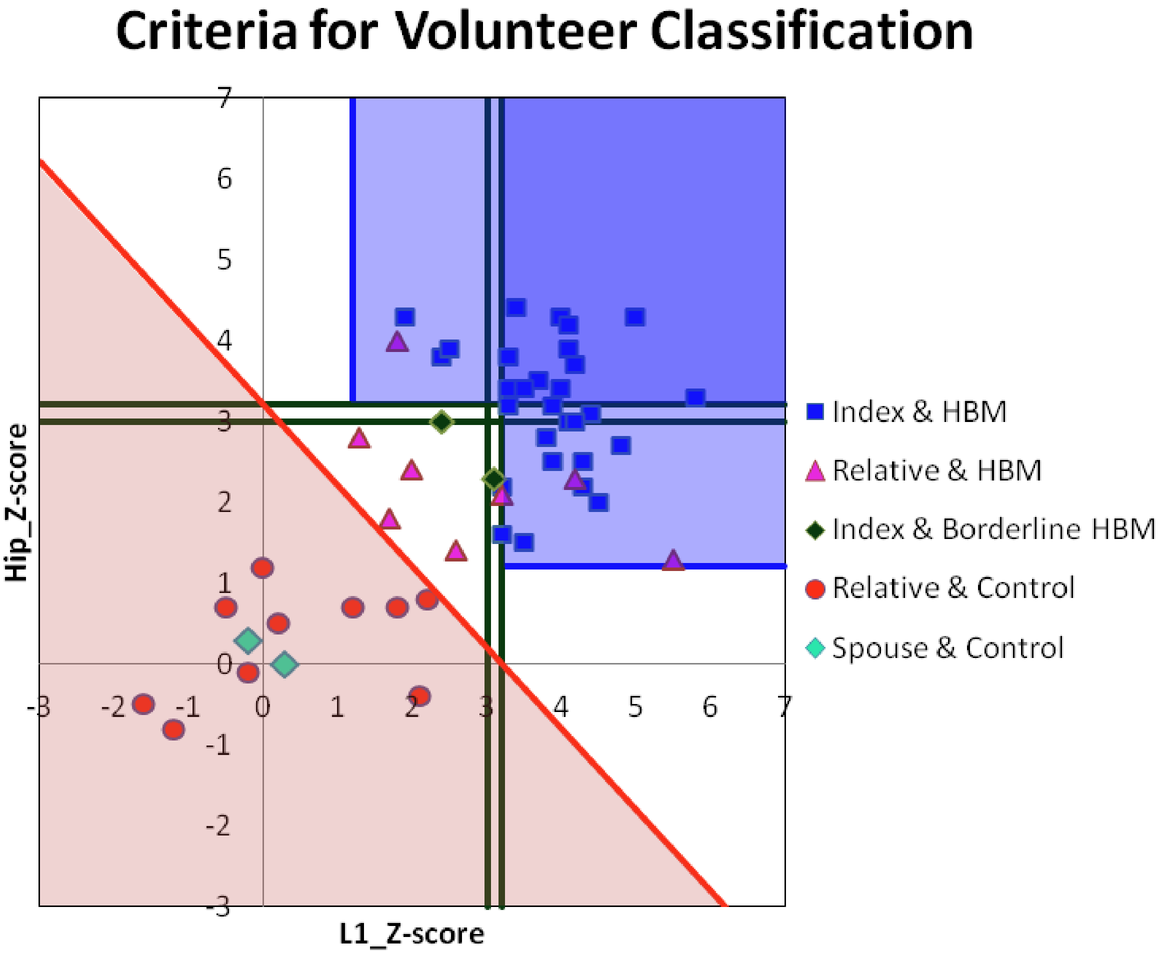

Figure 8-1 The scatter plot of the hip and L1 Z-scores of all the volunteers who underwent MR examination with regions based on the individual criteria. The blue region is the criteria for HBM categorisation for all the index and spouses. The region between the green lines is the criteria for borderline HBM categorisation for the index population. The region above the red line is the criteria for HBM categorisation for all the relatives. The red region is the criteria of controls for all the relatives.

The 52 female individuals who underwent MR data acquisition were categorised based on the described classification criteria (see Table 8:2 and Table 8:3). A total of 38 individuals were classified as HBM, two individuals were classified as borderline HBM and the remaining 12 individuals were classified as controls. The two borderline HBM individuals were excluded from analysis due to their much smaller population size, thus the results from the remaining 50 individuals were used for statistical analysis.

Volunteers	HBM	Borderline HBM	Controls	Total
Index	30	2	0	32
Relatives	8	0	10	18
Spouses	0	0	2	2
Total	38	2	12	52

Table 8:2 Details of the volunteers who underwent MR data acquisition. The volunteers are described with their individual populations and their subsequent categorisation.

8.1.1 Missing Data

At distal radius two HBM classified volunteers did not have pQCT measurements due to non availability of the equipment and due to gross motion artefact. Thus the pQCT measurements from distal radius contained 36 individuals from the HBM and 12 individuals from the control population for statistical analysis (see Table 8:3).

The quantitative measurements from MRI at distal radius were dependent on the functionality of the processing software and the signal uniformity in the image. The images from distal radius for some volunteers were affected with unsuccessful processing (as detailed in section 7.1.3), which resulted in exclusion of BVF and TA measurements for them during statistical analysis. A total of 12 BVF measurements were excluded, out of which nine were from the HBM and three were from the control population. Thus from the 50 BVF measurements at distal radius, there were 29 individuals from the HBM and 9 individuals from the control population available for analysis (see Table 8:3). A total of two TA measurements from the HBM population were also excluded. Thus from the total of 50 TA measurements, there were 36 individuals from the HBM population and 12 individuals from the control population available for analysis (see Table 8:3).

At distal tibia one HBM classified volunteer did not have pQCT measurements due to non availability of the equipment. Thus the pQCT measurements from distal tibia contained 37 individuals from the HBM and 12 individuals from the control population for statistical analysis (see Table 8:3). The BVF and TA measurements from distal tibia were processed from all the 50 individuals in the HBM study.

A total of two HBM classified volunteers did not have DEXA data during the study (2008-2010) from lumbar vertebrae as well as the BMI data. An additional HBM classified volunteer did not have MR measurements from lumbar vertebrae due to her refusal for lumbar spine examination.

Index	Sex	Age	BMI	Relationship	Classification	Missing Data
1	**Female**	**64**	**26.57**	**Index**	**HBM**	
2	**Female**	**68**	**27.69**	**Index**	**HBM**	**No BVF and Texture at Radius**
3	**Female**	**57**	**30.26**	**Index**	**HBM**	
4	**Female**	**59**	**26.49**	**Index**	**HBM**	
5	**Female**	**27**	**-**	**Index**	**HBM**	**No DEXA**
6	**Female**	**82**	**29.49**	**Index**	**HBM**	
7	**Female**	**38**	**27.29**	**Index**	**HBM**	**No BVF at Radius**
8	**Female**	**66**	**25.08**	**Index**	**HBM**	
9	**Female**	**74**	**34.25**	**Index**	**HBM**	
10	**Female**	**71**	**-**	**Index**	**HBM**	**No DEXA and No BVF & Texture at Radius**
11	**Female**	**66**	**26.93**	**Index**	**HBM**	**No BVF at Radius**
12	**Female**	**58**	**39.16**	**Index**	**HBM**	**No BVF at Radius**
13	**Female**	**61**	**25.46**	**Index**	**HBM**	**No BVF at Radius**
14	**Female**	**55**	**36.65**	**Index**	**HBM**	
15	**Female**	**49**	**35.88**	**Index**	**HBM**	**No BVF at Radius**
16	**Female**	**60**	**36.58**	**Index**	**HBM**	
17	**Female**	**64**	**23.12**	**Index**	**HBM**	
18	**Female**	**71**	**37.11**	**Index**	**HBM**	**No BVF at Radius**
19	**Female**	**79**	**27.19**	**Index**	**HBM**	**No pQCT at Radius and Tibia**
20	**Female**	**62**	**24.32**	**Index**	**HBM**	
21	**Female**	**72**	**32.44**	**Index**	**HBM**	
22	**Female**	**61**	**35.35**	**Index**	**HBM**	**No BVF at Radius**
23	**Female**	**56**	**34.37**	**Index**	**HBM**	**No pQCT at Radius**
24	**Female**	**74**	**26.17**	**Index**	**HBM**	
25	**Female**	**55**	**28.08**	**Index**	**HBM**	
26	**Female**	**44**	**39.11**	**Index**	**HBM**	
27	**Female**	**65**	**25.08**	**Index**	**HBM**	
28	**Female**	**44**	**22.98**	**Index**	**HBM**	
29	**Female**	**64**	**35.03**	**Index**	**HBM**	
30	**Female**	**52**	**31.20**	**Index**	**HBM**	
31	**Female**	**62**	**33.97**	**Index**	**Borderline HBM**	**Excluded from statistics**
32	**Female**	**61**	**23.76**	**Index**	**Borderline HBM**	**Excluded from statistics**
33	**Female**	**26**	**25.35**	**Relative**	**HBM**	
34	**Female**	**72**	**26.84**	**Relative**	**HBM**	
35	**Female**	**68**	**30.32**	**Relative**	**HBM**	
36	**Female**	**43**	**28.65**	**Relative**	**HBM**	
37	**Female**	**68**	**28.90**	**Relative**	**HBM**	
38	**Female**	**60**	**21.93**	**Relative**	**HBM**	
39	**Female**	**59**	**33.61**	**Relative**	**HBM**	
40	**Female**	**42**	**24.51**	**Relative**	**HBM**	
41	**Female**	**61**	**25.20**	**Relative**	**Control**	
42	**Female**	**70**	**43.81**	**Relative**	**Control**	**No BVF at Radius**
43	**Female**	**41**	**30.33**	**Relative**	**Control**	
44	**Female**	**48**	**23.44**	**Relative**	**Control**	
45	**Female**	**44**	**25.85**	**Relative**	**Control**	
46	**Female**	**42**	**25.25**	**Relative**	**Control**	
47	**Female**	**39**	**31.52**	**Relative**	**Control**	
48	**Female**	**55**	**31.23**	**Relative**	**Control**	
49	**Female**	**80**	**29.10**	**Relative**	**Control**	**No BVF at Radius**
50	**Female**	**43**	**26.56**	**Relative**	**Control**	
51	**Female**	**59**	**23.09**	**Spouse**	**Control**	**No BVF at Radius**
52	**Female**	**49**	**26.27**	**Spouse**	**Control**	

Table 8:3 The list of volunteers who underwent MR examination with details of their clinical features.

8.2 Magnetic Resonance versus X-ray Techniques

The aim in this section is to identify associations and differences between MR and quantitative X-ray techniques by using the Pearson linear correlation. The measurements from MR, pQCT and DEXA were compared with each other at multiple skeletal sites for all the volunteers.

8.2.1 Volumetric BMD versus BVF

The BVF measurement from MRI quantifies the density of the trabecular bone network and the volumetric BMD from pQCT measures the density of matter present inside the region of interest (ROI) in the trabecular bone region. The hypothesis in this section was that these two density measurements from the bones provide similar information, thus the aim was to observe good correlation between the two measurements at both distal radius and tibia.

Results demonstrated significant positive correlation (see Figure 8-2 & Figure 8-3) between volumetric BMD and BVF at both radius ($R^2 = 0.563$, $p < 0.001$) and tibia ($R^2 = 0.670$, $p < 0.001$). In conclusion the results demonstrated that volumetric density measurement from pQCT correlate well with structural measurement from MRI at both radius and tibia, indicating that both the modalities are quantifying similar properties of the bone.

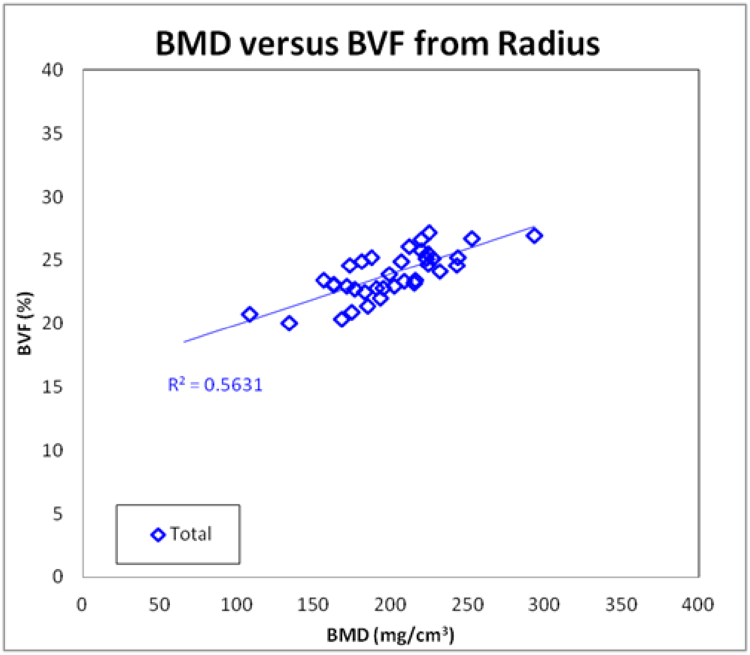

Figure 8-2 The scatter plot for correlation between volumetric BMD and BVF at distal radius. Note the significant correlation between the two measurements.

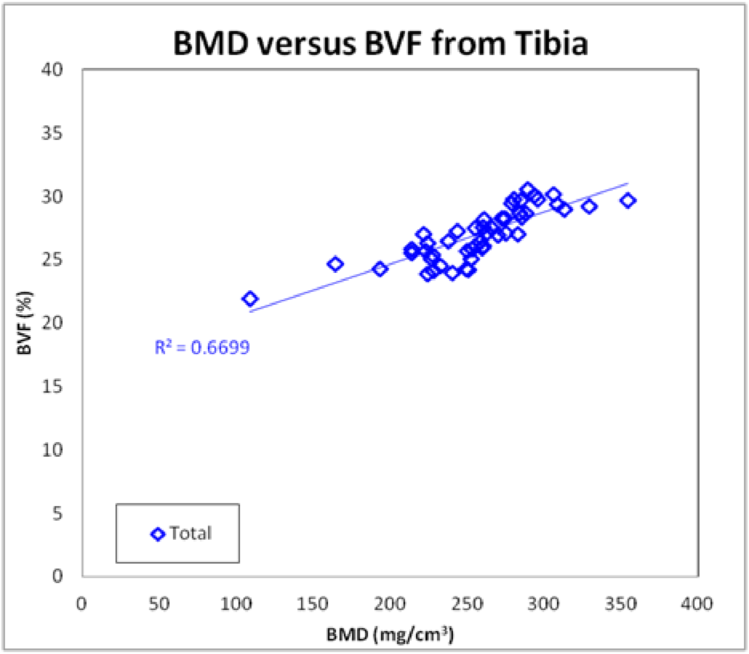

Figure 8-3 The scatter plot for correlation between volumetric BMD and BVF at distal tibia. Note the significant correlation between the two measurements.

8.2.2 Bone Area versus Trabecular Area

The bone area from pQCT measures the total area of the bone including the cortex and the trabecular bone component, and the trabecular area from MRI measures only the area of the trabecular bone component. The pQCT data were acquired in low resolution and thus they were not able to effectively differentiate between cortical and trabecular bone regions, hence the total bone area from pQCT data were used. T_1-weighted images were used for MR data acquisition from distal radius and tibia in this thesis, and they were not able to effectively segment the cortical bone component, and thus only the trabecular bone component was evaluated. The acquisition of IDEAL images in future could possibly be used for the segmentation of both cortical and trabecular bone. The hypothesis in this section was that the dimensional properties of the bone measured using pQCT and MRI would be very similar, thus the aim was to observe good correlation between the two measurements at both distal radius and tibia.

Results demonstrated significant positive correlation (see Figure 8-4 & Figure 8-5) between bone area and trabecular area at both radius ($R^2 = 0.758$, $p < 0.001$) and tibia ($R^2 = 0.733$, $p < 0.001$). In conclusion the results demonstrated that bone area measurement from pQCT correlates well with trabecular area measurement from MRI at both radius and tibia, indicating that both the modalities are able to quantify the dimensions of the bone and are very similar.

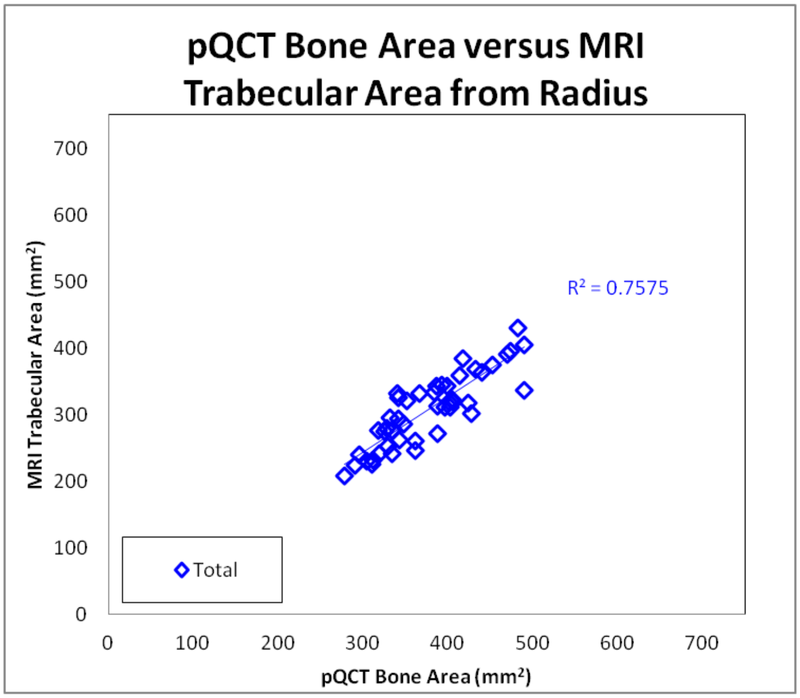

Figure 8-4 The scatter plot for correlation between pQCT bone area and MRI trabecular area at distal radius. Note the significant correlation between the two measurements.

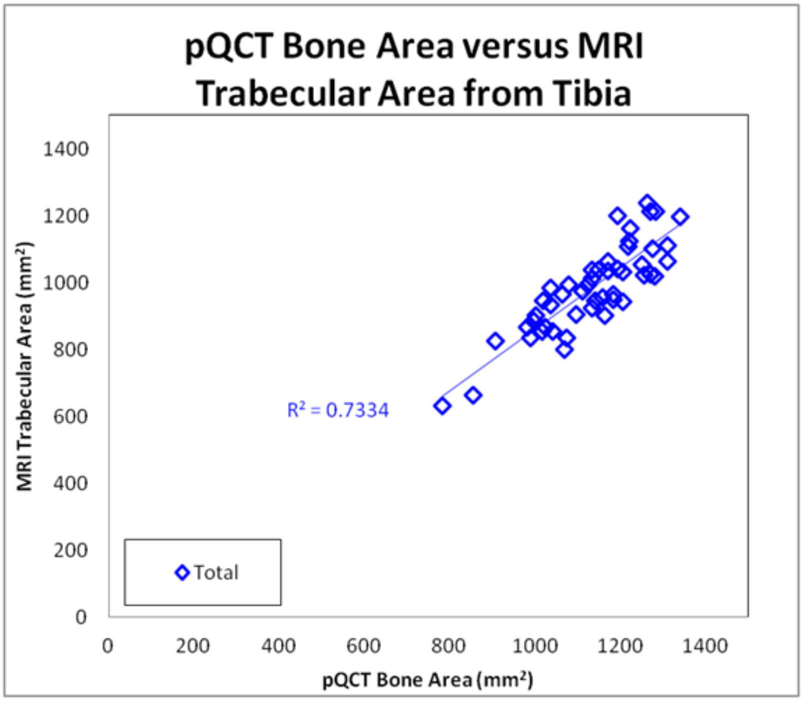

Figure 8-5 The scatter plot for correlation between pQCT bone area and MRI trabecular area at distal tibia. Note the significant correlation between the two measurements.

8.2.3 Volumetric BMD versus Entropy

The statistical test between volumetric BMD and Entropy demonstrated (see Figure 8-6 & Figure 8-7) no significant correlation for radius ($R^2 = 0.070$, $p = 0.075$), but mild positive correlation was observed for tibia ($R^2 = 0.106$, $p = 0.023$). In conclusion the results demonstrated poor to mild correlation between volumetric BMD and Entropy at distal radius and tibia, indicating a weak relationship between the two techniques.

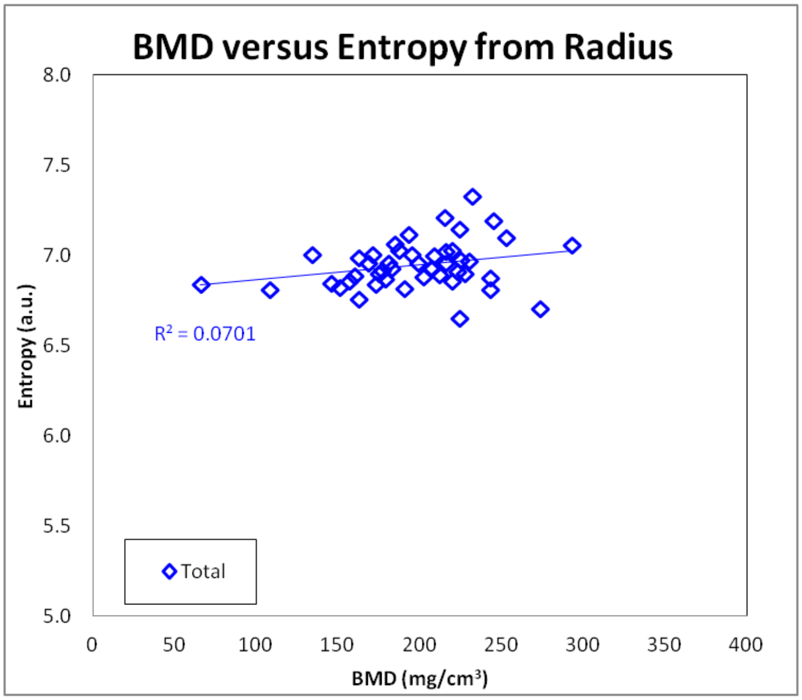

Figure 8-6 The scatter plot for correlation between pQCT BMD and MRI Entropy at distal radius. Note the poor correlation between the two measurements.

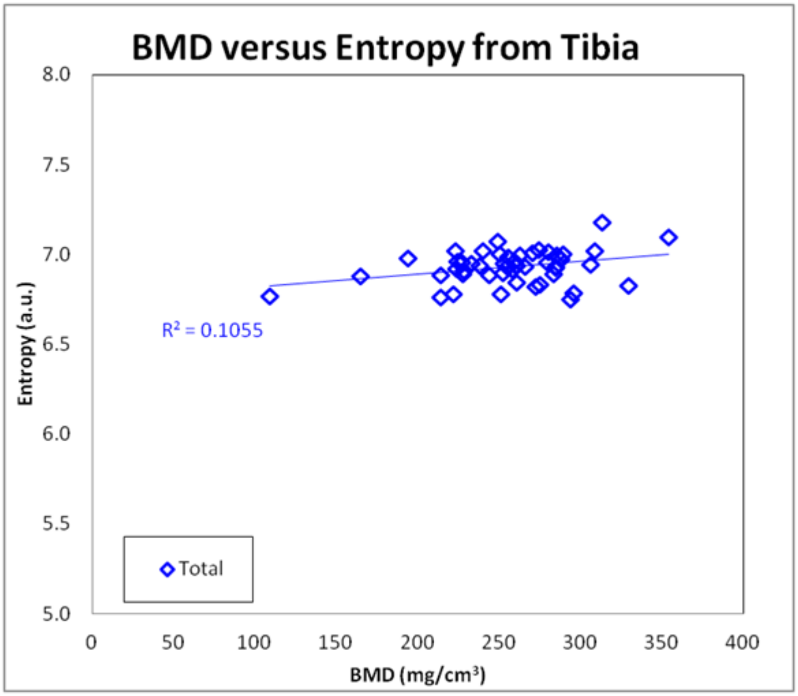

Figure 8-7 The scatter plot for correlation between pQCT BMD and MRI Entropy at distal tibia. Note the mild correlation between the two measurements.

8.2.4 Volumetric BMD versus Textural Analysis

The MRI data from trabecular bone region were processed to measure four textural properties that quantify the different types of pixel intensity variations in the trabecular bone, which is an indirect method of observing the structural properties of the bone. The hypothesis in this section was that the TA measurements from the bone would be related to volumetric density measurements from pQCT, since both are measuring the structural information of the bone. The aim of this section was to investigate which TA property, if any correlates with pQCT at distal radius and tibia. pQCT data were not included for TA measurements since the pQCT images were acquired in very low resolution and were not able to differentiate the trabecular network within the bone.

8.2.4.1 Volumetric BMD versus TA Contrast

The statistical test between volumetric BMD and TA Contrast demonstrated (see Figure 8-8 & Figure 8-9) significant positive correlation for radius ($R^2 = 0.313$, $p < 0.001$) and tibia ($R^2 = 0.205$, $p = 0.001$). In conclusion the results demonstrated moderate correlation between volumetric BMD and TA Contrast at distal radius and tibia, indicating that the TA Contrast which measures the local variation of pixel intensity in the image is providing structural information that matches moderately with the volumetric BMD.

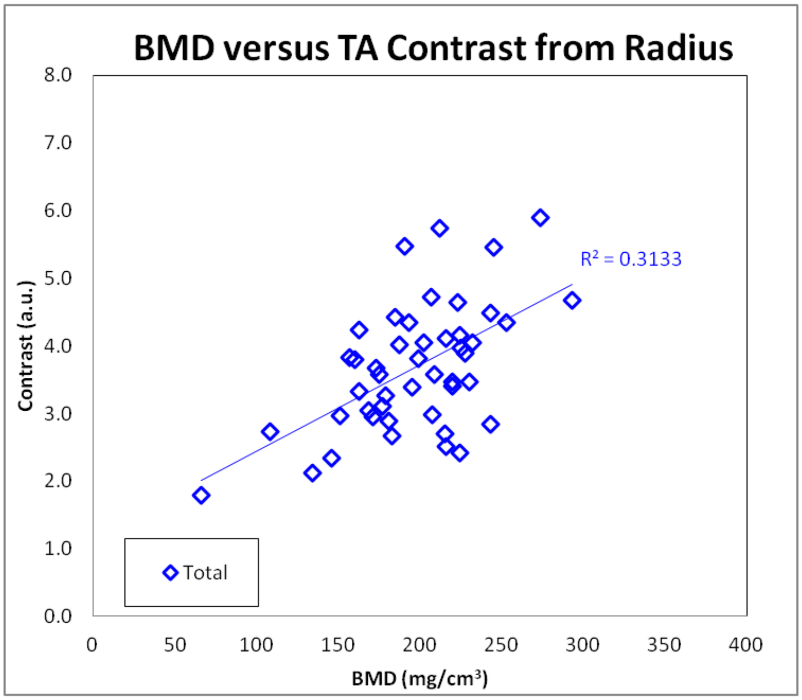

Figure 8-8 The scatter plot for correlation between pQCT volumetric BMD and MRI TA Contrast at distal radius. Note the good correlation between the two measurements.

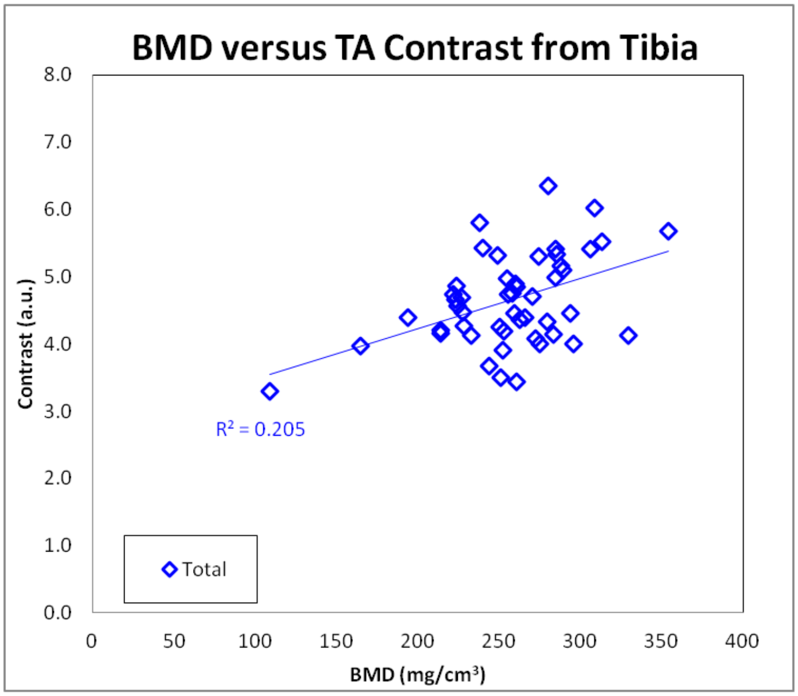

Figure 8-9 The scatter plot for correlation between pQCT volumetric BMD and MRI TA Contrast at distal tibia. Note the good correlation between the two measurements.

8.2.4.2 Volumetric BMD versus TA Correlation

The statistical test between volumetric BMD and TA Correlation demonstrated (see Figure 8-10 & Figure 8-11) significant negative correlation for radius (R^2 = 0.245, $p <$ 0.001) and tibia (R^2 = 0.357, $p < 0.001$). In conclusion the results demonstrated good correlation between volumetric BMD and TA Correlation at distal radius and tibia, indicating that the TA Correlation which measures the local linearity of pixel intensity in the image is providing structural information that matches well with the volumetric BMD.

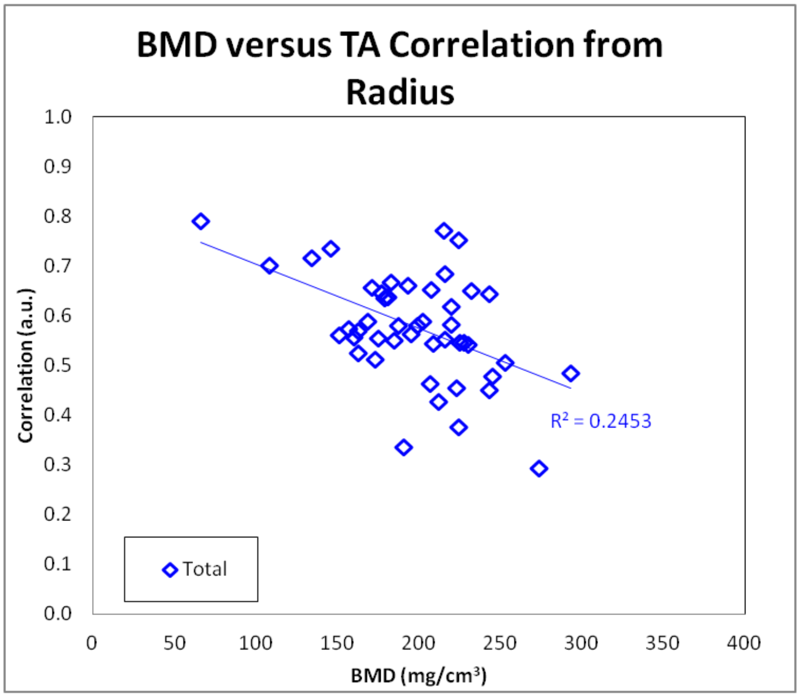

Figure 8-10 The scatter plot for correlation between pQCT volumetric BMD and MRI TA Correlation at distal radius. Note the good correlation between the two measurements.

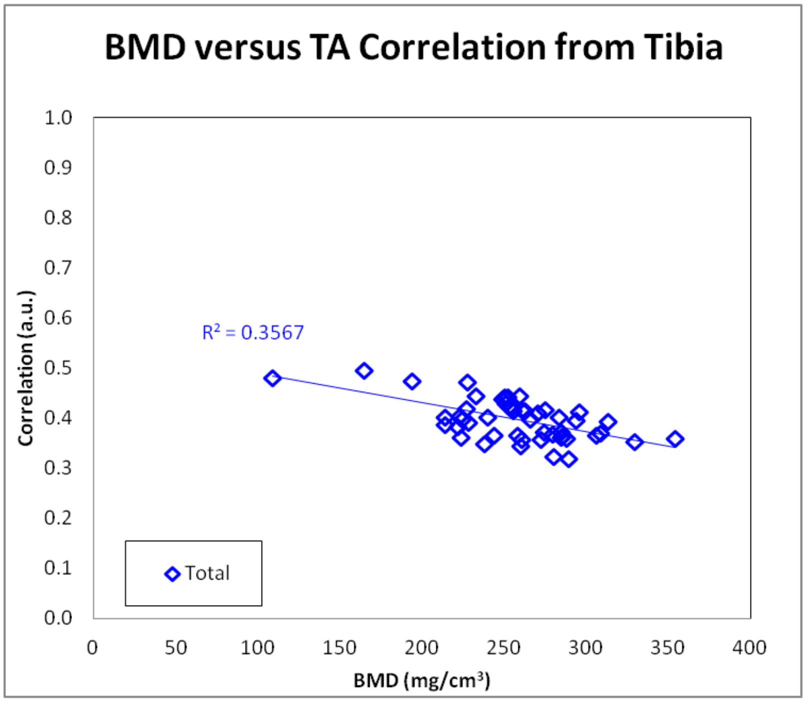

Figure 8-11 The scatter plot for correlation between pQCT volumetric BMD and MRI TA Correlation at distal tibia. Note the good correlation between the two measurements.

8.2.4.3 Volumetric BMD versus TA Energy

The statistical test between volumetric BMD and TA Energy demonstrated (see Figure 8-12 & Figure 8-13) good to mild negative correlation for radius ($R^2 = 0.398$, $p < 0.001$) and tibia ($R^2 = 0.111$, $p = 0.019$). In conclusion the results demonstrated good correlation between volumetric BMD and TA Energy at distal radius and tibia, indicating that the TA Energy which measures the sum of squared elements in the processed matrix is providing structural information that matches well with the volumetric BMD.

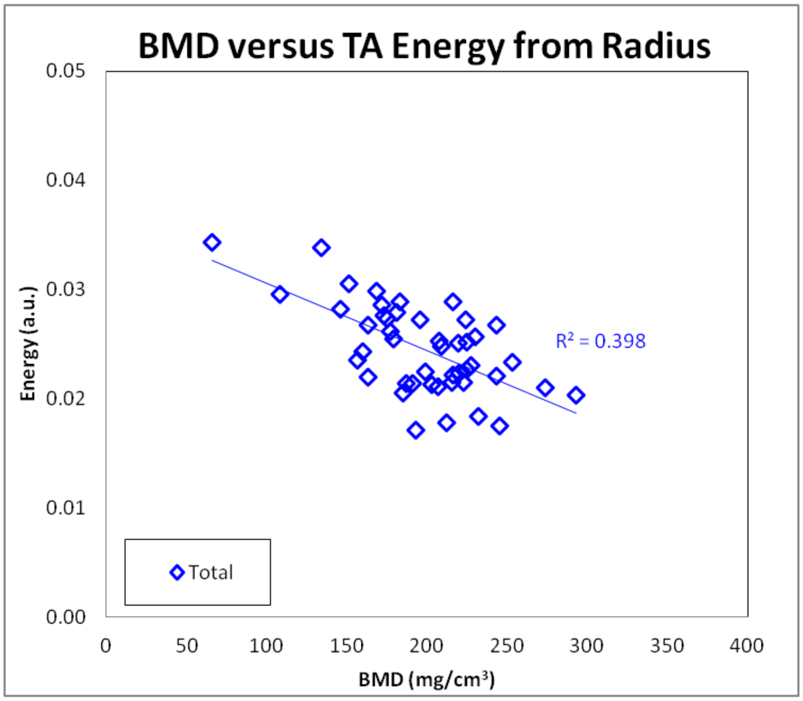

Figure 8-12 The scatter plot for correlation between pQCT volumetric BMD and MRI TA Energy at distal radius. Note the good correlation between the two measurements.

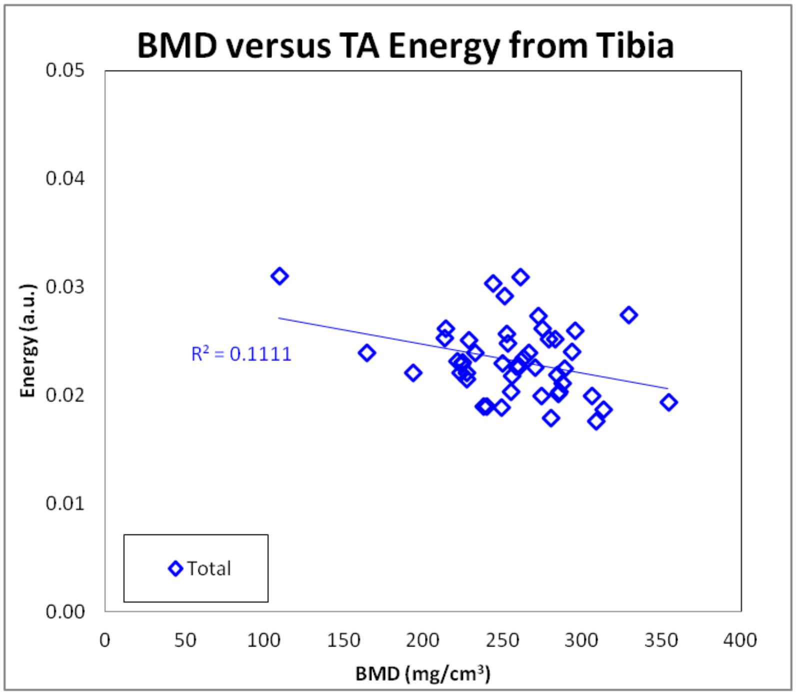

Figure 8-13 The scatter plot for correlation between pQCT volumetric BMD and MRI TA Energy at distal tibia. Note the mild correlation between the two measurements.

8.2.4.4 Volumetric BMD versus TA Homogeneity

The statistical test between volumetric BMD and TA Homogeneity demonstrated (see Figure 8-14 & Figure 8-15) good negative correlation for radius (R^2 = 0.447, $p < 0.001$) and tibia (R^2 = 0.223, $p < 0.001$). In conclusion the results demonstrated good correlation between volumetric BMD and TA Homogeneity at distal radius and tibia, indicating that the TA Homogeneity which measures the closeness of distribution of elements in the processed matrix is providing structural information that matches well with the volumetric BMD.

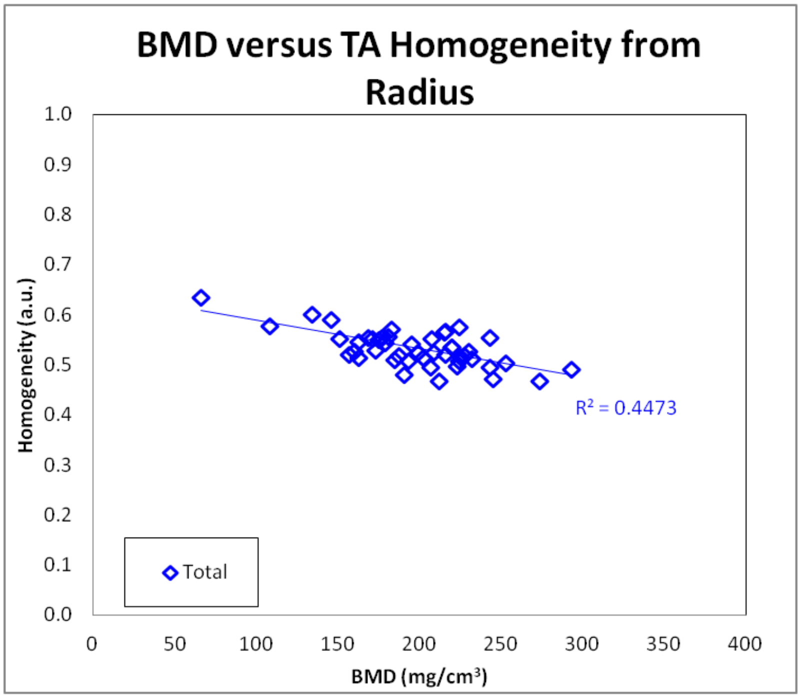

Figure 8-14 The scatter plot for correlation between pQCT volumetric BMD and MRI TA Homogeneity at distal radius. Note the good correlation between the two measurements.

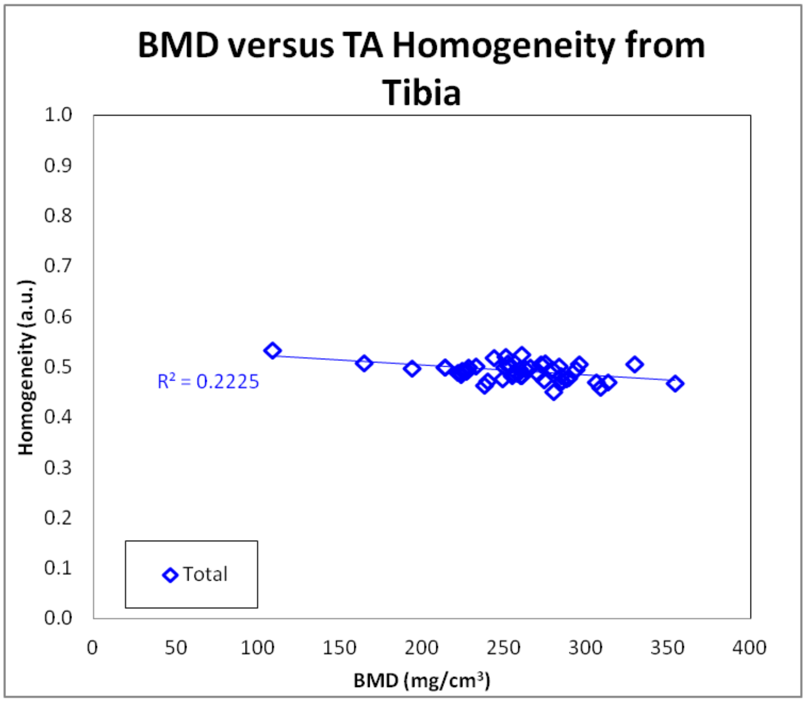

Figure 8-15 The scatter plot for correlation between pQCT volumetric BMD and MRI TA Homogeneity at distal tibia. Note the good correlation between the two measurements.

8.2.5 DEXA versus Water and Lipid FWHM from MRS

The four DEXA measurements from lumbar vertebrae measure the areal density of the vertebrae (see Table 8:1). The FWHM of spectroscopy peaks (water and lipid) from lumbar vertebrae is related to the T_2* which is influenced by the magnetic susceptibility effect of the bones and marrow, and believed to be the surrogate marker of the density of the trabecular bone and marrow. The hypothesis in this section was that the FWHM of water and lipid peaks from the bone would be related to density measurements from DEXA, since both are measuring the structural information of the bone, thus the aim was to observe good correlation between DEXA and FWHM.

8.2.5.1 Z-score versus Water and Lipid FWHM from MRS

The statistical test between Z-score and water FWHM at lumbar vertebrae demonstrated (see Figure 8-16) moderate positive correlation (R^2 = 0.168, p = 0.004), indicating that the water FWHM which measures the density of the trabecular bone is providing density information that matches well with the Z-score.

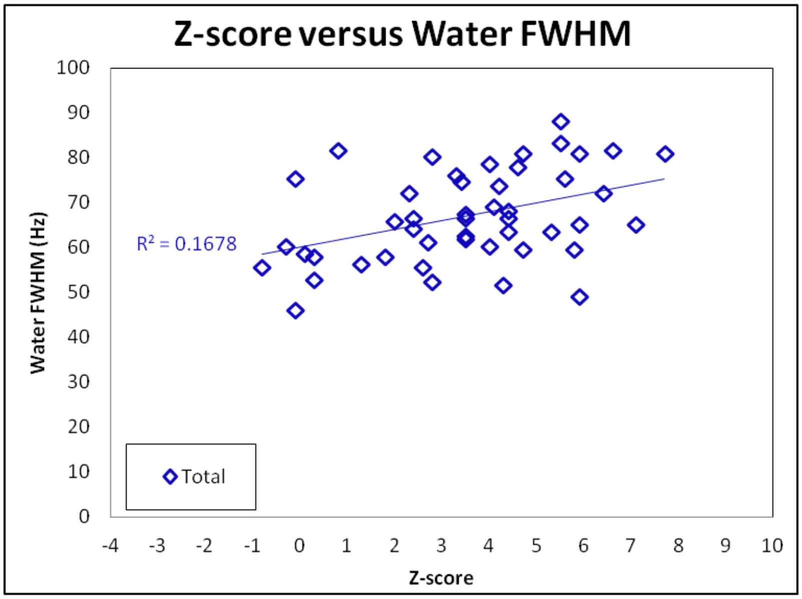

Figure 8-16 The scatter plot for correlation between Z-score and water FWHM at lumbar vertebrae. Note the moderate correlation between the two measurements.

The statistical test between Z-score and lipid FWHM at lumbar vertebrae demonstrated (see Figure 8-17) good positive correlation ($R^2 = 0.234$, $p < 0.001$), indicating that the lipid FWHM which measures the density of the trabecular bone marrow is related to the Z-score of the vertebra.

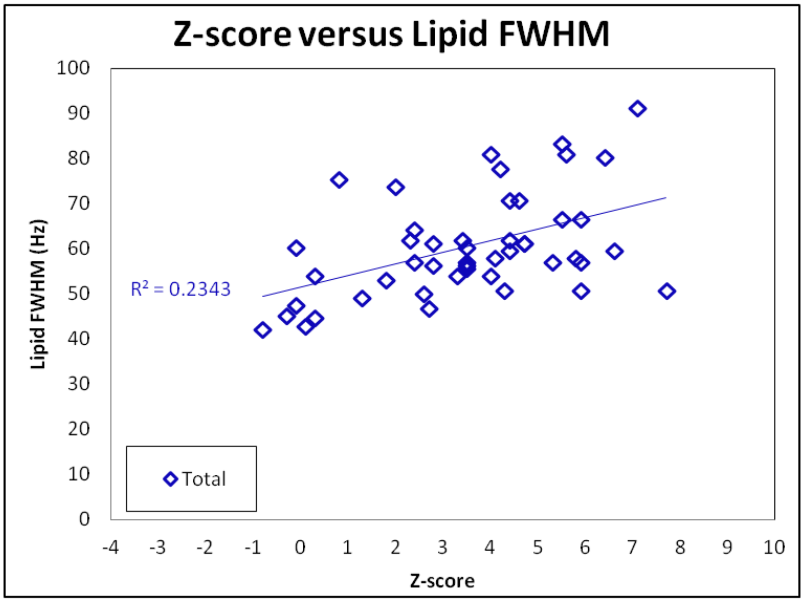

Figure 8-17 The scatter plot for correlation between Z-score and lipid FWHM at lumbar vertebrae. Note the good correlation between the two measurements.

8.2.5.2 T-score versus Water and Lipid FWHM from MRS

The statistical test between T-score and water FWHM at lumbar vertebrae demonstrated (see Figure 8-18) moderate positive correlation (R^2 = 0.144, p = 0.008), indicating that the water FWHM which measures the density of the trabecular bone is providing density information that matches well with the T-score.

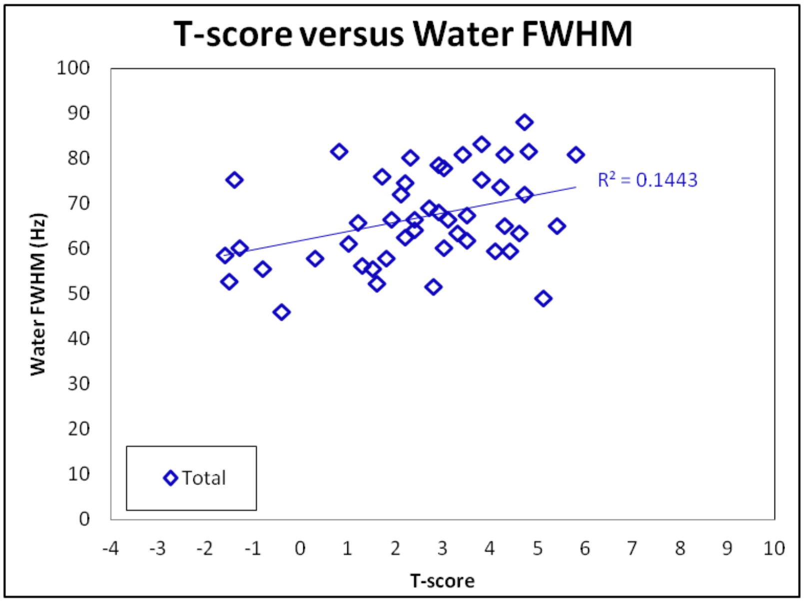

Figure 8-18 The scatter plot for correlation between T-score and water FWHM at lumbar vertebrae. Note the moderate correlation between the two measurements.

The statistical test between T-score and lipid FWHM at lumbar vertebrae demonstrated (see Figure 8-19) good positive correlation ($R^2 = 0.268$, $p < 0.001$), indicating that the lipid FWHM which measures the density of the trabecular bone marrow is related to the T-score of the vertebra.

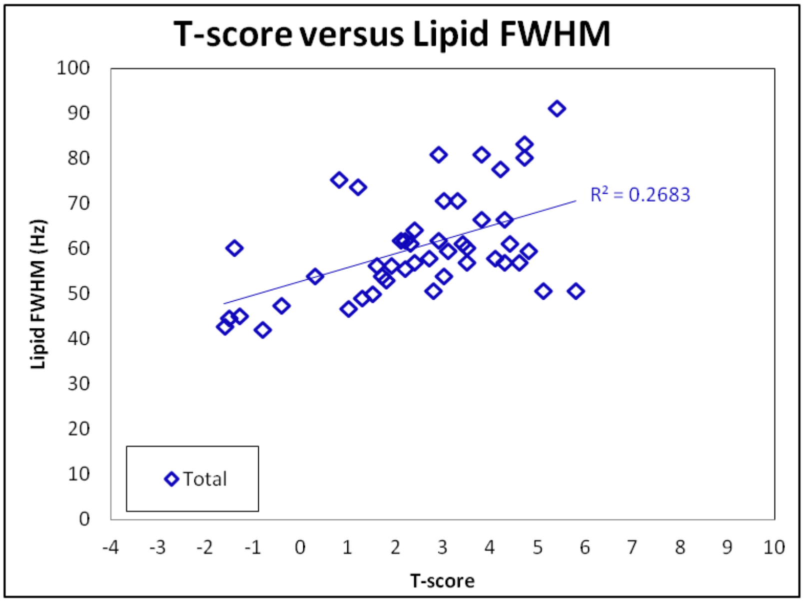

Figure 8-19 The scatter plot for correlation between T-score and lipid FWHM at lumbar vertebrae. Note the good correlation between the two measurements.

8.2.5.3 Areal BMC versus Water and Lipid FWHM from MRS

The statistical test between areal BMC and water FWHM at lumbar vertebrae demonstrated (see Figure 8-20) no significant correlation ($R^2 = 0.027$, $p = 0.269$), indicating that the water FWHM which measures the density of the trabecular bone is not directly related to the areal BMC of the vertebra.

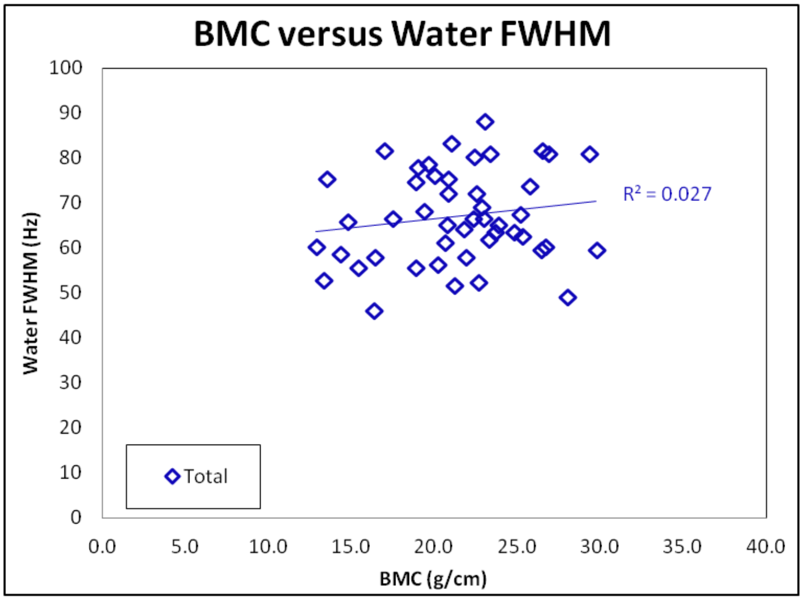

Figure 8-20 The scatter plot for correlation between areal BMC and water FWHM at lumbar vertebrae. Note the poor correlation between the two measurements.

The statistical test between areal BMC and lipid FWHM at lumbar vertebrae demonstrated (see Figure 8-21) no significant correlation (R^2 = 0.035, p = 0.206), indicating that the lipid FWHM which measures the density of the trabecular bone marrow is not related to the direct areal BMC measurement of the vertebra.

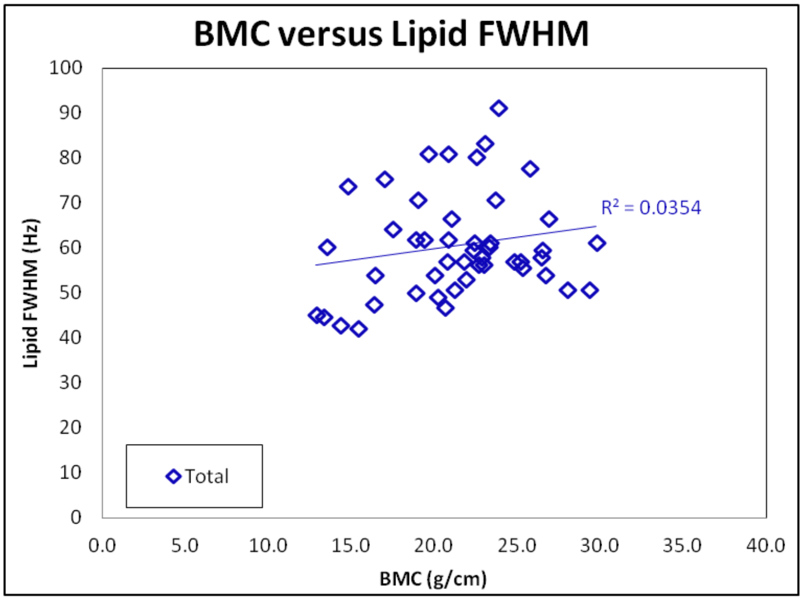

Figure 8-21 The scatter plot for correlation between areal BMC and lipid FWHM at lumbar vertebrae. Note the poor correlation between the two measurements.

8.2.6 DEXA versus Unsaturation Index from MRS

The unsaturation index (UI) measures the amount of unsaturated fatty acid present in the bone marrow which is known to decrease with patients who suffer from conditions like osteoporosis, as well as with low bone density and age. Thus it was believed that the UI would decrease with low bone density and would increase with high bone density. Based on this assumption, the hypothesis in this section was that the UI would be positively related to density measurements from DEXA, thus the aim was to observe good positive correlation between the two techniques.

The UI was compared with the four DEXA measurements and the results demonstrated (see Table 8:4) no significant correlation for any of the measurements, which demonstrated that in this thesis the UI was not dependent on the density of the bones. The poor significance could be due to the difficulty in fitting of the 5.3 ppm (olefinic) peak when the 4.7 ppm (water) peak was large.

Lumbar Vertebrae		Unsaturation Index
Z-score	Pearson correlation (r)	0.2001
	Significance (p)	0.1774
	Regression	y=0.0012x+0.0270
	Sample size (N)	47
T-score	r	0.1742
	p	0.2417
	Regression	y=0.0012x+0.0284
	N	47
Areal BMC (g/cm)	r	0.1734
	p	0.2437
	Regression	y=0.0005x+0.0199
	N	47

Table 8:4 The Pearson correlation results for comparison of DEXA measurements with UI at lumbar vertebrae. Note the poor correlation for all the measurements.

8.2.7 DEXA versus Fat-Fraction from MR

The FF measures the amount of fat present in the bone marrow which is known to increase with patients who suffer from conditions like osteoporosis, as well as with low bone density and age. The hypothesis in this section was that the FF would be inversely related to density measurements from DEXA, thus the aim was to observe good negative correlation between the two techniques.

The FF measurements from MRI and MRS were compared with the four DEXA measurements and the results demonstrated (see Table 8:5) no significant correlation for any of the measurements, which demonstrated that FF was not dependent on the density of the bones. The poor significance could be due to the volunteer population who were mostly with high bone density.

Lumbar Vertebrae		FF_MRS (%)	FF_IDEAL (%)
Z-score	r	0.0350	0.1386
	p	0.8153	0.3527
	Regression	y=0.189x+62.826	y=0.470x+54.583
	N	47	47
T-score	r	-0.1664	-0.0623
	p	0.2635	0.6772
	Regression	y=−1.015x+66.032	y=−0.223x+56.793
	N	47	47
Areal BMC (g/cm)	r	-0.1234	-0.0265
	p	0.4087	0.8597
	Regression	y=−0.341x+70.772	y=−0.039x+57.056
	N	47	47

Table 8:5 The Pearson correlation results for comparison of DEXA measurements with FF from MRI and MRS at lumbar vertebrae. Note the poor correlation for all the measurements.

8.3 Associations and Differences between HBM and Controls

The aim in this section is to identify associations and differences between the individual populations of HBM-affected individuals and controls by using the measurements of MR and pQCT and comparing them with potential covariates of age and BMI. Age was selected as the covariate for all the measurements and BMI was selected as a potential covariate for only the MR measurements from lumbar vertebrae, since lumbar vertebrae is more likely to show differences with BMI compared to measurements from extremities.

The statistical analyses were performed in a logical cascade of individual stages as explained in Figure 8-22. In this section the two populations of HBM-affected and controls were grouped for each measurement of MR and pQCT, and then preliminary analysis were performed by using Pearson linear correlation with covariates of age or BMI to identify relationships. If neither population correlated with age or BMI, then age and BMI were not considered to be influential covariates to the data. Thus the data were processed with T-test to identify the differences in mean between the populations. If either populations correlated with the covariates, then the covariates were considered influential and additional processing was applied by calculating the 95% confidence interval (CI) of the difference between the slopes of the individual populations to identify if they were different or the same. If the slopes were different then significant differences were observed between the populations. If the slopes were the same then further analysis was applied to identify if there was any significant distance between the parallel slopes. If there were no significant distances observed between the slopes, then the slopes were assumed to be the same for both the populations within experimental error.

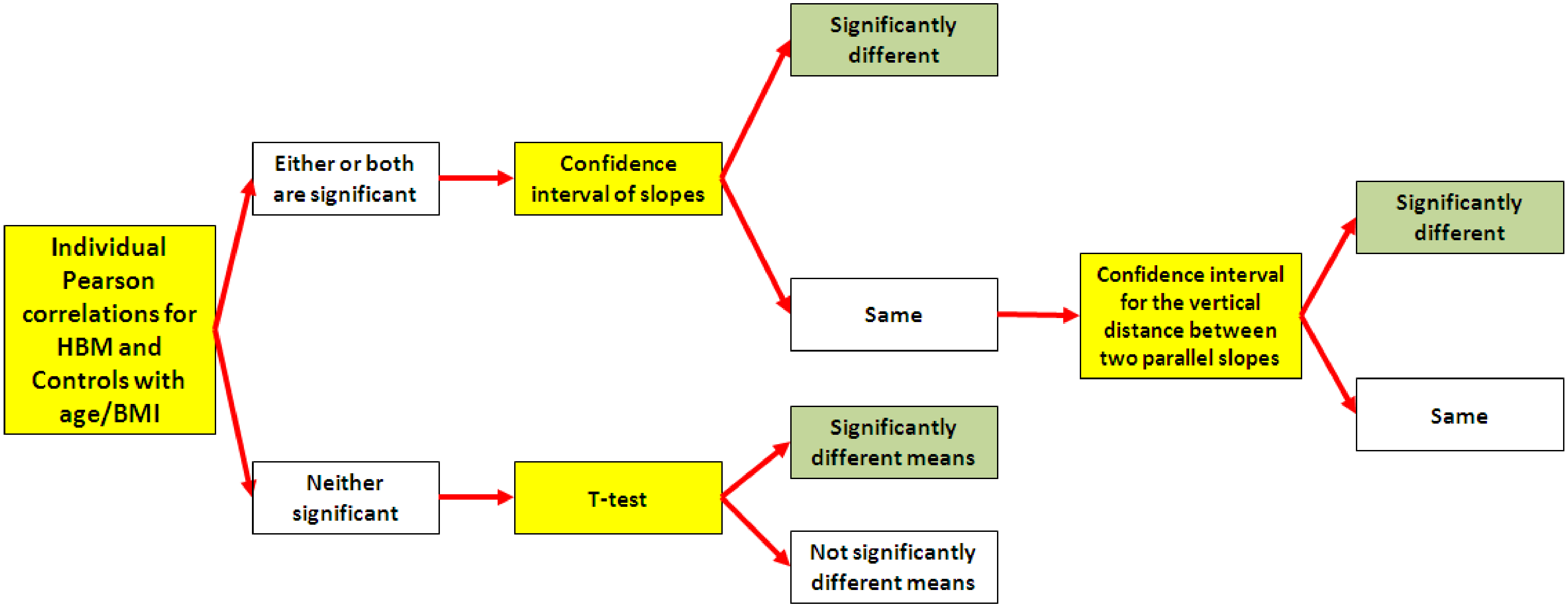

Figure 8-22 Flow chart used for the statistical processing of MR and pQCT data to identify associations and differences between HBM and controls.

8.3.1 Volumetric BMD and Age

The BMD measurements from bones are known to be influenced by age, thus the aim was to observe significant correlation between age and BMD for either populations of HBM and controls. The pQCT volumetric BMD measurement from radius and tibia were correlated with age to identify associations by using the Pearson linear correlation. The results demonstrated (see Table 8:6, Figure 8-23 & Figure 8-24) that the control population were significantly correlated with age for both radius (R^2 = 0.377, p = 0.034) and tibia (R^2 = 0.673, p = 0.001) illustrating that volumetric BMD for the control population is dependent on age. The HBM population did not have significant correlation with age for both radius (R^2 = 0.022, p = 0.390) and tibia (R^2 = 0.002, p = 0.813) illustrating that volumetric BMD for the HBM population is not dependent on age.

pQCT			Radius Volumetric BMD (mg/cm^3)	Tibia Volumetric BMD (mg/cm^3)
Age (years)	HBM	r	0.1476	0.0403
		p	0.3904	0.8128
		Regression	y=0.372x+185.740	y=0.095x+264.390
		N	36	37
	Controls	r	**-0.6139**	**-0.8202**
		p	**0.0337**	**0.0011**
		Regression	**y=−2.243x+283.380**	**y=−2.818x+364.390**
		N	12	12

Table 8:6 Pearson correlation results between age and pQCT volumetric BMD at radius and tibia in relation to individual populations. Note the significant correlation for the control population when compared with the HBM population at both skeletal sites.

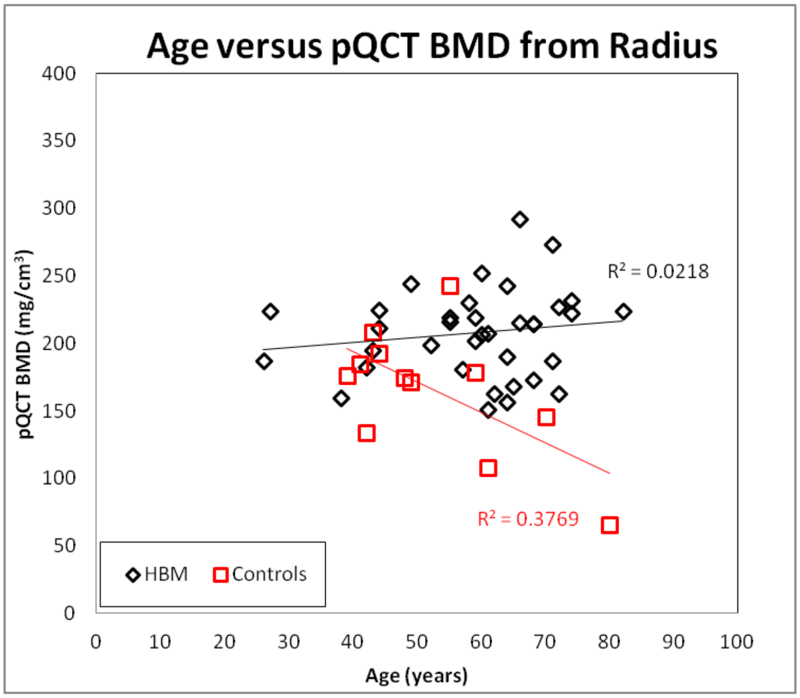

Figure 8-23 The scatter plot for correlation between age and pQCT volumetric BMD at radius in relation to individual populations. Note the significant correlation for the control population when compared with the HBM population.

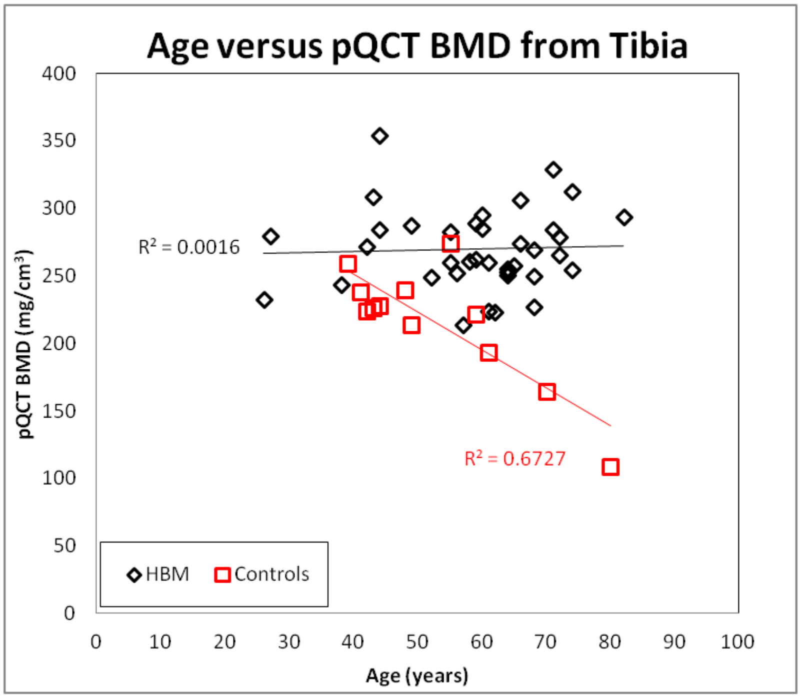

Figure 8-24 The scatter plot for correlation between age and pQCT volumetric BMD at tibia in relation to individual populations. Note the significant correlation for the control population when compared with the HBM population.

The results demonstrated that age was a significant covariate for pQCT volumetric BMD measurements at radius and tibia. The 95% CI for the slopes of HBM and controls were then evaluated to identify if the populations were significantly different after taking into consideration that age is a significant covariate. The 95% CIs for the difference between the slopes of HBM and control population was non-zero for both radius (upper 95% CI = 4.462, lower 95% CI = 0.767) and tibia (upper 95% CI = 4.508, lower 95% CI = 1.319), which demonstrated that there is a significant difference between the two populations and pQCT data were able to differentiate the populations.

8.3.2 Bone Area and Age

The aim in this section was to observe whether bone area from pQCT changed with age and also to identify if there was any significant difference in bone area between HBM and control population. The results demonstrated (see Table 8:7) no significant correlation between age and bone area for either populations at both radius and tibia, which demonstrated that age was not a covariate for bone area measurements.

pQCT			Radius Bone Area (mm^2)	Tibia Bone Area (mm^2)
Age (years)	HBM	*r*	-0.1457	-0.0549
		p	0.3967	0.7468
		Regression	y=−0.638x+426.020	y=−0.552x+1180.600
		N	36	37
	Controls	*r*	-0.2954	0.2945
		p	0.3513	0.3527
		Regression	y=−1.082x+402.630	y=2.256x+975.310
		N	12	12

Table 8:7 Pearson correlation results between age and pQCT bone area at radius and tibia in relation to individual populations. Note the poor correlation for all the measurements at both skeletal sites.

The results demonstrated that age was not a significant covariate for pQCT bone area measurements at radius and tibia, thus T-test was applied to identify if there was any significant differences between the HBM and control populations from the bone area measurement. The T-test results demonstrated a significant difference between HBM and controls at radius (p = 0.023), but no significant differences were observed at tibia (p = 0.186). In conclusion, the results from T-test illustrate that the bone area is different between HBM and controls at radius, but they are not different at tibia.

8.3.3 BVF and Age

The aim in this section was to observe whether BVF from MRI changed with age and also to identify if there was any significant difference in BVF between HBM and control population. The results demonstrated (see Table 8:8) no significant correlation between age and BVF for either populations at both radius and tibia, which demonstrated that age was not a covariate for BVF measurements.

MRI			Radius BVF (%)	Tibia BVF (%)
Age (years)	HBM	*r*	-0.1182	-0.0686
		p	0.5415	0.6824
		Regression	y=−0.014x+25.388	y=−0.010x+28.062
		N	29	38
	Controls	*r*	0.1243	-0.3532
		p	0.7500	0.2601
		Regression	y=0.027x+20.927	y=−0.046x+27.574
		N	9	12

Table 8:8 Pearson correlation results between age and MRI BVF at radius and tibia in relation to individual populations. Note the poor correlation for all the measurements at both skeletal sites.

The results demonstrated that age was not a significant covariate for MRI BVF measurements at radius and tibia, thus a T-test was applied to identify if there was any significant differences between the HBM and control populations from the BVF measurement. The T-test results demonstrated (see Figure 8-25 & Figure 8-26) a significant difference between HBM and controls for both radius ($p < 0.001$) and tibia ($p < 0.001$). In conclusion, the results from T-test illustrate that MRI measured BVF is able to differentiate between HBM and controls at radius and tibia, but not related to age.

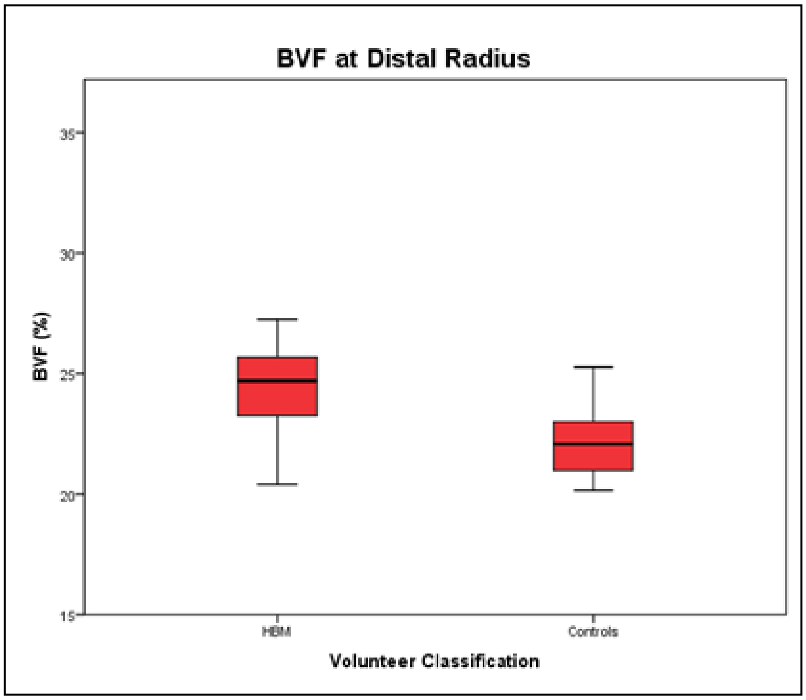

Figure 8-25 Box plot for BVF measurement at distal radius in relation to HBM and controls.

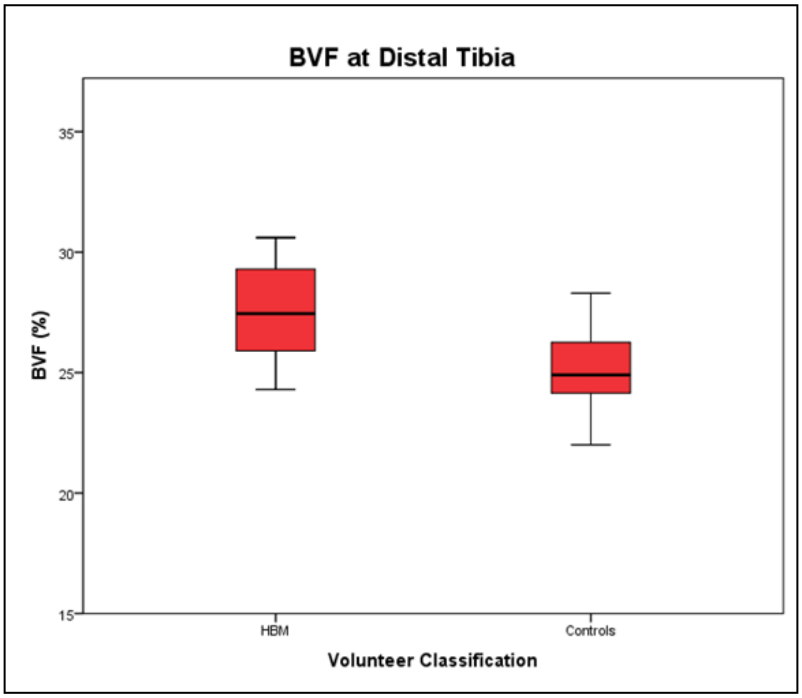

Figure 8-26 Box plot for BVF measurement at distal tibia in relation to HBM and controls.

8.3.4 Trabecular Area and Age

The aim in this section was to observe whether trabecular area measured from MRI changed with age and also to identify if there was any significant difference in trabecular area between HBM and control population. The results demonstrated (see Table 8:9) no significant correlation between age and trabecular area for either populations at both radius and tibia, which demonstrated that age was not a covariate for trabecular area measurements.

MRI			Radius Trabecular Area (mm^2)	Tibia Trabecular Area (mm^2)
Age (years)	HBM	*r*	-0.2816	-0.0524
		p	0.0961	0.7548
		Regression	y=−1.152x+383.530	y=−0.553x+1027.400
		N	36	38
	Controls	*r*	-0.2696	0.1945
		p	0.3967	0.5446
		Regression	y=−0.931x+324.600	y=1.879x+834.680
		N	12	12

Table 8:9 Pearson correlation results between age and MRI trabecular area at radius and tibia in relation to individual populations. Note the poor correlation for all the measurements at both skeletal sites.

The results demonstrated that age was not a significant covariate for MRI trabecular area measurements at radius and tibia, thus a T-test was applied to identify if there was any significant differences between the HBM and control population from the trabecular area measurement. The T-test results demonstrated a significant difference between HBM and controls for radius (p = 0.024), but no significant differences were observed at tibia (p = 0.175). In conclusion, the results from T-test illustrate that MRI measured trabecular area is able to differentiate between HBM and controls at radius, but not at tibia.

8.3.5 Entropy and Age

The results demonstrated (see Table 8:10) significant correlation between age and Entropy for the control population at distal radius and no significant correlation was observed for the HBM population, which demonstrated that age was a covariate for Entropy measurement at radius. No significant correlation was observed between age and Entropy for all the population at distal tibia, thus age was ruled out as a covariate at tibia.

MRI			Radius Entropy (a.u.)	Tibia Entropy (a.u.)
Age (years)	HBM	r	0.1266	-0.2302
		p	0.4620	0.1645
		Regression	y=0.001x+6.875	y=−0.002x+7.033
		N	36	38
	Controls	r	**-0.6987**	-0.4833
		p	**0.0115**	0.1114
		Regression	**y=−0.006x+7.230**	y=−0.004x+7.102
		N	12	12

Table 8:10 Pearson correlation results between age and MRI Entropy at radius and tibia in relation to individual populations. Note the good correlation of Entropy from radius with age for the control population.

The results demonstrated that age was a significant covariate for Entropy measurements at radius (see Figure 8-27 & Table 8:10), thus 95% CI for the slopes of HBM and controls were evaluated to identify if the populations were significantly different after taking into consideration that age is a significant covariate. The 95% CIs for the difference between the slopes of HBM and control population was non-zero for radius (upper 95% CI = 0.0138, lower 95% CI = 0.0001) which demonstrated that there is a significant difference between the two populations and MRI is able to differentiate the populations.

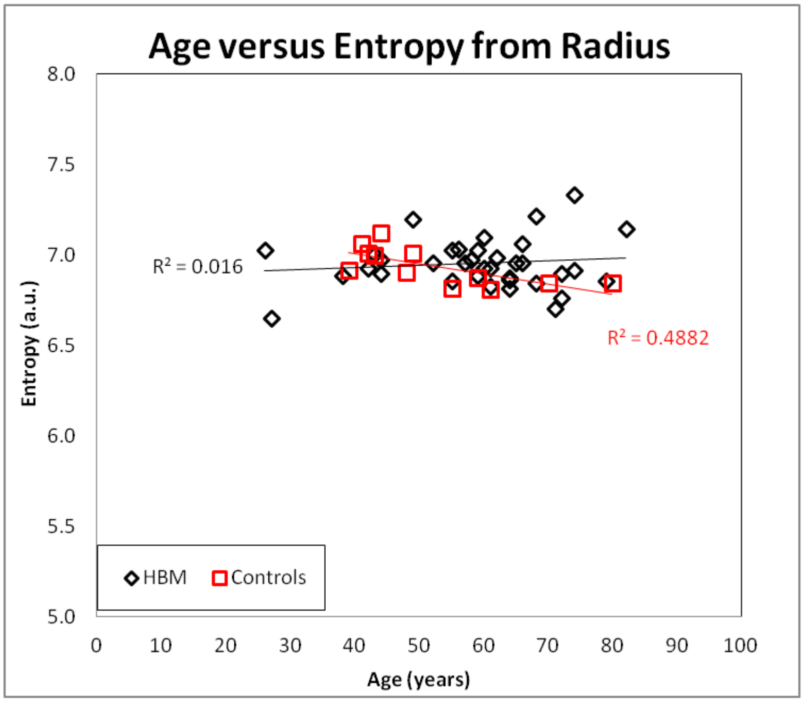

Figure 8-27 The scatter plot for correlation between age and MRI Entropy at radius in relation to individual population. Note the significant correlation for the control population when compared with the HBM population.

The results also demonstrated that age was not a significant covariate for Entropy measurements at tibia, thus T-test was applied to identify if there was any significant differences between the HBM and control population from the Entropy measurement. The T-test results demonstrated no significant difference between HBM and controls for tibia (p = 0.504). In conclusion, the results from T-test illustrate that MRI measured Entropy at tibia is not able to differentiate between HBM and controls.

8.3.6 Textural Analysis and Age

The aim in this section was to observe whether TA measurements from MRI were influenced by age and also to identify if there was any significant difference in TA between HBM and control population at both radius and tibia.

8.3.6.1 TA Contrast and Age

The results demonstrated (see Table 8:11) significant correlation between age and TA Contrast for the control population at distal tibia and no significant correlation was observed for the HBM population, which demonstrated that age was a covariate for TA Contrast measurement at tibia. No significant correlation was observed between age and TA Contrast for all the population at distal radius, thus age was ruled out as a covariate at radius.

MRI			Radius TA Contrast (a.u.)	Tibia TA Contrast (a.u.)
Age (years)	HBM	*r*	-0.1113	-0.2825
		p	0.5182	0.0857
		Regression	y=−0.008x+4.296	y=−0.016x+5.554
		N	36	38
	Controls	*r*	-0.5502	**-0.6051**
		p	0.0638	**0.0371**
		Regression	y=−0.039x+5.266	**y=−0.032x+6.285**
		N	12	12

Table 8:11 Pearson correlation results between age and MRI TA Contrast at radius and tibia in relation to individual populations. Note the good correlation of TA Contrast from tibia with age for the control population.

The results demonstrated that age was a significant covariate for TA Contrast measurements at tibia (see Figure 8-28 & Table 8:11), thus 95% CI for the slopes of HBM and controls were evaluated to identify if the populations were significantly different after taking into consideration that age is a significant covariate. The 95% CIs for the difference between the slopes of HBM and control population contained zero (upper 95% CI = 0.0527, lower 95% CI = -0.0199) which demonstrated that there was no significant differences between the slopes. Further CI test was applied to observe if there was any significant distance observed between the intercepts of the two slopes. The 95% CI for the vertical distance between the intercepts of the slopes contained zero (upper 95% CI = 0.616, lower 95% CI = -0.303), which demonstrated that there were no significant distance between the slopes. Thus the results demonstrated that there were no significant differences between the two populations and MRI was not able to differentiate the populations.

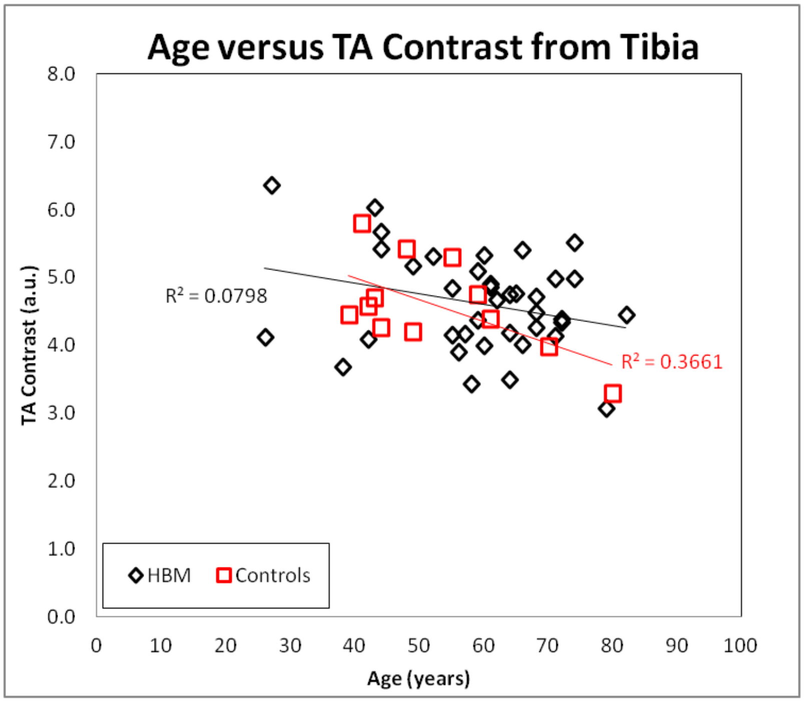

Figure 8-28 The scatter plot for correlation between age and MRI TA Contrast at tibia in relation to individual population. Note the significant correlation for the control population when compared with the HBM population.

The results also demonstrated that age was not a significant covariate for TA Contrast measurements at radius, thus T-test was applied to identify if there was any significant differences between the HBM and control population from the TA Contrast measurement. The T-test results demonstrated significant difference between HBM and controls for radius (p = 0.041). In conclusion, the results from T-test illustrate that MRI measured TA Contrast at radius is able to differentiate between HBM and controls.

8.3.6.2 TA Correlation and Age

The results demonstrated (see Table 8:12) significant correlation between age and TA Correlation for the control population at distal tibia and no significant correlation was observed for the HBM population, which demonstrated that age was a covariate for TA Correlation measurement at tibia. No significant correlation was observed between age and TA Correlation for all the population at distal radius, thus age was ruled out as a covariate at radius.

MRI			Radius TA Correlation (a.u.)	Tibia TA Correlation (a.u.)
Age (years)	HBM	*r*	0.1798	0.2832
		p	0.2940	0.0849
		Regression	y=0.001x+0.476	y=0.001x+0.345
		N	36	38
	Controls	*r*	0.5192	**0.6409**
		p	0.0836	**0.0247**
		Regression	y=0.004x+0.432	**y=0.002x+0.294**
		N	12	12

Table 8:12 Pearson correlation results between age and MRI TA Correlation at radius and tibia in relation to individual populations. Note the good correlation of TA Correlation from tibia with age for the control population.

The results demonstrated that age was a significant covariate for TA Correlation measurements at tibia (see Figure 8-29 & Table 8:12), thus 95% CI for the slopes of HBM and controls were evaluated to identify if the populations were significantly different after taking into consideration that age is a significant covariate. The 95% CIs for the difference between the slopes of HBM and control population contained zero (upper 95% CI = 0.0005, lower 95% CI = -0.0035) which demonstrated that there was no significant differences between the slopes. Further CI test was applied to observe if there was any significant distance observed between the intercepts of the two slopes. The 95% CI for the vertical distance between the intercepts of the slopes (upper 95% CI = -0.006, lower 95% CI = -0.057) was non-zero, which demonstrated significant distance between the intercepts of the slopes. Thus the results demonstrated that there were significant differences between the two populations with parallel slopes, and MRI was able to differentiate the population.

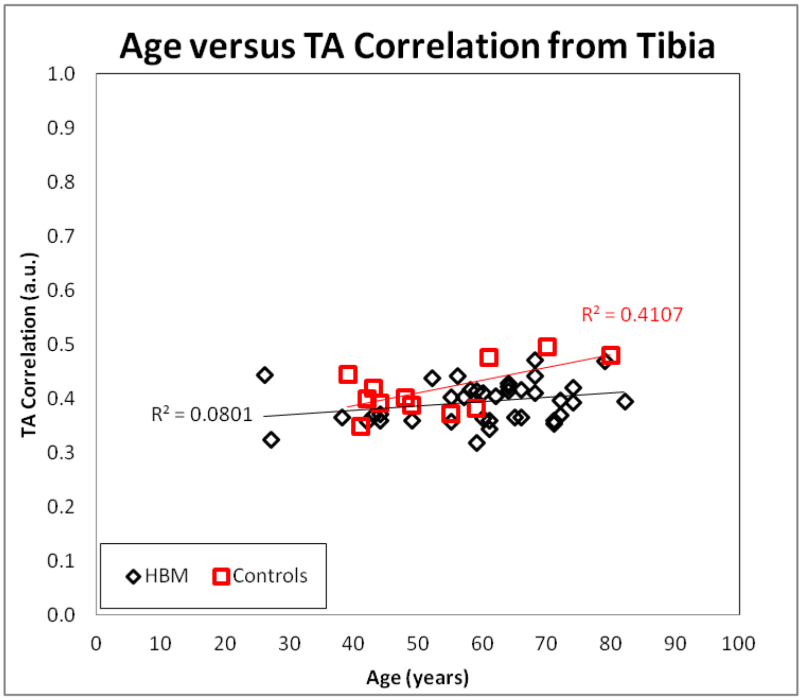

Figure 8-29 The scatter plot for correlation between age and MRI TA Correlation at tibia in relation to individual population. Note the significant correlation for the control population when compared with the HBM population.

The results also demonstrated that age was not a significant covariate for TA Correlation measurements at radius, thus T-test was applied to identify if there was any significant differences between the HBM and control population from the TA Correlation measurement. The T-test results demonstrated significant difference between HBM and controls for radius (p = 0.019). In conclusion, the results from T-test illustrate that MRI measured TA Correlation at radius is able to differentiate between HBM and controls.

8.3.6.3 TA Energy and Age

The results demonstrated (see Table 8:13) no significant correlation between age and TA Energy for either populations at both radius and tibia, which demonstrated that age was not a covariate for TA Energy measurements.

MRI			Radius TA Energy (a.u.)	Tibia TA Energy (a.u.)
Age (years)	HBM	*r*	-0.0385	0.1785
		p	0.8234	0.2836
		Regression	y=−0.0000x+0.0244	y=0.0000x+0.0205
		N	36	38
	Controls	*r*	0.4716	0.5719
		p	0.1217	0.0520
		Regression	y=0.0002x+0.0168	y=0.0001x+0.0153
		N	12	12

Table 8:13 Pearson correlation results between age and MRI TA Energy at radius and tibia in relation to individual populations. Note the poor correlation of TA Energy for all the measurements.

The results demonstrated that age was not a significant covariate for MRI TA Energy measurements at radius and tibia, thus T-test was applied to identify if there was any significant differences between the HBM and control population from the TA Energy measurement. The T-test results demonstrated a significant difference between HBM and controls for radius (p = 0.038), but no significant differences were observed at tibia (p = 0.749). In conclusion, the results from T-test illustrate that MRI measured TA Energy is able to differentiate between HBM and controls at radius, but not at tibia.

8.3.6.4 TA Homogeneity and Age

The results demonstrated (see Table 8:14) significant correlation between age and TA Homogeneity for the control population at distal radius and tibia and no significant correlation was observed for the HBM population, which demonstrated that age was a covariate for TA Homogeneity measurement at radius and tibia.

MRI			Radius TA Homogeneity (a.u.)	Tibia TA Homogeneity (a.u.)
Age (years)	HBM	*r*	0.1129	0.2622
		p	0.5121	0.1117
		Regression	y=0.0002x+0.5106	y=0.0004x+0.4700
		N	36	38
	Controls	*r*	**0.6048**	**0.6739**
		p	**0.0372**	**0.0163**
		Regression	**y=0.0020x+0.4514**	**y=0.0010x+0.4434**
		N	12	12

Table 8:14 Pearson correlation results between age and MRI TA Homogeneity at radius and tibia in relation to individual populations. Note the good correlation of TA Homogeneity with age for the control population of radius and tibia.

The results demonstrated that age was a significant covariate for TA Homogeneity measurements at radius and tibia (see Figure 8-30, Figure 8-31 & Table 8:14), thus 95% CI for the slopes of HBM and controls were evaluated to identify if the populations were significantly different after taking into consideration that age as a significant covariate.

At radius the 95% CIs for the difference between the slopes of HBM and control population was non-zero (upper 95% CI = -0.0001, lower 95% CI = -0.0034) indicating a significant difference between them. Thus the results demonstrated that there were significant differences between the two populations, and MRI was able to differentiate the population.

At tibia the 95% CIs for the slopes of HBM and control population contained zero (upper 95% CI = 0.0004, lower 95% CI = -0.0015) which demonstrated that there was no significant differences between the slopes. Further CI test was applied for tibia measurements to observe if there were any significant distance observed between the intercepts of the two slopes. The 95% CI for the vertical distance between the intercepts of the two slopes contained zero (upper 95% CI = 0.007, lower 95% CI = -0.017), which demonstrated that there were no significant distance between the slopes. Thus the results demonstrated that there were no significant differences between the two populations and MRI was not able to differentiate the populations.

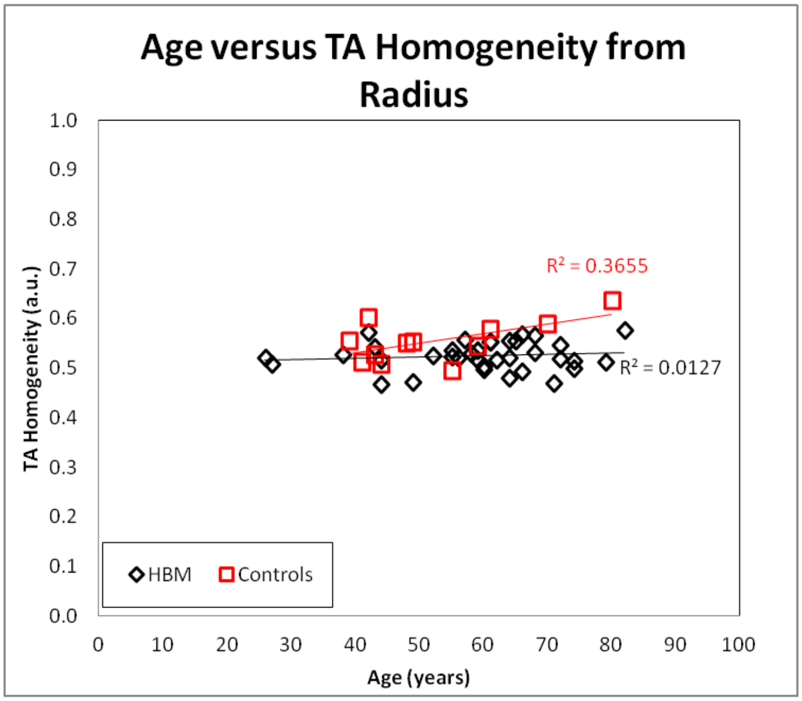

Figure 8-30 The scatter plot for correlation between age and MRI TA Homogeneity at radius in relation to individual population. Note the significant correlation for the control population when compared with the HBM population.

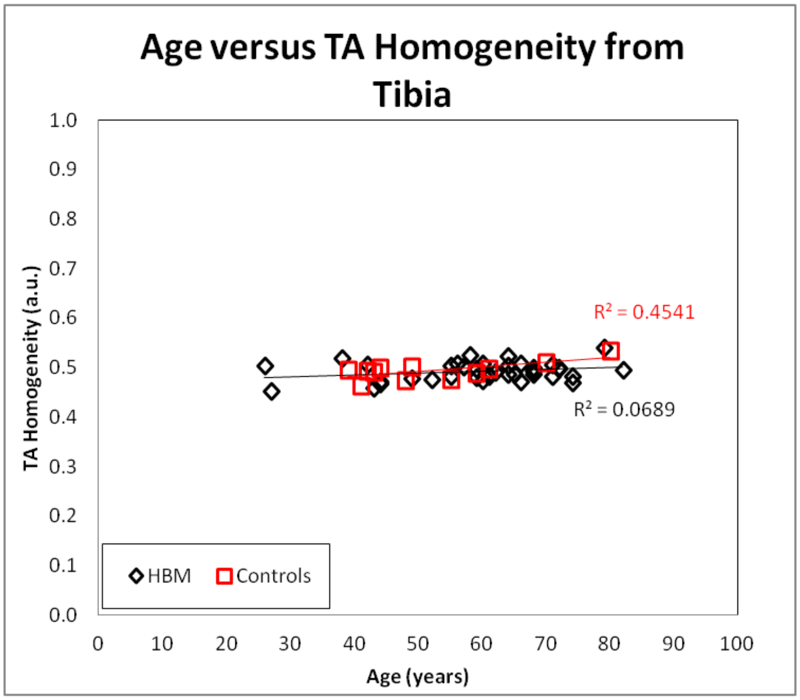

Figure 8-31 The scatter plot for correlation between age and MRI TA Homogeneity at tibia in relation to individual population. Note the significant correlation for the control population when compared with the HBM population.

8.3.7 Water and Lipid FWHM from MRS with Age and BMI

The aim in this section was to observe whether water and lipid FWHM from MRS were influenced by age and BMI, and also to identify if there was any significant difference in water and lipid FWHM between HBM and control population at lumbar vertebrae

The results demonstrated (see Table 8:15) no significant correlation between age and water/lipid FWHM as well as BMI and water/lipid FWHM for all the populations which demonstrated that age and BMI were not covariates for water and lipid FWHM measurement at lumbar vertebrae.

MRS			Water FWHM (Hz)	Lipid FWHM (Hz)
Age (years)	HBM	*r*	0.2428	0.0322
		p	0.1477	0.8498
		Regression	y=0.183x+58.073	y=0.026x+61.285
		N	37	37
	Controls	*r*	-0.1091	-0.2756
		p	0.7356	0.3859
		Regression	y=−0.087x+66.398	y=−0.247x+67.240
		N	12	12
BMI (kg/m^2)	HBM	*r*	0.0286	-0.0563
		p	0.8704	0.7482
		Regression	y=0.056x+67.113	y=−0.122x+66.249
		N	35	35
	Controls	*r*	-0.1882	-0.1595
		p	0.5581	0.6205
		Regression	y=−0.342x+71.569	y=−0.326x+63.524
		N	12	12

Table 8:15 Pearson correlation results for age and BMI with water and lipid FWHM at lumbar vertebrae in relation to individual populations. Note the poor correlation for all the measurements.

The results demonstrated that age and BMI were not a significant covariate for water and lipid FWHM measurements at lumbar vertebrae, thus T-test was applied to identify if there was any significant differences between the HBM and control population from both water and lipid FWHM measurements. The T-test results demonstrated a significant difference between HBM and controls for both water FWHM ($p = 0.032$) and lipid FWHM ($p = 0.020$). In conclusion, the results from T-test demonstrated that MRS measured FWHM which is a surrogate measurement of trabecular bone and marrow density is able to differentiate between HBM and controls at lumbar vertebrae.

8.3.8 Unsaturation Index from MRS with Age and BMI

The aim in this section was to observe whether UI from MRS was influenced by age and BMI, and also to identify if there was any significant difference in UI between HBM and control population at lumbar vertebrae

The results demonstrated (see Table 8:16) non significant correlation for age and BMI with UI for all the population which demonstrated that age and BMI were not covariates for UI measurement at lumbar vertebrae.

MRS			Unsaturation Index
Age (years)	HBM	*r*	-0.0392
		p	0.8178
		Regression	y=−0.0000x+0.0364
		N	37
	Controls	*r*	0.1813
		p	0.5728
		Regression	y=0.0002x+0.0158
		N	12
BMI (kg/m^2)	HBM	*r*	0.1561
		p	0.3704
		Regression	y=0.0004x+0.0208
		N	35
	Controls	*r*	0.2281
		p	0.4757
		Regression	y=0.0006x+0.0097
		N	12

Table 8:16 Pearson correlation results for age and BMI with UI at lumbar vertebrae in relation to individual populations. Note the poor correlation for all the measurements.

The results demonstrated that age and BMI were not a significant covariate for UI measurement at lumbar vertebrae, thus T-test was applied to identify if there was any significant differences between the HBM and control population from UI measurement. The T-test results demonstrated non significant difference between HBM and controls for the UI measurement (p = 0.095). In conclusion, the results from T-test demonstrated that MRS measured UI which is a measurement of the amount of unsaturated fatty acid in the bone marrow is not able to differentiate between HBM and controls at lumbar vertebrae.

8.3.9 Fat-Fraction from IDEAL with Age and BMI

The aim in this section was to observe whether FF from IDEAL imaging was influenced by age and BMI, and also to identify if there was any significant difference in FF between HBM and control population at lumbar vertebrae

The results demonstrated (see Table 8:17) significant correlation between age and FF from IDEAL for both the HBM and control population, but no significant correlation was observed between BMI and FF from IDEAL for both the HBM and the control population. Thus the results demonstrated that BMI was not a significant covariate for FF measurement, but age was a significant covariate for FF measurement.

MRS			FF from IDEAL (%)
Age (years)	HBM	*r*	**0.5364**
		p	**0.0006**
		Regression	**y=0.291x+39.218**
		N	37
	Controls	*r*	**0.6446**
		p	**0.0236**
		Regression	**y=0.378x+35.038**
		N	12
BMI (kg/m^2)	HBM	*r*	-0.1142
		p	0.5134
		Regression	y=−0.157x+61.353
		N	35
	Controls	*r*	0.0643
		p	0.8426
		Regression	y=0.101x+52.056
		N	12

Table 8:17 Pearson correlation results for age and BMI with FF from IDEAL imaging at lumbar vertebrae in relation to individual populations. Note the significant correlation with age for both the HBM and control populations.

The results demonstrated that age was a significant covariate for FF measurement at lumbar vertebrae (see Table 8:17 & Figure 8-32), thus 95% CI for the slopes of HBM and controls were evaluated to identify if the populations were significantly different after taking into consideration that age is a significant covariate. The 95% CIs for the difference between the slopes of HBM and control population contained zero (upper 95% CI = 0.232, lower 95% CI = -0.406) which demonstrated that there were no significant differences between the slopes. Further CI test was applied for FF measurements to observe if there was any significant distance observed between the intercepts of the two slopes. The 95% CI for the vertical distance between the intercepts of the slopes contained zero (upper 95% CI = 3.599, lower 95% CI = -4.410), which demonstrated that there were no significant distance between the slopes. Thus the results demonstrated that there were no significant differences between the two populations and MRI measurement of FF from the vertebrae which quantifies the amount of fat in the bone marrow was not able to differentiate the population.

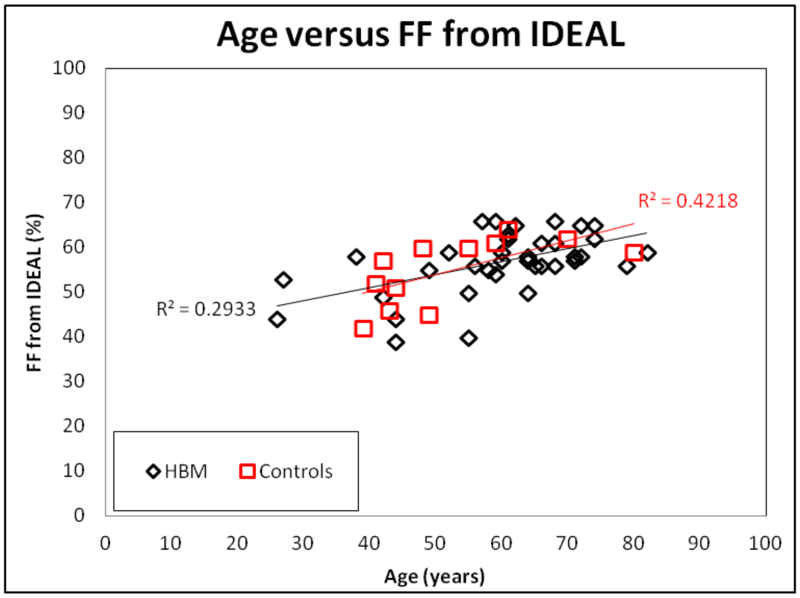

Figure 8-32 The scatter plot for correlation between age and FF from IDEAL at lumbar vertebrae in relation to individual populations. Note the significant correlation for both the populations.

8.3.10 Fat-Fraction from MRS with Age and BMI

The aim in this section was to observe whether FF from MRS was influenced by age and BMI, and also to identify if there was any significant difference in FF between HBM and control population at lumbar vertebrae

The results demonstrated (see Table 8:18) significant correlation between age and FF from MRS for both the HBM and control population. The results also demonstrated significant correlation between BMI and FF from MRS for the HBM population, but not the control population, indicating that BMI is a significant factor for HBM subjects. In conclusion the results demonstrated that both age and BMI were significant covariates for FF measurement at lumbar vertebrae.

MRS			FF from MRS (%)
Age (years)	HBM	*r*	**0.5598**
		p	**0.0003**
		Regression	**y=0.499x+33.460**
		N	37
	Controls	*r*	**0.6594**
		p	**0.0197**
		Regression	**y=0.628x+30.127**
		N	12
BMI (kg/m^2)	HBM	*r*	**-0.3977**
		p	**0.0180**
		Regression	**y=−0.915x+90.820**
		N	35
	Controls	*r*	-0.0867
		p	0.7889
		Regression	y=−0.167x+67.930
		N	12

Table 8:18 Pearson correlation results for age and BMI with FF from MRS at lumbar vertebrae in relation to individual populations. Note the significant correlation with age for both the HBM and control populations, and the significant correlation with BMI for the HBM population.

The results demonstrated that both age and BMI were significant covariates for FF measurement at lumbar vertebrae (see Table 8:18, Figure 8-33 & Figure 8-34), thus 95% CI for the slopes of HBM and controls were evaluated to identify if the populations were significantly different after taking into consideration that age and BMI as significant covariates.

The 95% CIs for the difference between the slopes of HBM and control population was evaluated by keeping the age as the covariate and the results contained zero (upper 95% CI = 0.385, lower 95% CI = -0.644) which demonstrated that there were no significant difference between the slopes. Further CI test was applied for FF measurements to observe if there was any significant distance observed between the intercept of the two slopes. The 95% CI for the vertical distance between the intercept of the slopes contained zero (upper 95% CI = 2.999, lower 95% CI = -9.911), which demonstrated that there were no significant distance between the slopes. Thus the results demonstrated that there were no significant differences between the two populations and MRS measurement of FF from the vertebrae was not able to differentiate the populations with age as the covariate.

The 95% CIs for the difference between the slopes of HBM and control population was evaluated by keeping the BMI as the covariate and the results contained zero (upper 95% CI = 0.692, lower 95% CI = -2.188) which demonstrated that there was no significant differences between the slopes. Further CI test was applied for FF measurements to observe if there was any significant distance observed between the intercept of the two slopes. The 95% CI for the vertical distance between the intercept of the slopes contained zero (upper 95% CI = 8.493, lower 95% CI = -6.506), which demonstrated that there were no significant distance between the slopes. Thus the results demonstrated that there were no significant differences between the two populations and MRS measurement of FF from the vertebrae was not able to differentiate the populations with BMI as the covariate.

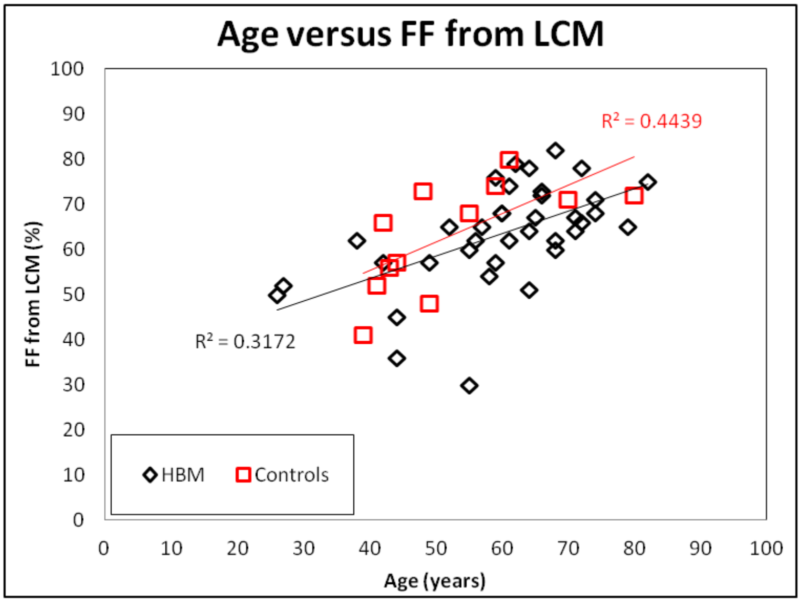

Figure 8-33 The scatter plot for correlation between age and FF from MRS at lumbar vertebrae in relation to individual population. Note the significant correlation for both the population.

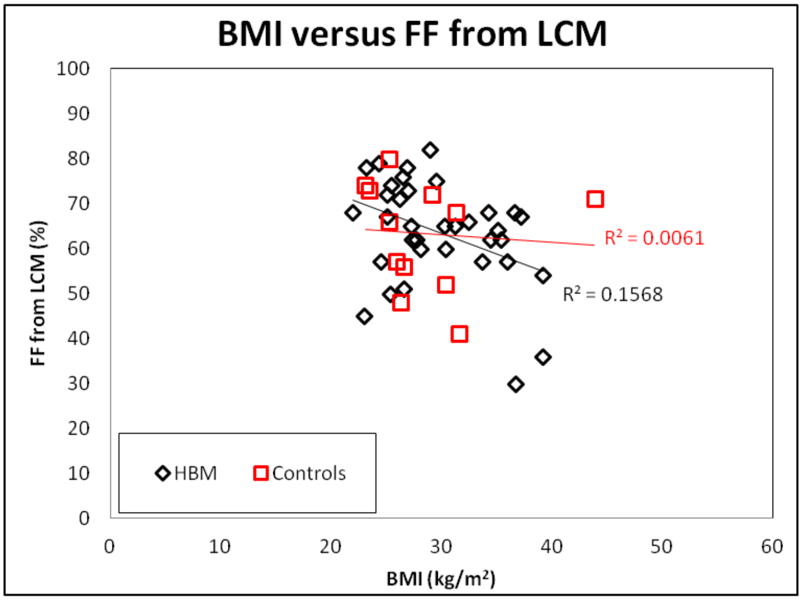

Figure 8-34 The scatter plot for correlation between BMI and FF from MRS at lumbar vertebrae in relation to individual population. Note the significant correlation for the HBM population.

8.4 Comparison of FF from IDEAL and MRS

The FF measurements acquired using IDEAL imaging and MRS was compared with each other, by using MRS as the gold standard measurement. The comparison was performed by using Bland-Altman plot to identify if both the techniques provided similar information. The FF measurements from each vertebra acquired using IDEAL and MRS were averaged (mean) to produce an effective single measurement representative of the whole lumbar vertebrae. The results demonstrated (see Figure 8-35) a clear trend where the FF from IDEAL was always overestimating for lower FF values and underestimating for higher FF values when compared with MRS. This trend was observed in all the lumbar vertebrae under investigation and has also been previously demonstrated in this centre [173, 194].

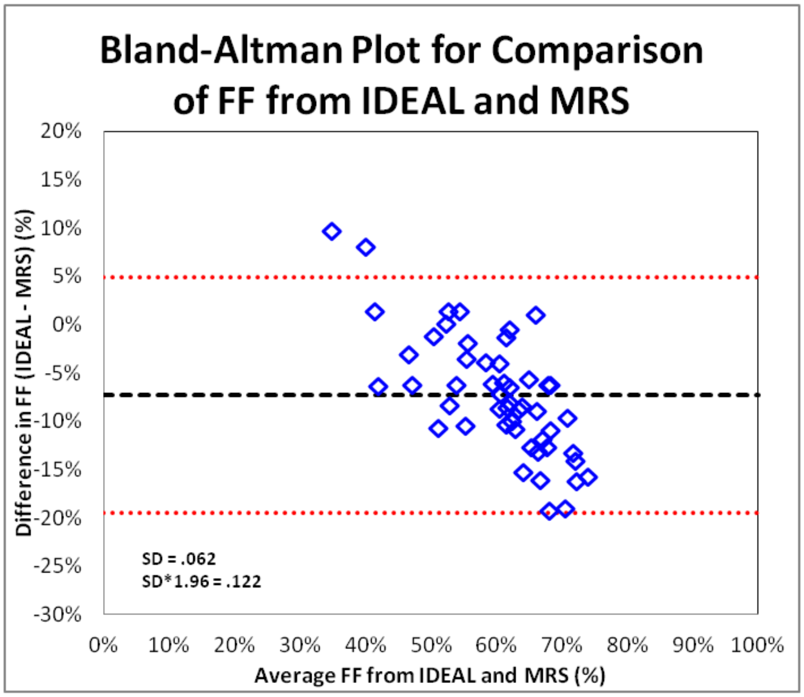

Figure 8-35 The Bland-Altman plot for comparison of FF from IDEAL and MRS.

Further investigation of the individual FF values demonstrated (see Figure 8-36) that the dynamic range for the FF values from IDEAL were smaller when compared with MRS and this was observed as the trend in the Bland-Altman plot.

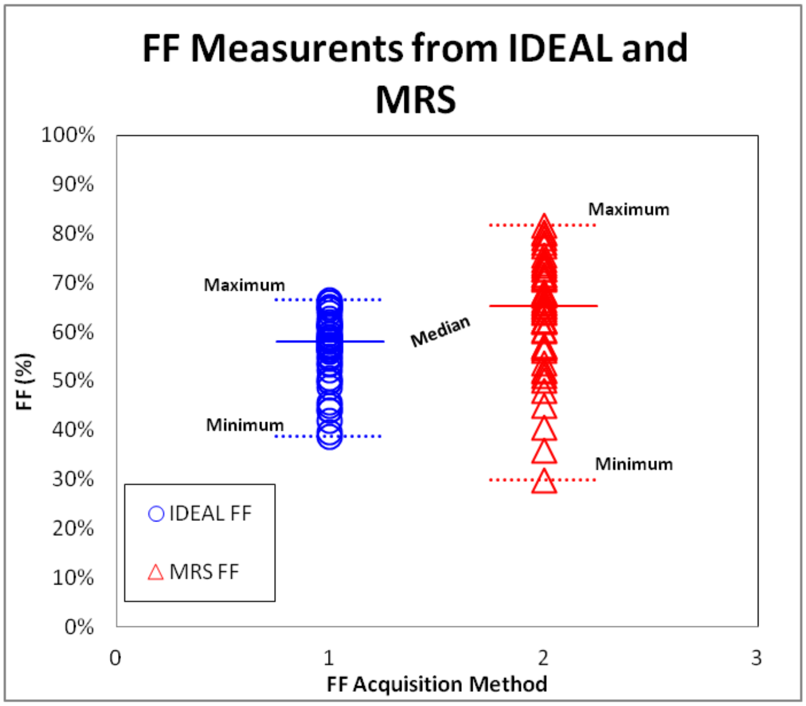

Figure 8-36 The display of FF measurements from IDEAL and MRS.

The possible reason for the poor range of the IDEAL technique may be due to the acquisition method, since the IDEAL technique that was used in this thesis was a three-point Dixon technique and it is well known [109, 110] that this method of acquisition assumes fat and water as only two components, but in reality fat has up to six components that can be seen *in vivo*. The IDEAL technique may not be able to separate fat and water as efficiently as MRS, and thus results in contamination of fat and water images.

The solution may be achieved by using advanced IDEAL technique like IDEAL-IQ that recognises the multiple components of fat and acquires data with better representation of fat and water [110].

8.5 General Discussion

In conclusion, the results from this section fulfilled both the aims of: (i) good correlation between MR and X-ray quantitative techniques and (ii) effective differentiation of affected and non-affected populations based on MR quantitative measurements.

The results from distal radius and tibia demonstrated good correlation between pQCT volumetric density measurements with MRI measurements of BVF, entropy and four TA properties (see Figure 8-2, Figure 8-3, Figure 8-7, Figure 8-8, Figure 8-9, Figure 8-10, Figure 8-11, Figure 8-12, Figure 8-13, Figure 8-14 & Figure 8-15) illustrating that the MRI method of bone quantification is providing similar information to pQCT and is also providing additional structural properties from TA that cannot be measured by pQCT. The results from lumbar vertebrae illustrate that FWHM of water and lipid peaks, which are the surrogate markers of trabecular bone and marrow density correlate well with areal DEXA measurements from spine in relation to Z-score and T-score (see Figure 8-16,.Figure 8-17, Figure 8-18 & Figure 8-19). There were no significant correlations observed between areal BMC and any of the MR measurements. The FF and UI from MR also did not correlate with any of the DEXA measurements, which conflicts with the results from previously published works.

At distal radius and tibia, some of the MRI measurements were able to differentiate the HBM and the control populations, which demonstrated the potential of using MR measurements for identification of bone abnormalities. At lumbar vertebrae, the FWHM of water and lipid peaks were able to differentiate the populations with good significance. The measurements of UI and FF were not able to differentiate between the populations, which also conflicts with the results from previously published works, probably due to this thesis containing a new population of HBM-affected individuals.

The results in this thesis illustrate that quantitative measurements from MR are providing information similar to X-ray quantitative techniques and are also able to differentiate between different types of populations based on their bone properties.

9 Conclusion and Developments

9.1 Conclusion

The techniques of magnetic resonance imaging and spectroscopy (MRI & MRS) have been successfully used at multiple skeletal sites to acquire quantitative information in relation to bone quantity and quality. Acquisition protocols have been successfully optimised at 3.0 T to acquire different types of quantitative data.

In-house software has been successfully developed and validated to process and quantify bone data from multiple skeletal locations. The method of textural analysis has been successfully used for bone quantification at extremities with promising results. The software has been successfully used in a cohort of volunteers to identify differences in their bone condition.

The MRI data from distal radius and tibia were compared with peripheral quantitative computed tomography (pQCT) and the results demonstrated good correlation between each other for most of the MRI measurements, which demonstrated that the MRI method of quantitative data acquisition is as good as the gold standard techniques with the added advantage of acquiring new information that is not achieved by other modalities.

The MRI data from distal radius and tibia were used for comparisons of subjects of high bone mass (HBM) and normal controls, and the statistical analysis shows that MRI measurements of bone volume fraction (BVF), entropy and some textural properties at distal radius and tibia were able to differentiate the HBM and the control populations. These results illustrate that MRI data are able to identify the structural and density changes in bones in relation to this bone condition.

The MRI and MRS measurements from lumbar vertebrae were compared with dual-energy X-ray absorptiometry (DEXA) measurements from lumbar vertebrae to identify relationships and differences. The FWHM of both water and lipid peaks were moderately related with spinal areal DEXA measurements and were also able to differentiate the HBM and the control populations. These results illustrate that MRS data can give useful structural and chemical composition and are able to differentiate changes in relation to different bone conditions.

The fat-fraction (FF) measurements from imaging and spectroscopy at lumbar vertebrae were correlated with areal DEXA data and the results demonstrated no significant correlation between the two measurements, which negates the observations from previous studies that have demonstrated a negative relationship between FF and areal DEXA data from the lumbar vertebrae. This conflict in the results may be due to the presence of the HBM subjects who may have different biological changes in the bone. The FF data were also correlated with age and body mass index (BMI) for both populations, and the results demonstrated a linear increase in FF with age for both the HBM population and controls, and there were no significant differences observed between HBM and controls.

Previous studies [179, 182, 183, 194, 201, 205, 217, 218, 237] have demonstrated a linear increase in FF with age for controls, and also an increase in FF for osteoporosis (OP) affected individuals. The OP subjects have lower bone density which is believed to cause higher FF in the bone marrow. The results in this thesis demonstrated a higher FF for the HBM and they were also similar to the normal subjects. The observations from this thesis illustrate that FF from the lumbar vertebrae is positively related to age but not to the areal bone density measurements. The HBM condition was more dependent on the structural property (FWHM) of the bone rather than the changes in bone marrow composition (FF).

The unsaturation index (UI) from MRS is the measure of the amount of unsaturated fatty acids present in the bone marrow. Previous studies [217, 238] have demonstrated a decrease in UI with OP when compared with controls. The results in this thesis demonstrated no significant correlation between UI and areal DEXA measurements, as well as the UI measurements were also not able to differentiate between the HBM and control population.

The combined results from this thesis demonstrate that MRI and MRS are both sensitive techniques for quantifying bone quantity and bone quality, and that they are ready to be applied to studying the bones of patients for observing changes in relation to bone abnormalities. The results from this thesis add to other work in the international community that use MR modality and its multiple quantitative measurements to study the HBM-affected population. This thesis shows the value of adding these techniques and software for the non invasive non-ionising evaluation of bones that could be added onto clinical scans in patients.

9.2 Limitations

The current thesis has several limitations. The sample size for HBM and controls was limited and was not balanced in terms of number of subjects which may reduce the power of the statistical tests used, leading to true differences not being detected. Larger and more balanced populations would be ideal for effective evaluation in future. This thesis was also limited to caucasian women due to their greater prevalence in the HBM study population, and thus the results are specific to this group. Populations with equal number of men and women would be preferable in future. The images from distal tibia were acquired using a birdcage head coil which resulted in reduced signal-to-noise ratio (because of a poor filling factor) when compared with the wrist coil that was used for image acquisition at distal radius. Ideally a dedicated coil should be used for distal tibia. The IDEAL imaging technique used in this thesis is known for poor differentiation of fat and water signals, resulting in contamination of water and fat images, because of the small number of echoes used (three). The advanced IDEAL sequence, IDEAL IQ, with more echoes for better modelling of all of the fat peaks should more effectively differentiate fat and water in future. At distal radius and tibia, data were acquired as T_1-weighted SE images providing structural information only, but high-resolution IDEAL images from extremities could be used for quantifying both structural and bone marrow composition.

9.3 Preliminary Work Towards Future Directions

The aim in future is to use the full potential of the MR techniques to acquire better and additional quantitative information from musculoskeletal regions.

9.3.1 Ovarian Cancer Bone Project

It is known that both chemotherapy and hormonal therapy can cause a loss of bone density and a concomitant increase in the risk of osteoporosis for men and women potentially causing severe morbidity [40, 42, 239]. Detailed data and long-term experience to assess the risks are urgently needed, and constitute an important research topic. MR imaging and spectroscopy offer the potential to study bone strength and marrow composition non-invasively.

This thesis illustrates that the quantitative MRI and MRS techniques that have been developed are sensitive enough to demonstrate clear differences between study populations. It is hoped that these techniques will provide useful information in on-going studies of breast and ovarian cancer chemotherapy patients. The hope is that MRI and/or MRS will be able to detect subtle changes in bone density and structure, and bone marrow quality (red/yellow marrow fraction) which will permit a better scientific understanding of treatment side-effects and, perhaps, a clinically useful way of identifying those individuals who are at greater risk of future bone fractures who would, therefore, benefit from some kind of prophylactic therapeutic intervention.

The aim of the chemotherapy project is to acquire pre-baseline, during- and post-treatment MR data at lumbar vertebrae to identify changes in bone properties due to the cancer treatment. R&D and ethics approval were acquired from the local NHS trust and the local research ethics committee respectively for the project. The MR data are acquired by using the IDEAL MRI acquisition from all the lumbar vertebrae and single voxel PRESS MRS at first, third and fifth lumbar vertebrae (L1, L3 and L5). Parameter maps of FF will be produced off-line from the IDEAL images which would then be compared to FF values from MRS data, a presumed gold-standard, in all the patients. Trabecular density will also be estimated from MRS by analysing the width of the spectral peaks, along with spectroscopic UI which would allow us to explore bone integrity in terms of both structural and functional parameters. Longitudinal changes will be assessed using Friedman's rank test for k related samples. Preliminary data were acquired as pre and post treatment acquisition from one ovarian cancer patient as described in Figure 9-1.

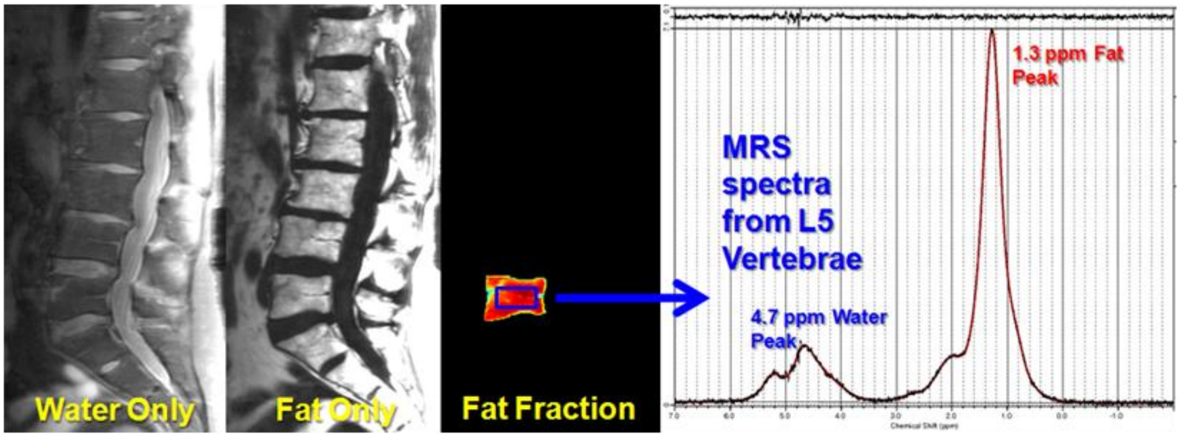

Figure 9-1 The MR IDEAL chemical-shift images (providing separate water- and fat-only images) obtained sagitally through the lumbar spine to obtain the fat fraction of bone as shown in the colour map. The spectrum on the right shows the corresponding gold-standard chemical data from the body of L5, as obtained from the VOI shown in blue on the colour map, with the water and dominant fat peaks resonating at 4.7 and 1.3 p.p.m. respectively.

9.3.2 Development of Advanced Imaging at Distal Radius

All the data in this thesis for distal radius were acquired by using the eight channel phased array (PA) coil. The use of the PA coil resulted in images being affected by inhomogeneity artefacts. The data from this thesis did not use any of the default correction techniques of PURE or SCIC (see Chapter 7). The aim is to examine these methods in the scanner and to identify the ideal processing tool that could be used for all image acquisition in future.

The aim in future is to acquire high-resolution IDEAL imaging at distal radius and tibia, which could be used as a single image acquisition to measure combined quantitative information of bone structure and FF, with added advantage of cortical bone segmentation that could be used for the measurement of cortical thickness. Preliminary results from one of the best IDEAL acquisition at distal radius, by using the wrist coil, demonstrated (see Figure 9-2) improved image quality with good differentiation of trabecular structures in the fat-only image, but there were mild flow artefacts observed in the water-only image. The images were acquired with a slice thickness of 1 mm and with an in-plane resolution of 156 × 117 µm. Note the improvements in image quality when compared with previously acquired fat (see Figure 5-5) and water only (see Figure 3-18) images.

Figure 9-2 The high-resolution IDEAL images acquired at 4% length of distal radius by using the wrist coil. The image on top contains the water-only component and the image on the bottom contains the fat only component. Note the good image quality from both the images.

The results illustrate the potential of acquiring high-resolution IDEAL images at distal radius and tibia to collect additional quantitative information from the bones. Further work is required to optimise these acquisitions with newer and better IDEAL sequences (e.g. IDEAL-IQ) that are able to differentiate fat and water with better precision due to the use of an increased number of echo-times that differentiate the multiple fat components [110].

9.3.3 Analysis of Skeletal Muscle by Using MRI and MRS

The aim in future is also to acquire quantitative information from muscles that could be used as an adjunct to markers of bone strength, as bone and muscle strength are inter-linked [195, 240-244]. The muscles could be evaluated using imaging and multi-nuclear spectroscopy (e.g. ^{1}H, ^{31}P).

Preliminary experimental data were acquired at calf region by using IDEAL imaging and ^{1}H spectroscopy. The IDEAL images (see Figure 9-3) were acquired using the knee coil and with a slice thickness of 1 mm. The images provided good separation of the fat and water components for measurement of FF, and with good delineation of the individual muscles in the calf region. The spectrum was acquired at soleus muscle by using the single voxel PRESS technique. The acquired spectrum (see Figure 9-4) provided information of the individual components of intramyocellular lipids (IMCL) and extramyocellular lipids (EMCL), and additional metabolite information in relation to creatinine (Cr2 and Cr3) and trimethylamines (TMA).

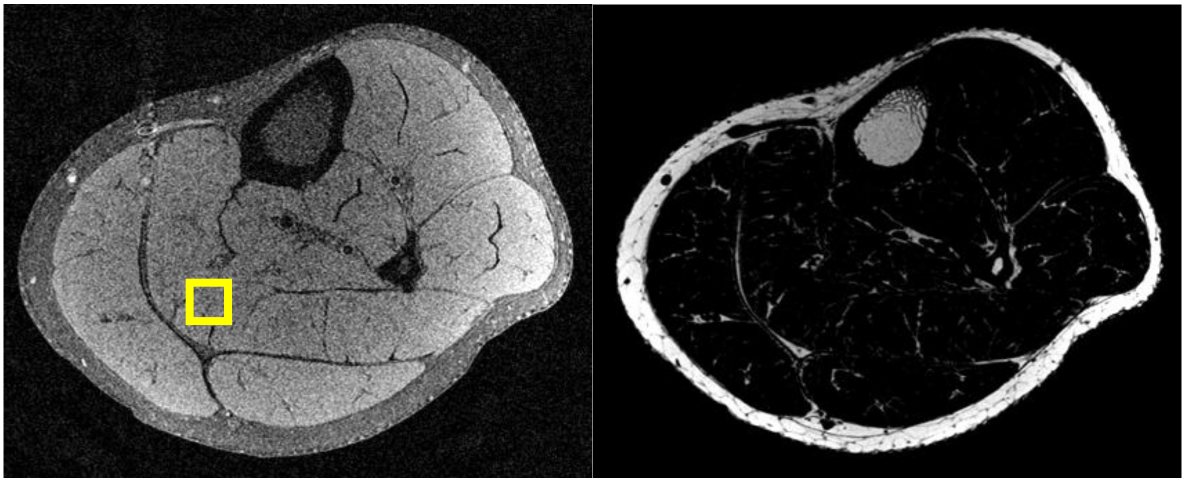

Figure 9-3 IDEAL images from calf region. The image on the left illustrates the water component with the yellow box illustrating the position of the MRS acquisition voxel. The image on the right illustrates the fat component. Note the good image quality with delineation of the individual muscles.

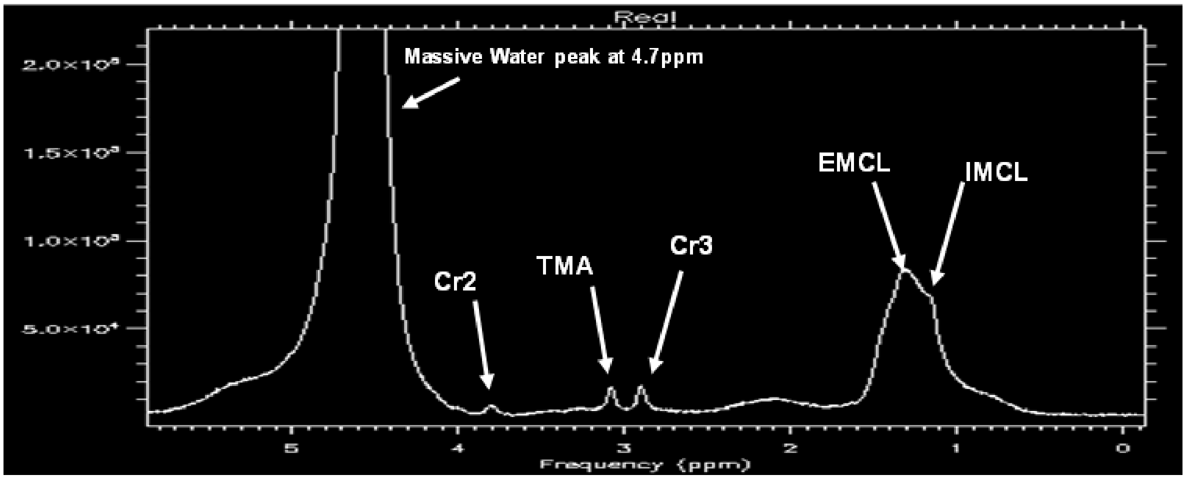

Figure 9-4 Single voxel ^{1}H PRESS spectrum from soleus muscle, with illustration of the various metabolites.

The results illustrate the potential of acquiring MR data at muscular regions, which could be used for clinical or research analysis of abnormalities and diseases in muscles as well as adjacent skeletal tissues. Additional metabolic data could also be acquired by using ^{31}P spectroscopy (e.g. ATP/ADP concentrations) and other types of imaging techniques (e.g. diffusion, perfusion) in the future.

9.3.4 Optimal Classification of Volunteers from the HBM Study

The volunteers in the HBM study comprised primary index people who were selected based on their previous DEXA scores, in addition to their relatives and/or spouses. All subjects were classified by the principal investigators of the HBM study at Bristol with a set of default classification criteria for HBM, borderline HBM and controls, by using their Z-scores from first lumbar vertebra and hip (see Figure 9-5). All the statistical analyses in this thesis were based on the recommended criteria for the wider study [36], which were different for each type of family member, as explained in Chapter 8 (with the index and spouses treated in the same way and relatives treated differently when identifying HBM-affected individuals). For classification of the individual populations the investigators have used the old (pre-study) Z-scores for some people and the new (intra-study) Z-scores for others. The criteria were also different, and complex for each population due to varied clinical reasons like age and genetic compatibility.

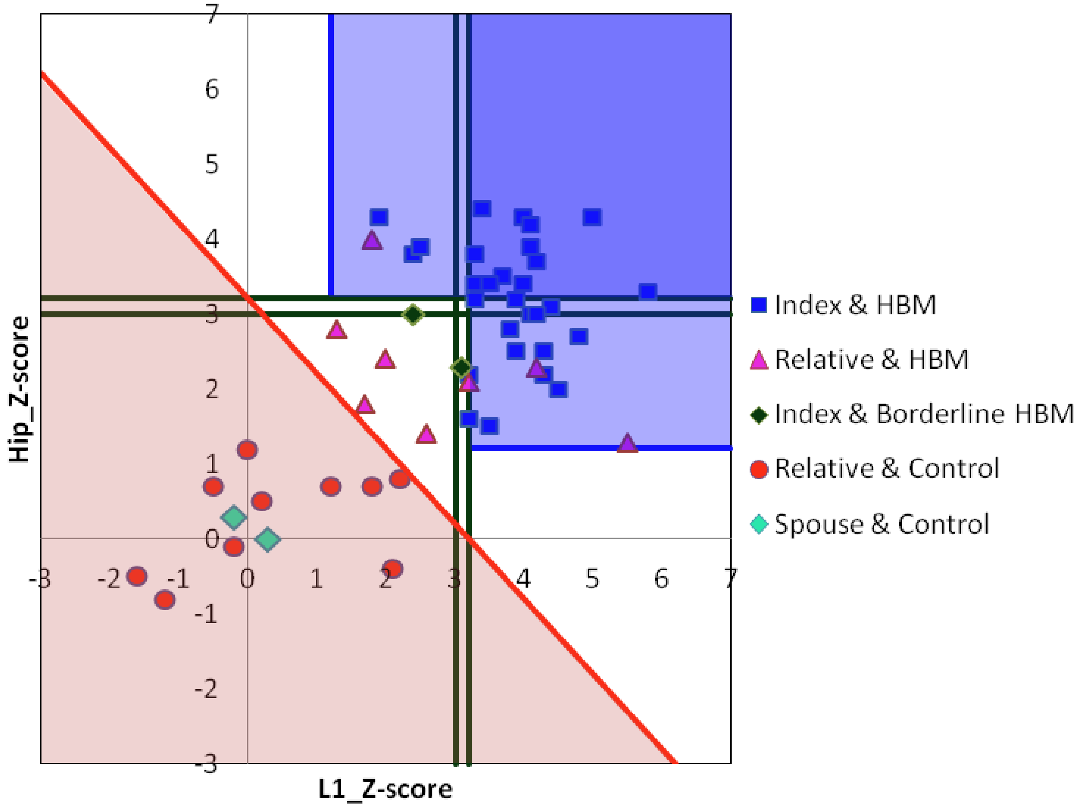

Figure 9-5 Reproduces Figure 8-1 and shows the classification scheme used in this thesis for each type of populations.

The aim in this final section is to illustrate the potential of using an alternative criterion that could be simpler in differentiating the HBM-affected and control volunteers. The alternative criterion was based on the genetics work by Little *et al*. [224] for investigation of high bone mass due to a mutation in LRP5 gene. Their work determined a clear difference between affected individuals and controls and they recommended a criterion which differentiated them effectively, based on the combined Z-score of hip and spine being greater or lower than 4. Their criterion worked well for all types of populations as well as for different age groups. The aim in future is, therefore, to use the simplified criterion for re-classification of all subjects into HBM-affected and controls and then to determine how results and conclusions are affected. The exclusive use of the most recent DEXA measurements only for classification is also to be investigated.

Following is an example plot (see Figure 9-6) for all the volunteers in this thesis who were classified based on the new criterion and also by using the DEXA scores recommended by the Bristol team. Based on the new classification, one relative who was previously classified as HBM has now been reclassified as control, thus there are now 13 controls (an increase of 8%). The previously classified HBM individuals still remain as HBM-affected, and the two index borderline HBM individuals are now reclassified as HBM. Thus there are now 39 HBM-affected individuals (an increase of 3%).

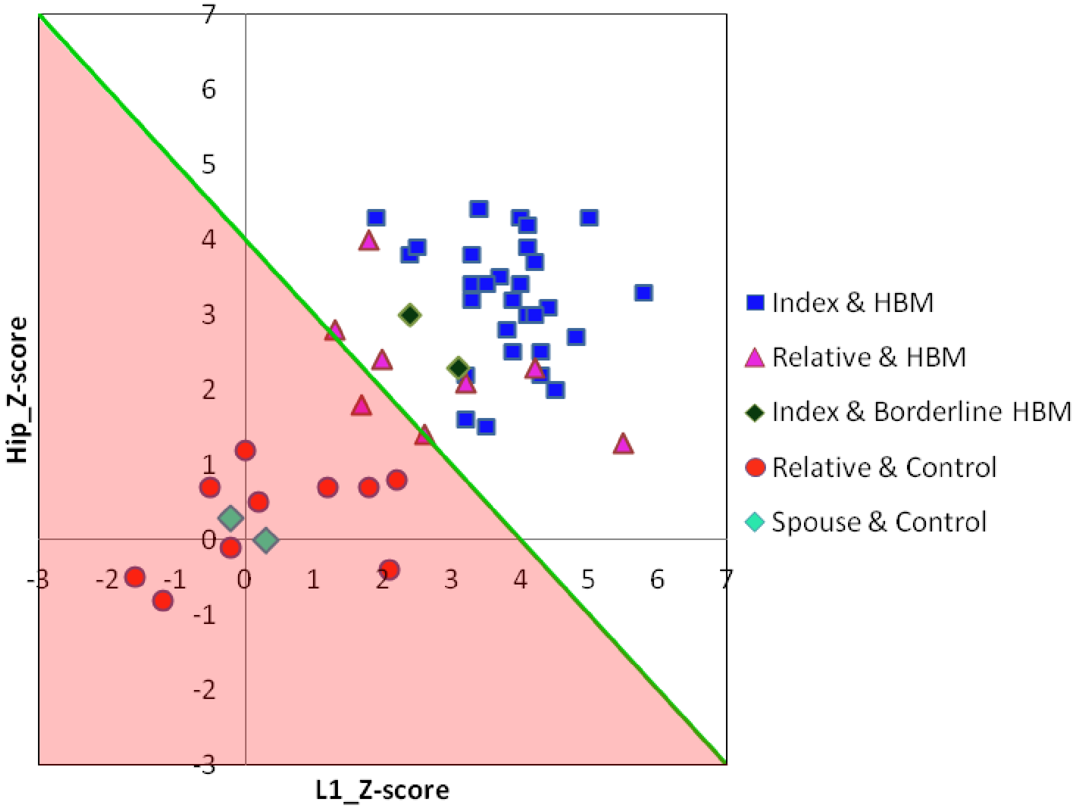

Figure 9-6 Presents the actual Z-score data that was used in this thesis for the classification and also shows the single line used in the simpler scheme of Little et al. The red region is for controls and the white region is for HBM-affected. The symbols used for each datum are the same as used in Figure 9-5, and this shows that one relative who was previously classified as HBM has now become a control. The two index borderline HBM individuals are now classified as HBM, and all the index HBM individuals still remain HBM. Note that there is one relative who has a combined Z-score of 4.0 and lies exactly on the criterion line and is classified as HBM-affected.

Following is an example plot (see Figure 9-7) for all the volunteers in this thesis who were classified based on the new criterion and by using only the intra-study DEXA scores. Based on the new classification, one relative who was previously classified as HBM has now been reclassified as control, thus there are now 13 controls (an increase of 8% over Figure 9-5). The previously classified HBM individuals still remain as HBM-affected, and the two index borderline HBM individuals are now reclassified as HBM. Two index individuals did not undergo DEXA examination during the study, thus they were excluded. Now there are 37 HBM-affected individuals (a decrease of 3% over Figure 9-5).

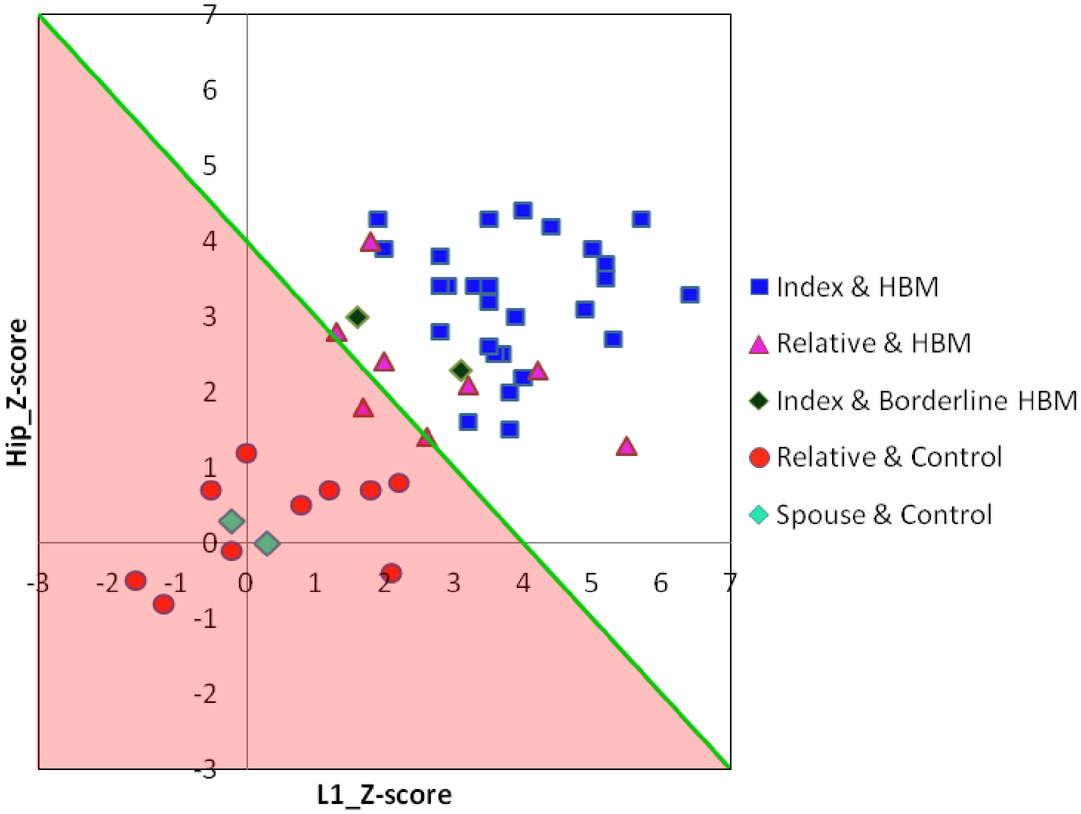

Figure 9-7 Presents intra-study Z-score data only and also shows the single line used in the simpler scheme of Little et al. The symbols used for each datum are the same as used in Figure 9-5 & Figure 9-6, and there is no difference in the number of newly classified HBM and controls when compared with Figure 9-6, except for two missing data from index individuals who did not have DEXA examination during the study. Note that there is one relative who has a combined Z-score of 4.0 and lies exactly on the criterion line and is classified as HBM-affected.

The change in criteria showed negligible changes for the number of individuals being reclassified as HBM-affected or controls.

9.4 Future Work

9.4.1 Repeatability of MR Measurements

The MR technique has demonstrated the potential of acquiring various types of *in vivo* data from bones, which have been processed to measure different types of quantitative information. It is important to note that only some of the quantitative data (e.g. FF, BVF) have been previously assessed to illustrate the repeatability of the results. The MR measurements from patients may be affected by various factors like instrumental changes, data analysis, physiological activity, diet, medications and age which may result in variations in some or all of the MR data. The aim in future is also to acquire repeated measurements from volunteers, both HBM and controls, to observe possible changes in the MR measurements.

10 Work Supporting This Thesis

10.1 Presentations

1. *Lazar V.R., Liney G.P., Manton D.J. and Turnbull L.W.* “Use of MRI and MRS for Quantification of Bones” Research Presentation, Bone Research Unit, Sheffield, UK. (August 2011)

2. *Lazar V.R., Liney G.P., Manton D.J., Langton C., Fagan M.J. and Turnbull L.W.* “Micro Imaging Phantom on a Clinical MRI Scanner” 20th Annual Postgraduate Symposium of the British Chapter - International Society for Magnetic Resonance in Medicine (BC-ISMRM), Cambridge, UK. (March 2011)

3. *Lazar V.R., Liney G.P., Manton D.J., Gibbs P., Lowry M., Gregson C.L., Steel S., Rittweger J., Langton C., Tobias J.H. and Turnbull L.W.* “Multi-Modality Imaging for Bone Quantification” Clinical Biosciences Institute Research Day, Hull, UK. (July 2010)

4. *Lazar V.R., Liney G.P., Manton D.J., Gibbs P., Lowry M., Gregson C.L., Steel S., Rittweger J., Langton C., Tobias J.H. and Turnbull L.W.* “Software Tools for MR and pQCT Bone Quantification” Yorkshire Cancer Research (YCR) Annual Scientific Meeting, Harrogate, UK. (June 2010)

10.2 Abstracts

1. *Gregson C.L., Sayers A., Lazar V.R., Steel S., Rittweger J. and Tobias J.H.* “The High Bone Mass Phenotype is Characterised by Increased Subcutaneous and Intra-muscular Fat, but Decreased Marrow Fat” Proc at American Society for Bone and Mineral Research (ASBMR), San Diego, USA. (September 2011)

2. *Lazar V.R., Liney G.P., Manton D.J. and Turnbull L.W.* “Identifying the Method of Measuring Ideal Water and Lipid Signal using Single Voxel PRESS MR Spectroscopy at 3.0 T” Poster No - 49, YCR Annual Scientific Meeting, Harrogate, UK. (June 2011)

3. *Lazar V.R., Liney G.P., Manton D.J., Gibbs P., Gregson C.L., Steel S., Rittweger J., Tobias J.H. and Turnbull L.W.* “Quantification using Textural Analysis on MR Bone Data” Electronic-Poster, ISMRM, Montreal, Canada. (May 2011)

4. *Lazar V.R., Liney G.P., Manton D.J., Gibbs P., Lowry M., Gregson C.L., Steel S., Rittweger J., Langton C., Tobias J.H. and Turnbull L.W.* “Software for Bone Quantification using Multi-modality Imaging” Poster No – 785, ISMRM, Stockholm, Sweden. (May 2010)

5. *Lazar V.R., Liney G.P., Manton D.J., Gibbs P., Lowry M., Gregson C.L., Steel S., Rittweger J., Langton C., Tobias J.H. and Turnbull L.W.* “Preliminary *in vivo* bone quantification results using MR and pQCT” Poster No – 784, ISMRM, Stockholm, Sweden. (May 2010)

6. *Lazar V.R., Liney G.P., Manton D.J., Schirmer T., Noeske R., Lowry M., Lorch M. and Turnbull L.W.* “Anomalous lipid signal investigation when measuring water/lipid signal with unsuppressed 1H MR Spectroscopy” Poster No – 936, ISMRM, Stockholm, Sweden. (May 2010)

7. *Manton D.J., Lazar V.R., Schirmer T., Noeske R., Liney G.P., Lowry M., Lorch M. and Turnbull L.W.* “Measuring water:lipid signal ratios with proton MR spectroscopy: dealing with anomalous lipid signal behaviour” Proc at European Society for Magnetic Resonance in Medicine and Biology (ESMRMB), Antalya, Turkey. (October 2009)

8. *Lazar V.R., Liney G.P., Manton D.J., Gibbs P., Lowry M., Gregson C.L., Steel S., Rittweger J., Langton C., Tobias J.H. and Turnbull L.W.* “Software for Bone Quantification using Multi-modality Imaging” Proc at BC-ISMRM, Cardiff, UK. (September 2009)

9. *Gregson C.L., Rittweger J., Lazar V.R., Steel S. and Tobias J.H.* “The High Bone Mass phenotype is characterised by increased trabecular density and reduced endosteal expansion” Proc at ASBMR, Denver, USA. (September 2009)

11 References

1. [http://depts.washington.edu/bonebio/ASBMRed/ASBMRed.html]

2. Boron WF, Boulpaep EL: *Medical Physiology:* 2nd ed. Saunders; 2008.

3. Boron WF, Boulpaep EL: *Medical Physiology: A Cellular and Molecular Approach:* USA: Saunders; 2005.

4. Compston JE: **Bone marrow and bone: a functional unit.** J Endocrinol 2002, **173**(3):387-394.

5. Gentry SD, Bramblett CA: *The Anatomy and Biology of the Human Skeleton:* Texas A&M University Press; 1988.

6. Marieb KH, Nicpon E: *Human Anatomy and Physiology:* 7th ed. USA: Benjamin Cummings; 2007.

7. Netter FH: *Musculoskeletal system: anatomy, physiology and metabolic disorders:* USA: Ciba-Geigy Corporation; 1987.

8. Sommerfeldt DW, Rubin CT: **Biology of bone and how it orchestrates the form and function of the skeleton.** *European Spine Journal* 2001, **10**(0)**:**S86-S95.

9. Tortora GJ, Derrickson B: *Principles of Anatomy and Physiology:* 11th ed. USA: John Wiley & Sons; 2006.

10. Lajeunesse D, Busque L, Menard P, Brunette MG, Bonny Y: **Demonstration of an Osteoblast Defect in Two Cases of Human Malignant Osteopetrosis.** Journal of Clinical Investigation 1996, **98**(8):1835-1842.

11. Rodan GA, Martin TJ: **Role of osteoblasts in hormonal control of bone resorption--a hypothesis.** Calcif Tissue Int 1981, **33**(4):349-351.

12. Seynnes OR, Rittweger J: **What is new in musculoskeletal interactions? Lateral force transmission, botox, calcium and bone strength, and osteoccyte apoptosis.** J Musculoskelet Neuronal Interact 2010, **10**(2):124-127.

13. Teitelbaum SL: **Osteoclasts: what do they do and how do they do it?** Am J Pathol 2007, **170**(2):427-435.

14. Martin TJ, Sims NA: **Osteoclast-derived activity in the coupling of bone formation to resorption.** Trends Mol Med 2005, **11**(2):76-81.

15. Field RA, Riley ML, Mello FC, Corbridge JH, Kotula AW: **Bone Composition in Cattle, Pigs, Sheep and Poultry.** Journal of Animal Science 1974, **39**(3):493-499.

16. Gurevitch O, Slavin S, Feldman AG: **Conversion of red bone marrow into yellow – Cause and mechanisms.** Med Hypotheses 2007, **69**(3):531-536.

17. Knothe G, Kenar JA: **Determination of the fatty acid profile by 1H-NMR spectroscopy.** European Journal of Lipid Science and Technology 2004, **106**(2):88-96.

18. Snyder F: **Triglyceride biosynthesis in irradiated bone marrow.** Radiat Res 1966, **27**(3):375-383.

19. Stevens SK, Moore SG, Kaplan ID: **Early and Late Bone-Marrow Changes After Irradiation: MR Evaluation.** American Journal of Radiology 1990, **154**:745-750.

20. Szczepaniak LS, Babcock EE, Schick F, Dobbins RL, Garg A, Burns DK, McGarry DJ, Stein DT: **Measurement of intracellular triglyceride stores by H spectroscopy: validation in vivo.** American Journal of Physiology - Endocrinology And Metabolism 1999, **276**(5):E977-E989.

21. Burkhardt R, Kettner G, Böhm W, Schmidmeier M, Schlag R, Frisch B, Mallmann B, Eisenmenger W, Gilg T: **Changes in trabecular bone, hematopoiesis and bone marrow vessels in aplastic anemia, primary osteoporosis, and old age: A comparative histomorphometric study.** Bone 1987, **8**(3):157-164.

22. Belloque J: **High-Resolution NMR of Milk and Milk Proteins.** 2006, **:**1631-1635.

23. Lazner F, Gowen M, Pavasovic D, Kola I: **Osteopetrosis and osteoporosis: two sides of the same coin.** Hum Mol Genet 1999, **8**(10):1839-1846.

24. Kanis JA: **Assessment of fracture risk and its application to screening for postmenopausal osteoporosis: Synopsis of a WHO report.** *Osteoporosis International* 1994, **4**(6)**:**368-381.

25. Kanis JA: **Diagnosis of osteoporosis and assessment of fracture risk.** The Lancet 2002, **359**(9321):1929-1936.

26. Harris ST, Jaffe RB, Shoback D: **Menopause and Bone Loss.** J Clin Endocrinol Metab 2006, **91**(3):0.

27. Baylink DJ: **Glucocorticoid-induced osteoporosis.** N Engl J Med 1983, **309**(5):306-308.

28. Baur A, Huber A, Ertl-Wagner B, Durr R, Zysk S, Arbogast S, Deimling M, Reiser M: **Diagnostic Value of Increased Diffusion Weighting of a Steady-state Free Precession Sequence for Differentiating Acute Benign Osteoporotic Fractures from Pathologic Vertebral Compression Fractures.** AJNR Am J Neuroradiol 2001, **22**(2):366-372.

29. Mankin HJ: **Rickets, osteomalacia, and renal osteodystrophy. An update.** Orthop Clin North Am 1990, **21**(1):81-96.

30. Paunier L: **RICKETS AND OSTEOMALACIA.** In *Nutrition in Preventive Medicine.* 1st edition. Edited by Beaton GH, Bengoa JM. Geneva: World Health Organization; 1976:111-119.

31. Del Fattore A, Cappariello A, Teti A: **Genetics, pathogenesis and complications of osteopetrosis.** Bone 2008, **42**(1):19-29.

32. Marks SC,Jr, Lane PW: **Osteopetrosis, a new recessive skeletal mutation on chromosome 12 of the mouse.** J Hered 1976, **67**(1):11-18.

33. Michou L, Brown JP: **Genetics of bone diseases: Paget's disease, fibrous dysplasia, osteopetrosis, and osteogenesis imperfecta.** Joint Bone Spine 2010.

34. Tolar J, Teitelbaum SL, Orchard PJ: **Osteopetrosis.** N Engl J Med 2004, **351**(27):2839-2849.

35. Gregson CL, Tobias J: **Interpretation of high bone mineral density measurements.** Osteoporosis Review 2007, **15**(2):1-6.

36. Gregson CL, Steel SA, O'Rourke KP, Allan K, Ayuk J, Bhalla A, Clunie G, Crabtree N, Fogelman I, Goodby A, Langman CM, Linton S, Marriott E, McCloskey E, Moss KE, Palferman T, Panthakalam S, Poole KE, Stone MD, Turton J, Wallis D, Warburton S, Wass J, Duncan EL, Brown MA, Davey-Smith G, Tobias JH: **'Sink or swim': an evaluation of the clinical characteristics of individuals with high bone mass.** Osteoporosis International 2011.

37. Levasseur R, Lacombe D, Christine de Vernejoul M: **LRP5 mutations in osteoporosis-pseudoglioma syndrome and high-bone-mass disorders.** Joint Bone Spine 2005, **72**(3):207-214.

38. Whyte MP, Reinus WH, Mumm S: **High-bone-mass disease and LRP5.** New England Journal of Medicine 2004, **20**(350):2096-2099.

39. Yadav VK, Ducy P: **Lrp5 and bone formation: A serotonin-dependent pathway.** Ann N Y Acad Sci 2010, **1192**:103-109.

40. Shapiro CL, Manola J, Leboff M: **Ovarian failure after adjuvant chemotherapy is associated with rapid bone loss in women with early-stage breast cancer.** J Clin Oncol 2001, **19**(14):3306-3311.

41. Mitchell MJ, Logan MP: **Radiation-induced Changes in Bone.** RadioGraphics 1998, **18**:1125-1136.

42. Khan A, Khan N: **Cancer Treatment Related Bone Loss.** Current Oncology 2007, **15**(0).

43. Legros R, Balmain N, Bonel G: **Age-related changes in mineral of rat and bovine cortical bone.** Calcif Tissue Int 1987, **41**(3):137-144.

44. Sode M, Burghardt AJ, Kazakia GJ, Link TM, Majumdar S: **Regional variations of gender-specific and age-related differences in trabecular bone structure of the distal radius and tibia.** Bone 2010, **46**(6):1652-1660.

45. Wust RCI, Winwood K, Wilks DC, Morse CI, Degens H, Rittweger J: **Effects of Smoking on Tibial and Radial Bone Mass and Strength May Diminish with Age.** J Clin Endocrinol Metab 2010, **95**(6):2763-2771.

46. Ward KAea: **Influence of age and sex steroids on bone density and geometry in middle-aged and elderly European men [abstract].** *Osteoporosis Int* 2010.

47. Tornvig L, Mosekilde L, Justesen J, Falk E, Kassem M: **Troglitazone Treatment Increases Bone Marrow Adipose Tissue Volume but Does not Affect Trabecular Bone Volume in Mice.** Calcified Tissue International 2001, **69**:46-50.

48. Manolides AS, Cullen DM, Akhter MP: **Effects of glucocorticoid treatment on bone strength.** J Bone Miner Metab 2010, **28**(5):532-539.

49. McIlwain HH: **Glucocorticoid-induced osteoporosis: pathogenesis, diagnosis, and management.** Prev Med 2003, **36**(2):243-249.

50. Benito M, Vasilic B, Wehrli FW, Bunker B, Wald M, Gomberg B, Wright AC, Zemel B, Cucchiara A, Snyder PJ: **Effect of Testosterone Replacement on Trabecular Architecture in Hypogonadal Men.** Journal of Bone and Mineral Research 2005, **20**(10):1785-1791.

51. Giustina A, Angeli A, Canalis E: *Glucocorticoid-Induced Osteoporosis:* Switzerland: Karger; 2002.

52. Guest I, Uetrecht J: **Drugs toxic to the bone marrow that target the stromal cells.** Immunopharmacology 2000, **46**(2):103-112.

53. Stoico Rea: **Quality control protocol for in vitro micro-computed tomography [abstract].** *J Microsc* 2009.

54. Jiang Y, Zhao J, Genant HK: **Macro- and Microimaging of Bone Architecture.** In *Principles of Bone Biology (Second Edition).* Edited by Bilezikian JP, Raisz LG, Rodan GA. San Diego: Academic Press; 2002:1599-1623.

55. Curry TS, Dowdey JE, Murry RC: *Christen's Physics of Diagnostic Radiology:* 4th ed. USA: Lea & Febiger; 1990.

56. Bauer JS, Link TM: **Advances in osteoporosis imaging.** Eur J Radiol 2009, **71**(3):440-449.

57. Langton CM, Njeh CF: *The Physical Measurement Of Bone:* UK: Institute of Physics Publishing; 2004.

58. Evans W: **Principles of Operation of DXA Systems.** 2006, **:**.

59. Guglielmi G, Gluer CC, Majumdar S, Blunt BA, Genant HK: **Current methods and advances in bone densitometry.** European Radiology 1995, **5**:129-139.

60. Heaney RP: **BMD: The problem.** *Osteoporosis International* 2005, **16**(9)**:**1013-1015.

61. Kang C, Speller R: **Comparison of ultrasound and dual energy X-ray absorptiometry measurements in the calcaneus.** Br J Radiol 1998, **71**(848):861-867.

62. Kazakia GJ, Majumdar S: **New imaging technologies in the diagnosis of osteoporosis.** Rev Endocr Metab Disord 2006, **7**(1-2):67-74.

63. Kröger H, Vainio P, Nieminen J, Kotaniemi A: **Comparison of different models for interpreting bone mineral density measurements using DXA and MRI technology.** Bone 1995, **17**(2):157-159.

64. Wilson KE: **Emerging trends in dual energy X-ray absorptiometry.** Radiol Manage 2006, **28**(4):50-55.

65. Brahm H, Ström H, Piehl-Aulin K, Mallmin H, Ljunghall S: **Bone Metabolism in Endurance Trained Athletes: A Comparison to Population-Based Controls Based on DXA, SXA, Quantitative Ultrasound, and Biochemical Markers.** *Calcified Tissue International* 1997, **61**(6)**:**448-454.

66. Diederichs G, Link TM, Kentenich M, Schwieger K, Huber MB, Burghardt AJ, Majumdar S, Rogalla P, Issever AS: **Assessment of trabecular bone structure of the calcaneus using multi-detector CT: Correlation with microCT and biomechanical testing.** Bone 2009, **44**(5):976-983.

67. Issever AS, Link TM, Kentenich M, Rogalla P, Burghardt A, Kazakia G, Majumdar S, Diederichs G: **Assessment of trabecular bone structure using MDCT: comparison of 64- and 320-slice CT using HR-pQCT as the reference standard.** *European Radiology* 2010, **20**(2)**:**458-468.

68. Khider M, Taleb-Ahmed A, Dubois P, Haddad B: **Classification of trabecular bone texture from MRI and CT scan images by multi resolution analysis.** Conf Proc IEEE Eng Med Biol Soc 2007, **2007**:5589-5592.

69. Lang TF, Keyak JH, Heitz MW, Augat P, Lu Y, Mathur A, Genant HK: **Volumetric quantitative computed tomography of the proximal femur: Precision and relation to bone strength.** Bone 1997, **21**(1):101-108.

70. Link TM, Vieth V, Stehling C, Lotter A, Beer A, Newitt D, Majumdar S: **High-resolution MRI vs multislice spiral CT: Which technique depicts the trabecular bone structure best?** European Radiology 2003, **13**:663-671.

71. Link TM, Majumdar S, Lin JC, Newitt D, Augat P, Ouyang X, Mathur A, Genant HK: **A Comparative Study of Trabecular Bone Properties in the Spine and Femur using High Resolution MRI and CT.** Journal of Bone and Mineral Research 1998, **13**(1):122-132.

72. Lang T, Augat P, Majumdar S, Ouyang X, Genant HK: **Noninvasive assessment of bone density and structure using computed tomography and magnetic resonance.** Bone 1998, **22**(5 Suppl):149S-153S.

73. Adams JEea: **Recommendations for Thresholds for Cortical Bone Geometry and Density Measurement by Peripheral Quantitative Computed Tomography [abstract].** *Calcif Tissue Int* 2005; .

74. Augat Pea: **Accuracy of cortical and trabecular bone measurements with peripheral quantitative computed tomography (pQCT) [abstract].** *Phys Med Biol* 1998; **43:**2873.

75. Braun MJea: **Clinical evaluation of a high-resolution new peripheral quantitative computerized tomography (pQCT) scanner for the bone densitometry at the lower limbs [abstract].** *Phys Med Biol* 1998; **43:**2279.

76. Capozza RF, Feldman S, Mortarino P, Reina PS, Schiessl H, Rittweger J, Ferretti JL, Cointry GR: **Structural analysis of the human tibia by tomographic (pQCT) serial scans.** J Anat 2010, **216**(4):470-481.

77. Issever AS, Link TM, Newitt D, Munoz T, Majumdar S: **Interrelationships between 3-T-MRI-derived cortical and trabecular bone structure parameters and quantitative-computed-tomography-derivedbone mineral density.** Magn Reson Imaging 2010, **28**(9):1299-1305.

78. Jiang Y, Zhao J, Augat P, Ouyang X, Lu Y, Majumdar S, Genant HK: **Trabecular bone mineral and calculated structure of human bone specimens scanned by peripheral quantitative computed tomography: relation to biomechanical properties.** J Bone Miner Res 1998, **13**(11):1783-1790.

79. Sekhon K, Kazakia GJ, Burghardt AJ, Hermannsson B, Majumdar S: **Accuracy of volumetric bone mineral density measurement in high-resolution peripheral quantitative computed tomography.** Bone 2009, **45**(3):473-479.

80. Tysarczyk-Niemeyer G: **New Noninvasive pQCT Devices to Determine Bone Structure.** The Journal of the Japanese Society for Bone Morphometry 1997, **7**:97-105.

81. Vokes TJ, Favus MJ: **Noninvasive assessment of bone structure.** Curr Osteoporos Rep 2003, **1**(1):20-24.

82. Wilks DC, Winwood K, Gilliver SF, Kwiet A, Chatfield M, Michaelis I, Sun LW, Ferretti JL, Sargeant AJ, Felsenberg D, Rittweger J: **Bone mass and geometry of the tibia and the radius of master sprinters, middle and long distance runners, race-walkers and sedentary control participants: A pQCT study.** Bone 2009, **45**(1):91-97.

83. Faulkner KG, McClung MR, Coleman LJ, Kingston-Sandahl E: **Quantitative ultrasound of the heel: correlation with densitometric measurements at different skeletal sites.** Osteoporos Int 1994, **4**(1):42-47.

84. Foldes AJ, Rimon A, Keinan DD, Popovtzer MM: **Quantitative ultrasound of the tibia: A novel approach for assessment of bone status.** Bone 1995, **17**(4):363-367.

85. Gluer CC, Wu CY, Jergas M, Goldstein SA, Genant HK: **Three quantitative ultrasound parameters reflect bone structure.** *Calcified Tissue International* 1994, **55**(1)**:**46-52.

86. Hans D, Fuerst T, Duboeuf F: **Quantitative ultrasound bone measurement.** European Radiology 1997, **7**(2):S43-S50.

87. Langton CM, Langton DK: **Comparison of bone mineral density and quantitative ultrasound of the calcaneus: site-matched correlation and discrimination of axial BMD status.** The British journal of radiology 2000, **73**(865):31-35.

88. Langton CM, Njeh CF: **The Measurement of Broadband Ultrasonic Attenuation in Cancellous Bone-A Review of the Science and Technology.** Ultrasonics, Ferroelectrics and Frequency Control, IEEE Transactions on 2008, **55**(7):1546-1554.

89. Langton CM, Njeh CF: **Sound-Tissue Interaction: The Physical Basis of Bone Ultrasonometry and Limitations of Existing Methods.** Journal of Clinical Densitometry 1998, **1**(3):295-301.

90. Langton CM, Njeh CF, Hodgskinson R, Currey JD: **Prediction of mechanical properties of the human calcaneus by broadband ultrasonic attenuation.** Bone 1996, **18**(6):495-503.

91. Lin JD, Chen JF, Chang HY, Ho C: **Evaluation of bone mineral density by quantitative ultrasound of bone in 16862 subjects during routine health examination.** British Journal of Radiology 2001, **74**:602-606.

92. Njeh CF, Fuerst T, Diessel E, Genant HK: **Is quantitative ultrasound dependent on bone structure? A reflection.** Osteoporos Int 2001, **12**(1):1-15.

93. Bakhtiary M, Ryiahi-Alam N, Oghabian MA, Ghasemzadeh A, Ghanaati H, Sarkar S, Larijani B, Hamidy-Abarghouie Z, Shakery N: **MRI-relaxometry BMD-measurements using conventional phase symmetrized rapid increased flip spin echo (PRISE) and standard gradient echo (GE).** In *IFMBE Proceedings.* Edited by Anonymous Springer Berlin Heidelberg; 2007:1384-1387.

94. Balliu E, Vilanova JC, Peláez I, Puig J, Remollo S, Barceló C, Barceló J, Pedraza S: **Diagnostic value of apparent diffusion coefficients to differentiate benign from malignant vertebral bone marrow lesions.** Eur J Radiol 2009, **69**(3):560-566.

95. Capuani S, Rebuzzi M, Fasano F, Hagberg G, Mario MD, Maraviglia B, Vinicola V: **MR Multi-parametric approach to evaluate osteoporosis at 3T: T2, T2*, ADC, Gi and 1H-MRS measurements in healthy, osteopenic and osteoporic subjects [abstract].** 2009; .

96. Lammentausta E, Hakulinen MA, Jurvelin JS, Nieminen MT: **Prediction of mechanical properties of trabecular bone using quantitative MRI.** Physics in Medicine and Biology 2006, **51**:6187-6198.

97. Sell CA, Masi JN, Burghardt A, Newitt D, Link TM, Majumdar S: **Quantification of Trabecular Bone Structure Using Magnetic Resonance Imaging at 3 Tesla - Calibration Studies Using Microcomputed Tomography as a Standard of Reference.** Calcified Tissue International 2005, **76**:355-364.

98. Drost DJ, Riddle WR, Clarke GD: **Proton magnetic resonance spectroscopy in the brain: report of AAPM MR Task Group #9.** Med Phys 2002, **29**(9):2177-2197.

99. Hashemi RH, Bradley Jr WG, Lisanti CJ: *MRI The Basics:* 3rd ed. USA: Lippincott Williams & Wilkins; 2010.

100. Liney GP: *MRI from A to Z:* UK: Springer; 2010.

101. McRobbie DW, Moore EA, Graves MJ, Prince MR: *MRI From Picture to Proton:* 2nd ed. USA: Cambridge University Press; 2010.

102. McRobbie DW, Moore EA, Graves MJ, Prince MR: *MRI From Picture to Proton:* 2nd ed. UK: Cambridge University Press; 2007.

103. University of Aberdeen: **Deeper Study 3: Magnetic Resonance Imaging.** 2007, **2006-2007**.

104. Bottomley PA: **Spatial Localization in NMR Spectroscopy in Vivo.** Annals of the New York Academy of Sciences 1987, **508**:333-348.

105. Starck G, Carlsson A, Ljungberg M, Forssell-Aronsson E: **k-space analysis of point-resolved spectroscopy (PRESS) with regard to spurious echoes in *in vivo* ^{1}H MRS.** NMR in Biomedicine 2008, **22**(2):137-147.

106. Du J, Chiang A, Takahashi AM, Chung CB, Bydder GM: **Bulk Susceptibility Mapping Using Ultrshort TE Spectroscopic Imaging (UTESI) [abstract].** 2009.

107. Dixon TW: **Simple Proton Spectroscopic Imaging.** Radiology 1984, **153**:189-194.

108. Kim H, Taksali SE, Dufour S, Befroy D, Goodman RT, Petersen KF, Shulman GI, Caprio S, Constable TR: **Comparative MR study of hepatic fat quantification using single-voxel proton spectroscopy, two-point dixon and three-point IDEAL.** Magnetic Resonance in Medicine 2008, **59**(3):521-527.

109. Reeder SB, Pineda AR, Wen Z, Shimakawa A, Yu H, Brittain JH, Gold GE, Beaulieu CH, Pelc NJ: **Iterative decomposition of water and fat with echo asymmetry and least-squares estimation (IDEAL): Application with fast spin-echo imaging.** Magnetic Resonance in Medicine 2005, **54**(3):636-644.

110. Reeder SB, Robson PM, Yu H, Shimakawa A, Hines CDG, McKenzie CA, Brittain JH: **Quantification of hepatic steatosis with MRI: The effects of accurate fat spectral modeling.** Journal of Magnetic Resonance Imaging 2009, **29**(6):1332-1339.

111. Reeder SB, Wen Z, Yu H, Pineda AR, Gold GE, Markl M, Pelc NJ: **Multicoil Dixon chemical species separation with an iterative least-squares estimation method.** Magnetic Resonance in Medicine 2004, **51**(1):35-45.

112. Barger AV, DeLone DR, Bernstein MA, Welker KM: **Fat Signal Suppression in Head and Neck Imaging Using Fast Spin-Echo-IDEAL Technique.** American Journal of Neuroradiology 2006, **27**:1292-1294.

113. Chang JS, Taouli B, Salibi N, Hecht EM, Chin DG, Lee VS: **Opposed-phase MRI for fat quantification in fat-water phantoms with 1H MR spectroscopy to resolve ambiguity of fat or water dominance.** AJR Am J Roentgenol 2006, **187**(1):W103-6.

114. Kovanlikaya A, Guclu C, Desai C, Becerra R, Gilsanz V: **Fat Quantification Using Three-point Dixon Technique: In Vitro Validation1.** Acad Radiol 2005, **12**(5):636-639.

115. Kozawa E, Song HK, Wehrli FW, Takahashi M, Hilaire L: **Quantitative Measurement of Bone Marrow Composition Using a Multi-Echo Gradient-Echo Sequence and 3-Point Dixon Processing [abstract].** 2000.

116. Song HK, Wright AC, Wolf RL, Wehrli FW: **Comparison of 2- and 3-Point dixon Techniques in RF- and Readout-Shifted FSE Sequences [abstract].** 2000.

117. Zhuo J, Gullapalli RP: **MR Artifacts, Safety, and Quality Control1.** Radiographics January-February 2006, **26**(1):275-297.

118. Hood MN, Ho VB, Smirniotopoulos JG, Szumowski J: **Chemical Shift: The Artifact and Clinical Tool Revisited.** RadioGraphics 1999, **19**:357-371.

119. Clare S: **Functional MRI: Methods and Applications: Chapter 2 - Principles of Magnetic Resonance Imaging.** University of Nottingham, 1997

120. Juchem C, Muller-Bierl B, Schick F, Logothetis NK, Pfeuffer J: **Combined passive and active shimming for in vivo MR spectroscopy at high magnetic fields.** Journal of Magnetic Resonance 2006, **183**:278-289.

121. Steckner M: **MO-B-ValB-01: Advances in MRI Equipment Design, Software, and Imaging Procedures.** Med Phys 2006, **33**(6):2156-2157.

122. Skoch A, Jiru F, Bunke J: **Spectroscopic imaging: Basic principles.** Eur J Radiol 2008, **67**(2):230-239.

123. Tosetti M, Schirmer T, D'Alesio V, Costanzo AD, Scarabino T: **3.0 T MR Spectroscopy.** In *High Field Brain MRI.* Edited by Anonymous Springer Berlin Heidelberg; 2006:51-65.

124. Costanzo AD, Trojsi F, Tosetti M, Schirmer T, Lechner SM, Popolizio T, Scarabino T: **Proton MR spectroscopy of the brain at 3 T: an update.** European Radiology 2007, **17**(7):1651-1662.

125. Cox IJ: **Development and applications of in vivo clinical magnetic resonance spectroscopy.** Prog Biophys Mol Biol 1996, **65**(1-2):45-81.

126. Kreis R: **^{1}H MR Spectroscopy: Clinical Applications.** In *Methodology, Spectroscopy and Clinical MRI.* 1st edition. Edited by Cerdan S, Haase A, Terrier F. Springer; 2000.

127. van der Graaf M: **In vivo magnetic resonance spectroscopy: basic methodology and clinical applications.** *European Biophysics Journal* 2010, **39**(4)**:**527-540.

128. Ross AJ, Sachdev PS: **Magnetic resonance spectroscopy in cognitive research.** Brain Research Reviews 2004, **44**:83-102.

129. Passe TJ, Charles CH, Rajagopalan P, Krishnan RK: **Nuclear Magnetic Resonance Spectroscopy: A Review of NeuroPsychiatric Applications.** Prog Neuropsychopharmacol Biol Psychiatry 1995, **19**:541-563.

130. Barker PB, Lin DDM: **In vivo proton MR spectroscopy of the human brain.** Progress in Nuclear Magnetic Resonance Spectroscopy 2006, **49**:99-128.

131. Hamilton G, Middleton MS, Bydder M, Yokoo T, Schwimmer JB, Kono Y, Patton HM, Lavine JE, Sirlin CB: **Effect of PRESS and STEAM sequences on magnetic resonance spectroscopic liver fat quantification.** Journal of Magnetic Resonance Imaging 2009, **30**(1):145-152.

132. Kreis R: **Quantitative localized 1H MR spectroscopy for clinical use.** Prog Nucl Magn Reson Spectrosc 1997, **31**(2-3):155-195.

133. Klose U: **In vivo proton spectroscopy in presence of eddy currents.** Magnetic Resonance in Medicine 1990, **14**(1):26-30.

134. Provencher SW: **Automatic quantitation of localized in vivo1H spectra with LCModel.** NMR Biomed 2001, **14**(4):260-264.

135. Provencher SW: **Estimation of metabolite concentrations from localized in vivo proton NMR spectra.** Magn Reson Med 1993, **30**(6):672-679.

136. Provencher SW, Vogel RH: **Information loss with transform methods in system identification: a new set of transforms with high information content.** Math Biosci 1980, **50**(3-4):251-262.

137. Natt O, Bezkorovaynyy V, Michaelis T, Frahm J: **Use of phased array coils for a determination of absolute metabolite concentrations.** Magn Reson Med 2005, **53**(1):3-8.

138. Bydder M, Hamilton G, Yokoo T, Sirlin CB: **Optimal phased-array combination for spectroscopy.** Magn Reson Imaging 2008, **26**(6):847-850.

139. Brown MA: **Time-domain combination of MR spectroscopy data acquired using phased-array coils.** Magnetic Resonance in Medicine 2004, **52**(5):1207-1213.

140. Jost G, Harting I, Heiland S: **Quantitaive Single-Voxel Spectroscopy: The Reciprocity Principle for Receive-Only Head Coils.** Journal of Magnetic Resonance Imaging 2005, **21**:66-71.

141. Allein S, Majumdar S, De Bisschop E, Newitt DC, Luypaert R, Eisendrath H: **In vivo comparison of MR phase distribution and 1/T2* with morphologic parameters in the distal radius.** J Magn Reson Imaging 1997, **7**(2):389-393.

142. Carballido-Gamio J, Krug R, Huber MB, Hyun B, Eckstein F, Majumdar S, Link TM: **Geodesic Topological Analysis of Trabecular Bone Microarchitecture from High-Spatial Resolution Magnetic Resonance Images.** Magnetic Resonance in Medicine 2009, **61**:448-456.

143. Carballido-Gamio J, Phan C, Link TM, Majumdar S: **Characterization of trabecular bone structure from high-resolution magnetic resonance images using fuzzy logic.** Magn Reson Imaging 2006, **24**(8):1023-1029.

144. Chung HW, Wehrli FW, Williams JL, Wehrli SL: **Three-dimensional nuclear magnetic resonance microimaging of trabecular bone.** Journal of Bone and Mineral Research 1995, **10**(10):1452-1461.

145. De Bisschop E, Luypaert R, Allein S, Osteaux M: **Quantification of trabecular structure in the distal femur using magnetic resonance phase imaging.** Magn Reson Imaging 1996, **14**(1):11-20.

146. Genant HK, Gordon C, Jiang Y, Lang TF, Link TM, Majumdar S: **Advanced imaging of bone macro and micro structure.** Bone 1999, **25**(1):149-152.

147. Gomberg BR, Saha PK, Wehrli FW: **Method for cortical bone structural analysis from magnetic resonance images.** Acad Radiol 2005, **12**(10):1320-1332.

148. Griffith JF, Genant HK: **Bone mass and architecture determination: state of the art.** Best Practice & Research Clinical Endocrinology & Metabolism 2008, **22**(5):737-764.

149. Krug R, Banerjee S, Han ET, Newitt DC, Link TM, Majumdar S: **Feasibility of in vivo structural analysis of high-resolution magnetic resonance images of the proximal femur.** Osteoporos Int 2005, **16**(11):1307-1314.

150. Krug R, Carballido-Gamio J, Banerjee S, Burghardt AJ, Link TM, Majumdar S: **In vivo ultra-high-field magnetic resonance imaging of trabecular bone microarchitecture at 7 T.** Journal of Magnetic Resonance Imaging 2008, **27**(4):854-859.

151. Krug R, Carballido-Gamio J, Banerjee S, Stahl R, Carvajal L, Xu D, Vigneron D, Kelley DAC, Link TM, Majumdar S: **In vivo bone and cartilage MRI using fully-balanced steady-state free-precession at 7 tesla.** Magnetic Resonance in Medicine 2007, **58**(6):1294-1298.

152. Krug R, Carballido-Gamio J, Burghardt A, Kazakia G, Hyun B, Jobke B, Banerjee S, Huber M, Link TM, Majumdar S: **Assessment of trabecular bone structure comparing magnetic resonance imaging at 3 Tesla with high-resolution peripheral quantitative computed tomography ex vivo and in vivo.** *Osteoporosis International* 2008, **19**(5)**:**653-661.

153. Link TM, Majumdar S, Grampp S, Guglielmi G, Kuijk CV, Imhof H, Glueer C, Adams JE: **Imaging of trabecular bone structure in osteoporosis.** European Radiology 1999, **9**:1781-1788.

154. Majumdar S: **Magnetic resonance imaging for osteoporosis.** *Skeletal Radiology* 2008, **37**(2)**:**95-97.

155. Majumdar S, Genant HK, Grampp S, Jergas MD, Newitt DC, Gies AA: **Analysis of trabecular bone structure in the distal radius using high-resolution MRI.** European Radiology 1994, **4**:517-524.

156. Majumdar S, Genant HK, Grampp S, Newitt DC, Truong VH, Lin JC, Mathur A: **Correlation of Trabecular Bone Structure with Age, Bone Mineral Density, and Osteoporotic Status: In Vivo Studies in the Distal Radius Using High Resolution Magnetic Resonance Imaging.** Journal of Bone and Mineral Research 1997, **12**(1):111-118.

157. Majumdar S, Kothari M, Augat P, Newitt DC, Link TM, Lin JC, Lang T, Lu Y, Genant HK: **High-Resolution Magnetic Resonance Imaging: Three-Dimensional Trabecular Bone Architecture and Biomechanical Properties.** Bone 1998, **22**(5):445-454.

158. Majumdar S, Link TM, Augat P, Lin JC, Newitt D, Lane NE, Genant HK: **Trabecular Bone Architecture in the Distal Radius Using Magnetic Resonance Imaging in Subjects with Fractures of the Proximal Femur.** Osteoporosis International 1999, **10**:231-239.

159. Majumdar S, Newitt D, Jergas M, Gies A, Chiu E, Osman D, Keltner J, Keyak K, Genant H: **Evaluation of technical factors affecting the quantification of trabecular bone structure using magnetic resonance imaging [abstract].** *Bone* 1995; **17:**417-430.

160. Majumdar S, Newitt D, Mathur A, Osman D, Gies A, Chiu E, Lotz J, Kinney J, Genant H: **Magnetic Resonance Imaging of Trabecular Bone Structure in the Distal Radius: Relationship with X-ray Tomographic Microscopy and Biomechanics.** Osteoporosis International 1996, **6**:376-385.

161. Odgaard A: **Three-dimensional methods for quantification of cancellous bone architecture.** Bone 1997, **20**(4):315-328.

162. Wehrli FW, Gomberg BR, Saha PK, Song HK, Hwang SN, Snyder PJ: **Digital Topological Analysis of In Vivo Magnetic Resonance Microimages of Trabecular Bone Reveals Structural Implications of Osteoporosis.** Journal of Bone and Mineral Research 2001, **16**(8):1520-1531.

163. Wehrli FW, Ladinsky GA, Jones C, Benito M, Magland J, Vasilic B, Popescu AM, Zemel B, Cucchiara AJ, Wright AC, Song HK, Saha PK, Peachey H, Snyder PJ: **In Vivo Magnetic Resonance Detects Rapid Remodeling Changes in the Topology of the Trabecular Bone Network After Menopause and the Protective Effect of Estradiol.** Journal of Bone and Mineral Research 2008, **23**(5):730-740.

164. Wehrli FW, Song HK, Saha PK, Wright AC: **Quantitative MRI for the assessment of bone structure and function.** NMR Biomed 2006, **19**(7):731-764.

165. Wehrli FW, Hilaire L, Fernández-Seara M, Gomberg BR, Song HK, Zemel B, Loh L, Snyder PJ: **Quantitative Magnetic Resonance Imaging in the Calcaneus and Femur of Women With Varying Degrees of Osteopenia and Vertebral Deformity Status.** Journal of Bone and Mineral Research 2002, **17**(12):2265-2273.

166. Zuo J, Bolbos R, Hammond K, Li X, Majumdar S: **Reproducibility of the quantitative assessment of cartilage morphology and trabecular bone structure with magnetic resonance imaging at 7 T.** Magn Reson Imaging 2008, **26**(4):560-566.

167. Newitt DC, van Rietbergen B, Majumdar S: **Processing and Analysis of In Vivo High-Resolution MR Images of Trabecular Bone for Longitudinal Studies: Reproducibility of Structural Measures and Micro-Finite Element Analysis Derived Mechanical Properties.** Osteoporosis Int 2002, **13**(4):278-287.

168. Kazakia GJ, Hyun B, Burghardt AJ, Krug R, Newitt DC, de Papp AE, Link TM, Majumdar S: **In Vivo Determination of Bone Structure in Postmenopausal Women: A Comparison of HR-pQCT and High-Field MR Imaging.** Journal of Bone and Mineral Research 2008, **23**(4):463-474.

169. Ladinsky GA, Vasilic B, Popescu AM, Wald M, Zemel BS, Snyder PJ, Loh L, Song HK, Saha PK, Wright AC, Wehrli FW: **Trabecular structure quantified with the MRI-based virtual bone biopsy in postmenopausal women contributes to vertebral deformity burden independent of areal vertebral BMD.** J Bone Miner Res 2008, **23**(1):64-74.

170. Gibbs P, Turnbull LW: **Textural analysis of contrast-enhanced MR images of the breast.** Magnetic Resonance in Medicine 2003, **50**(1):92-98.

171. Haralick RM: **Statistical and structural approaches to texture.** Proceedings of the IEEE 1979, **67**(5):786-804.

172. Haralick RM, Shanmugam K, Dinstein I: **Textural Features for Image Classification.** Systems, Man and Cybernetics, IEEE Transactions on 1973, **3**(6):610-621.

173. Bernard CP, Liney GP, Manton DJ, Turnbull LW, Langton CM: **Comparison of Fat Quantification Methods: A Phantom Study at 3.0 T.** Journal of Magnetic Resonance Imaging 2008, **27**:192-197.

174. Biffar A, Dietrich O, Sourbron S, Duerr H, Reiser MF, Baur-Melnyk A: **Diffusion and perfusion imaging of bone marrow.** Eur J Radiol 2010, **76**(3):323-328.

175. Boesch C, Kreis R: **Observation of Intramyocellular Lipids by ^{1}H-Magnetic Resonance Spectroscopy.** Annals of the New York Academy of Sciences 2006, **904**:25-31.

176. Bouxsein ML: **Bone quality: where do we go from here?** Osteoporosis Int 2003, **14**(0):118-127.

177. Chen WT, Shih TT: **Correlation between the bone marrow blood perfusion and lipid water content on the lumbar spine in female subjects.** J Magn Reson Imaging 2006, **24**(1):176-181.

178. Chen WT, Shih TT, Chen RC, Lo SY, Chou CT, Lee JM, Tu HY: **Vertebral bone marrow perfusion evaluated with dynamic contrast-enhanced MR imaging: significance of aging and sex.** Radiology 2001, **220**(1):213-218.

179. De Bisschop E, Luypaert R, Louis O, Osteaux M: **Fat fraction of lumbar bone marrow using in vivo proton nuclear magnetic resonance spectroscopy.** Bone 1993, **14**(2):133-136.

180. Donnelly E: **Methods for Assessing Bone Quality: A Review.** Clin Orthop Relat Res 2010.

181. Fanucci E, Manenti G, Masala S, Laviani F, Di Costanzo G, Ludovici A, Cozzolino V, Floris R, Simonetti G: **Multiparameter characterisation of vertebral osteoporosis with 3-T MR.** *La Radiologia Medica* 2007, **112**(2)**:**208-223.

182. Griffith JF, Yeung DK, Antonio GE, Wong SY, Kwok TC, Woo J, Leung PC: **Vertebral marrow fat content and diffusion and perfusion indexes in women with varying bone density: MR evaluation.** Radiology 2006, **241**(3):831-838.

183. Griffith JF, Yeung DKW, Ahuja AT, Choy CWY, Mei WY, Lam SSL, Lam TP, Chen ZY, Leung PC: **A study of bone marrow and subcutaneous fatty acid composition in subjects of varying bone mineral density.** Bone 2009, **44**(6):1092-1096.

184. Hans D, Fuerst T, Lang T, Majumdar S, Lu Y, Genant HK, Gluer C: **How can we measure bone quality?** Baillieres Clin Rheumatol 1997, **11**(3):495-515.

185. Hatipoglu HG, Selvi A, Ciliz D, Yuksel E: **Quantitative and Diffusion MR Imaging as a New Method To Assess Osteoporosis.** AJNR Am J Neuroradiol 2007, **28**(10):1934-1937.

186. Herneth AM, Friedrich K, Weidekamm C, Schibany N, Krestan C, Czerny C, Kainberger F: **Diffusion weighted imaging of bone marrow pathologies.** Eur J Radiol 2005, **55**(1):74-83.

187. Hilaire L, Wehrli FW, Song HK: **High-speed spectroscopic imaging for cancellous bone marrow R2∗ mapping and lipid quantification.** Magn Reson Imaging 2000, **18**(7):777-786.

188. Ishijima H, Ishizaka H, Horikoshi H, Sakurai M: **Water Fraction of Lumbar Vertebral Bone Marrow estimated from Chemical Shift Misregistration on MR Imaging: Normal Variations with Age and Sex.** American Journal of Radiology 1996, **167**:355-358.

189. Ishizaka H, Tomiyoshi K, Matsumoto M: **MR Quantification of Bone Marrow Cellularity: Use of Chemical-Shift Misregistration Artifact.** American Journal of Radiology 1993, **160**:572-574.

190. Justesen J, Stenderup K, Ebbesen EN, Mosekilde L, Steiniche T, Kassem M: **Adipocyte tissue volume in bone marrow is increased with aging and in patients with osteoporosis.** Biogerontology 2001, **2**(3):165-171.

191. Kakitsubata Y, Nabeshima K, Kakitsubata S, Watanabe K: **Evaluation of lumbar vertebral bone marrow changes with MR imaging].** Nippon Igaku Hoshasen Gakkai Zasshi 1993, **53**(11):1267-1282.

192. Kugel H, Jung C, Schulte O, Heindel W: **Age-and Sex-Specific Differences in the ^{1}H-Spectrum of Vertebral Bone Marrow.** Journal of Magnetic Resonance Imaging 2001, **13**:263-268.

193. Lendinara L, Accorsi C, Agostini C, Angelini G, Baruffaldi F, Fini M, Motta M, Giavaresi G: **Proton magnetic relaxation in bone marrow related to age and bone mineral density: low-resolution in vitro studies.** Magnetic Resonance Imaging 2001, **19**:745-753.

194. Liney GP, Bernard CP, Manton DJ, Turnbull LW, Langton CM: **Age, gender, and skeletal variation in bone marrow composition: A preliminary study at 3.0Tesla.** Journal of Magnetic Resonance Imaging 2007, **26**(3):787-793.

195. Machann J, Stefan N, Schick F: **1H MR spectroscopy of skeletal muscle, liver and bone marrow.** Eur J Radiol 2008, **67**(2):275-284.

196. Mauricio C: **Diffusion-Weighted Imaging of the Spine: Is It Reliable?** AJNR Am J Neuroradiol 2003, **24**(6):1251-1253.

197. Miyake Y, Yokomizo K, Matsuzaki N: **Determination of unsaturated fatty acid composition by high-resolution nuclear magnetic resonance spectroscopy.** *Journal of the American Oil Chemists' Society* 1998, **75**(9)**:**1091-1094.

198. Noeske R, Schirmer T: **Spectroscopic Determination of Lipid Content in the Presence of Chemical Shift Displacement [abstract].** 2008; .

199. Nonomura Y, Yasumoto M, Yoshimura R, Haraguchi K, Ito S, Akashi T, Ohashi I: **Relationship between bone marrow cellularity and apparent diffusion coefficient.** Journal of Magnetic Resonance Imaging 2001, **13**(5):757-760.

200. Raya JG, Dietrich O, Reiser MF, Baur-Melnyk A: **Techniques for diffusion-weighted imaging of bone marrow.** Eur J Radiol 2005, **55**(1):64-73.

201. Ren J, Dimitrov I, Sherry DA, Malloy CR: **Composition of adipose tissue and marrow fat in humans by 1H NMR at 7 Tesla.** Journal of Lipid Research 2008, **49**(9):2055-2062.

202. Rozman M, Mercader JM, Aguilar JL, Montserrat E, Rozman C: **Estimation of bone marrow cellularity by means of vertebral magnetic resonance.** Haematologica 1997, **82**(2):166-170.

203. Schellinger D, Lin CS, Fertikh D, Lee JS, Lauerman WC, Henderson F, Davis B: **Normal lumbar vertebrae: anatomic, age, and sex variance in subjects at proton MR spectroscopy--initial experience.** Radiology 2000, **215**(3):910-916.

204. Schellinger D, Lin CS, Hatipoglu HG, Fertikh D: **Potential Value of Vertebral Proton MR Spectroscopy in Determining Bone Weakness.** American Journal of Neuroradiology 2001, **22**:1620-1627.

205. Schellinger D, Lin CS, Lim J, Hatipoglu HG, Pezzullo JC, Singer AJ: **Bone Marrow Fat and Bone Mineral Density on Proton MR Spectroscopy and Dual-Energy X-Ray Absorptiometry: Their Ratio as a New Indicator of Bone Weakening.** Am J Roentgenol 2004, **183**(6):1761-1765.

206. Schick F: **Bone marrow NMR in vivo.** Prog Nucl Magn Reson Spectrosc 1996, **29**(3-4):169-227.

207. Schick F: **The distribution of the magnetic field in the spine depends on the composition of bone marrow.** J Magn Reson B 1995, **108**(1):1-11.

208. Schmidt GP, Reiser MF, Baur-Melnyk A: **Whole-body imaging of bone marrow.** Semin Musculoskelet Radiol 2009, **13**(2):120-133.

209. Shen W, Chen J, Punyanitya M, Shapses S, Heshka S, Heymsfield S: **MRI-measured bone marrow adipose tissue is inversely related to DXA-measured bone mineral in Caucasian women.** *Osteoporosis International* 2007, **18**(5)**:**641-647.

210. Shih TTF, Liu HC, Chang CJ, Wei SY, Shen LC, Yang PC: **Correlation of MR Lumbar Spine Bone Marrow Perfusion with Bone Mineral Density in Female Subjects1.** Radiology 2004, **233**(1):121-128.

211. Siegel MJ: **MRI of Bone Marrow.** American Roentgen Ray Society 2005, :169-179.

212. Tang GY, Lv ZW, Tang RB, Liu Y, Peng YF, Li W, Cheng YS: **Evaluation of MR spectroscopy and diffusion-weighted MRI in detecting bone marrow changes in postmenopausal women with osteoporosis.** Clin Radiol 2010, **65**(5):377-381.

213. Traber F, Block W, Layer G, Braucker G, Gieseke J, Kretzer S, Hassan I, Schild HH: **Determination of 1H Relaxation Times of Water in Human Bone Marrow by Fat-Suppressed Turbo Spin Echo in Comparison to MR Spectroscopic Methods.** Journal of Magnetic Resonance Imaging 1996, **6**(3):541-548.

214. Wehrli FW, Ford JC, Chung HW, Wehrli SL, Williams JL, Grimm MJ, Kugelmass SD, Jara H: **Potential role of nuclear magnetic resonance for the evaluation of trabecular bone quality.** Calcif Tissue Int 1993, **53 Suppl 1**:S162-9.

215. Weis J, Ciray I, Ericsson A, Lindman H, Astrom G, Ahlstrom H, Hemmingsson A: **Spectroscopic imaging of bone marrow composition in vertebral bodies.** MAGMA 2001, **13**(1):15-18.

216. Weiss KL, Sun D, Cornelius RS, Weiss JL: **Iterative Decomposition of Water and Fat with Echo Asymmetric and Least-Squares Estimation (IDEAL) Automated Spine Survey Iterative Scan Technique (ASSIST).** Magnetic Resonance Insights 2008, **1**:3-8.

217. Yeung DKW, Griffith JF, Antonio GE, Lee FKH, Woo J, Leung PC: **Osteoporosis is associated with increased marrow fat content and decreased marrow fat unsaturation: A proton MR spectroscopy study.** Journal of Magnetic Resonance Imaging 2005, **22**(2):279-285.

218. Yeung DKW, Lam SL, Griffith JF, Chan ABW, Chen Z, Tsang PH, Leung PC: **Analysis of bone marrow fatty acid composition using high-resolution proton NMR spectroscopy.** Chem Phys Lipids 2008, **151**(2):103-109.

219. Yeung DKW, Wong SYS, Griffith JF, Lau EMC: **Bone marrow diffusion in osteoporosis: Evaluation with quantitative MR diffusion imaging.** Journal of Magnetic Resonance Imaging 2004, **19**(2):222-228.

220. Zhang CY, Rong R, Wang XY: **Age-related changes of bone marrow of normal adult man on diffusion weighted imaging.** Chin Med Sci J 2008, **23**(3):162-165.

221. Bandeira FF, Miranda CR, Waechter C, Bandeira ME: **High bone mass associated with berardinelli lipodystrophy.** Endocr Pract 2007, **13**(7):764-769.

222. Gong Y, Slee RB, et al: **LDL Receptor-Related Protein 5 (LRP5) Affects Bone Accrual and Eye Development.** Cell 2001, **107**(4):513-523.

223. Johnson ML, Gong G, Kimberling W, Recker SM, Kimmel DB, Recker RR: **Linkage of a Gene Causing High Bone Mass to Human Chromosome 11 (11q12-13).** The American Journal of Human Genetics 1997, **60**(6):1326-1332.

224. Little RD, Folz C, Manning SP, Swain PM, Zhao SC, Eustace B, Lappe MM, Spitzer L, Zweier S, Braunschweiger K, Benchekroun Y, Hu X, Adair R, Chee L, FitzGerald MG, Tulig C, Caruso A, Tzellas N, Bawa A, Franklin B, McGuire S, Nogues X, Gong G, Allen KM, Anisowicz A, Morales AJ, Lomedico PT, Recker SM, Van Eerdewegh P, Recker RR, Carulli JP, Del Mastro RG, Dupuis J, Osborne M, Johnson ML: **A Mutation in the LDL Receptor–Related Protein 5 Gene Results in the Autosomal Dominant High–Bone-Mass Trait.** The American Journal of Human Genetics 2002, **70**(1):11-19.

225. Patel MS, Karsenty G: **Regulation of Bone Formation and Vision by LRP5.** N Engl J Med 2002, **346**(20):1572-1574.

226. Qiu W, Andersen TE, Bollerslev J, Mandrup S, Abdallah BM, Kassem M: **Patients with high bone mass phenotype exhibit enhanced osteoblast differentiation and inhibition of adipogenesis of human mesenchymal stem cells.** J Bone Miner Res 2007, **22**(11):1720-1731.

227. Boyden LM, Mao J, Belsky J, Mitzner L, Farhi A, Mitnick MA, Wu D, Insogna K, Lifton RP: **High Bone Density Due to a Mutation in LDL-Receptor–Related Protein 5.** N Engl J Med 2002, **346**(20):1513-1521.

228. Gonzalez RC, Woods RE, Eddins SL: *Digital Image Processing Using MATLAB:* USA: Prentice Hall; 2003.

229. Jiru F: **Introduction to post-processing techniques.** European Journal of Radiology 2008, **67**:202-217.

230. Otsu N: **A Threshold Selection Method from Gray-Level Histograms.** Systems, Man and Cybernetics, IEEE Transactions on 1979, **9**(1):62-66.

231. Bharati MH, Liu JJ, MacGregor JF: **Image texture analysis: methods and comparisons.** Chemometrics Intellig Lab Syst 2004, **72**(1):57-71.

232. Herlidou S, Grebe R, Grados F, Leuyer N, Fardellone P, Meyer ME: **Influence of age and osteoporosis on calcaneus trabecular bone structure: a preliminary in vivo MRI study by quantitative texture analysis.** Magn Reson Imaging 2004, **22**(2):237-243.

233. Herlidou S, Peretti II, Grebe R, Grados F, Lecuyer N, Fardellone P: **Quantitative Evaluation of Trabecular Bone Structure by Calcaneus MR Images Texture Analysis of Healthy volunteers and Osteoporotic Subjects.** 2001, :2340-2342.

234. Field A: *Discovering Statistics using SPSS:* 3rd ed. SAGE; 2009.

235. Gardner MJ, Altman DG: *Statistics With Confidence - Confidence intervals and statistical guidelines:* UK: British Medical Journal; 1993.

236. Howell DC: *Satistical Methods for Psychology:* 1st ed. USA: PWS; 1982.

237. Zhao LJ, Jiang H, Papasian CJ, Maulik D, Drees B, Hamilton J, Deng HW: **Correlation of obesity and osteoporosis: effect of fat mass on the determination of osteoporosis.** J Bone Miner Res 2008, **23**(1):17-29.

238. Jones C, Wehrli SL, Magland J, Wehrli FW: **Spatially resolved measurement of bone marrow fat content and unsaturation index via spectroscopic MR imaging [abstract].** 2007.

239. Brufsky AM: **Cancer Treatment-Induced Bone Loss: Pathophysiology and Clinical Perspectives.** Oncologist 2008, **13**(2):187-195.

240. Deux J, Malzy P, Paragios N, Bassez G, Luciani A, Zerbib P, Roudot-Thoraval F, Vignaud A, Kobeiter H, Rahmouni A: **Assessment of calf muscle contraction by diffusion tensor imaging.** *European Radiology* 2008, **18**(10)**:**2303-2310.

241. Boesch C, Machann J, Vermathen P, Schick F: **Role of proton MR for the study of muscle lipid metabolism.** NMR in Biomedicine 2006, **19**:968-988.

242. Škoch A, Jirák D, Vyhnanovská P, Dezortová M, Fendrych P, Rolencová E, Hájek M: **Classification of calf muscle MR images by texture analysis.** *Magnetic Resonance Materials in Physics, Biology and Medicine* 2004, **16**(6)**:**259-267.

243. May DA, Disler DG, Jones EA, Balkissoon AA, Manaster BJ: **Abnormal Signal Intensity in Skeletal Muscle at MR Imaging: Patterns, Pearls, and Pitfalls1.** Radiographics 2000, **20**(suppl 1):S295-S315.

244. Rittweger J, Beller G, Ehrig J, Jung C, Koch U, Ramolla J, Schmidt F, Newitt D, Majumdar S, Schiessl H, Felsenberg D: **Bone-muscle strength indices for the human lower leg.** Bone 2000, **27**(2):319-326.